

**Synthesis,
Structural Characterisation
and Self Assembly
of Nanoparticles.**

by

John D. Watt

A thesis

submitted to the Victoria University of Wellington

in fulfillment of the

requirements for the degree of

Doctor of Philosophy

in Chemistry

Victoria University of Wellington

August 2010

'When the going gets weird, the weird turn pro.'

Hunter S. Thompson

Abstract

This thesis is concerned with the synthesis, structural characterisation and self assembly of various nanocrystalline materials. These materials include gold, lead sulfide and lead selenide with substantial focus given to the noble metal palladium. The aim of this research was to obtain size and shape control over nanoparticles formed from solution phase synthesis for various applications. This was realised with chemical techniques using organic surfactants as growth controlling agents. The morphology, composition, internal crystal structure and applicable properties of the as synthesised nanoparticles were fully investigated to give a complete characterisation. Characterisation was carried out using a number of techniques including Super and High Resolution Transmission Electron Microscopy (SHREM, HREM), Synchrotron Powder X-Ray Diffraction (XRD), Selected Area Electron Diffraction (SAED) and Energy Dispersive X-Ray Spectroscopy (EDS).

The first chapter in this thesis focuses on the synthesis and self assembly of monodisperse gold nanoparticles into nanoparticle superlattices (NPSLs), an exciting new type of material. The nanoparticles were prepared using a well known chemical method at room temperature. They were then arranged into NPSLs by a simple evaporation technique. Intermediate structures to the SLs were isolated which gave an insight into their formation. This showed that the NPs first self assembled into an energetically unfavourable bilayer before forming the most thermodynamically preferred three dimensional structure. This behaviour was due to the presence of organic capping ligands.

The second chapter is concerned with the synthesis and characterisation of lead chalcogenide nanoparticles (lead sulfide and lead selenide). These are semiconductor materials which can provide a photocurrent when illuminated with infra-red radiation

which makes them ideal candidates for solar cell technology. The nanoparticles were synthesised using a bench top solvothermal method. By varying the nature of the surfactant system, the precursor and the reaction time and temperature a wide range of nanoparticles with different sizes and shapes were prepared. A type of lead sulfide nanoparticles was then chosen for capping ligand exchange experiments. The new method developed here provides a facile route to water soluble lead chalcogenide nanoparticles and a means to more easily extract a photocurrent when used in solar cell applications.

The remainder of this thesis is focussed on the synthesis and structural characterisation of palladium nanoparticles. Palladium is a very important catalytic metal therefore control over its size and shape on the nanoscale is of primary concern. In the third chapter of this thesis various types of palladium nanoparticles were produced using solution phase techniques in a pressure reaction vessel. By varying the nature of the surfactant system, the precursor and the reaction pressure, temperature and time the size and shape of the resulting nanoparticles could be controlled. These included spherical and worm-like nanoparticles as well as novel pod-like and highly branched palladium nanostructures. These complex shapes were the first evidence of this kind of morphology for palladium and provide a new and exciting material for catalytic applications.

The final chapter in this thesis features a full structural characterisation and growth mechanism for the novel, complex palladium nanostructures along with an investigation into their catalytic and hydrogen absorption properties. The structural characterisation of a palladium tripod provides the first direct evidence of complex growth from a symmetrical nanoparticle core possessing the face centred cubic crystal structure. The growth of the highly branched palladium nanostructures is then tracked in real time. It is shown that the growth involves the formation of nuclei followed by tripod intermediates and finally highly branched nanostructures. By varying the nature of the surfactant

system the kinetics of the reaction and hence the morphology of the resulting nanostructures can be controlled. A full growth mechanism is therefore proposed. The catalytic activity of the highly branched palladium nanostructures towards a simple organic transformation reaction is investigated. Finally, the hydrogen absorption and desorption properties of the highly branched nanostructures is explored. The results presented here regarding palladium nanoparticles are applicable to other industrially important noble metals such as gold, silver and platinum.

A final conclusion chapter is then presented along with ideas for future research.

Acknowledgements

This thesis would not have been possible without the help of a long list of people. In particular I would like to thank;

My supervisor Dr Richard Tilley for his direction in performing this research. I would also like to thank Richard for his invaluable guidance in the forming and nurturing of working relationships and in the writing of scientific literature.

My co-supervisor and Head of School Prof John Spencer for discussions regarding the organometallic aspects of this research and for his ongoing support throughout.

David Flynn for his ongoing and invaluable support with the Electron Microscopes.

Prof Angus Kirkland, Dr Neil Young and Dr Sarah Haigh from Oxford University's Department of Materials.

Dr Mike Toney and Dr Bridget Ingham from Stanford Synchrotron Radiation Lightsource.

Dr James Cookson and Dr Peter Bishop from Johnson Matthey.

The entire Tilley Research Group for their discussions and ongoing support in particular Soshan Cheong, Amane Shiohara and Sujay Prabaker.

The General Staff of the School of Chemical and Physical Sciences for all their help over the past 3 years.

All other students in the School of Chemical and Physical Sciences who have helped me along the way.

And finally, my family and friends for their moral and financial support throughout my student life.

Table of Contents

Abstract	ii
Acknowledgments	v
Table of Contents	vi
Chapter 1 : Introduction	1
1.1 General Overview	1
1.2 General Synthetic Considerations	3
1.3 Semiconductors	6
1.4 Noble Metals	13
1.5 Palladium	17
1.6 Superlattices	21
References	24
Chapter 2 : Characterisation Techniques	25
2.1 High Resolution Transmission Electron Microscopy (HREM)	26
2.2 Diffraction Theory and Application	31
2.2.1 Selected Area Electron Diffraction (SAED)	33
2.2.2 Synchrotron X-Ray Diffraction (XRD)	34
2.3 Energy Dispersive X-Ray Spectroscopy (EDS)	36
References	38

Chapter 3 : Nanoparticle Superlattices (NPSL)	42
3,1 Synthesis and Characterisation of Gold Nanoparticles	43
3.2 Formation of Gold Nanoparticle Superlattices (NPSL)	45
3.2.1 Effect of size distribution on the formation of Gold NPSL	45
3.2.2 Effect of concentration on the formation of Gold NPSL	50
3.3 Discussion on Formation of Gold NPSL	56
3.4 Summary	60
References	61
Chapter 4 : Solution Phase Syntheses of Lead Chalcogenide Nanoparticles	62
4,1 Solution Phase Syntheses of PbSe Nanoparticles	63
4.2 Solution Phase Syntheses of PbS Nanoparticles	78
4.2.1 Reactions of Pb(Ac) ₂ in Hexadecylamine (HDA)	78
4.2.2 Reactions in Oleylamine (OLA)	85
4.3 Capping Exchange Experiments on PbS Nanoparticles	97
4.4 Summary	103
References	104
Chapter 5 : Solution Phase Syntheses of Palladium Nanostructures	106
5,1 Reactions with Pd(PPh ₃) ₄	107
5.2 Reactions with [PdCl ₂ (NCMe) ₂]	118
5.3 Reactions with [PdCl ₂ (NCMe) ₂] at Room Temperature : Changing the Surfactant System and Structural Evolution	128
5.4 Reactions with [PdCl ₂ (NCMe) ₂] : Effect of Surfactant System	148
5.5 Summary	158
References	159

Chapter 6 : Full Characterisation and Growth Mechanism of Palladium Nanostructures	161
6.1 Super High Resolution Electron Microscopy (SHREM) of Palladium Tripod Nanoparticles	162
6.2 Super High Resolution Electron Microscopy (SHREM) of Other Interesting Morphologies	172
6.3 In-Situ Synchrotron X-ray Diffraction Studies on the Growth of Palladium Nanostructures	177
6.4 Growth Mechanism for the Formation of Highly Branched Palladium Nanostructures	191
6.5 Catalytic Studies of Highly Branched Palladium Nanostructures	197
6.6 In-Situ Synchrotron X-ray Diffraction Studies on the Formation of Palladium Hydride	201
6.7 Summary	212
References	214
Chapter 7 : Conclusions and Future Work	216
7,1 Nanoparticle Superlattices	216
7.2 Solution Phase Syntheses of Lead Chalcogenide Nanoparticles	217
7.3 Synthesis, Characterisation and Growth of Palladium Nanoparticles	218
References	221
Appendix	222

Chapter 1. Introduction

1.1 General Overview

Due to substantial interest over the past decade, there is now a significant amount of well-developed synthetic methodology for the production of differing nanocrystalline species. Due to their small size (typically 1 – 100 nm), nanoparticles can exhibit unique electronic and physical properties to the corresponding bulk phase. The field has been extensively pursued, not only for their many technological applications but also for their fundamental scientific interest {Klabunde 2001}. The boundaries between the molecular, nanocrystalline and bulk regimes are material dependant and cannot be wholly defined. However, a range of around 100 to 10 000 atoms per nanoparticle can be considered as a rough estimate of sizes for which the nanocrystalline regime occurs. At this length scale the surface area to volume ratio of the material is exceedingly large. Therefore the surface becomes very important in determining the properties of the system; that is, the materials properties can be manipulated by varying the size and shape of the nanoparticles.

The main goal in nanoparticle synthesis is the formation of nanoparticles with uniform size, morphology, composition, internal structure and surface chemistry. This is critical to the interpretation of most characterisation techniques and essential to successfully mapping their size dependant properties. Recently, there has been substantial focus on the shape control of nanoparticles into complex morphologies such as rods, wires and branched 'pod-like' structures, as materials with designable properties become a possibility.

The research literature concerning synthesis of nanoparticles is extensive and envelopes a wide array of chemical and physical techniques which are broadly separated into the 'top-down' approach, which utilises physical methods and the 'bottom-up' approach, which employs solution phase colloidal chemistry. Physical methods often result in a large yield however size and morphology control is limited. Solution phase chemical techniques can be used to synthesise nanoparticles with controlled size and morphology due to the use of organic surfactant molecules.

Surfactant molecules play a dual role in nanoparticle synthesis, i) they can act as inhibitors in the growth stage thereby controlling the nanoparticle size and ii) they can act as capping agents for the formed nanoparticles, enabling facile dispersion in a target solvent. This enables the synthesis of uniform nanoparticles that can, for instance; be easily deposited on a substrate, added as additives in polymeric coatings or used in biological applications. Surfactant mediated synthetic methods include; the use of inverse micelles, the hot injection method and Fischer-Porter bottle synthesis. There are general synthetic aspects common to all solution phase syntheses that enable the formation of a uniform sample. To prepare monodisperse spherical nanocrystals it is essential to induce a single nucleation event and prevent additional nucleation during the subsequent growth regime. This is commonly referred to as 'burst nucleation' and 'the separation of nucleation and growth' {Peng 1998, Peng 2002}.

The aim of the project is to employ solution phase chemical techniques to synthesise various monodisperse nanocrystalline materials including Au, PbS, PbSe and Pd. These will be utilised for further applications including the formation of superlattices and for use in solar cells. Special attention will be placed on morphology control of Pd nanoparticles in an attempt to enhance catalytic activity. Structural investigation will involve Super and High Resolution Transmission Electron Microscopy (SHREM, HREM), Synchrotron Powder X-Ray Diffraction (XRD), Selected Area Electron Diffraction (SAED) and Energy Dispersive X-Ray Spectroscopy (EDS).

1.2 General Synthetic Considerations

The separation of nucleation and growth has been demonstrated in synthetic procedures that undergo both heterogeneous and homogeneous nucleation. This is most easily realised in heterogeneous nucleation where a seed mediated growth mechanism physically separates the two regimes. Here, preformed nuclei are introduced into the reaction solution and monomer is supplied to enable growth. The additional monomer concentration is kept below the critical homogenous nucleation concentration to suppress additional nucleation. In the target syntheses for this project, homogeneous nucleation is the main process and will be discussed below.

The concept of 'burst nucleation' in homogeneous systems was proposed by LaMer and colleagues who also developed the LaMer plot, a useful tool for visualizing burst nucleation {La Mer 1950}.

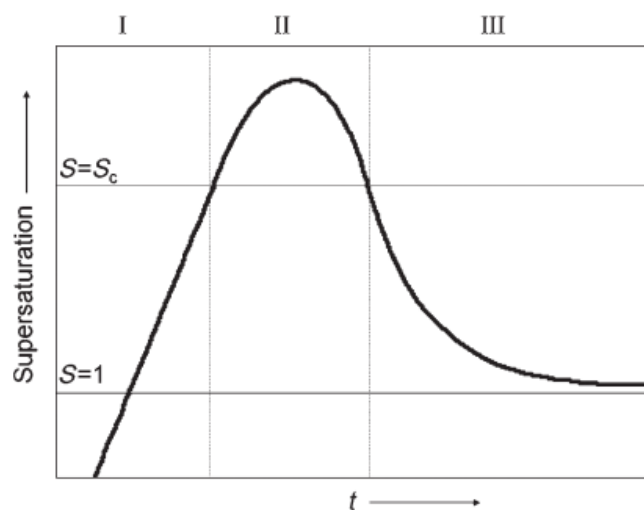


Figure 1. La Mer plot showing the change of degree of supersaturation over time {Park 2007}.

In stage I the concentration of monomer steadily increases with time due to either reduction or decomposition of precursor. The energy barrier for homogeneous nucleation is large enough that not all levels of supersaturation will induce nucleation. In stage II the degree of supersaturation is high enough to overcome this energy barrier and nucleation occurs. Nuclei form which reduces the monomer concentration. When the residual monomer concentration falls below the critical nucleation concentration, no new nuclei are formed and the system enters stage III, the growth stage. Here the nanoparticle concentration reaches a maximum and all residual monomer is used for growth.

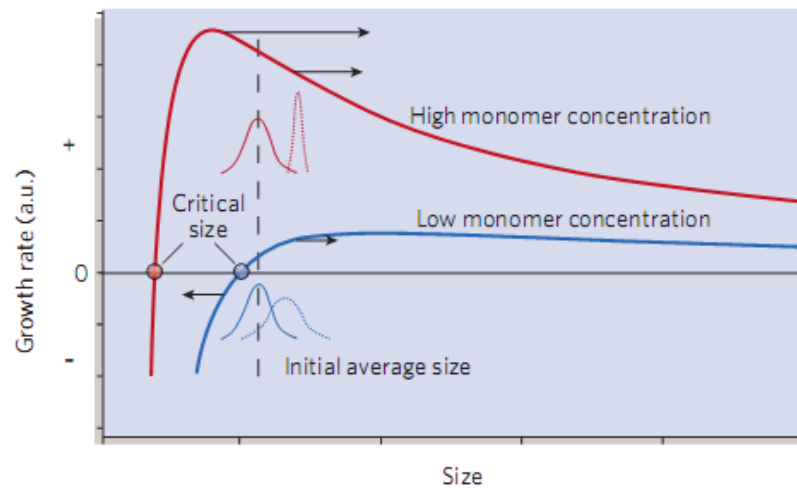


Figure 2. Shows the growth process of nanoparticles as a function of monomer concentration and critical size {Yin 2005}.

The degree of supersaturation has previously been strongly correlated to the size distribution by the Alivisatos group {Peng 1998}. They observed a fast increase in nanoparticle size and a simultaneous narrowing of the size distribution in the early stages of growth followed by an increase in the polydispersity as the growth rate decreases. An injection of further precursor in the late stages of growth again induced the preferred effect seen in the initial period.

The narrowing of the size distribution can be understood by considering the dependence of the growth rate on the average size of the nanocrystal as shown in Fig 2. Nanoparticles with radii on the left hand side of the curve are unstable and experience a negative growth rate, or dissolution, due to a large percentage of high energy surface atoms. Nanoparticles with radii on the right hand side of the curve experience a positive growth rate. The point at which neither dissolution nor growth occurs is called the critical size and is dependent on the monomer concentration.

In a low monomer concentration regime, growth is slow and the critical size is likely to lie within the distribution of nanoparticle sizes. This results in Ostwald ripening – where the smaller nanoparticles dissolve and the resultant monomer is added to the growth of the larger nanoparticles – resulting in a broad size distribution {Yin 2005}.

The size distribution can be narrowed by the rapid addition of more monomer which results in a high monomer concentration regime. This shifts the critical size to a smaller value which may be smaller than the average nanoparticle size. This means that all the nanoparticles are now larger than the critical size and positive growth occurs. A narrowing of the size distribution is realised as smaller nanoparticles are known to grow more rapidly than larger ones in high monomer concentration {Reiss 1951}.

Lately, more focus has been placed on morphology control of nanoparticles as materials with designable chemical and physical properties become possible. For example; the exposing of different crystal facets in Pt nanoparticles to enhance catalytic activity or the tuning of longitudinal and transverse surface plasmon resonances in noble metal rods and wires {Tian 2007, Murphy 2008}. The two main explanations for morphology control are the specific binding of surfactant molecules to different crystal facets and the introduction of twinning in the nanoparticle nuclei. The surface energy of a crystal facet is important as the energy barrier to monomer addition is inversely proportional to the surface energy so higher energy crystallographic faces grow faster {Lee 2003}. By the addition of a surfactant molecule that selectively binds to a specific facet, you can lower the energy of that face and promote the growth of the unbound facets. This has been used as an explanation for the formation of PbS cubes, rods and multi-pods with the selective addition of dodecanethiol {Lee 2002}. Twinning in nanoparticle nuclei has been demonstrated to yield varying morphologies of Pd and Pt nanoparticles where the degree of twinning is mainly determined by the reduction rate of the precursor {Xiong 2007 (a)}.

Post-synthetic purification is essential to removing excess surfactant as this can reduce the efficiency of the nanoparticles target properties e.g., photoluminescence can be quenched or it can reduce access to the surface of catalytically active materials. The nanoparticles may be purified by adding a small amount of non-solvent that is miscible with the original solvent, e.g. ethanol to a solution of nanoparticles dispersed in hexane. This increases the interparticle attraction and causes the nanoparticles to precipitate out. The solution can then be centrifuged, the supernatant discarded and the nanoparticles dispersed in the required solvent, e.g. hexane, toluene, dichloromethane etc. Since the adsorption of the capping ligand is dynamic there

needs to be a small excess in solution to ensure solubility. Other methods of purification include liquid-liquid phase separation and size exclusion high performance liquid chromatography (HPLC) {Tilley 2006, Wilcoxon 2006}.

1.3 Semiconductors

When semiconductor materials are synthesised on the nanoscale, electronic and optical properties can be observed which are not seen in the bulk phase. The properties of these so called 'quantum dots' (QDs) can be explained by the quantum confinement effect.

The band gap of a material can be defined as the difference in energy between the valence and conduction bands and is typically in the range of 1.5 – 3 eV for a semiconductor. When an electron is promoted to the conduction band a hole remains in the valence band leading to an electron-hole pair or exciton. In a bound state the electron-hole interaction occurs over a material dependant length scale, termed the Bohr radius, which is determined by the strength of their Coulombic interaction {Klimov 2006}.

If the physical nanoparticle diameter reduces below the Bohr radius, the energy levels in the conduction and valence band become discrete (Fig 3). In addition, the exciton becomes spatially confined and the materials band gap (E_g) increases resulting in a 'blue shift' of the optical properties. In semiconductor materials, the blue shift becomes significant when nanoparticles are reduced to between 1 and 10 nm in size. The quantum confinement effect can be thought of as analogous to the 'particle in a box' phenomenon which is why QDs are often referred to as 'artificial atoms'.

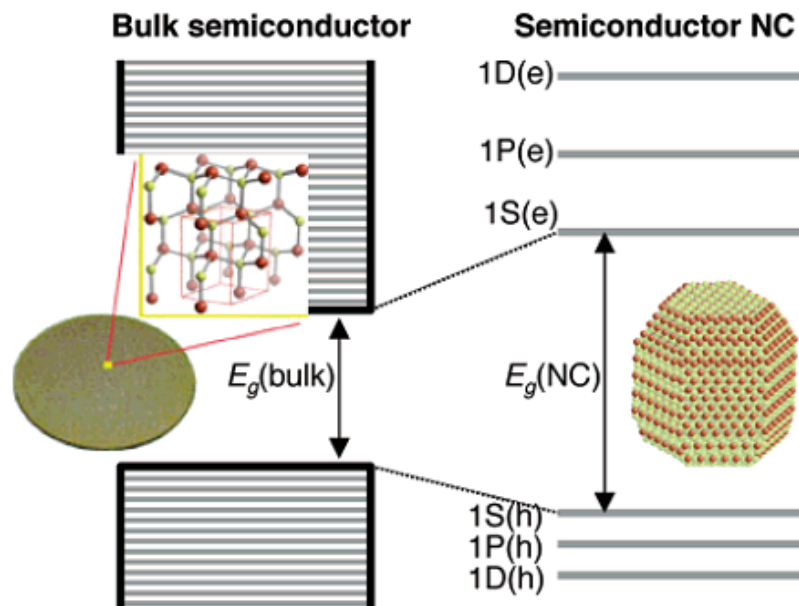


Figure 3. Bulk semiconductors have continuous conduction and valence bands with a fixed energy gap, E_g , in contrast to nanoparticles which have discrete energy levels and a size dependant E_g {Klimov 2007}.

The first evidence of photoluminescence from nanoscale semiconductor QDs was in 1993 from the Bawendi group who produced CdE (E = S, Se, Te) nanocrystals from a synthetic procedure involving the high temperature thermolysis of precursors {Murray 1993}. The hot injection method used involved the rapid injection of a cold trioctylphosphine (TOP) solution containing Cd and the chalcogenide precursors into a hot trioctylphosphine oxide (TOPO) solution. This created a supersaturated solution that was relieved by a burst of nucleation. The overall monomer concentration dropped below the critical nucleation concentration and concomitantly the temperature was lowered which suppressed any subsequent nucleation events. All residual monomer was therefore used for growth. With post preparative size selection processes they were able to reduce the polydispersity to $\sigma = 5\%$. The nanoparticles formed ranged in size from ~ 1.2 nm to 11.5 nm and displayed a variation in emission wavelength of ~ 410 nm to ~ 680 nm, indicating size dependant electronic transitions.

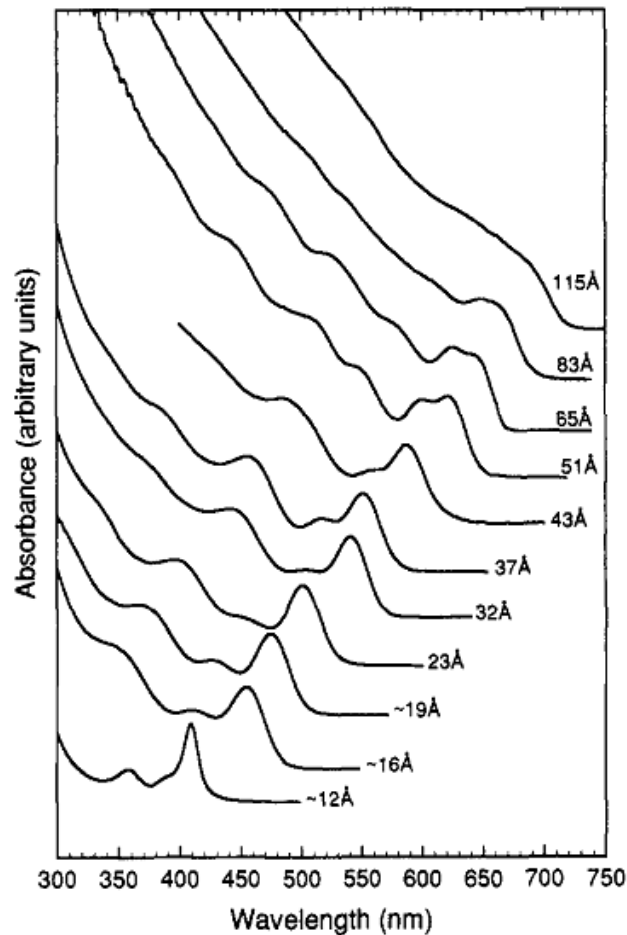


Figure 4. Room temperature optical absorption spectra of CdSe nanoparticles dispersed in hexane and ranging in size from 1.2 nm to 11.5 nm {Murray 1993}.

By controlled addition of hexadecylamine (HDA), Weller and co-workers were able to improve on the synthesis and gain a polydispersity of only $\sigma = 4\%$ without post preparative size selection procedures {Talpin 2001}. This outlines the importance of the proper choice of coordinating surfactants in controlling growth. Bulkier surfactants provide greater steric hindrance and hence slow nanoparticle growth. For example, tributylphosphines provide smaller nanoparticles than triphenylphosphines {Park 2005}. Certain capping species may be useful for controlling growth but ineffective at enabling adequate dispersion. Therefore a mixture of trialkylphosphines and carboxylic acids can be used to allow the nanoparticles sufficient freedom to grow whilst limiting aggregation {Sun 1999}. An increase in concentration ratio of surfactant to precursor can promote the formation of a greater number of smaller nuclei and hence a smaller nanoparticle size {Murray 2001}.

Lead chalcogenide (IV-VI) semiconductor nanocrystals are infrared (IR) emitting nanoparticles that are promising candidates for many applications including;

fluorescent contrast agents for biomedical imaging, photodetectors, photovoltaic cells and optical amplification media for telecommunications system {Sargent 2005}. Lead chalcogenide nanoparticles have been synthesised in varying morphologies including spheres, cubes, rods, hollow spheres, stars and dendritic structures {Rogach 2007}. Since they are photoactive in the IR they show potential for harvesting the 45% of terrestrial solar radiation that lies in this region of the spectrum {Lopez-Luke 2008}. Lead chalcogenides nanocrystals have several advantages that make them promising materials. They possess direct band gap transitions and have relatively narrow band gaps (0.41, 0.278 and 0.31 eV for PbS, PbSe and PbTe respectively). In a direct band-gap semiconductor the conduction and valence bands are directly above one another in space and therefore recombination can occur with conservation of momentum. An indirect band-gap semiconductor involves loss of momentum of the carrier through the emission of a phonon (a quantum of heat manifested as the excitation of molecular or lattice vibrations). This is a non radiative process and results in weak emission strength. So direct band gap transitions typically have stronger emission strength and are preferred for optical applications. The materials have large exciton Bohr radii, 18 nm and 46 nm for PbS and PbS respectively, meaning that strong quantum confinement effects can be seen in relatively large nanoparticles. They also crystallize in the simple face centred cubic (*fcc*) crystal structure, which enables ease of imaging and characterization.

The first reported hot injection synthesis of PbSe was by Murray et al in 2001 by injecting trioctylphosphine selenide (TOPSe) into a solution of lead oleate, with diphenyl ether as a solvent under nitrogen {Murray 2001}. By varying the temperature from 90 – 220 °C they were able to tune the nanoparticle size from 3.5 nm to 15 nm. They also observed the characteristic blue shift of the absorption edge in the resulting absorption spectra. Guyot-Sionnest used this system to investigate the optical transitions and determined a quantum yield of up to 85 % - around 180 times that of the most efficient and stable IR dye {Wehrenberg 2002}. This work was followed by the formation of solution phase synthesized PbS nanocrystals which employed oleic acid and TOP as the surfactants and was carried out in various high boiling point organic solvents {Hines 2003}. The importance in the choice of the right precursor was outlined by Houtepen et al in their synthesis of PbSe nanoparticles. They showed that to obtain spherical nanoparticles the use of Pb-oleate precursor completely free of acetate was essential. The presence of acetate causes star shaped

nanoparticles to form through an oriented attachment mechanism due to the PbSe nanoparticles inherent dipole moment {Houtepen 2006}.

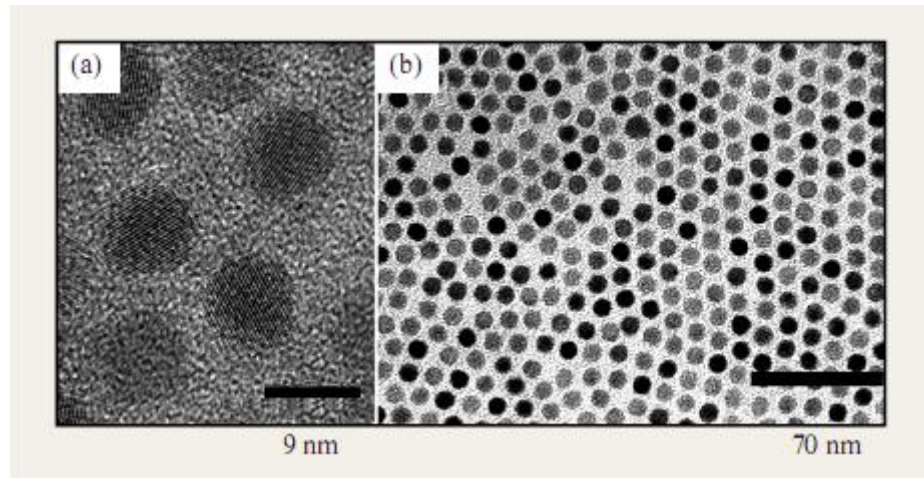


Figure 5. TEM images of PbSe nanoparticles at; (a) high resolution showing lattice fringes and (b) low resolution displaying the monodispersity of the sample {Murray 2001}.

The photoluminescence of a semiconductor nanoparticle is related to the breaking of crystal symmetry at the nanoparticle surface and therefore the condition of the surface can affect quantum efficiency. Trap states that exist on the surface, for example, crystal defects such as steps can cause non-radiative recombination. Organic capping ligands serve to reduce the number of trap states at the surface and provide electronic passivation of surface dangling bonds. However, epitaxial growth of an inorganic material with higher E_g onto the surface of the QD can more effectively reduce phonon-assisted recombination. These so called ‘core-shell’ structures have been synthesised from many materials including PbSe/PbS and CdSe/CdTe {Cui 2007, Chin 2007, Koktysh 2007}. The dominant mode of exciton deactivation in semiconductor nanoparticles is Auger recombination. Auger recombination is a non-radiative process where the energy released from an electron-hole recombination is not emitted as a photon but is transferred to a third particle (electron or hole) which is shifted to a higher energy. This decay has a relatively low efficiency in bulk systems but is enhanced in quantum confined nanoparticles {Klimov 2007}. While this effect reduces the efficacy of QDs in photovoltaic applications, the understanding of Auger decay has been an important step to understanding the fundamentals behind nanoparticle lasers {Klimov 2000, Schaller 2006}.

The usual assumption is that the absorption of one photon by a semiconductor produces one exciton with the photon energy in excess of E_g dissipated as phonons.

This indicates that the quantum efficiency for one photon is either 100 % or 0 % {Schaller 2006}. However, this limit can be overcome through carrier multiplication where one photon with energy $\hbar\omega > 2E_g$ can potentially produce two excitons with the number of generated excitons increasing by one as the photon energy increases by E_g . While this effect occurs with low efficiencies in bulk semiconductors, it becomes extremely efficient in ultra-small semiconductors {Schaller 2004}. Quantum yields of 300 % have been shown for PbS and PbSe QDs where the threshold for multiple exciton generation was twice the lowest absorption energy {Ellingson 2005}. This was improved upon by Schaller et al who showed photon to exciton conversion efficiencies of up to 700 %, reducing the energy loss due to heat by 80 % {Schaller 2006}. This has positive implications for the production of QD solar cells. The current maximum power conversion efficiency from a single junction solar cell is ~ 30 % based on the assumption that one exciton is produced per photon {Shockley 1961}. With carrier multiplication this can be increased to 42 % with a quantum yield of 200 % and 43 % with a quantum yield of 300 % {Hanna 2006}.

This project will involve the synthesis of PbS and PbSe nanoparticles of varying size and morphologies with the target end use being solar cell technology. The hot injection method will be the main synthetic procedure for the formation of the lead chalcogenide nanoparticles. The surface of the QDs will be modified by addition of a linking group. This will attach the nanoparticles to TiO_2 which will act as a wide band gap (3.2 eV) semiconductor, electron acceptor material. Therefore, under IR irradiation the lead chalcogenide nanoparticles will inject electrons into the TiO_2 providing a photocurrent. The presence of lead chalcogenide nanoparticles will provide a much greater conversion efficiency when compared to TiO_2 itself which absorbs only around 5% of the solar spectrum {Lopez-Luke 2008}.

1.4 Noble Metals

The nanocrystalline states of the noble metals have experienced extensive research over the past decade due to their interesting properties and the facile control over their size and morphology. Gold nanoparticles have been in use for centuries with the colour in stained glass windows and royal purple dye being attributed to the presence of the finely divided colloid {Daniel 2004}. The colour of the nanoparticles of noble metals can be changed by variation of their size and morphology. The observed colour is due to a collective oscillation of electrons in the conduction band known as surface plasmon resonance. The mean free path of electrons in gold and silver is ~ 50 nm so when the nanoparticle size is reduced below this, all electron interactions are expected to occur at the surface {Eustis 2006}. When the wavefront of light with wavelength larger than the nanoparticle size passes across the nanoparticle it causes the electrons to polarize to one surface. As the waveform continues to travel it can set up a standing oscillation of free electrons or surface plasmon resonance. This means that the colour of the nanoparticle is directly related to the electron density at the surface and hence dependant on its size and shape. Nanorods have been shown to possess two distinct plasmon resonances; a transverse oscillation which is independent of aspect ratio and a longitudinal oscillation which occurs at longer wavelengths and varies with the aspect ratio {El-Sayed 2001}. Therefore, introducing anisotropy into a system can have a profound effect on the surface plasmon resonance. Hao et al produced branched gold nanoparticles that showed a 130 – 180 nm red shift of the surface plasmon resonance in relation to spherical nanoparticles {Hao 2004}. Through electromagnetic simulations they showed that the nanoparticle tips dominated the optical properties which agrees with the idea that plasmon resonance is a surface effect. The electron oscillation also imparts a strong interparticle van der Waals force on noble metal nanoparticles {Eustis 2006}.

The electron density of the environment will affect the ability of the nanoparticle surface to hold charge and will also have an effect on the surface plasmon resonance. This includes the dielectric constant of the solvent as well as the structure of the capping molecule. The dependence of the resonance on the capping species can be utilised for sensing purposes as a chemically bonded species will change the electronic environment and induce an observable colour change.

A common method for producing monodisperse gold and silver nanoparticles is the use of reverse micelles or microemulsion. A microemulsion is a thermodynamically stable dispersion of two relatively immiscible liquids stabilised by surfactant molecules {Lin 2006}. surfactant molecules can self assemble as normal micelles (oil-in-water), or reverse micelles (water-in-oil). nanoparticles such as Au, Ag and Pd are commonly synthesised in a reverse micelle system consisting of cetyltrimethylammonium bromide (CTAB) as the surfactant, butanol as a cosurfactant and octane as the oil phase. At an appropriate concentration the CTAB creates a spherical reverse micelle surrounding a pool of water which subsequently dissolves the metal salt precursor {Pileni 2003}. The metal salt is then reduced by the addition of a reducing agent, e.g. NaBH_4 . This reducing agent is unstable with respect to hydrolysis in neutral aqueous solution and is therefore used as a highly alkaline solution {Wilcoxon 2006}. Most metal salts used in this technique are soluble only at concentrations of 0.01 M to 0.1 M using surfactant concentrations of $\sim 5 - 10$ wt% (~ 0.2 M) {Hanna 2006}. This corresponds to only a few precursor molecules per micelle and hence, the nanoparticle size is a result of micellar diffusion and collision. Due to the small size of the reverse micelles they are subject to Brownian motion at ambient temperatures {Cushing 2004}. Occasionally, a short-lived dimer will form with the two reverse micelles evenly distributing the contents of their aqueous cores. They will then separate, resulting in the eventual equilibrium distribution of all aqueous contents and a product with nearly uniform size and shape.

The size of the product nanoparticle is related to the size of the reverse micelle which increases linearly with increasing water content {Pileni 1997}. However, above a water-surfactant ratio of $\sim 10 - 15$, the nanoparticle size does not drastically change and an increase in polydispersity is observed.

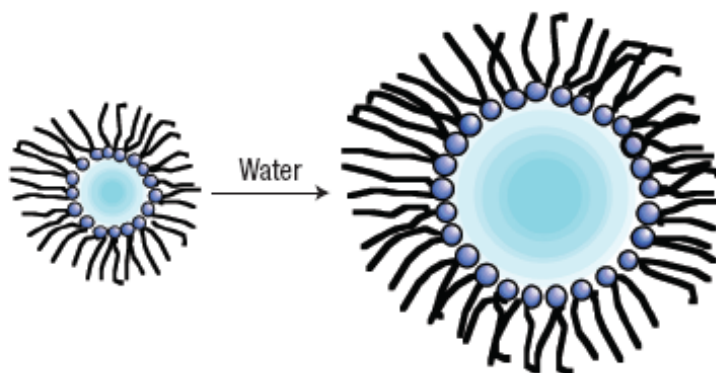


Figure 6. Reverse micelles showing control of size by water content.

The nanoparticles then undergo a ligand exchange step where the CTAB molecules surrounding the metal nanoparticles are displaced by a desired capping species, e.g., dodecanethiol. Here, the metal-thiol bond is typically stronger than the surfactant-metal interaction and a spontaneous displacement of surfactant molecules will occur. The dodecanethiol ensures solubility in an organic phase and the excess surfactant can be removed by washing with a highly polar solvent such as n-methylformamide. Further purification is carried out via introduction of a non-solvent and centrifugation.

In some cases this procedure can yield a product with a significant degree of polydispersity. A polydisperse product can be converted to a monodisperse one by *digestive ripening* {Prasad 2002}. This involves refluxing the nanoparticles in the presence of excess capping ligand and is highly effective in reducing the size distribution for noble metal nanoparticles. The exact mechanism for this phenomenon is not clear however it is evident that the efficacy of the technique relies on the strength of the Au-ligand interaction {Prasad 2003}. It has also been proposed that the electrostatic energy of the charged nanoparticles is the balancing force for the increased curvature introduced into the system {Lee 2007}.

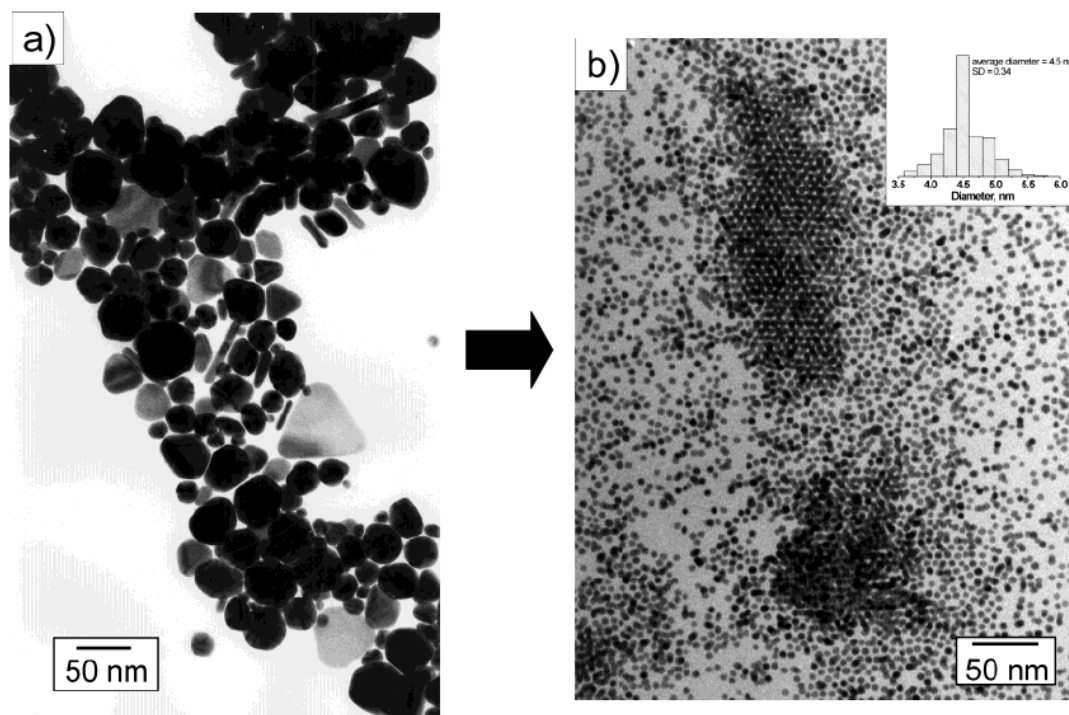


Figure 7. TEM micrographs of Au nanoparticles before and after digestive ripening {Prasad 2002}.

This project will utilise the reverse micelle method to produce monodisperse Au and Ag nanoparticles for formation of nanoparticle superlattices as their facile synthesis and propensity for undergoing digestive ripening make them ideal candidates. The dependence of their optical properties on the surrounding environment means that their inclusion into nanoparticle superlattices could yield some interesting effects.

1.5 Palladium

The synthesis of platinum group metal nanoparticles with controllable size and morphology has recently received much focus with a substantial amount of research into palladium nanoparticles. Palladium serves as a primary catalyst for low-temperature reduction of harmful emissions from automobiles or for organic processes, such as the Suzuki, Heck and Stille coupling reactions {Xiong 2005 (a)}. When used as a catalyst in the automobile industry only about 10 % of the metal is active due to accessibility and poisoning issues. Therefore development of high surface area, high performance Pd catalysts are of primary concern. It is well known for its extraordinary capacity for hydrogen absorption – of which it can store up to 900 times its own volume - which makes it a promising material for hydrogen sensing as well as energy storage for fuel cells. The crystalline structure of Pd is face centred cubic (*fcc*) with a lattice constant of $a = 3.8898 \text{ \AA}$. Small Pd nanoparticles (typically <10 nm) in size show a surface plasmon resonance in the UV region which gives them a black colour. This makes its optical properties difficult to observe due to strong absorption at these wavelengths by glass and most solvents {Creighton 1991}. However, calculations have indicated that the resonance peaks can be tuned from the UV (330 nm) to the visible (530 nm) by morphology control {Kelly 2003}. A free Pd atom has the configuration [Kr] $4d^{10}$ and is non magnetic at room temperature. Yet upon reduction to the nanoscale the onset of ferromagnetism has been observed due to i) reduced coordination at the surface, ii) the expansion of the lattice parameter, and iii) breaking of local symmetry i.e., twinning {Sampredo 2003}.

For catalytically active materials, e.g., Pt and Pd the catalytic performance relies heavily on the nanoparticle morphology. Anisotropic growth can greatly enhance performance by increasing surface area and concomitantly exposing high index crystal facets. El-Sayed and co-workers established the link between morphology and catalytic properties through the formation of tetrahedral and spherical Pt nanoparticles {Narayanan, 2004, Narayanan 2005}. Tian et al showed the importance of the nature of the crystal facet in optimising the catalytic performance {Tian 2007}. Extensively branched or porous nanostructures have the added benefit of possessing absorption sites that are in close vicinity to each other through space. This has the potential to increase the catalytic performance for reactions which involve two or

more reactants as all molecules needed for the target reaction can be absorbed in close proximity to each other reducing the need for diffusion across the catalyst surface {Teng 2006}. The control of branched growth in nanoparticle systems is well established in materials with polymorphism, e.g. CdS and CdSe {Joo 2003}. Here, the controlled nucleation of a zinc-blende core is followed by the growth of wurtzite phase branches which occurs along the inherently anisotropic c-axis of the hexagonal cell structure. This type of polymorphism is not seen in highly symmetrical face centred cubic (*fcc*) structures. Thus, while methods for producing isotropic nanoparticles for noble metals are well established, the formation of branched structures has yet to be comprehensively achieved.

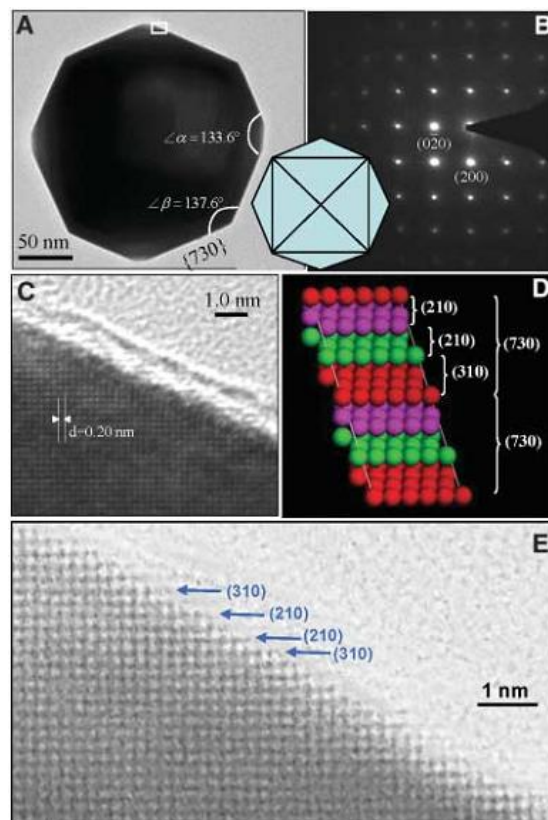


Figure 8. Series of images showing the introduction of high index facets in tetrahedral Pt nanoclusters which saw an improvement in catalytic activity {Tian 2007}.

Common solution phase synthetic procedures for the formation of Pd nanoparticles include; the reverse micelle synthesis, the polyol process, which uses a polymer, generally poly(vinylpyrrolidone) (PVP) as a capping agent, thermolysis and precursor decomposition/reduction in a pressure reaction vessel (Fischer-Porter bottle). Palladium nanoparticles synthesised by reverse micelles are commonly monodisperse and isotropic and have been used in the seed-mediated synthesis of

anisotropic nanoparticles {Xiong 2005 (b)}. The polyol synthesis has been used for the synthesis of uniform single crystal cuboctahedra nanoparticles by Xia et al, where oxidative etching of the nuclei removed twinning and reduced anisotropy {Xiong 2005 (a)}. Xiong et al furthered this work by producing single crystal nanoboxes and nanocages as well as observing a size dependence of the surface plasmon resonance for Pd and core shell Pd/PdO nanocubes {Xiong 2005 (b), Xiong 2005 (c)}. Twinned Pd nanostructures were produced in the polyol synthesis through the removal of oxidative etching from the reaction system and Pd nanobars and nanorods were formed through the introduction of a second polymer (ethylene glycol) with different reduction properties {Xiong 2007 (b), Xiong 2007 (c)}. The polyol synthesis has recently been most effective in controlling the morphology of Pd nanoparticles however this project will focus on Fischer-Porter bottle synthesis. Fischer-Porter bottles (shown in Fig 10) have previously been used to demonstrate the effect of organo-metallic precursor on nanoparticle formation {Ramirez 2004}.

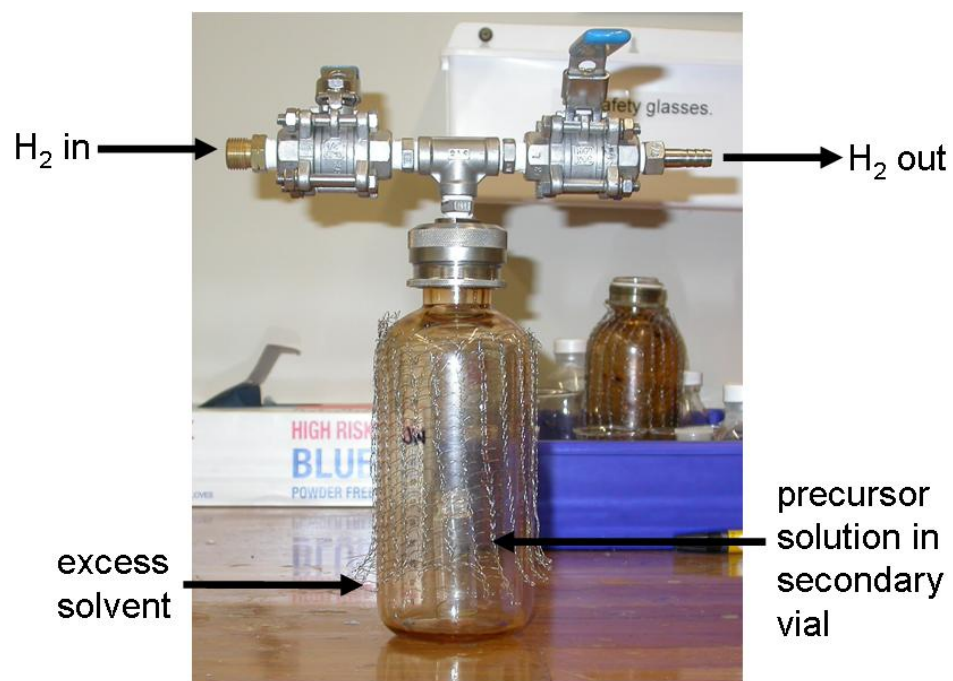


Figure 9. Picture of Fischer-Porter pressure reaction vessel.

The main goal of this project is the synthesis of Pd nanoparticles with morphological control with the aim of increasing catalytic performance and gaining an understanding of the fundamentals of complex nanoparticle growth. This will primarily be achieved through the use of surfactant mixtures of differing ratios that will serve to i) regulate the surface energy on different crystal facets controlling

growth rate and ii) control the reduction kinetics which determines the degree of twinning in the nanoparticle nuclei {Xiong 2007 (a)}. The reduction kinetics control the rates of nucleation and growth which can influence morphology through so called kinetic shape control {Yin 2005}.

1.6 Superlattices

The self-assembly of size selected nanoparticles into ordered arrays or 'superlattices' presents an opportunity to form new and exciting materials with designable chemical and physical properties. Here, the nanoparticles can be considered as 'artificial atoms' which self assemble into structures analogous to atomic crystals. The nanoparticles reside in the lattice positions just as atoms do in atomic crystals. This presents the possibility for collective properties arising due to their close proximity and periodicity. The formation of superlattices requires a system of highly monodisperse nanoparticles, usually with a polydispersity of less than 5%. The resulting structure of the superlattice is dictated by a balance between attractive van der Waals and dipolar forces and short range repulsions {Shevchenko 2006 (a)}. Nanoparticle superlattices were first reported in 1989 and since then have attracted increasing attention. Early work included the assembly of CdSe nanoparticles into 3D superlattices and the assembly of Ag₂S nanoparticles of differing sizes (3 to 6 nm) into 2D monolayers and 3D arrays {Bentzon 1989, Murray 1995, Motte 1995}. Work has been carried out on superlattices of the noble metals Au and Ag which experience a strong interparticle attraction due to an enhanced van der Waals force {Prasad 2003}.

Superlattices with a binary phase are also possible when two different sizes of nanoparticle are self assembled. Shevchenko et al, produced an AB₅ type superlattice of 4.5 nm and 2.6 nm CoPt₃ nanoparticles with a structure analogous to CaCu₅ {Shevchenko 2006 (b)}. Recently, superlattices containing two different types of nanoparticle have been presented by the Murray group at IBM. These binary nanoparticle superlattices (BNSL) have been dubbed 'meta-materials'. The first BNSL presented consisted of 11 nm γ -Fe₂O₃ and 6 nm PbSe nanoparticles and displayed AB₁₃ and AB₂ type structures analogous to the intermetallic phases NaZn₁₃ and AlB₂ respectively {Redl 2003}. Recently, Murray et al have presented BNSLs with AB, AB₂, AB₃, AB₄, AB₅, AB₆ and AB₁₃ stoichiometry possessing cubic, hexagonal, tetragonal and orthorhombic symmetries {Shevchenko 2006 (a)}. Assemblies with the same stoichiometry were produced in several polymorphous forms isostructural with various intermetallic compounds, e.g. AlB₂ and MgZn₂. Also presented were BNSL with no known atomic equivalent, indicating that the discovery of further novel crystal structures is a possibility.

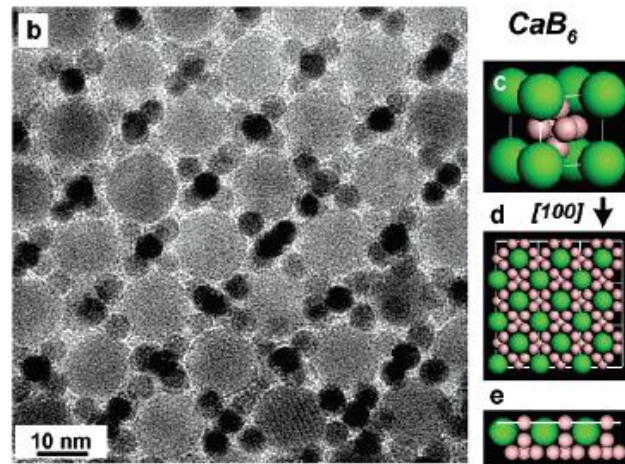


Figure 10. TEM micrograph of a BNSL isostructural with CaB_6 made from 13.4 nm Fe_2O_3 and 5.0 nm Au nanoparticles {Shevchenko 2006 (a)}.

A major contributor to the properties of nanoparticles is the choice of capping agent. The spacing between nanoparticles can be changed by varying the length of the alkyl chain. Nanoparticles also undergo interdigitation (overlap) of the capping species and therefore the nature of branching of the alkyl chain is also important. The capping species helps to dictate the structural and thermal stability of the superlattice. By changing the interparticle distance, electronic transitions can be introduced. This has been demonstrated for Ag nanoparticles, where a reversible insulator-metal transition was demonstrated as the interparticle distance was changed from 12 to less than 5 angstroms at near ambient conditions {Collier 1997}. Binary nanoparticle superlattices of Ag_2Te and PbTe have shown synergistic effects leading to enhanced p-type conductivity {Urban 2007}.

There are myriad forces responsible for NPSL formation. In the self assembly of model hard spheres entropy is the main driving force however additional forces must be considered in the self assembly of nanoparticles. Sterically stabilised nanoparticles can hold one or two noncompensated positive or negative elemental charges per nanoparticle {Shevchenko 2006 (a)}. Also, semiconductor nanoparticles can exhibit large dipole moments and polarisabilities {Cho 2005, Shanbhag 2006}. This is due to different terminating species on the crystalline facets, e.g., Pb or Se, which gives them a polar nature. The distribution of polar facets results in a dipole moment.

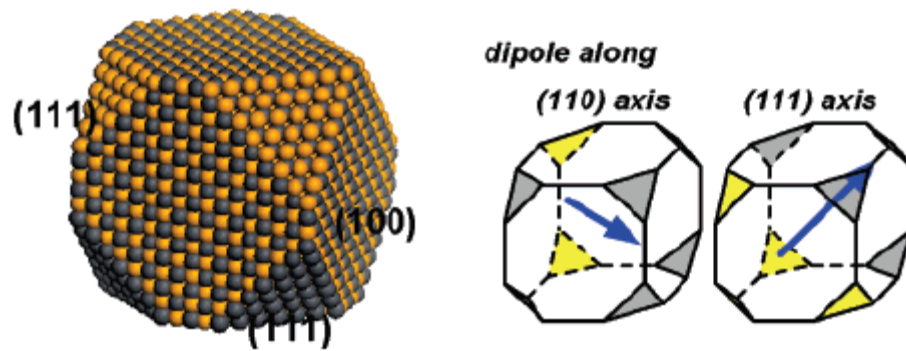


Figure 11. Atomic reconstruction of the PbSe nanocrystal showing the difference in terminating species of the facets and the direction of the resulting dipole moment {Lee 2003}.

The selective adsorption of capping ligand can also enhance the dipole-dipole interactions between nanoparticles {Zhang 2005}. The capping agent exerts an influence in nanoparticle self-assembly through steric hindrance and vdW interactions. So in addition to entropy, the following interactions must be considered;

- Coulombic – repulsive and attractive.
- electric and magnetic dipole
- van der Waals
- steric hindrance
- higher order moments of charge distribution – charge-dipole, dipole-induced dipole etc.

It is the balance between these forces and entropy as well as the nanoparticle size ratio and relative concentrations which can give rise to new BNSL structures beyond close packed.

Superlattices will be prepared by evaporating the colloidal solution directly onto transmission electron microscopy (TEM) grids for ease of imaging. The important variables to consider in SL formation are;

- nature of the substrate
- solvent choice
- concentration
- temperature
- pressure

- interfacial surface area

The electron transparent substrates used are generally amorphous carbon but can be formed by other materials, e.g. silicon nitride. Nanoparticle-substrate binding is dynamic and therefore the nanoparticle-substrate affinity is important. The nanoparticle must have a long enough residence time on the substrate to begin crystallisation but also retain enough diffusional freedom to migrate across the substrate and reach a position of minimum energy {Sigman 2004}. To form the SL, the colloidal solution will be evaporated on the TEM grid. As the solvent evaporates the nanoparticle concentration close to the three phase contact point (liquid-air-substrate) increases until crystallisation occurs {Siffalovic 2007}. Therefore, the meniscus of the solvent becomes important as this is the position of the three phase contact point. The choice of solvent with the desired boiling point and polarity is important. The boiling point dictates the speed of evaporation and by changing solvent polarity the interparticle potential and the nanoparticle-substrate affinity can be tuned. Solvent mixtures can be employed to further control the evaporation and nanoparticle potentials. For example, a mixture of octane and octanol can be used. As the lower boiling point octane evaporates the octanol percentage in the mixture rises. This increases the interparticle potential and induces crystallisation. Temperature and pressure are both pivotal to controlling evaporation rate however ambient conditions are usually sufficient.

This project will focus on the formation of superlattices from Au nanoparticles. Attention will be given to the analysis and characterisation of nanoparticle packing and defects.

References

See end of Chapter 2.

Chapter 2. Characterisation Techniques

Solution phase synthesis provides a facile method for controlling the overall size, morphology and size distribution of various species of nanoparticles. These can be suspended in organic solvents due to a passivating layer of organic surfactants. Purification steps are carried out to minimise the amount of excess surfactant in solution which enables characterisation. The sample is then characterised using Super and High Resolution Transmission Electron Microscopy (SHREM, HREM), Synchrotron Powder X-Ray Diffraction (XRD), Selected Area Electron Diffraction (SAED) and Energy Dispersive X-Ray Spectroscopy (EDS).

HREM provides instant information on the size and morphology of the nanoparticles as well as the size distribution. It allows us to directly observe the atomic packing of the crystal surface and gives an insight into the overall crystal structure. EDS is used in conjunction with electron microscopy and imparts information on the elemental composition of a target sample. SAED provides information on the phase and orientation of the material. It serves as a very valuable alternative to traditional X-ray diffraction as it allows the analysis of single crystals on the nanometre length scale. Synchrotron radiation will be used to gain real time data on the growth of our nanostructures. By using this high energy X-ray source we are able to obtain XRD spectra from various stages throughout the reaction and thus, an insight into their growth.

2.1 High Resolution Transmission Electron Microscopy (HREM)

Over the past 75 years electron microscopy has developed into a sophisticated technique for nanoscale imaging. By using electrons for imaging, electron microscopes have realised resolution and magnification superior to traditional optical techniques. The resolution or resolving power is defined as the closest spacing between two points which still enables them to be distinguished as separate. Traditional optical microscopes suffer from a resolution limit due to their reliance on visible light where the maximum resolution possible is restricted by the wavelength of optical light such that;

$$resolution = \frac{\lambda}{2}$$

The wave-particle duality nature of the electron indicates that as its energy increases its wavelength decreases. Therefore by controlling the energy of the electron you can control its wavelength and ultimately surpass the resolution limit that restricts optical microscopy.

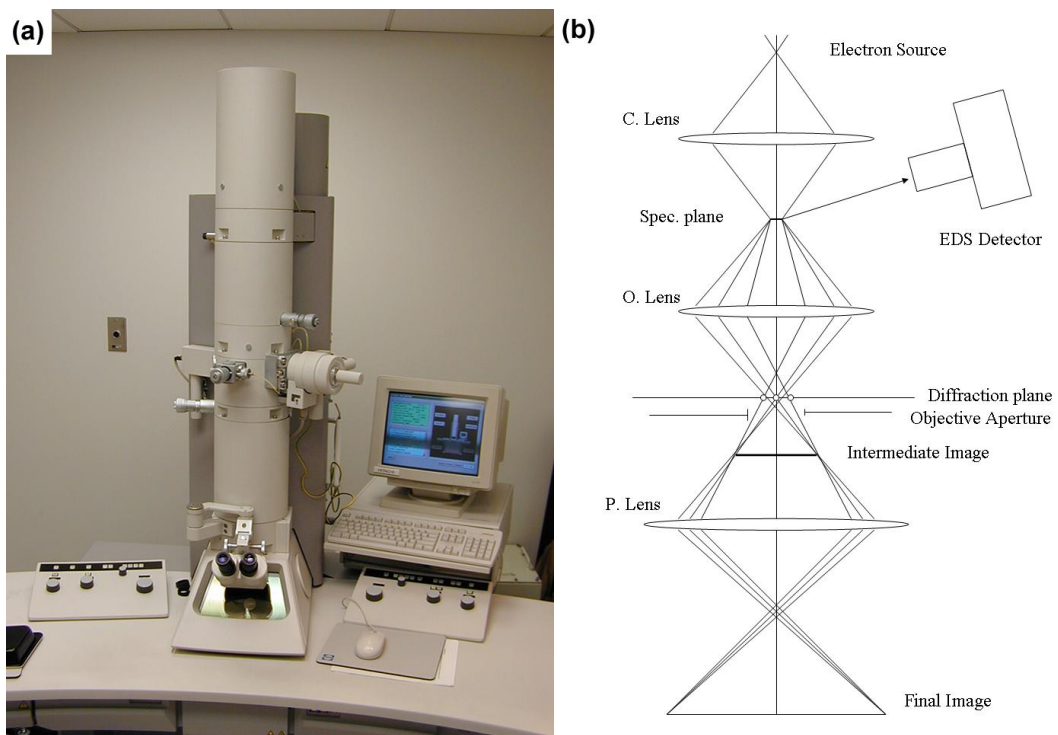


Figure 13. (a) shows an HREM and (b) a schematic representation of the electron beam.

High resolution transmission electron microscopy (HREM) is a powerful tool that allows direct probing of structural information at the atomic level. A picture of an HREM is shown in Fig 13a along with a schematic ray diagram in Fig 13b. The HREM consists of an electron source which provides a beam of electrons that is then controlled and focussed by magnetic fields to image materials and create electron diffraction patterns. The electrons are produced by thermionic emission (Edison effect) from either a tungsten filament or a lanthanum hexaboride (LaB₆) single crystal. Our instrument employs a self-biasing type LaB₆ emitter which possesses a lower work function and operates at a lower temperature than a tungsten filament. The electrons are then accelerated by a potential difference of 200 kV down the optical axis enabling wavelengths ($\lambda = 0.0251 \text{ \AA}$) much smaller than the inter-atomic distances in crystal lattices. Such a large potential difference accelerates the electrons to velocities close to the speed of light which means relativistic effects become important. Therefore the precise wavelength of the electrons is given by;

$$\lambda = \frac{h(1 - \beta^2)^{1/4}}{(2m_e e_0 E)^{1/2}}$$

Where h is Planck's constant, m_e is the rest mass of the electron, e_0 is the charge on an electron, E is the accelerating voltage and $\beta = v/c$, where v and c are the velocities of the electron and light in a vacuum respectively.

Below the electron gun are two or more condenser lenses. These focus the electrons into an approximately parallel beam and control its diameter as it hits the specimen, enabling the operator to control the intensity of illumination. Below the condenser lens is the specimen chamber which allows a very small specimen to be placed directly in line of the beam. Specific sample holders are used that can move the sample along the plane normal to the optical axis, tilt the sample in relation to the plane (double-tilt holder) or create variations in temperature (variable temperature stage). The sample is immersed well within the magnetic field of the objective lens which will be discussed below.

The electron beam passes through the sample where some electrons are diffracted imparting partial structural information. The diffracted beam and the primary beam are then recombined by the objective lens. The role of the objective lens is to form the

first intermediate image and diffraction pattern, one of which will be enlarged by the subsequent projector lenses.

The first projector lens can be switched between two modes, image and diffraction. In image mode the lens is focussed on the intermediate image plane of the objective lens and an image is formed with the final magnification controlled by the remaining projector lenses. In diffraction mode the projector lens is focussed on the back focal plane of the objective lens and a diffraction pattern is projected. So by manipulating the projector lens either an image or a diffraction pattern can be propagated down the optical axis and viewed on a fluorescent screen, photographic plate or CCD digital camera.

There are key advantages to the use of electrons over X-rays. Due to the far stronger interaction of electrons compared to X-rays with atoms, it is possible to image individual sub-micron crystals. This is not possible with X-ray techniques such as powder X-ray diffraction. A second advantage relates to the 'phase problem' inherent in X-ray diffraction. The recombination of the diffracted beams by the objective lens during the imaging process retains the phase information and eliminates the need for subsequent mathematical operations.

Due to imperfections in the microscope, there are limitations to the structural resolution that can be obtained. As the lens that recombines the diffracted beams, imperfections in the objective lens become the limiting factor. Consideration should be given to astigmatism, spherical aberration, chromatic aberration and beam divergence. Astigmatism is caused by a deviation of the beam from a cylindrical nature at a normal to the optical axis. In theory this can be completely corrected by electromagnetic coils in the microscope. Therefore astigmatism requires a high degree of control over the magnetic field. Spherical aberration occurs when parts of the beam are focussed more strongly than others bringing them into focus on different planes. In optical systems this can be corrected by using non-spherical lenses. This cannot be employed in electron microscopes as the lens is the magnetic field between the pole pieces of the objective lens and is difficult to control. The effect can be somewhat countered by defocusing the beam resulting in a slight elongation of the focal length. However, this results in poorer spatial resolution so may not always be desirable. Chromatic aberration occurs because the focal length of the magnetic

lens is dependent on the electron energies. A range of electron energies occur due to the spread of thermal energies inherent in thermionic emission, as well as fluctuations in the accelerating voltage. Beam divergence relates to a non-parallel incident beam which occurs as the filament degrades from a point source to a larger area of electron emission.

Recently, the use of aberration correction in electron microscopy has reduced achievable point resolution to under 1 Å {Kirkland 2008}. This can be achieved either through direct or indirect methods, or a combination of both. Indirect methods include exit wave reconstruction. This technique require a series of images to be obtained along a focal path at nominal focal increments. The images are then reconstructed *a posteriori* to create an aberration corrected image {Kirkland 2007}. Direct methods involve the insertion of correctors into the electron optical column which correct for the positive spherical aberration inherent in magnetic lenses {Kirkland 2008}. These correctors contain pairs of hexapole and round doublet transfer lenses and can correct all spherical aberrations out to third order {Hutchison 2005}.

Other techniques for reducing the point resolution of an electron microscope include decreasing the chromatic aberration and introducing an in-column energy loss filter. For example, if the energy spread in the emission gun is reduced from 1 eV to 0.5 eV the point resolution improves from 0.12 nm to less than 0.10 nm due to this decrease in chromatic aberration {Kirkland 2008}. An in-column omega-type electron energy filter further decreases the chromatic aberration by refining the spread of electron energies {Tanada 1999, Hutchison 2005}.

In this study a JEOL 2011 TEM operating at 200 keV was primarily used for HREM analyses. Samples were prepared by evaporating a colloidal solution onto a TEM grid (strong carbon film on 200 mesh copper) purchased from ProSciTech (GSCu200C). The software Gatan DigitalMicrograph was used to i) capture and process images and ii) perform a fast Fourier transform (FFT) analysis on a high resolution HREM image to a produce power spectrum. The software Crystal Maker was used to produce model crystal structures.

Chapter 2: *Characterisation Techniques*

Additional SHREM experiments were performed on a JEOL 2200MCO field-emission TEM with double aberration correctors operating at 200 keV located at Oxford University Department of Materials.

2.2 Diffraction Theory and Application

The phenomenon of diffraction is the interference caused by an object in the path of propagating electromagnetic waves. This gives rise to a diffraction pattern that can impart valuable structural information on the object. The analysis of diffraction patterns is an important technique for the characterisation of nanocrystalline materials.

A detailed account on diffraction theory is given by Atkins and also Williams and Carter {Atkins 2006, Williams 1996}. One approach to the analysis of diffraction patterns is to model the crystal as stacks of reflecting lattice planes d (see Fig 14 below). Consider two adjacent planes reflecting two parallel incident rays of the same wavelength. The first ray strikes the upper plane at point D however the second ray must travel an additional distance AB before striking the lower plane. The reflected rays will have an additional path difference of BC. Therefore the net path difference between the two rays will be

$$AB + BC = 2d \sin \theta$$

where θ is the glancing angle.

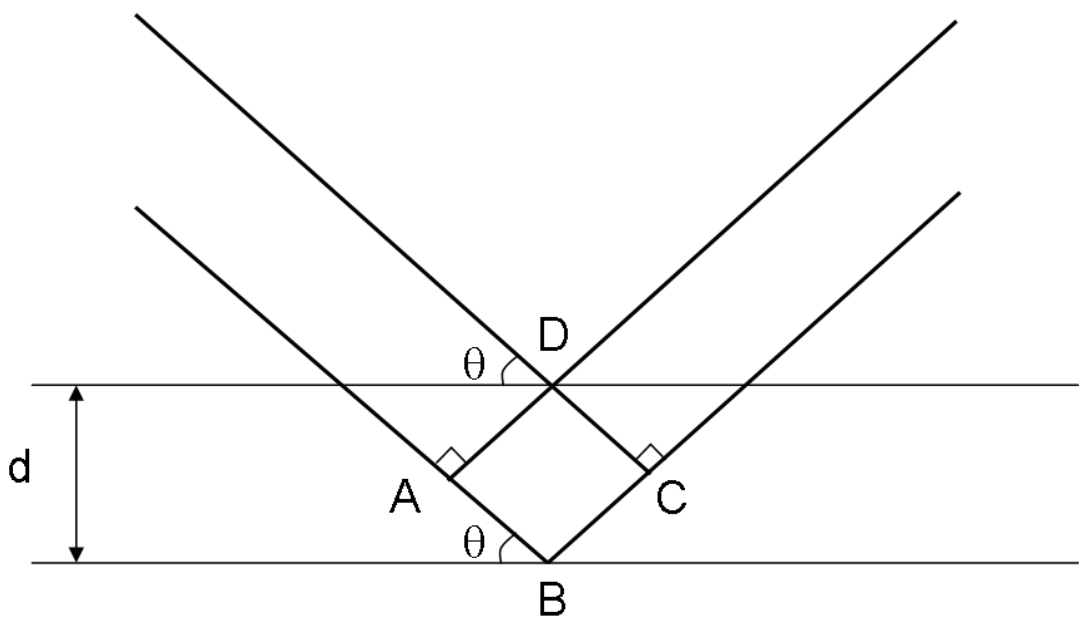


Figure 14. Schematic representation of Bragg's Law showing the path-length difference of AB + BC for two parallel incident rays of the same wavelength.

If the path length difference is not an integer number, the wave interference will be destructive and no structural information given. However, if the path-length difference is an integer number i.e., $AB + BC = n\lambda$ then the reflected waves interfere constructively and a diffraction pattern is observed. This is expressed as Braggs Law:

$$n\lambda = 2d \sin \theta$$

Braggs Law allows for the investigation of spacing between the lattice planes; once θ has been determined, d may be easily calculated. This in turn enables determination of the crystal structure.

In this thesis structural information is taken from X-Ray Diffraction and Selected Area Electron Diffraction techniques.

2.2.1 Selected Area Electron Diffraction (SAED)

One of the great advantages of TEM analysis is the ability to observe images and diffraction patterns for the same region simply by adjusting the electromagnetic lenses. Diffraction information can be extracted by inserting an aperture in the imaging plane of the objective lens. Only electrons passing through the aperture contribute to the diffraction information. As the electrons travel through the specimen, they may be scattered or remain unaffected by the specimen. This creates a non-uniform distribution of electrons which contains all the structural and chemical information of the specimen {Williams 1996}.

Single crystal SAED reveals a series of spots on the imaging surface that can be indexed to the appropriate crystal structure and reveal its orientation. Diffraction of a large number of randomly oriented crystals results in diffraction rings as shown in Fig 15. Selected area diffraction is one of the major electron microscopy techniques for identifying phases and determining the orientation of materials. In this study SAED patterns were taken on film using a JEOL 2011 TEM operating at 200 keV.

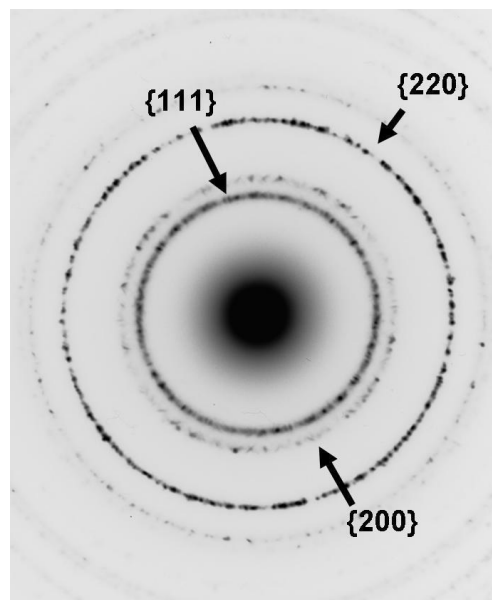


Figure 15. SAED pattern of fcc palladium clearly showing well developed rings.

2.2.2 Synchrotron X-ray Diffraction (XRD)

Synchrotron radiation is the emission of light which occurs when a charged particle is forced into a curved trajectory, e.g., an electron under the influence of the magnetic field. When the target particles are accelerated to relativistic velocities, i.e. close to the speed of light, radiation is emitted in a very narrow cone at a tangent to the electron orbit. The energy of synchrotron radiation is therefore dependant on the velocity of the orbiting electrons as well as the curvature or the ring which enables radiation from infra-red to X-rays to be produced. The diffraction of the emitted X-ray radiation when passed through a specimen imparts valuable structural information which is crucial to form a complete characterisation. X-rays emitted in a synchrotron have a number of important properties different to a lab source;

- high brightness – the radiation is hundreds of thousands of times brighter than a lab source.
- highly collimated – this means the beam is parallel and experiences minimal divergence.
- is emitted in very short pulses which can give real time information.

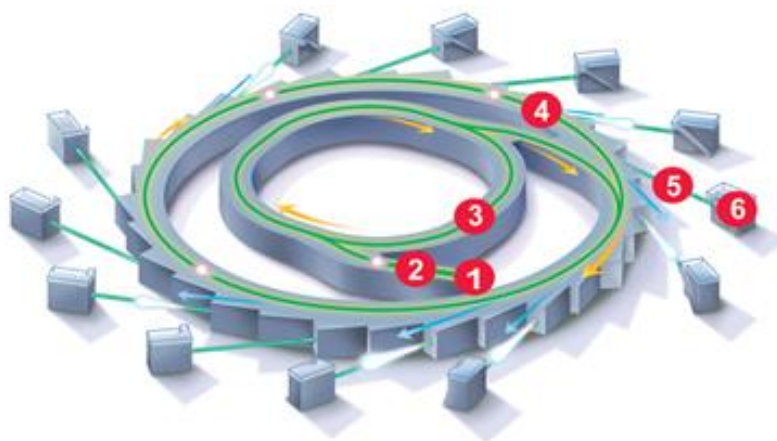


Figure 16. Schematic of a synchrotron radiation source.

Therefore synchrotron radiation can give superior resolution to lab source XRD techniques as well as giving information on dynamic processes which enables the user to monitor a reaction as it progresses.

A schematic diagram of a synchrotron is shown in Fig 16. Electrons are generated in the electron gun (1) and then accelerated to relativistic velocities by the linear accelerator (2). The electrons have their energies increased in the booster ring (3) and then are transferred to the outer storage ring (4). As the electrons are deflected by the magnetic ring they emit radiation that travels down the beamline (5) to the user end station (6).

In this study XRD analyses was taken from beamlines at both the Stanford Synchrotron Radiation Lightsource (SSRL) at Stanford, California (Beamline # BL7-2) and the Australian Synchrotron in Melbourne (Powder Diffraction Beamline).

2.3 Energy Dispersive X-ray Spectroscopy (EDS)

Energy dispersive X-ray spectroscopy (EDS) is a useful analytical technique used in conjunction with HREM that can impart valuable information on the composition of a system. It uses the characteristic X-ray signature generated by a sample when bombarded with electrons to reveal its elemental composition. Quantitative data can also be obtained by comparing peak heights or measuring unknowns against a standard. This technique also allows the detection of impurities that may be too low in concentration to be detected by powder XRD. Data collection and analysis is a relatively quick and easy process because the complete spectrum of energies is obtained simultaneously.

When a beam of high energy electrons strikes a sample, X-rays may be generated. Two processes occur; elastic scattering, used in X-ray imaging and inelastic scattering, used for EDS. In elastic scattering the energy of the electron is conserved and its propagating direction is changed by the potential of the target. In an inelastic scattering process there is a finite change in the energy of the electron. The electrons produced in the microscope are accelerated by a 200 kV potential difference and thus possess enough energy to ionise an atom upon collision by removing an electron before continuing on with reduced kinetic energy. If the electron is removed from one of its inner shells an electron from an outer shell can relax into the vacancy thus restabilising the atom. The energy loss associated with the relaxation from a higher energy position to a lower energy position can either be emitted as a photon (X-ray) or transferred to a secondary electron which is then emitted from the atom (Auger electron). This energy is characteristic of the energy level separation of a specific element and can therefore be used for elemental identification. An EDS spectrum of Pd nanoparticles is shown in Fig 17. The peaks labelled Cu and C are due to these materials being present in the TEM grid. Note that heavier elements such as Pd will give rise to a higher number of transitions than lighter elements.

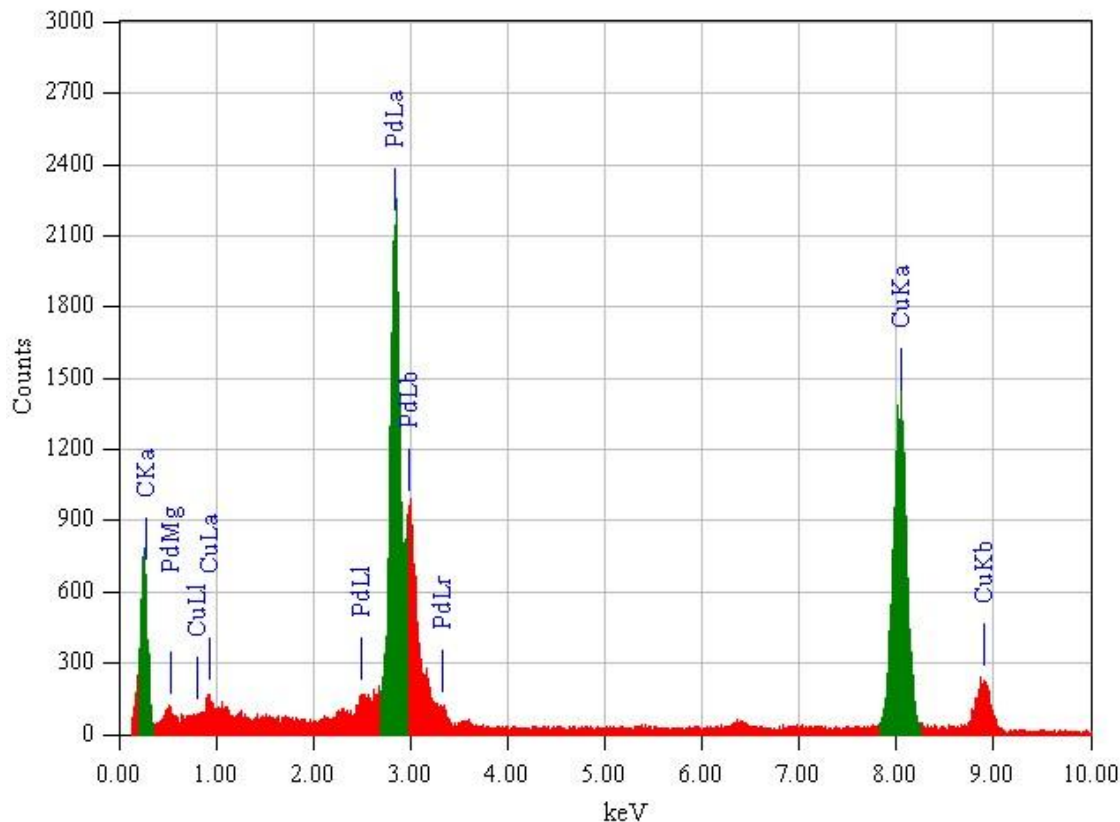


Figure 17. EDS spectrum of Pd nanoparticles.

X-rays generated deep within a thick crystal can be absorbed by the surrounding crystal structure and lead to erroneous data. Therefore, EDS analysis is optimised when dealing with small or very thin crystals. X-ray detection is achieved through the use of a lithium doped silicon semiconductor. This absorbs the X-ray which produces an electron hole pair that in turn generates a current. The amount of X-rays the detector can process at any given time is limited and therefore the input must be optimised. An input that is too strong will enable detection of undesirable lower energy emissions which can result in misleading data whereas a weak input will give an unsatisfactory signal to noise ratio.

For EDS analysis JEOL Analysis Station software was used to analyse data obtained from an EDS unit integrated into the a JEOL 2011 TEM.

References

- Alivisatos, A. P., *Science* **1996**, 271, (5251), 933-937.
- Atkins, P., De Paula, J., *Physical Chemistry*, Oxford University Press, **2006**.
- Bentzon, M. D.; Vanwonterghem, J.; Morup, S.; Tholen, A., *Philosophical Magazine B- Physics of Condensed Matter Statistical Mechanics Electronic Optical and Magnetic Properties* **1989**, 60, (2), 169-178.
- Berhault, G.; Bausach, M.; Bisson, L.; Becerra, L.; Thomazeau, C.; Uzio, D., *Journal of Physical Chemistry C* **2007**, 111, (16), 5915-5925.
- Chin, P. T. K.; Donega, C. D. M.; Bavel, S. S.; Meskers, S. C. J.; Sommerdijk, N.; Janssen, R. A. J., *Journal of the American Chemical Society* **2007**, 129, 14880-14886.
- Cho, K. S.; Talapin, D. V.; Gaschler, W.; Murray, C. B., *Journal of the American Chemical Society* **2005**, 127, 7140-7147.
- Collier, C. P.; Saykally, R. J.; Shiang, J. J.; Henrichs, S. E.; Heath, J. R., *Science* **1997**, 277, (5334), 1978-1981. Creighton, J. A.; Eadon, D. G., *Journal of the Chemical Society-Faraday Transactions* **1991**, 87, (24), 3881-3891.
- Cui, D.; Xu, J.; Paradee, G.; Xu, S. Y.; Wang, A. Y., *Journal of Experimental Nanoscience* **2007**, 2, 13-21.
- Cushing, B. L.; Kolesnichenko, V. L.; O'Connor, C. J., *Chemical Reviews* **2004**, 104, 3893-3946.
- Daniel, M. C.; Astruc, D., *Chemical Reviews* **2004**, 104, 293-346.
- El-Sayed, M. A., *Accounts of Chemical Research* **2001**, 34, (4), 257-264.
- Ellingson, R. J.; Beard, M. C.; Johnson, J. C.; Yu, P. R.; Micic, O. I.; Nozik, A. J.; Shabaev, A.; Efros, A. L., *Nano Letters* **2005**, 5, (5), 865-871.
- Eustis, S.; El-Sayed, M. A., *Chemical Society Reviews* **2006**, 35, (3), 209-217.
- Hanna, M. C.; Nozik, A. J., *Journal of Applied Physics* **2006**, 100, (7).
- Hao, E.; Bailey, R. C.; Schatz, G. C.; Hupp, J. T.; Li, S. Y., *Nano Letters* **2004**, 4, (2), 327-330.
- Hines, M. A.; Scholes, G. D., *Advanced Materials* **2003**, 15, (21), 1844-1849.
- Houtepen, A. J.; Koole, R.; Vanmaekelbergh, D. L.; Meeldijk, J.; Hickey, S. G., *Journal of the American Chemical Society* **2006**, 128, (21), 6792-6793.
- Hutchison, J. L.; Titchmarsh, J. M.; Cockayne, D. J. H.; Doole, R. C.; Hetherington, C. J. D., Kirkland, A. I.; Sawada, H., *Ultramicroscopy* **2005**, 103, 7.

- Joo, J.; Na, H. B.; Yu, T.; Yu, J. H.; Kim, Y. W.; Wu, F. X.; Zhang, J. Z.; Hyeon, T., *Journal of the American Chemical Society* **2003**, 125, (36), 11100-11105.
- Kelly, K. L.; Coronado, E.; Zhao, L. L.; Schatz, G. C., *Journal of Physical Chemistry B* **2003**, 107, (3), 668-677.
- Kirkland, A. I., Sloan, J., Haigh, S., *Ultramicroscopy* **2007**, 107, 501.
- Kirkland, A., Chang, L. Y., Haigh, S., Hetherington, C., *Current Applied Physics* **2008**, 8, 425.
- Klabunde, K. J., *Nanoscale Materials in Chemistry*. John Wiley & Sons: 2001.
- Klimov, V. I.; Mikhailovsky, A. A.; Xu, S.; Malko, A.; Hollingsworth, J. A.; Leatherdale, C. A.; Eisler, H. J.; Bawendi, M. G., *Science* **2000**, 290, (5490), 314-317.
- Klimov, V. I., *Journal of Physical Chemistry B* **2006**, 110, (34), 16827-16845.
- Koktysh, D. S.; McBride, J. R.; Dixit, S. K.; Feldman, L. C.; Rosenthal, S. J., *Nanotechnology* **2007**, 18. Lamer, V. K.; Dinegar, R. H., *Journal of the American Chemical Society* **1950**, 72, (11), 4847-4854.
- Lee, S. M.; Jun, Y. W.; Cho, S. N.; Cheon, J., *Journal of the American Chemical Society* **2002**, 124, (38), 11244-11245.
- Lee, S. M.; Cho, S. N.; Cheon, J., *Advanced Materials* **2003**, 15, (5), 441-444.
- Lee, D. K.; Park, S. I.; Lee, J. K.; Hwang, N. M., *Acta Materialia* **2007**, 55, 5281-5288.
- Lin, X. M.; Samia, A. C. S., *Journal of Magnetism and Magnetic Materials* **2006**, 305, (1), 100-109.
- Lopez-Luke, T., Wolcott, A., Xu, L. P., Chen, S. W., Wcn, Z. H., Li, J. H., De La Rosa, E., Zhang, J. Z., *Journal of Physical Chemistry C* **2008**, 112, 1282.
- Motte, L.; Billoudet, F.; Pileni, M. P., *Journal of Physical Chemistry* **1995**, 99, (44), 16425-16429.
- Murphy, C. J.; Gole, A. M.; Hunyadi, S. E.; Stone, J. W.; Sisco, P. N.; Alkilany, A.; Kinard, B. E.; Hankins, P., *Chemical Communications* **2008**, (5), 544-557.
- Murray, C. B.; Norris, D. J.; Bawendi, M. G., *Journal of the American Chemical Society* **1993**, 115, (19), 8706-8715.
- Murray, C. B.; Kagan, C. R.; Bawendi, M. G., *Science* **1995**, 270, (5240), 1335-1338.
- Murray, C. B.; Sun, S. H.; Gaschler, W.; Doyle, H.; Betley, T. A.; Kagan, C. R., *Ibm Journal of Research and Development* **2001**, 45, (1), 47-56.
- Narayanan, R.; El-Sayed, M. A., *Journal of Physical Chemistry B* **2005**, 109, (39), 18460-18464.
- Narayanan, R.; El-Sayed, M. A., *Nano Letters* **2004**, 4, (7), 1343-1348.

- Ostwald, W., *Zeitschrift Fur Physikalische Chemie--Stoichiometrie Und Verwandtschaftslehre* **1900**, 34, (4), 495-503.
- Park, J.; Kang, E.; Son, S. U.; Park, H. M.; Lee, M. K.; Kim, J.; Kim, K. W.; Noh, H. J.; Park, J. H.; Bae, C. J.; Park, J. G.; Hyeon, T., *Advanced Materials* **2005**, 17, (4), 429-+.
- Park, J.; Joo, J.; Kwon, S. G.; Jang, Y.; Hyeon, T., *Angewandte Chemie-International Edition* **2007**, 46, 4630-4660.
- Peng, X. G.; Wickham, J.; Alivisatos, A. P., *Journal of the American Chemical Society* **1998**, 120, (21), 5343-5344.
- Peng, Z. A.; Peng, X. G., *Journal of the American Chemical Society* **2002**, 124, (13), 3343-3353.
- Pileni, M. P., *Langmuir* **1997**, 13, (13), 3266-3276.
- Pileni, M. P., *Nature Materials* **2003**, 2, (3), 145-150.
- Prasad, B. L. V.; Stoeva, S. I.; Sorensen, C. M.; Klabunde, K. J., *Langmuir* **2002**, 18, (20), 7515-7520.
- Prasad, B. L. V.; Stoeva, S. I.; Sorensen, C. M.; Klabunde, K. J., *Chemistry of Materials* **2003**, 15, (4), 935-942.
- Redl, F. X.; Cho, K. S.; Murray, C. B.; O'Brien, S., *Nature* **2003**, 423, (6943), 968-971.
- Reiss, H., *Journal of Chemical Physics* **1951**, 19, (4), 482-487.
- Ramirez, E.; Jansat, S.; Philippot, K.; Lecante, P.; Gomez, M.; Masdeu-Bulto, A. M.; Chaudret, B., *Journal of Organometallic Chemistry* **2004**, 689, (24), 4601-4610.
- Rogach, A. L.; Eychmuller, A.; Hickey, S. G.; Kershaw, S. V., *Small* **2007**, 3, (4), 536-557.
- Sampedro, B.; Crespo, P.; Hernando, A.; Litran, R.; Lopez, J. C. S.; Cartes, C. L.; Fernandez, A.; Ramirez, J.; Calbet, J. G.; Vallet, M., *Physical Review Letters* **2003**, 91, (23).
- Sargent, E. H., *Advanced Materials* **2005**, 17, 515-522.
- Schaller, R. D.; Klimov, V. I., *Physical Review Letters* **2004**, 92, (18).
- Schaller, R. D.; Sykora, M.; Pietryga, J. M.; Klimov, V. I., *Nano Letters* **2006**, 6, 424-429.
- Shanbhag, S.; Kotov, N. A., *Journal of Physical Chemistry B* **2006**, 110, (25), 12211-12217.
- Shevchenko, E. V.; Talapin, D. V.; Rogach, A. L.; Kornowski, A.; Haase, M.; Weller, H., *Journal of the American Chemical Society* **2002**, 124, (38), 11480-11485.
- (a) Shevchenko, E. V.; Talapin, D. V.; Murray, C. B.; O'Brien, S., *Journal of the American Chemical Society* **2006**, 128, (11), 3620-3637.
- (b) Shevchenko, E. V.; Talapin, D. V.; Kotov, N. A.; O'Brien, S.; Murray, C. B., *Nature* **2006**, 439, (7072), 55-59.

- Shockley, W.; Queisser, H. J., *Journal of Applied Physics* **1961**, 32, (3), 510-&.
- Siffalovic, P.; Majkova, E.; Chitu, L.; Jergel, M.; Luby, S.; Satka, A.; Roth, V., *Physical Review B* **2007**, 76, 195432.
- Sigman, M. B.; Saunders, A. E.; Korgel, B. A., *Langmuir* **2004**, 20, (3), 978-983.
- Sun, S. H.; Murray, C. B., *Journal of Applied Physics* **1999**, 85, (8), 4325-4330.
- Talapin, D. V.; Rogach, A. L.; Kornowski, A.; Haase, M.; Weller, H., *Nano Letters* **2001**, 1, (4), 207-211.
- Tanada, M.; Tsuda, K.; Terauchi, M.; Tsuno, K.; Kaneyama, T.; Honda, T.; Ishida, M., *Journal of Microscopy-Oxford* **1999**, 194, 219.
- Teng, X. W.; Liang, X. Y.; Maksimuk, S.; Yang, H., *Small* **2006**, 2, (2), 249-253.
- Tian, N.; Zhou, Z. Y.; Sun, S. G.; Ding, Y.; Wang, Z. L., *Science* **2007**, 316, (5825), 732-735.
- Tilley, R. D.; Yamamoto, K., *Advanced Materials* **2006**, 18, (15), 2053-2056.
- Urban, J. J., Talapin, D. V., Shevchenko, E. V., Kagan, C. R., Murray, C. B., *Nature Materials* **2007**, 6, 115.
- Wehrenberg, B. L.; Wang, C. J.; Guyot-Sionnest, P., *Journal of Physical Chemistry B* **2002**, 106, (41), 10634-10640.
- Wilcoxon, J. P.; Abrams, B. L., *Chemical Society Reviews* **2006**, 35, (11), 1162-1194.
- Williams, D. B., Carter, C. B., *Transmission Electron Microscopy*, Plenum Press, New York, **1996**.
- (a) Xiong, Y. J.; Chen, J. Y.; Wiley, B.; Xia, Y. N., *Journal of the American Chemical Society* **2005**, 127, (20), 7332-7333.
- (b) Xiong, Y. J.; Wiley, B.; Chen, J. Y.; Li, Z. Y.; Yin, Y. D.; Xia, Y. N., *Angewandte Chemie-International Edition* **2005**, 44, (48), 7913-7917.
- (c) Xiong, Y. J.; Chen, J. Y.; Wiley, B.; Xia, Y. A.; Yin, Y. D.; Li, Z. Y., *Nano Letters* **2005**, 5, (7), 1237-1242.
- (a) Xiong, Y. J.; Xia, Y. N., *Advanced Materials* **2007**, 19, (20), 3385-3391.
- (b) Xiong, Y. J.; Wiley, B.; Xia, Y. N., *Angewandte Chemie-International Edition* **2007**, 46, (38), 7157-7159.
- (c) Xiong, Y. J.; Cai, H. G.; Wiley, B. J.; Wang, J. G.; Kim, M. J.; Xia, Y. N., *Journal of the American Chemical Society* **2007**, 129, (12), 3665-3675.
- Yin, Y.; Alivisatos, A. P., *Nature* **2005**, 437, (7059), 664-670.
- Zhang, Z. P.; Sun, H. P.; Shao, X. Q.; Li, D. F.; Yu, H. D.; Han, M. Y., *Advanced Materials* **2005**, 17, (1), 42-+.

Chapter 3. Nanoparticle Superlattices (NPSL)

This chapter is concerned with the self organisation of monodisperse gold nanoparticles into NPSLs.

Gold nanoparticles were synthesised using a previously reported microemulsion method {Tilley 2003}. This technique presented a facile route to a monodisperse sample of small spherical gold nanoparticles as described in the introduction section. The gold nanoparticles synthesised here are capped with dodecanethiol. The strong Au-S interaction enables easy replacement of the growth directing agent and the long chain organic functionality provides sufficient stabilisation in organic solvents. Dodecanethiol was also chosen as the organic stabiliser as it has previously been shown to be the optimal length for forming ordered arrays of nanoparticles {Whetten 1999}.

Variables in NPSL formation include nature of the substrate, solvent, concentration, temperature, atmospheric pressure and interfacial surface area (i.e., tilt of the substrate). Here focus will be give to the concentration of the colloidal solution as this enables us to track the growth of the superlattices by forming intermediate structures. Size distribution analysis is performed in the following experiments by measuring the sizes of at least 2000 nanoparticles.

3.1. Synthesis and Characterisation of Gold Nanoparticles

Experimental

Gold Nanoparticle Synthesis

In a 100 mL beaker 0.0788 g (0.2 mmol) gold (III) chloride ($\text{HAuCl}_4(\text{H}_2\text{O})_3$) was added to 2 g of cetyltrimethylammonium bromide (CTAB). To this was added 16.4 mL of octane and 3.5 mL of 1-butanol. This was stirred which dissolved the gold salt resulting in a light orange turbid solution. To this was added 2 mL of water. The reaction solution was stirred and left to homogenise for 1 h resulting in a dark orange solution.

Once homogenised 30.2 mg of NaBH_4 in 8 mL H_2O was added dropwise resulting in a red wine/purple coloured solution. This was left to react for 1 h. After the completion of the reaction 0.4 mL of a 0.5 molL^{-1} (0.2 mmol) of dodecanethiol was added rapidly. This was left to stir overnight resulting in a dark purple colour.

For purification the gold nanoparticles were washed twice with N-methyl-formamide and once with water. The gold nanoparticles were soluble in various organic solvents including hexane, toluene and dichloromethane.

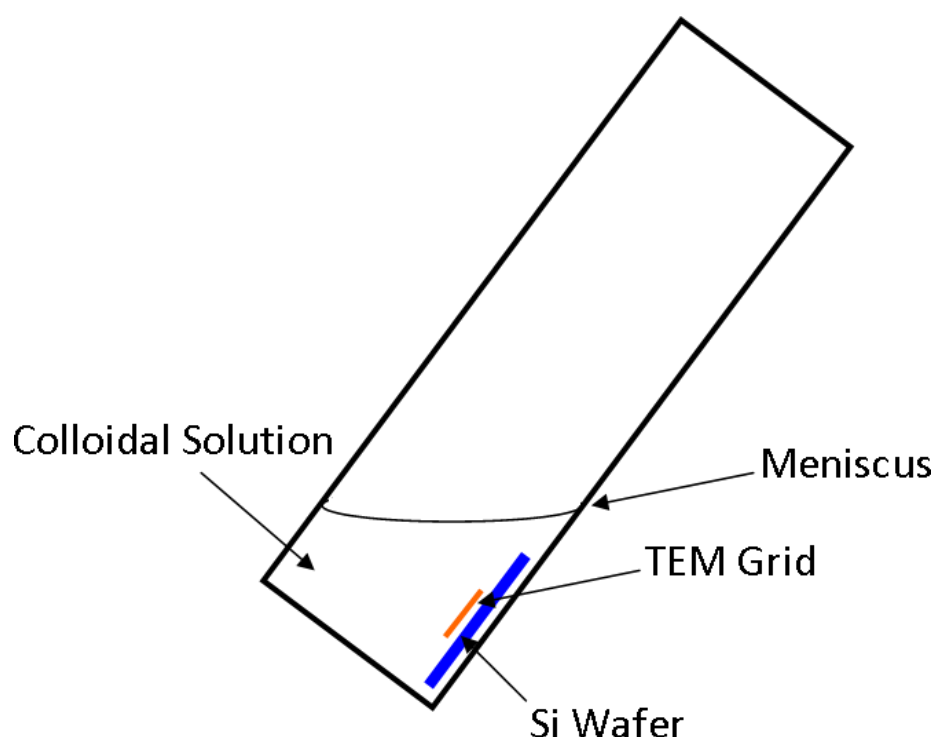
Results

When the reducing agent was added the reaction solution turned a red-wine/purple colour indicating the formation of nanostructured gold. The organic surfactant, CTAB, was then displaced by dodecanethiol resulting in a stable solution in various organic solvents. The first discarded N-methyl-formamide volume had a pale purple colour indicating some of the gold nanoparticles did not undergo ligand exchange with dodecanethiol, however the second and subsequent wash volumes were clear which shows the majority of the nanoparticles did undergo the exchange.

Figure 1 shows full characterisation of the as synthesised gold nanoparticles. Figure 1a shows a low magnification EM image of gold nanoparticles which are ~ 4 nm in size. Figure 1b shows a higher magnification EM image. The nanoparticles are

3.2 Formation of Gold Nanoparticle Superlattices (NPSL)

Scheme 1 shows the experimental setup for the formation of gold NPSL. A carbon coated TEM grid is applied to a silicon wafer with a drop of toluene which is then allowed to dry fixing the grid to the wafer. This is placed in a glass vial which is placed on a 45° angle. The TEM grid/Si wafer is then immersed in colloidal solution. This is left to completely evaporate at atmospheric temperature and pressure. The TEM grid is then removed from the Si wafer and left under a lamp for 5 min to remove any residual solvent.



Schematic 1. Experimental setup for forming NPSLs.

3.2.1 Effect of size distribution on the formation of Gold NPSL.

The following experiments were performed to demonstrate the need for a monodisperse product for the formation of NPSL. A polydispersity of less than 5 % is commonly required for 2D hexagonal and subsequent 3D colloidal crystallisation {Shevchenko 2006 (a), Urban 2007}. To control the size distribution of the resulting nanoparticles the reducing agent was added at different rates.

Results

Figure 2a shows an HREM image of gold nanoparticles formed when the reducing agent was added rapidly instead of dropwise. There are some regions of packed nanoparticles however there is no long range ordering and the nanoparticles can be regarded as being randomly positioned on the TEM grid. Figure 2b shows the size distribution profile of the as synthesised gold nanoparticles. The nanoparticles are 4.5 ± 0.8 nm with a polydispersity of $\sigma = 16.9$ %. Here, the polydispersity is calculated as the standard deviation from the mean nanoparticle size. The size distribution observed here is therefore well above the 5 % value required for superlattice formation. Figure 3 shows an HREM image of the as synthesised gold nanoparticles when applied in higher concentration to the TEM grid. The entire ensemble of nanoparticles is randomly agglomerated and there is no ordering of any type present.

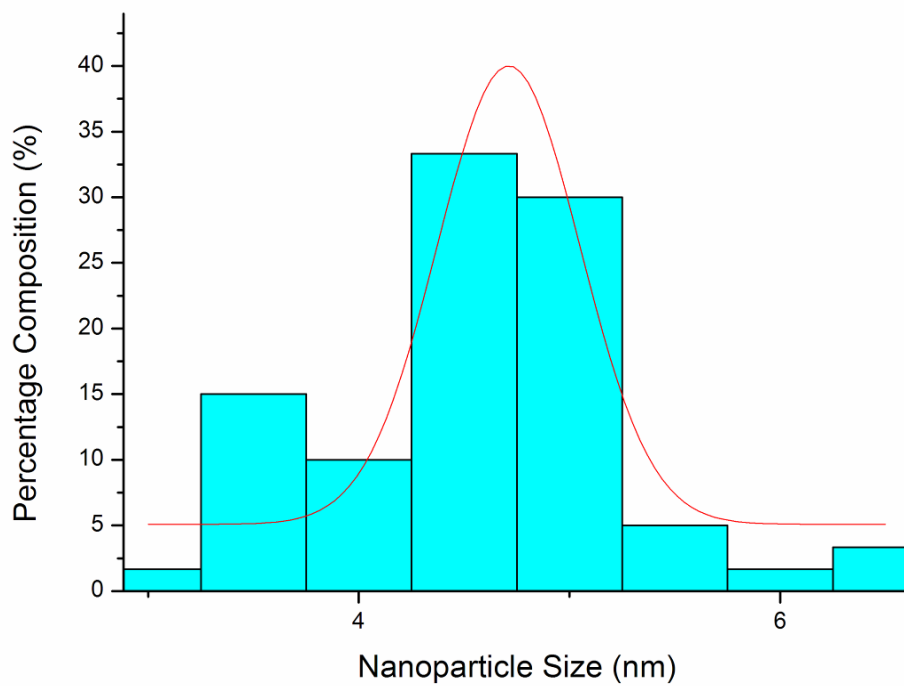
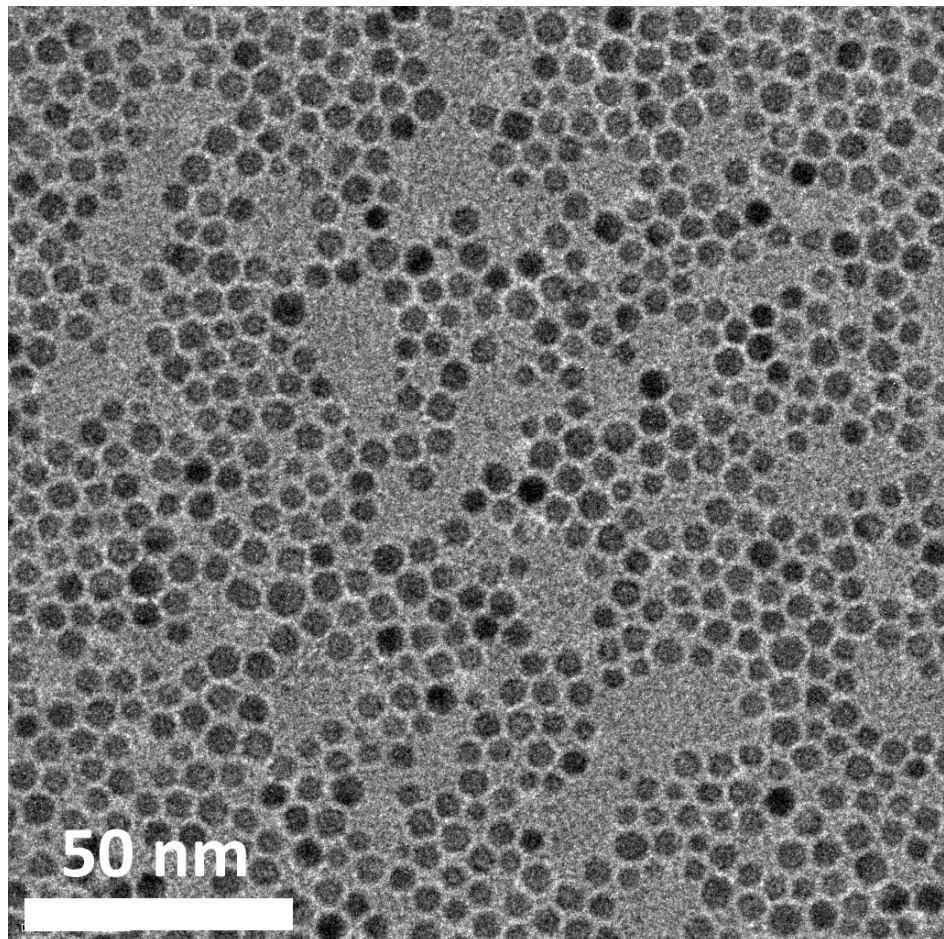


Figure 2. HREM image of Au nanoparticles formed by adding the reducing agent rapidly (a) and corresponding size distribution profile (b).

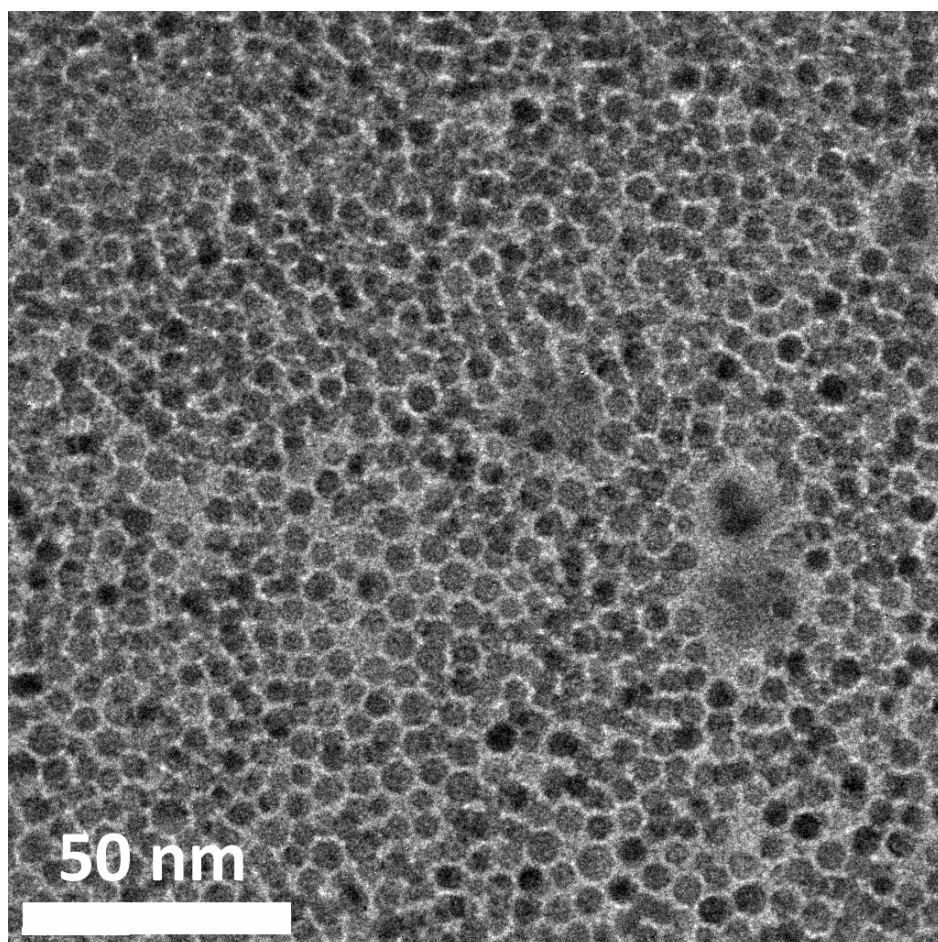


Figure 3. HREM image of Au nanoparticles formed by rapid addition of reducing agent.

Figure 4 displays gold nanoparticles formed when the reducing agent was added to the reaction solution dropwise resulting in a monodisperse product. Figure 4a shows an HREM image of the nanoparticles which can clearly be observed to form into a 2D hexagonal arrangement. The nanoparticles organise over micrometre length distances. This long range ordering is characteristic of a monodisperse product {Lin 2001, Rogach 2002}. Figure 4b shows a size distribution profile for nanoparticles imaged in Fig 4a. The nanoparticles are 4.5 ± 0.2 nm in size with a polydispersity from standard deviation of $\sigma = 4.7$ %. The average interparticle spacing (distance from edge to edge of adjacent nanoparticles) is 2.4 ± 0.2 nm. This value is lower than the length of two dodecanethiol molecules (average length ~ 1.5 nm each). This difference in length arises due to interdigitation of the organic capping molecules {Luedtke 1996}.

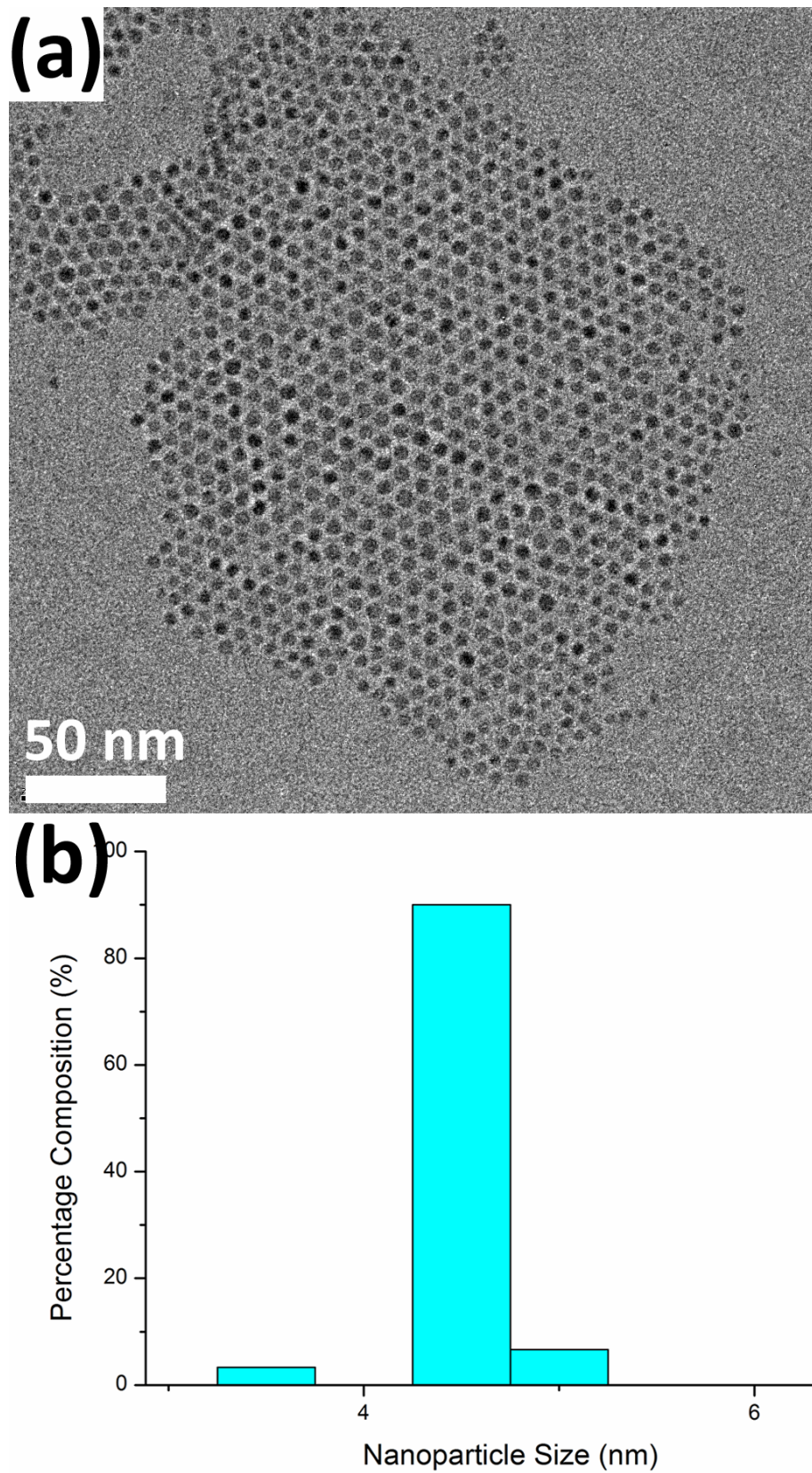


Figure 4. HREM image of Au nanoparticles formed by dropwise addition of reducing agent (a) and corresponding size distribution profile (b).

3.2.2 Effect of concentration on the formation of Gold NPSL

To investigate the formation of 3D NPSLs the concentration of the colloidal solution was incrementally increased before being deposited on the substrate. It was hoped that by increasing the concentration in stages structural intermediates in the formation of NPSLs could be isolated and characterised.

Results

Figure 5 shows the effect of doubling the concentration of gold nanoparticles in toluene. Figure 5a shows a monolayer of gold nanoparticles with a second layer of nanoparticles arranging directly above it. The monolayer is packed in a 2D hexagonal arrangement characteristic of monodisperse product as previously observed (Fig 4a). Again the nanoparticles are 4.5 ± 0.2 nm in size with a polydispersity of $\sigma = 4.7$ % and the average interparticle spacing is 2.4 ± 0.2 nm. A close up EM image is shown in Fig 5b which enables characterisation of the nanoparticle packing. This is shown schematically in Fig 5c where the blue spheres are the original monolayer and the red spheres represent those nanoparticles located in the second layer.

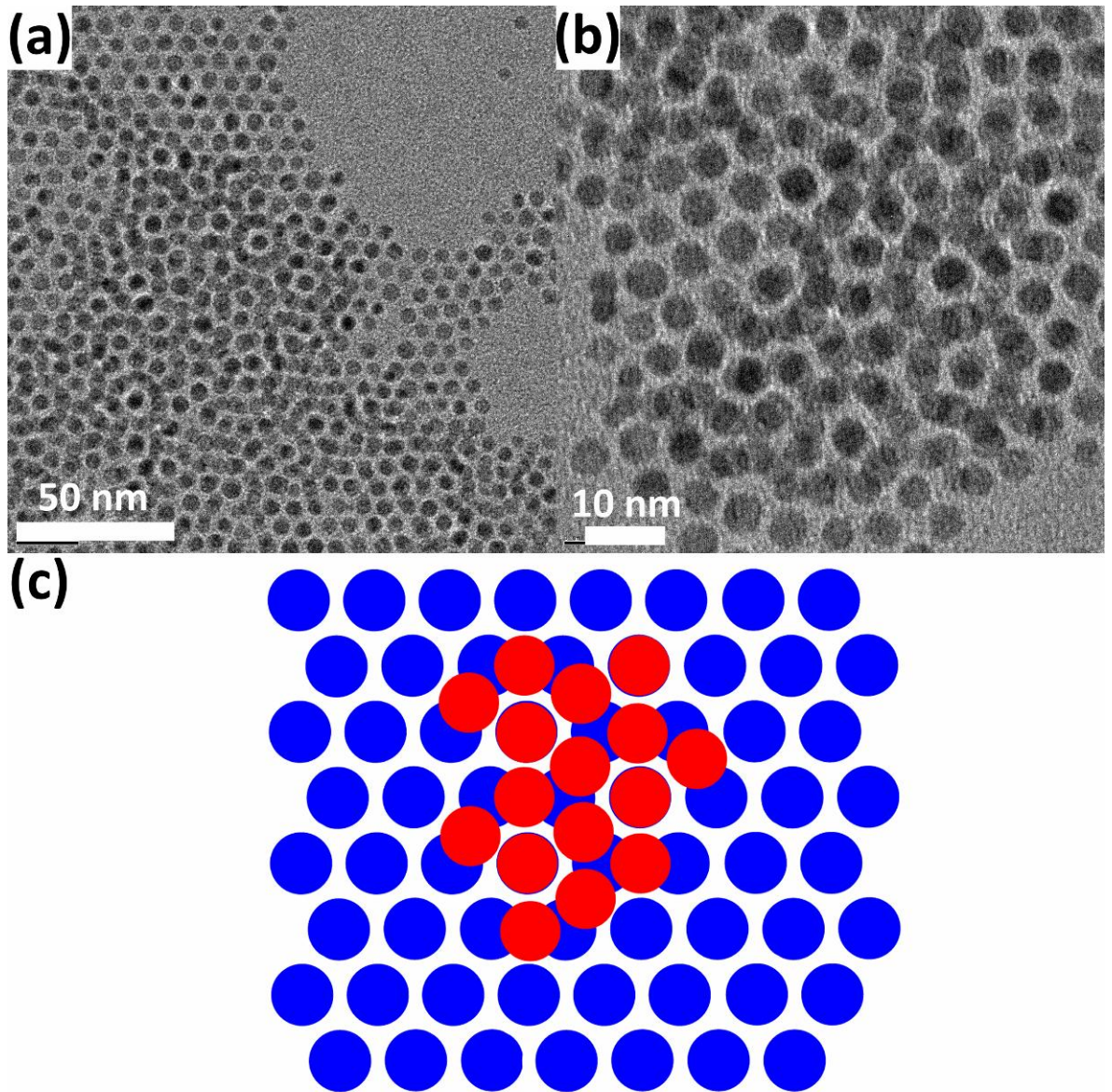


Figure 5. (a) HREM image of two layers of monodisperse Au nanoparticles. (b) High magnification HREM image of two layers of Au nanoparticles. (c) Schematic outlining the packing characteristics of the bilayer observed in TEM.

From the schematic we can see that the second layer forms by the addition of nanoparticles into the interstices between two adjacent nanoparticles on the initial monolayer, the so called 2-fold 'saddle' site {Fink 1998, Zanchet 1999, Gutierrez-Wing 2000}. This forms a 'ring' of nanoparticles on the second layer and creates a site for another nanoparticle to reside directly above a single nanoparticle on the first monolayer. Therefore the second layer consists of the same 2D arrangement as the first layer but rotated 30° . This creates a series of rings or 'eye' like formations on the second layer as observed in Fig 5b.

Figure 6 shows the formation of NPSL on a TEM substrate from a highly concentrated colloidal solution. The concentration was increased ten times that originally used for the formation of the monolayer in Fig 4a. The superlattice shown in Fig 6a is over $1 \mu\text{m}^2$ and shows rounded contours. Figure 6b shows that the nanoparticles are arranged in an cubic close packed type structure. The red arrows point to defects in the superlattice which are analogous to twin planes observed in atomic crystals. Note the presence of singular nanoparticle ranging in size from 2.1 nm to 5.2 nm on the TEM grid to the right of the superlattice.

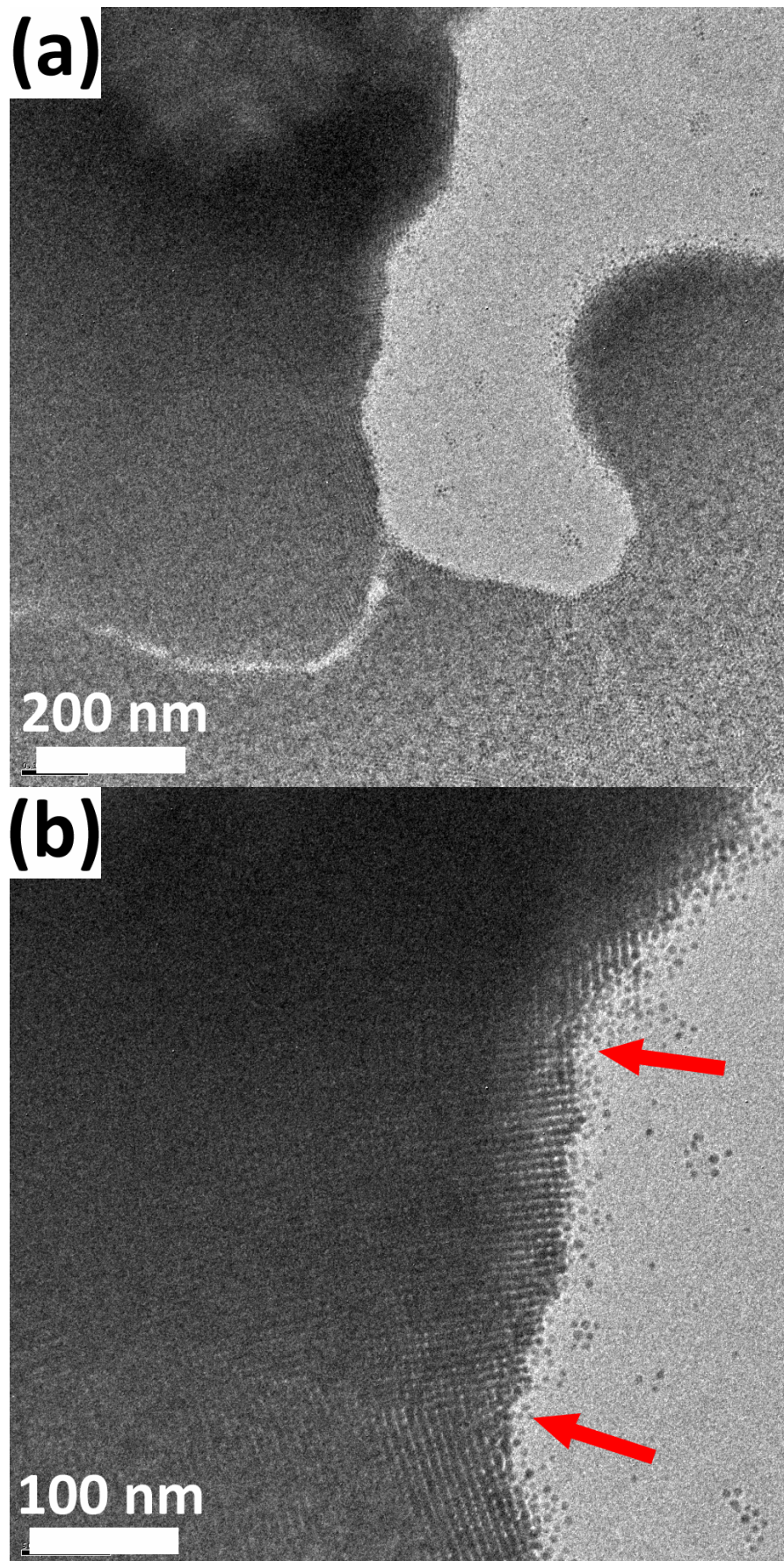


Figure 6. Low magnification HREM image of a Au NPSL (a), HREM image of a Au NPSL showing superlattice defects as indicated by the red arrows (b).

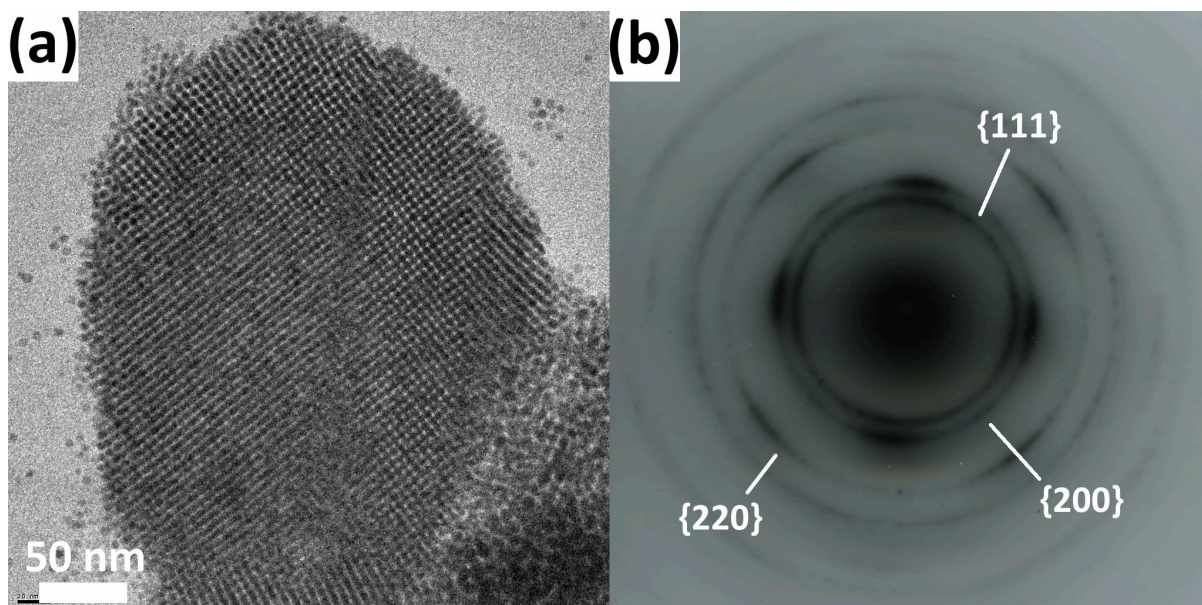


Figure 7. Low magnification HREM image of a Au NPSL (a), SAED of the imaged NPSL indicating oriented alignment (b).

Figure 7a shows a large NPSL 300 nm across and 400 nm long. The superlattice consists of gold nanoparticles in a cubic arrangement characteristic of *fcc* type packing viewed down a $\langle 100 \rangle$ zone axis. Figure 7b shows a SAED pattern with a band type reflection which is indexed to the *fcc* gold crystal structure.

To confirm the analogous crystal structure of the gold NPSL the specimen was tilted with respect to the electron beam and the projection compared to a model crystal structure. Figure 8a shows a high magnification HREM image of the NPSL viewed in Fig 7a clearly showing a cubic packing arrangement. This projection is comparable to a model of *fcc* Au metal viewed down a $\langle 100 \rangle$ zone axis (Fig 8b). To confirm the *fcc* like packing of the gold nanoparticles the specimen was tilted by -34.8° in the goniometer *y* direction. The HREM image of this projection is shown in Fig 8c. This projection is the same as is seen when the model crystal structure is tilted by the same degree (Fig 8d). Therefore the gold NPSL can be characterised as consisting of monodisperse gold nanoparticles arranged in a manner analogous to the *fcc* crystal structure.

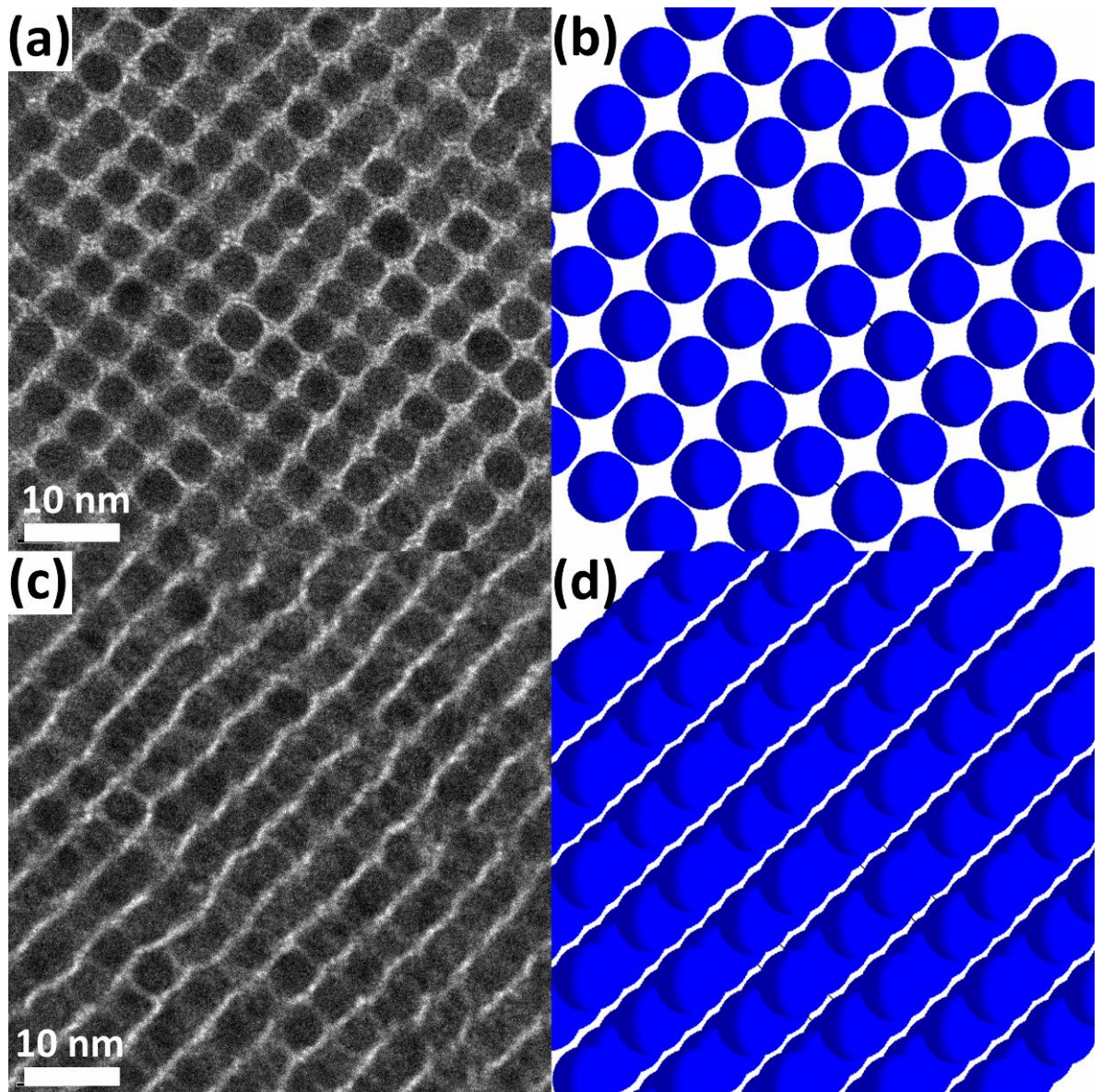


Figure 8. (a) High magnification HREM image of Au NPSL showing a cubic stacking arrangement, and corresponding image of model hard spheres (b). (c) The same region tilted by -34.8° in the goniometer y direction in relation to the electron beam, and corresponding image of model hard spheres (d).

3.3 Discussion on Formation of Gold NPSLs

The nanoparticles synthesised and displayed in Fig 1a-b show that the synthetic method chosen provides a facile route to monodisperse gold nanoparticles. While these nanoparticles are relatively monodisperse a 2D monolayer or 3D packing did not occur due to the low concentration of the colloidal solution.

When the reducing agent was added to the reaction solution rapidly a polydisperse nanoparticle ensemble was produced (Fig 2a). After evaporation of the colloidal solution only randomly positioned nanoparticles were observed, i.e., there was no evidence of long range ordering. When the concentration of the colloidal solution was increased only randomly aggregated nanoparticles were observed (Fig 3). These results indicate that i) adding the reducing agent dropwise is essential for a monodisperse product and ii) a monodisperse product is needed to obtain 2D and 3D packing.

The nanoparticles displayed in Fig 3a show the need for a monodisperse product in order to obtain 2D hexagonal ordering. From size analysis in Fig 3b the nanoparticles here have a polydispersity of $\sigma = 4.7\%$, a small value when compared to $\sigma = 16.9\%$ associated with the randomly positioned nanoparticles. This result confirms that a size distribution of less than $\sigma = 5\%$ is needed for long range nanoparticle ordering {Shevchenko 2006 (a), Urban 2007}.

When the concentration of the colloidal solution is increased we see the addition of a second layer of nanoparticles (Fig 5). In the second layer the nanoparticles occupy both two-fold saddle sites as well as being positioned directly above a nanoparticle on the first monolayer. This creates a 'ring' like projection that is characteristic of a CaCu_5 (AB_5) type crystal structure {Shevchenko 2002, Shevchenko 2006 (b)}. This is unexpected for NPSL as the thermodynamically favoured and most commonly observed position for a second layer nanoparticle is in the three-fold hollow sites characteristic of close packing {Motte 1997, Lin 2001, Rogach 2002} The room temperature equilibrium structure for dodecanethiol capped gold nanoparticles has previously been shown through molecular dynamics simulations to be tetragonally distorted *fcc*, a close packed structure {Luedtke 1996}. Therefore the anomalous

packing observed in Fig 5a-b can be considered relatively high energy. The nanoparticles positioned in two-fold saddle positions are not far from thermodynamic equilibrium with a potential energy difference of only ~ 3 meV (0.1 kT) when compared to a three-fold hollow site {Zanchet 1999}. However, the nanoparticles situated directly above another nanoparticle on the first monolayer would possess a considerably larger potential energy.

This difference in energy is reflected in the packing densities for analogous crystal structures of model hard spheres. Conventional close packed stacking has a packing density of $\phi = 0.74$ whereas the CaCu_5 type structure has a lower packing density of $\phi = 0.67$ {Steinhaus 1999, Uebayashi 2002}. This decrease in packing density creates a higher energy ensemble.

The self assembly of nanoparticles into ordered structures shows a direct dependence on the rate of crystallisation with slow growth rates tending towards the formation of *fcc* type structures {Pusey 1989}. The formation of energetically unfavourable structures would require rapid crystallisation. However, the present method for superlattice formation uses conditions which are much more mild than previous methods {Gutierrez-Wing 2000, Shevchenko 2002, Shevchenko 2006 (a), Shevchenko 2006 (b)}. As such, the crystallisation rate can be expected to be slow enough to produce the most thermodynamically preferred structure. Therefore crystallisation kinetics are most likely not the reason for the formation of the high energy packing observed.

In this case it is the presence of the soft organic capping ligand that promotes the formation of the energetically unfavourable CaCu_5 type structure. The organic capping ligand has two main effects on the packing through i) the balance between electrostatics and van der Waals forces and ii) steric repulsion.

Gold nanoparticles capped with dodecanethiol have been shown to possess either a neutral or negative charge making electrostatics important in their self-organisation {Shevchenko 2006 (b)}. Dispersion or van der Waals forces between the long alkyl chains of the organic capping ligand are also known to be a main driving force to direct the self assembly of nanoparticles {Zhang 2006, Shevchenko 2006 (a)}. Therefore, the balance between electrostatic repulsion and van der Waals attraction

is most likely a defining factor in the formation of the high energy CaCu_5 type structure {Fink 1998}.

The capping ligand also affects the packing through sterics. The interparticle spacing of 2.4 ± 0.2 nm observed here is considerably larger than that observed for other dodecanethiol capped gold nanoparticles {Gutierrez-Wing 2000}. This leads to an expansion of the monolayer in contact with the substrate. In this expanded state a hollow site would keep the nanoparticles further apart than their dynamic radius which results in an energy increase for that position {Zanchet 1999}. Therefore the 2-fold saddle sites becomes energetically comparable to the hollow site (within $0.1 kT$). This leaves an empty site directly above a nanoparticle which is stabilised by the presence of saddle occupied nanoparticles. This is subsequently filled resulting in the CaCu_5 type structure.

So while the final ordering of the two layers of atoms may not be the most thermodynamically stable, the route of formation is thermodynamically comparable to that of a close packed system.

The third layer then regains the thermodynamically favoured close packed ordering as the hollow site again becomes the most energetically favourable position {Zanchet 1999}. This provides the link between the CaCu_5 type structure observed in Fig 5a-b and the large close packed superlattices observed in Fig 6a-b.

When the concentration of the colloidal solution was increased large, micrometre superlattices were formed {Fig 6a-b}. These superlattices show rounded contours. The absence of well defined superlattice facets maybe due to the relatively short time of formation when compared to other methods which have produced highly faceted colloidal crystals {Stoeva 2003, Oonishi 2007}. Presumably the short period of formation does not provide enough time for nanoparticle diffusion across the superlattice surface to form defined facets, i.e., there is insufficient time and energy for superlattice 'annealing'.

Observed on the right hand side of the superlattice in Fig 6b are randomly positioned singular nanoparticles 2.1 nm to 5.2 nm in size. These nanoparticle sizes are outside the measured size distribution in Fig 4b and are therefore considered polydisperse

outliers. This is evidence of a kind of *in-situ* size selection procedure where only those monodisperse nanoparticles are incorporated into the formation of the superlattice while considerably smaller or larger nanoparticles are ejected.

The large superlattice observed in Fig 7a gave an SAED with a band-like reflection. This is characteristic of oriented alignment in NPSL which means the lattice planes of adjacent nanoparticles are aligned {Rogach 2002}. The bands are located on the {200} and {220} reflections. Their positioning is analogous to the spots observed from an SAED of a *fcc* crystal viewed down a $\langle 100 \rangle$ zone axis. This indicates that there is a significant number of nanoparticle in the superlattice shown in Fig 7a that are oriented along a $\langle 100 \rangle$ zone axis with respect to the electron beam.

The structure of the as formed superlattice is confirmed to be *fcc* through tilting experiments.

3.4 Summary

Monodisperse gold nanoparticles have been synthesised by a micro-emulsion synthesis. These were then used in the formation of gold NPSLs from a colloidal solution. Experiments show that a product with a small size distribution is needed for long range nanoparticle ordering.

When a low concentration colloidal solution is used, a 2D hexagonally packed monolayer is formed. As the concentration is increased a second layer is added and subsequently large micrometre NPSLs are formed.

The bilayer of nanoparticles arrange in a relatively high energy structure due to the presence of a soft organic capping ligand. The organic ligand promotes the formation of high energy packing through sterics, electrostatics and van der Waals forces. A third layer of nanoparticles then leads to a close packed thermodynamically favoured arrangement.

Tilting experiments were performed which showed that the gold NPSLs possessed an *fcc* type packing structure. Oriented alignment was shown to be present in the gold NPSL.

References

- Fink, J., Kiely, C. J., Bethell, D., Schiffrin, D. J., *Chemistry of Materials* **1998**, *10*, 922.
- Gutierrez-Wing, C., Santiago, P., Ascencio, J. A., Camacho, A., Jose-Yacaman, M., *Applied Physics a-Materials Science & Processing* **2000**, *71*, 237.
- Lin, X. M., Jaeger, H. M., Sorensen, C. M., Klabunde, K. J., *Journal of Physical Chemistry B* **2001**, *105*, 3353.
- Luedtke, W. D., Landman, U., *Journal of Physical Chemistry* **1996**, *100*, 13323.
- Motte, L., Billoudet, F., Lacaze, E., Douin, J., Pileni, M. P., *Journal of Physical Chemistry B* **1997**, *101*, 138.
- Oonishi, T., Sato, S., Yao, H., Kimura, K., *Journal of Applied Physics* **2007**, *101*,
- Pusey, P. N., Vanmegen, W., Bartlett, P., Ackerson, B. J., Rarity, J. G., Underwood, S. M., *Physical Review Letters* **1989**, *63*, 2753.
- Rogach, A. L., Talapin, D. V., Shevchenko, E. V., Kornowski, A., Haase, M., Weller, H., *Advanced Functional Materials* **2002**, *12*, 653.
- (a) Shevchenko, E. V., Talapin, D. V., Kotov, N. A., O'Brien, S., Murray, C. B., *Nature* **2006**, *439*, 55.
- (b) Shevchenko, E. V., Talapin, D. V., Murray, C. B., O'Brien, S., *Journal of the American Chemical Society* **2006**, *128*, 3620.
- Steinhaus, H., *Mathematical Snapshots*, 3rd ed., Dover, New York, **1999**.
- Stoeva, S. I., Prasad, B. L. V., Uma, S., Stoimenov, P. K., Zaikovski, V., Sorensen, C. M., Klabunde, K. J., *Journal of Physical Chemistry B* **2003**, *107*, 7441.
- Tilley, R. D., Saito, S., *Langmuir* **2003**, *19*, 5115.
- Uebayashi, K., Terao, K., Yamada, H., *Journal of Alloys and Compounds* **2002**, *346*, 47.
- Urban, J. J., Talapin, D. V., Shevchenko, E. V., Kagan, C. R., Murray, C. B., *Nature Materials* **2007**, *6*, 115.
- Whetten, R. L., Shafigullin, M. N., Khoury, J. T., Schaaff, T. G., Vezmar, I., Alvarez, M. M., Wilkinson, A., *Accounts of Chemical Research* **1999**, *32*, 397.
- Zanchet, D., Moreno, M. S., Ugarte, D., *Physical Review Letters* **1999**, *82*, 5277.
- Zhang, H., Edwards, E. W., Wang, D. Y., Mohwald, H., *Physical Chemistry Chemical Physics* **2006**, *8*, 3288.

Chapter 4. Solution Phase Syntheses of Lead Chalcogenide Nanoparticles

This part of the thesis is concerned with size and shape control of monodisperse lead chalcogenide nanoparticles synthesised in the solution phase. This will produce various types of nanoparticles which have application in solar cell technology. The syntheses involve the decomposition of a lead salt in the presence of an organic stabiliser ligand. For PbSe this is carried out in a non-coordinating solvent. For PbS the organic stabiliser species plays a dual role as high boiling point solvent. Both Se and S are used in their elemental state. A ligand exchange procedure will be attempted which will replace the long chain organic stabiliser ligands with a shorter chained species. This will allow for easier extraction of a photocurrent when used in solar cell technology.

The general procedure presented here is commonly referred to as the 'hot injection' method. The hot injection method employed involves the rapid injection of the chalcogenide source into a hot solution containing the lead salt and organic stabiliser. This creates a supersaturated solution that will be relieved by a burst of nucleation. The overall monomer concentration will then drop below the critical nucleation concentration and suppress any subsequent nucleation events. As a result, an ensemble of nanoparticles with a monodisperse size distribution is hoped to form.

4.1 Solution Phase Syntheses of PbSe Nanoparticles

PbSe nanostructures have previously been synthesised using chemical vapour deposition, ion beam assisted deposition and template assisted methods {Jian 2006, Bierman 2007, Sima 2008}. However, the present study involves the synthesis of PbSe nanoparticles in the solution phase. This method enables greater control over size and shape of the nanoparticles and ultimately leads to a more monodisperse product {Yin 2005}. Solution phase methods are less energy intensive than physical techniques. They also have the added advantage of producing a colloidal solution that can be easily applied to substrates leading to ease of fabrication for prototype solar cells.

This section outlines those experiments performed on the synthesis of PbSe nanoparticles using trioctylphosphine (TOP) as the organic stabiliser ligand. Size distribution analysis is performed in the following experiments by measuring the sizes of at least 2000 nanoparticles.

4.1.1 Reactions of $\text{Pb}(\text{Ac})_2$ in Trioctylphosphine (TOP) @ 150 °C – Effect of Reaction Time

In this series of experiments a lead salt ($\text{Pb}(\text{Ac})_2$) precursor was thermally decomposed in a coordinating solvent in the presence of a selenium source. The method employed here is based on the first reported hot injection synthesis of PbSe which produced monodisperse nanoparticles varying in size from 3.5 to 12 nm depending on reaction temperature {Murray 2001}. Therefore, this method was used in the following experiments with minor adjustments.

The following set of experiments looks at the structural evolution of PbSe nanoparticles by extracting intermediate structures at 1, 5 and 10 min and the final reaction product at 15 min.

Experimental

In a three necked round bottomed flask 0.5 g of $\text{Pb}(\text{Ac})_2$ and 2 mL of oleic acid (OA) was added to 5 mL of diphenyl ether. The flask was then purged and filled with N_2 to create an oxygen free atmosphere. The reaction solution was heated to 150 °C where it was left to stir for 30 minutes to ensure the lead salt was fully dissolved. This

Chapter 4: Solution Phase Syntheses of Lead Chalcogenide Nanoparticles

resulted in a yellow solution. In a separate beaker 0.8 g of elemental Se was added to 5 mL of trioctylphosphine (TOP). This was heated on a hot plate to dissolve the Se and form TOPSe.

The Pb(Ac)₂/OA/diphenyl ether solution and TOPSe were then both cooled to room temperature and mixed. In a separate three necked round bottomed flask 15 mL diphenyl ether was heated to 150 °C. The Pb(Ac)₂/OA/diphenyl ether/TOPSe solution was then rapidly injected. This was left to react for 1, 5, 10 and 15 min at 150 °C. After reaction completion the solution was left to cool for purification.

For purification of the sample, a 50:50 mixture of methanol and toluene was added to flocculate the as synthesised nanoparticles when the reaction solution had reached 70 °C. The solution was then cooled to room temperature and centrifuged at 14 000 rpm for collection of the solid nanoparticles. These were subsequently washed by suspending the pellet in toluene and ultrasonicing for 5 minutes. Additional methanol was added again to flocculate the nanoparticles followed by centrifuging. The purification process was repeated and the resulting purified sample was suspended in toluene for TEM investigation. The as synthesised PbSe nanoparticles could also be suspended in hexane, tetrachloroethylene and other non-polar solvents if required.

Results : Experiment 1 (1 min Reaction Time)

When the Pb/OA/diphenyl ether solution was added to the TOPSe a light brown colour resulted. This may be due to the formation of small nuclei. When the mixture was injected into the hot diphenyl ether a dark brown/black solution resulted indicating the formation of PbSe. An HREM image of the as synthesised nanoparticles is shown in Fig 1a.

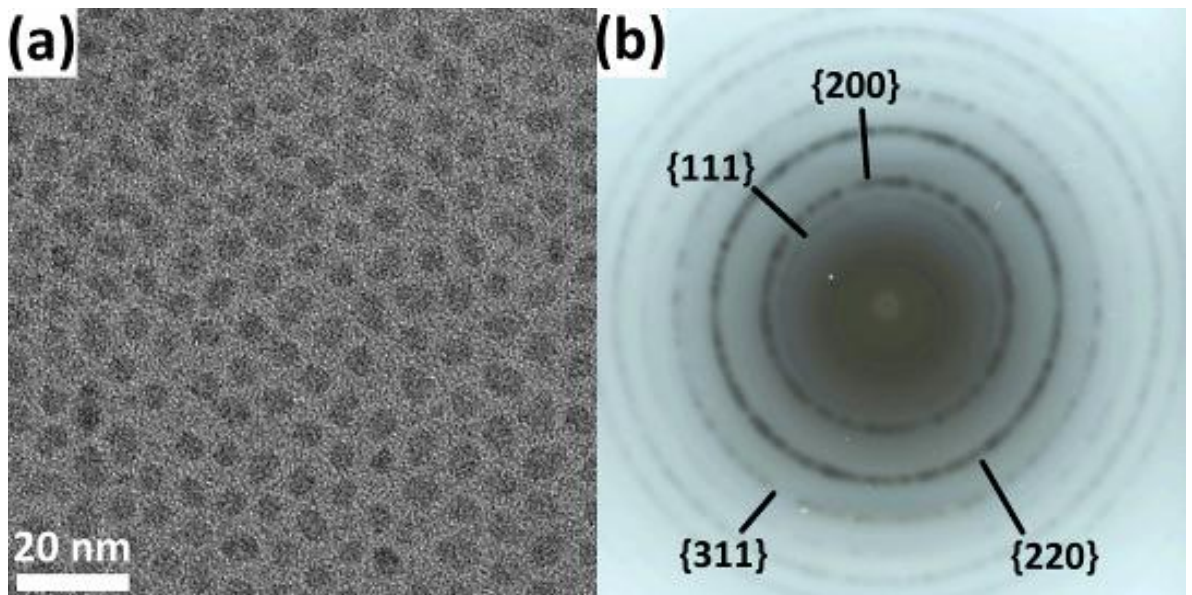


Figure 1. (a) HREM image of as synthesised PbSe nanoparticles formed after 1 min reaction time. (b) Corresponding SAED pattern indexed to the *fcc* crystal structure of PbSe.

The nanoparticles are 4.5 ± 0.5 nm in size and have a roughly spherical morphology however there is some elongation and irregularity to their shape. A SAED pattern is shown in Fig 1b which is indexed to the face centred cubic (*fcc*) crystal structure of PbSe (Space Group = *Fm-3m*). An EDS spectrum of the PbSe nanoparticles is shown in Fig 2. The product is 62 % Pb and 38 % Se with additional peaks corresponding to the copper grid and carbon film.

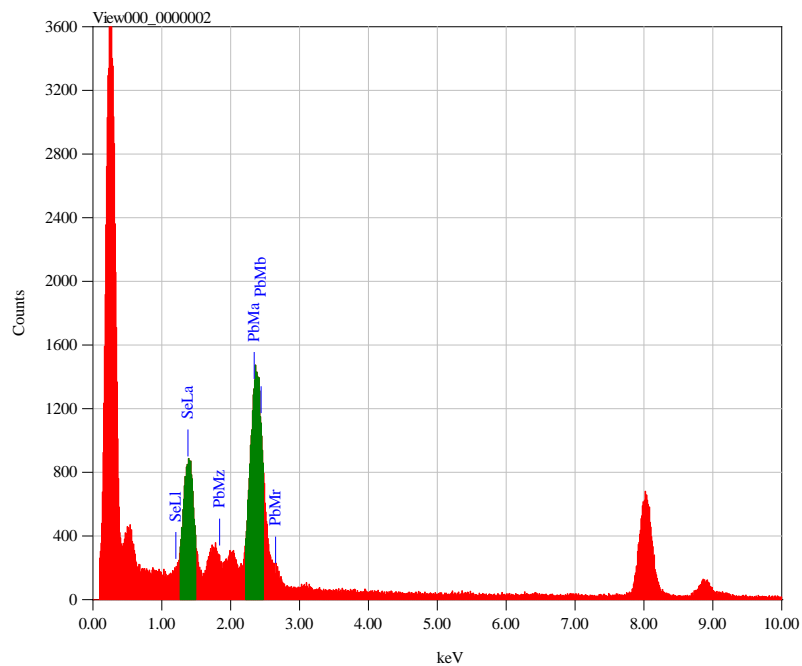


Figure 2. EDS spectrum of the as synthesised PbSe nanoparticles.

Results : Experiment 2 (5 min Reaction Time)

The as synthesised nanoparticles are shown in Fig 3a with size distribution analysis shown in Fig 3b. The nanoparticles are 6.6 ± 1 nm in size with a spherical morphology. They have a polydispersity from standard deviation of $\sigma = 6.3$ %. This is close to the theoretically predicted size distribution of 5 % required for colloidal crystallisation {Shevchenko 2006}. In fact, the HREM image shows the nanoparticles organising into a 2D hexagonal packing arrangement. This is indicative of a monodisperse product.

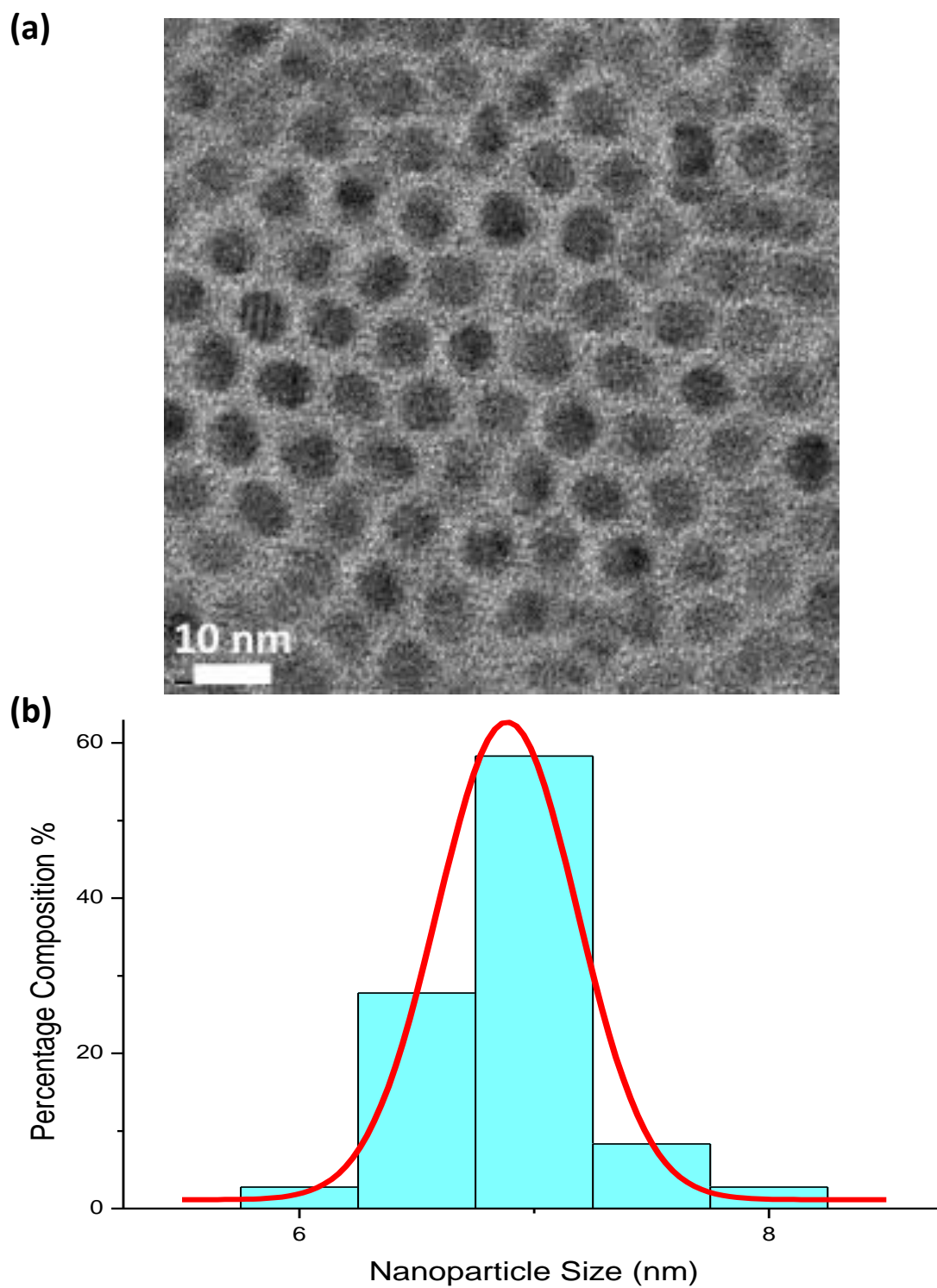


Figure 3. (a) HREM image of the as synthesised PbSe nanoparticles formed after 5 min reaction time and (b) the corresponding size distribution profile.

Results : Experiment 3 (10 min Reaction Time)

The as synthesised nanoparticles are shown in Fig 4a with size distribution analysis shown in Fig 4b. The nanoparticles are 7.9 ± 1.2 nm in size with a roughly spherical morphology and a polydispersity from standard deviation of $\sigma = 7.6$ %. This polydispersity is relatively large when compared to the value required for colloidal crystallisation which is confirmed by the lack of long range hexagonal packing in the HREM image. The nanoparticles are largely spherical however there is some faceting present.

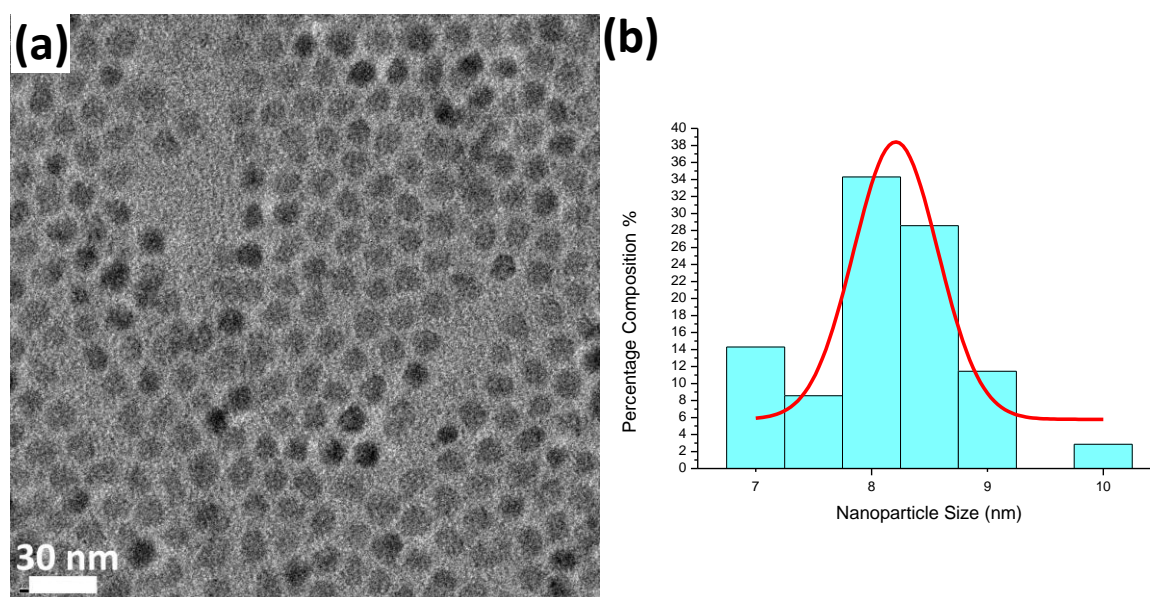


Figure 4. (a) HREM image of the as synthesised PbSe nanoparticles formed after 10 min reaction time and (b) the corresponding size distribution profile.

Results : Experiment 4 (15 min Reaction Time)

The as synthesised nanoparticles are shown in Fig 5a with a high magnification image shown in Fig 5b. The nanoparticles have a rounded cube shape and are 14 ± 1 nm in size. They are randomly agglomerated which is unexpected considering their relative monodispersity. The lattice planes of the two nanocubes shown in Figure 5b are not aligned confirming the random orientation of the nanoparticles.

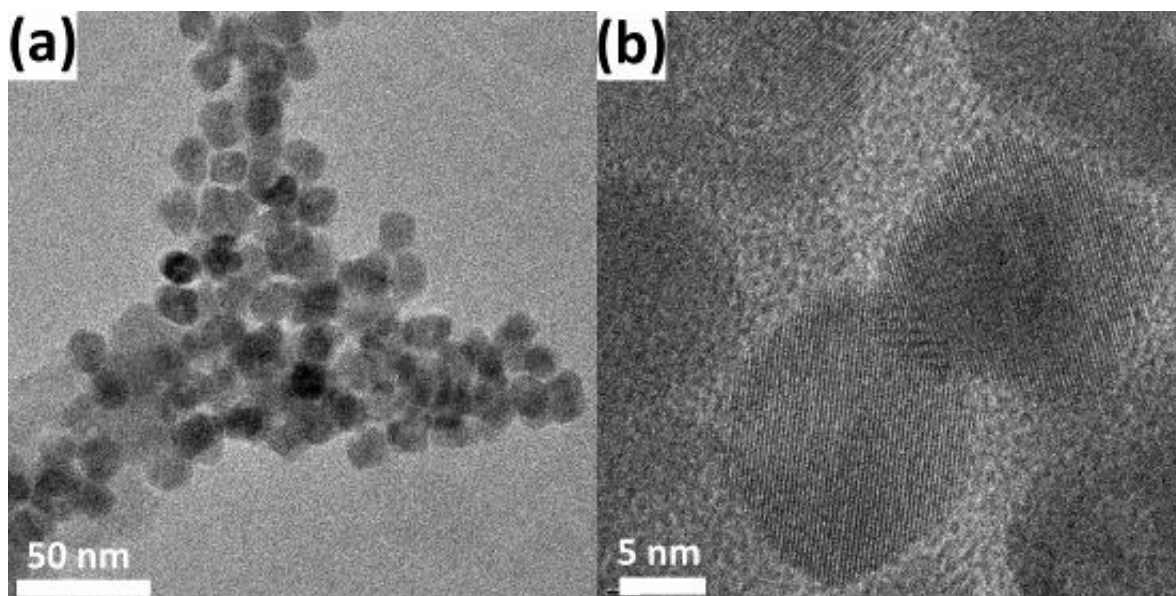


Figure 5. (a) HREM image of the as synthesized PbSe nanoparticles formed after 15 min reaction time and (b) high magnification TEM image.

4.1.2 Discussion Reactions of Pb(Ac)₂ in Trioctylphosphine (TOP) @ 150 °C – Effect of Reaction Time

Exp #	Precursor	Surfactant /Solvent	Rxn Time (min)	Rxn Temp (oC)	Product
1	Pb(Ac) ₂	TOP/ diphenyl ether	1	150	spheres 4.5 ± 0.5 nm
2	Pb(Ac) ₂	TOP/ diphenyl ether	5	150	spheres 6.6 ± 1 nm
3	Pb(Ac) ₂	TOP/ diphenyl ether	10	150	spheres/cubes 7.9 ± 1.2 nm
4	Pb(Ac) ₂	TOP/ diphenyl ether	15	150	rounded cubes 14 ± 1 nm

Table 1. Results of PbSe synthesis at 150 °C in diphenyl ether using TOP as surfactant.

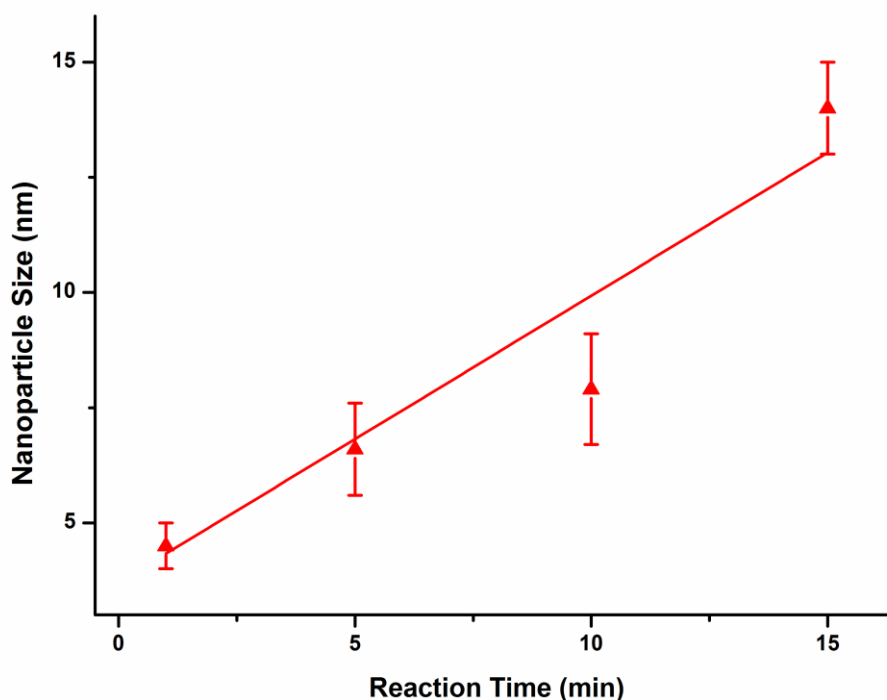


Figure 6. Plot showing the increase in size of PbSe nanoparticles with increasing reaction time when grown at 150 °C.

In the above set of experiments the structural evolution of the PbSe nanoparticles can be observed. When reacted for 1 min, 4 to 5 nm spherical nanoparticles are produced. As the reaction progresses the nanoparticles grow into 6.6 nm spheres, 7.9 nm rounded cubes and finally nanocubes 14 nm in size. The increase in the size of the nanoparticles with increasing reaction time can be seen in Fig 6. This increase can be understood as an increase in total monomer addition to the crystal with longer reaction time. However, the shape evolution from spherical to cubic morphology requires more discussion.

At small sizes surface energy considerations dominate and spheres form due to the minimisation of surface area to volume ratio {Pietryga 2004}. Therefore, in the present system the lowest-energy morphology for PbSe nanoparticles on the 4 to 5 nm size regime is spherical. As the nanoparticles grow the inherent crystalline energy begins to have a greater contribution on the overall energy. So, as the size of the nanoparticle increases a cubic shape, arising from the *fcc* crystal structure of the material, begins to emerge. Here, a cubic morphology is observed after 15 minutes

reaction time which indicates that inherent crystalline energy begins to dominate the overall nanoparticle energy at a size of ~ 14 nm. This leads to the emergence of a cubic morphology.

4.1.3 Reactions of $\text{Pb}(\text{Ac})_2$ in Trioctylphosphine (TOP) @ 200 °C – Effect of Reaction Time

In this set of experiments the reaction temperature was increased to 200 °C. Here it was hoped that a higher injection temperature would create a faster nucleation burst resulting in more distinct separation of the nucleation and growth steps and thus a more isotropic, monodisperse reaction product. Furthermore, it has been shown that the size at which the inherent crystalline energy begins to dominate the structure of the nanoparticle is temperature dependant, with high temperatures favouring the transition from a spherical to cubic shape at larger sizes {Lee 2002}. Therefore by increasing the temperature of the reaction it was also hoped that larger spherical nanoparticles could be formed.

Experimental

In a three necked round bottomed flask 0.25 g of $\text{Pb}(\text{Ac})_2$ and 1 mL of oleic acid (OA) was added to 2.5 mL of diphenyl ether. The flask was then purged and filled with N_2 to create an oxygen free atmosphere. The reaction solution was heated to 150 °C where it was left to stir for 30 minutes to ensure the lead salt was fully dissolved. This resulted in a yellow solution. In a separate beaker 0.4 g of elemental Se was added to 2.5 mL of trioctylphosphine (TOP). This was heated on a hot plate to dissolve the Se and form TOPSe.

The $\text{Pb}(\text{Ac})_2$ /OA/diphenyl ether solution and TOPSe were then both cooled to room temperature and mixed. In a separate three necked round bottomed flask 15 mL diphenyl ether was heated to 200 °C. The $\text{Pb}(\text{Ac})_2$ /OA/diphenyl ether/TOPSe solution was then rapidly injected. This was left to react for 5, 15 and 30 min at 200 °C. After reaction completion the solution was left to cool for purification which was carried out as above.

Results : Experiment 5 (5 min Reaction Time)

The as synthesised nanoparticles are shown in Fig 7a. The nanoparticles are roughly spherical in morphology however some faceting is present. They are 10 ± 0.8 nm in size which makes them relatively monodisperse however there was no long range ordering observed. Figure 7b shows an high magnification HREM image of the PbSe nanoparticles. This shows that the nanoparticles are not perfectly spherical with some elongation present.

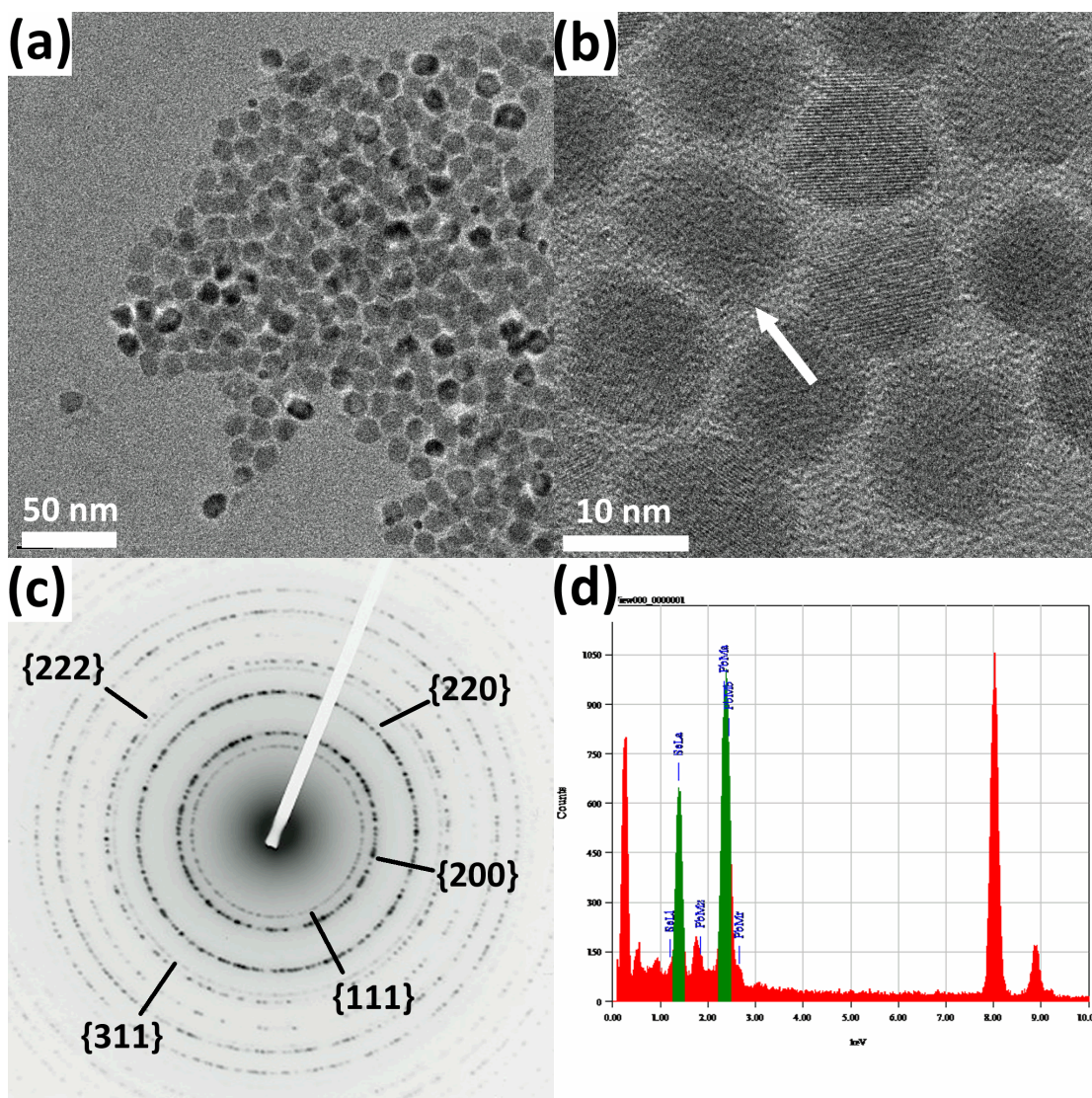


Figure 7. Plot (a) Low magnification HREM image of PbSe nanoparticles formed after 5 min reaction time at 200 °C. (b) High magnification HREM image of the PbSe nanoparticles with the white arrow indicating elongation in the nanoparticle morphology. (c) SAED indexed to the *fcc* PbSe crystal structure and (d) EDS spectrum of the as synthesised nanoparticles.

Chapter 4: Solution Phase Syntheses of Lead Chalcogenide Nanoparticles

The nanoparticle highlighted by the arrow has an elongated shape with an aspect ratio of 1.44. Figure 7c shows a SAED pattern which is indexed to the *fcc* crystal structure of PbSe. Figure 7d shows an EDS spectrum of the nanoparticles viewed in Fig 7a and indicates the sample is 55% Pb and 45% Se (the additional unlabeled peaks come from the carbon film and the copper grid).

Results : Experiment 6 (15 min Reaction Time)

The as synthesised nanoparticles are shown in Fig 8a. They are 14 ± 2 nm in size and possess a roughly cubic morphology however there are nanoparticles present with a more spherical shape. The inset shows a SAED that is indexed to PbSe cubic crystal structure. Figure 8b shows a single PbSe nanocube 14 nm in size. Atomic packing is visible and along with the power spectrum in the inset shows this nanoparticle is single crystal and is being viewed down a $\{100\}$ zone axis. This is the commonly observed terminating facet for a cubic nanoparticle. It possesses some shape deviation due to the increased growth on its right hand edge. By analysis of the angles of the lattice planes compared to the surface of the nanocube it can be observed that this extended growth gives rise to a (110) facet and a high index (411) facet terminating side of the nanocube.

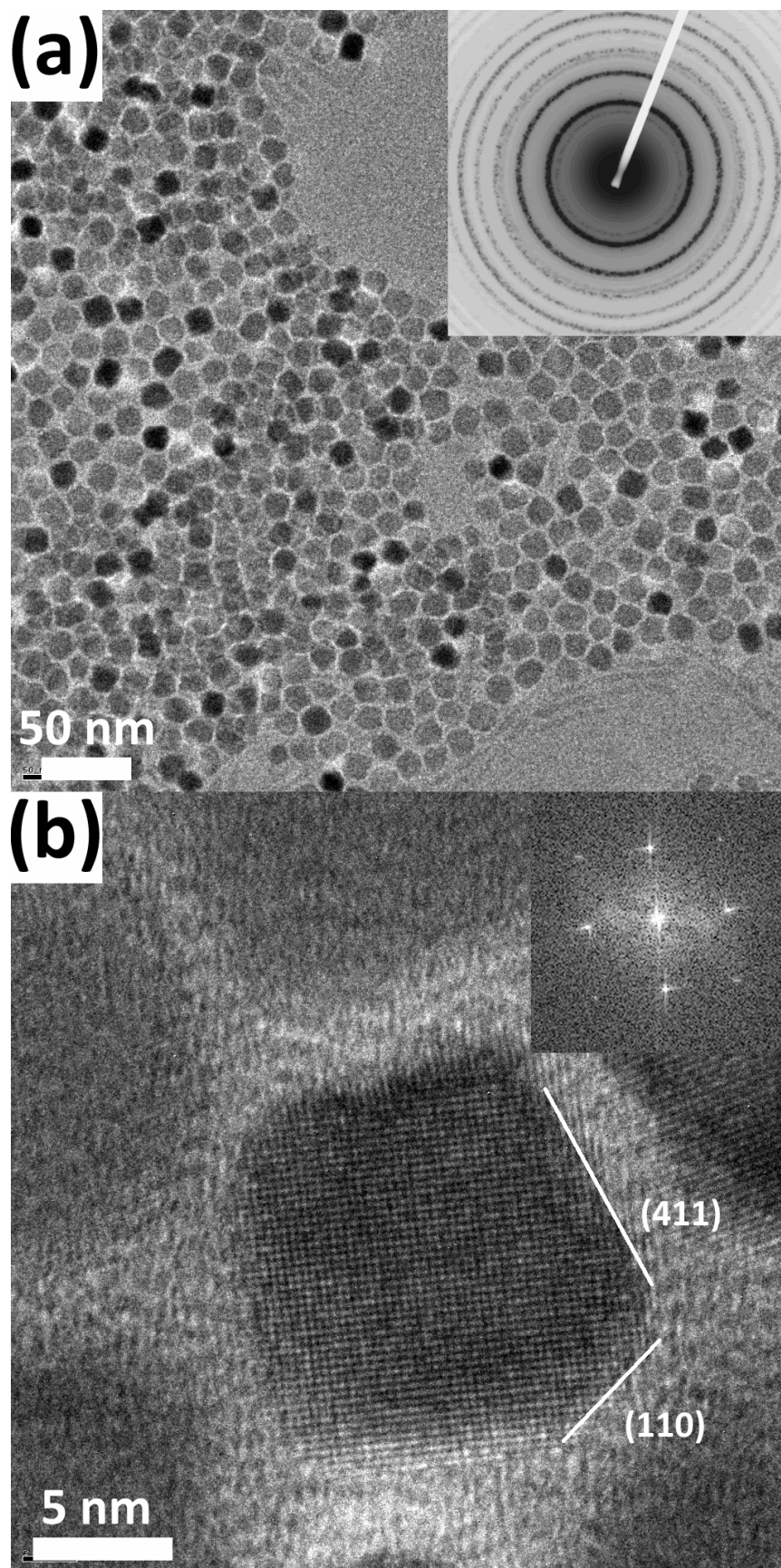


Figure 8. Plot (a) Low magnification HREM image of PbSe nanoparticles formed after 15 min reaction time and corresponding SAED pattern (inset). (b) High resolution HREM image of a single cubic PbSe nanoparticle with corresponding power spectrum (inset).

Results : Experiment 7 (30 min Reaction Time)

The as synthesised nanoparticles are shown in Fig 9. They have a highly faceted, cubic morphology and are 16 ± 4 nm in size. So, while the shape distribution is more uniform, the polydispersity has increased. This is evidenced by the lack of long range ordering characteristic of a monodisperse product.

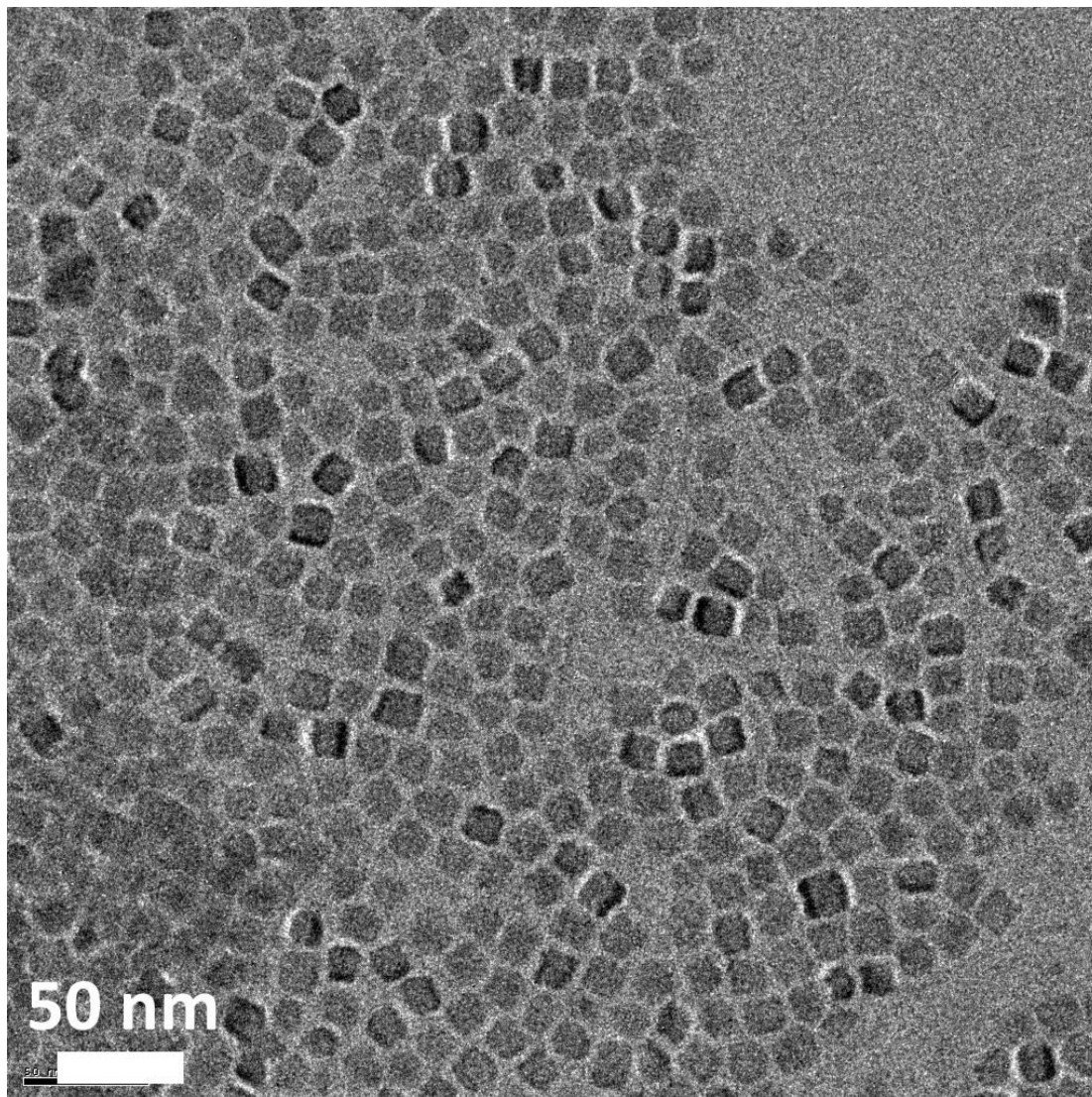


Figure 9. Plot (a) Low magnification HREM image of PbSe nanoparticles formed after 30 min reaction time.

4.1.4 Discussion Reactions of Pb(Ac)₂ in Trioctylphosphine (TOP) @ 200 °C – Effect of Reaction Time

Exp #	Precursor	Surfactant /Solvent	Rxn Time (min)	Rxn Temp (oC)	Product
5	Pb(Ac) ₂	TOP/ diphenyl ether	5	200	roughly spherical NPs 10 ± 0.8 nm
6	Pb(Ac) ₂	TOP/ diphenyl ether	15	200	rounded cubes 14 ± 2 nm
7	Pb(Ac) ₂	TOP/ diphenyl ether	30	200	highly faceted cubes 16 ± 4 nm

Table 2. Results of PbSe synthesis at 200 °C in diphenyl ether using TOP as surfactant.

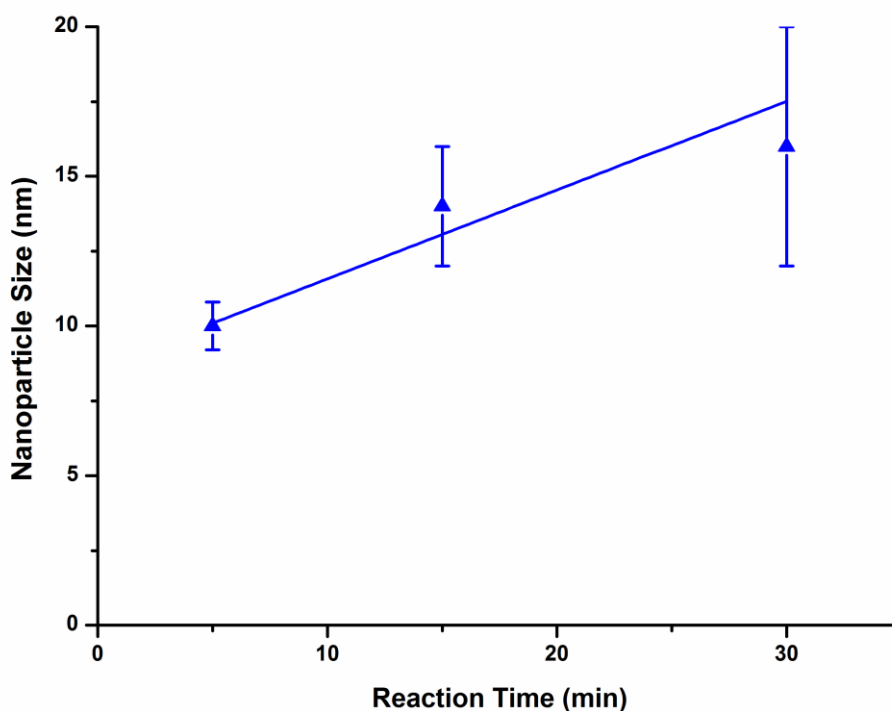


Figure 10. Plot showing the increase in size of PbSe nanoparticles with increasing reaction time when grown at 200 °C.

The above set of experiments shows the evolution of PbSe nanoparticles when grown at a reaction temperature of nanoparticle 200 °C. A similar evolution of nanoparticle morphology is observed as when grown at 150 °C. After 5 min slightly irregular spherical nanoparticles are formed. These evolve into rounded faceted 14 ± 2 nm

Chapter 4: *Solution Phase Syntheses of Lead Chalcogenide Nanoparticles*

nanoparticles at 15 min and finally highly faceted 16 ± 4 nm nanocubes after 30 min. A plot outlining the increase in nanoparticle size with longer reaction times is shown in Fig 10.

After 5 min reaction time the nanoparticles grown at 200 °C are larger and more faceted than those formed at 150 °C. After 15 min reaction time the nanoparticles are a similar size to those formed at 150 °C however they are much more faceted. Therefore, when produced at 200 °C the inherent crystalline anisotropy is beginning to dominate at a smaller nanoparticle size than when reacted at 150 °C. This is in direct contrast to the observations of Lee et al that a higher reaction temperature would cause the transition from spherical to cubic to occur at larger nanoparticle sizes.

This is due to the weak binding strength of TOP when compared to the dodecanethiol capping agent used by Lee et al. The energy barrier to nucleation on the {111} facets is reduced with weakly binding surfactants therefore growth is promoted along these directions {Sugimoto 1983}. So, in the presence of the relatively weak phosphine-Pb capping interaction monomer addition to the growing nanoparticle preferably occurs along the <111> directions. The rate of monomer addition on the {111} faces is then directly dependant on overcoming the associated energy barrier. Therefore the growth rate along the <111> direction is promoted at higher temperatures. This leads to the more faceted, cube like morphologies observed in smaller sized nanoparticles.

4.2 Solution Phase Syntheses of PbS Nanoparticles

In this series of experiments the hot injection method was used for the formation of PbS nanoparticles. A lead salt precursor was thermally decomposed in a coordinating solvent in the presence of a sulphur source; in this case elemental sulphur. Previous studies have involved the formation of PbS nanocubes in aqueous solution and through high temperature autoclave reactions {Jiang 2001, Qi 2005, Cao 2006}. While these experiments were able to easily produce cubic and rod-like nanoparticles, the polydispersity was large indicating insufficient reaction control. Here, the use of long chain organic stabilisers in a hot injection method is hoped to produce PbS nanoparticles with uniform size and shape distribution.

Size distribution analysis is performed in the following experiments by measuring the sizes of at least 2000 nanoparticles.

4.2.1 Reactions of Pb(Ac)₂ in Hexadecylamine (HDA)

Lead (II) acetate (Pb(Ac)₂) was chosen as the lead precursor as it has previously been shown to be effective in the formation of chalcogenide nanoparticles {Warner 2006}. Hexadecylamine was chosen as the solvent for these reactions as it has a high boiling point of 332 °C. The solvent also has an amine termination which means it serves a dual role as organic stabiliser. The reaction conditions presented here were modified from a previous study on the formation and self assembly of CdS nanocrystals {Warner 2006}.

4.2.1.1 Experiment 8 : Reaction of Pb(Ac)₂ in a 1:6 ratio of Pb:S in HDA

An excess of sulphur has previously been shown to induce spontaneous superlattice formation in the synthesis of CdS nanocrystals {Warner 2006}. For nanocrystal superlattices to form, a monodisperse size distribution ($\sigma \sim 5\%$) is required {Shevchenko 2006}. Therefore, in this experiment it was hoped that an excess of sulphur would lead to a monodisperse size distribution.

Experimental

In a three necked round bottomed flask 0.2 g of $\text{Pb}(\text{Ac})_2$ was added to 3 g HDA. The flask was then purged and filled with N_2 to create an oxygen free atmosphere. The reaction solution was heated to 190 °C where it was left to stir for 10 minutes to ensure the lead salt was fully dissolved. In a separate vial 100 mg of elemental S was added to 2 g HDA. This was heated on a hot plate to dissolve the S.

The S/HDA mixture was then injected rapidly into the $\text{Pb}(\text{Ac})_2$ /HDA solution. This was left to react for 35 min at 190 °C. After reaction completion the solution was left to cool for purification.

For purification of the sample, ethanol was added to flocculate the as synthesised nanoparticles when the reaction solution had reached 70 °C. The solution was then centrifuged at 14 000 rpm for collection of the solid nanoparticles. These were subsequently washed by suspending the pellet in toluene and ultrasonicing for 5 minutes. Additional ethanol was added again to flocculate the nanoparticles followed by centrifuging. The purification process was repeated and the resulting purified sample was suspended in toluene for TEM investigation. The as synthesised PbS nanoparticles could also be suspended in hexane, tetrachloroethylene and other non-polar solvents if required.

Results

After injection of the S/HDA mix the reaction solution went black immediately indicating the formation of PbS. An electron micrograph of the as-synthesised nanoparticles is shown in Fig 11. Figure 11a shows PbS nanoparticles stacked in a 3D arrangement. The nanoparticles range in size from 16 to 25 nm and have a highly faceted cube morphology.

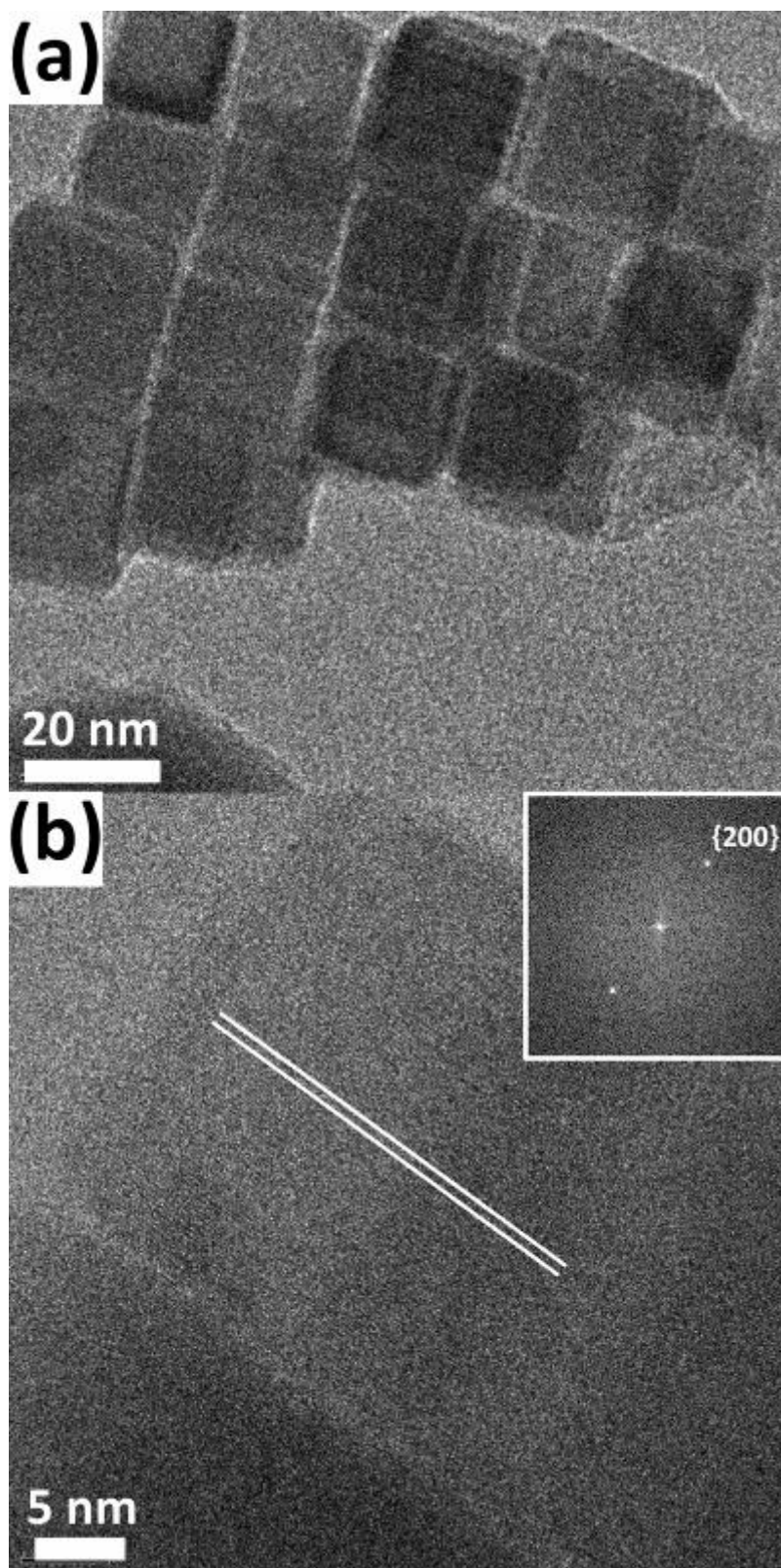


Figure 11. HREM image of PbS nanocubes formed with a 1:6 Pb:S ratio in HDA (a) and a high magnification HREM image showing oriented alignment of the nanocubes (b) with corresponding power spectrum (inset).

Figure 11b shows a close up HREM image of two PbS nanocubes arranged above one another. A fast Fourier transform (FFT) of the entire micrograph is shown in the

inset. It shows two spots corresponding to the (200) reflection of PbS which indicates the nanoparticles are being viewed down a <100> zone axis. The two nanocubes have their lattice planes aligned in so called 'oriented alignment' {Cho 2005}.

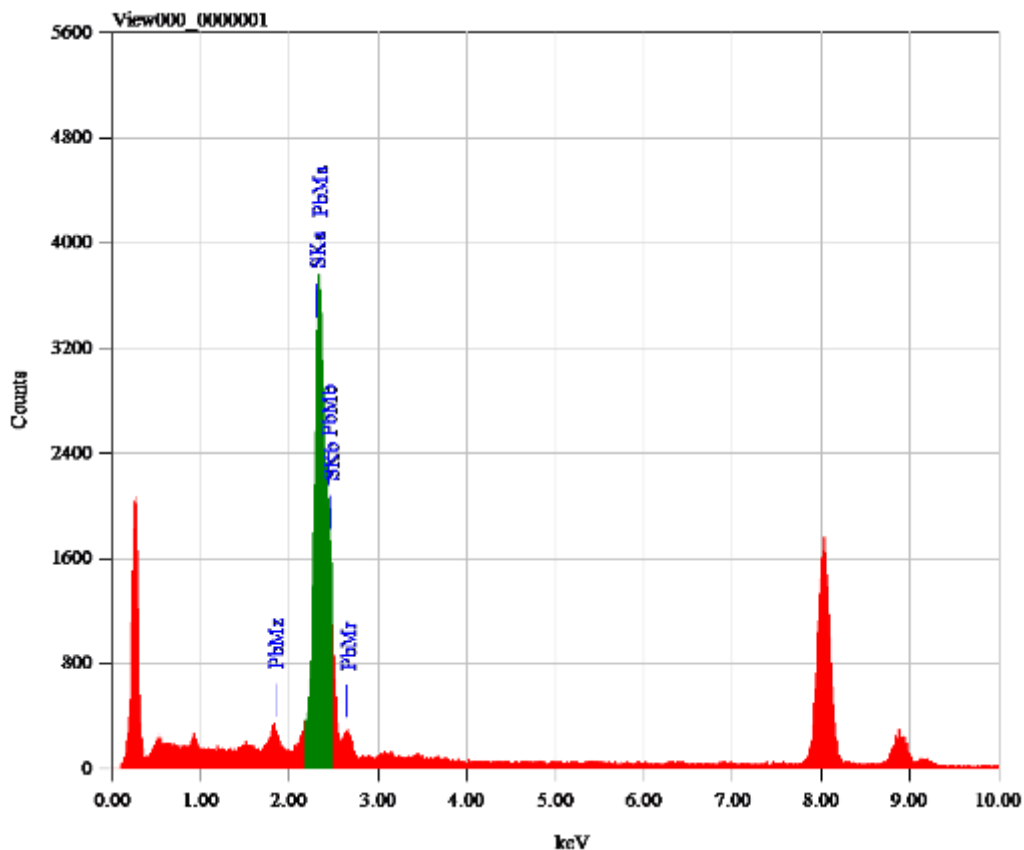


Figure 12. EDS spectrum of the as synthesised PbS nanocubes.

Figure 12 shows an EDS spectrum of the as-synthesised PbS nanocubes showing 52% Pb and 48% S (the additional unlabeled peaks come from the carbon film and the copper grid).

4.2.1.2 Experiment 9 : Reaction of $\text{Pb}(\text{Ac})_2$ in a 1:3 ratio of Pb:S in HDA

In this experiment the Pb:S ratio was increased to investigate the effect of a smaller S excess.

Experimental

In a three necked round bottomed flask 0.1 g of $\text{Pb}(\text{Ac})_2$ was added to 4 g HDA. The flask was then purged and filled with N_2 to create an oxygen free atmosphere. The reaction solution was heated to 175 °C where it was left to stir for 30 minutes to

Chapter 4: Solution Phase Syntheses of Lead Chalcogenide Nanoparticles

ensure the lead salt was fully dissolved. In a separate vial 26 mg of elemental S was added to 1 g HDA. This was heated on a hot plate to dissolve the S.

The S/HDA mixture was then injected rapidly into the $\text{Pb}(\text{Ac})_2/\text{HDA}$ solution. This was left to react for 5 min at 175 °C. After reaction completion the solution was left to cool. Purification was carried out as above.

Results

After injection of the S/HDA mix the reaction solution went black immediately indicating the formation of PbS. An electron micrograph of the as-synthesised nanoparticles is shown in Fig 13. Figure 13a shows PbS nanoparticles 30 to 100 nm in size and Fig 13b PbS nanoparticles 45 to 100 nm in size. Both micrographs show nanoparticle ensembles of varying morphologies with a large polydispersity.

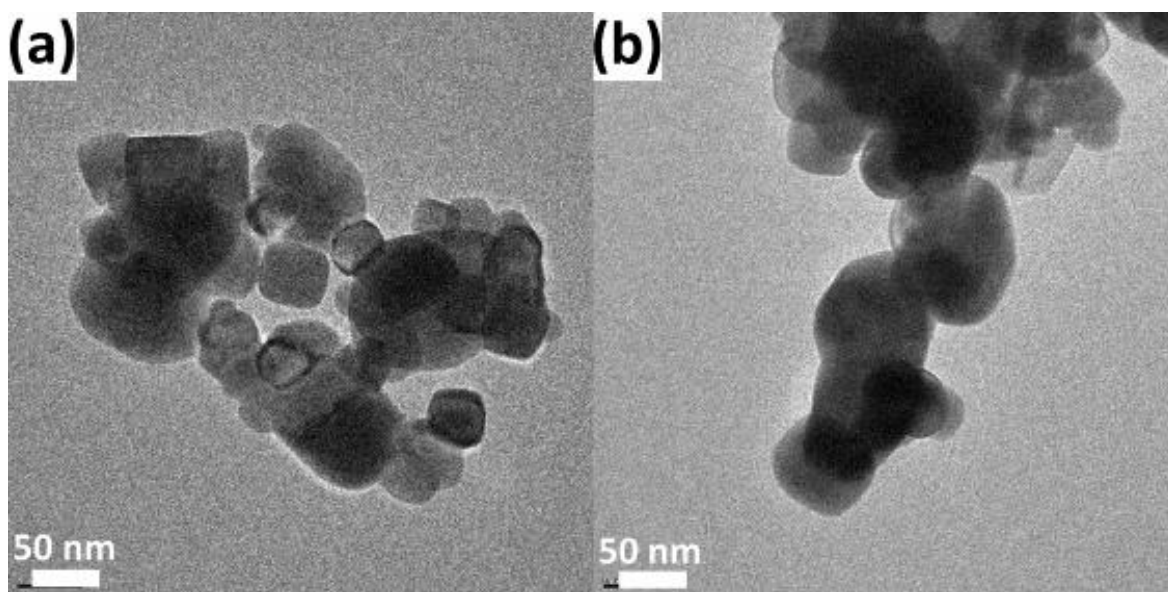


Figure 13. HREM images of PbS nanocubes formed with a 1:3 Pb:S ratio in HDA after 5 min reaction time (a) & (b).

4.2.1.3 Experiment 10 : Reaction of $\text{Pb}(\text{Ac})_2$ in a 2:1 ratio of Pb:S in HDA

In this experiment an excess of lead precursor was introduced. Evidently an excess of sulphur was not producing a monodisperse sample. An excess of lead was introduced for two reasons. Firstly, the amine functionality of the HDA is known to preferentially coordinate to Pb through its lone pair {Cademartiri 2006}. Therefore a Pb rich

Chapter 4: Solution Phase Syntheses of Lead Chalcogenide Nanoparticles

surface will experience stronger stabilisation resulting in smaller, more isotropic nanoparticles. Secondly, an excess of Pb means there is a high concentration of monomer in the growth stage. Previously a high supersaturation of monomer in the growth stage has been shown to be the ideal conditions for the growth of monodisperse nanocrystals due to a delay of the onset of Ostwald ripening {Talpin 2001}.

Experimental

In a three necked round bottomed flask 0.75 g of $\text{Pb}(\text{Ac})_2$ was added to 4 g HDA. The flask was then purged and filled with N_2 to create an oxygen free atmosphere. The reaction solution was heated to 165 °C where it was left to stir for 30 minutes to ensure the lead salt was fully dissolved. In a separate vial 32 mg of elemental S was added to 1 g HDA. This was heated on a hot plate to dissolve the S.

The S/HDA mixture was then injected rapidly into the $\text{Pb}(\text{Ac})_2$ /HDA solution. This was left to react for 5 min at 165 °C. After reaction completion the solution was left to cool. Purification was carried out as above.

Results

After injection of the S/HDA mix the reaction solution went black immediately indicating the formation of PbS. An electron micrograph of the as-synthesised nanoparticles is shown in Fig 14. The micrograph shows large platelet like nanostructures 50 to 100 nm in size. The rod like projections observed in the image can be considered platelets viewed down an edge.

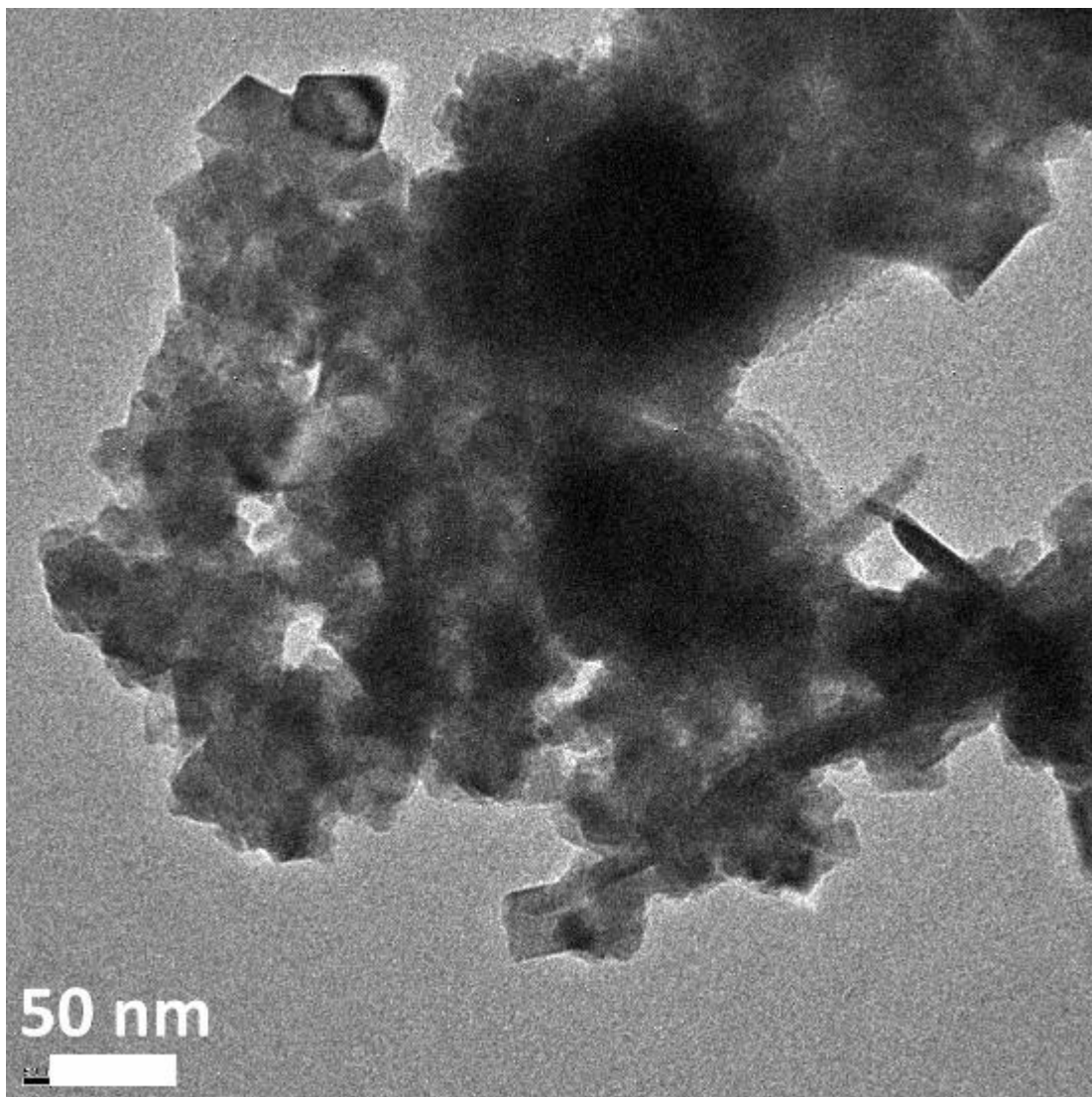


Figure 14. HREM image of PbS nano-platelets formed with a 2:1 ratio of Pb:S.

Exp #	Pb:S Ratio	Surfactant	Rxn Time (min)	Rxn Temp (°C)	Product
8	Pb(Ac) ₂ :S 1:6	HDA	35	190	highly faceted cubes 16 - 25 nm
9	Pb(Ac) ₂ :S 1:3	HDA	5	175	various rounded morphologies 30 - 100 nm
10	Pb(Ac) ₂ :S 2:1	HDA	5	165	platelets 50 - 100 nm

Table 3. Results of PbS synthesis using HDA as solvent and surfactant.

4.2.1.4 Discussion on Reactions of $\text{Pb}(\text{Ac})_2$ in Hexadecylamine (HDA)

The above set of experiments shows that increasing the Pb:S ratio in HDA results in an increase in the size of the nanostructures. However, an increase in the Pb:S ratio also results in the loss of shape control and a greater polydispersity. A ratio of 1:6 resulted in highly faceted, relatively monodisperse nanocubes. When this was increased to 1:3 the cubic morphology was largely maintained however the polydispersity of the sample was much greater. When an excess of Pb was introduced (2:1), size and shape control of the resulting nanoparticles was lost resulting in large polydisperse platelets. This is in contrast to the study performed by Cademartiri *et al.*, which showed that an excess of Pb monomer lead to smaller, more isotropic nanoparticles {Cademartiri 2006}. In this study, oleylamine (OLA) was used as the surfactant. This indicates that although HDA and OLA both have a long chain organic structure and a terminating amine functionality, their surface stabilisation behaviour is dissimilar.

The nanocubes formed in Exp 8 showed oriented alignment and organised into a 3D stacking arrangement. Oriented alignment occurs due to the origin of a dipole moment on the nanoparticle {Cho 2005}. This is counter-intuitive for the highly symmetrical *fcc* crystal structure but arises due to the different electro-negativities of Pb and S. A terminating facet covered exclusively in Pb or S will be polar in nature. Therefore a distribution of polar facets around the nanoparticle will lead to a local dipole moment.

4.2.2 Reactions in Oleylamine (OLA)

In the above experiments size and shape manipulation was not realised which indicates HDA does not provide sufficient control over nanoparticle growth. Therefore, oleylamine (OLA) was chosen as an alternative solvent/surfactant as it had previously been shown to yield monodisperse PbS nanoparticles {Joo 2003}. The following experiments are performed under synthetic conditions modified from the method of Joo *et al.*

4.2.2.1 Experiment 11 : Reaction of Pb(Ac)₂ in OLA

In the initial experiment a 1:1 ratio of Pb:S was used in accordance with the ratios used by Joo et al {Joo 2003}.

Experimental

In a three necked round bottomed flask 0.38 g of Pb(Ac)₂ was added to 4 mL OLA. The flask was then purged and filled with N₂ to create an oxygen free atmosphere. The reaction solution was heated to 90 °C where it was left to stir for 20 minutes to ensure the lead salt was fully dissolved. In a separate vial 32 mg of elemental S was added to 1 mL OLA. This was heated on a hot plate to dissolve the S.

The S/OLA mixture was then injected rapidly into the Pb(Ac)₂/OLA solution. This was left to react for 1 h at 200 °C. After reaction completion the solution was left to cool for purification.

For purification of the sample, 50/50 methanol and toluene was added to flocculate the as synthesised nanoparticles when the reaction solution had reached 70 °C. The solution was then centrifuged at 14 000 rpm for collection of the solid nanoparticles. These were subsequently washed by suspending the pellet in toluene and ultrasonicated for 5 minutes. Additional methanol was added again to flocculate the nanoparticles followed by centrifuging. The purification process was repeated and the resulting purified sample was suspended in toluene for TEM investigation.

Results

After injection of the S/HDA mix the reaction solution went black immediately indicating the formation of PbS. An electron micrograph of the as-synthesised nanoparticles is shown in Fig 15. Figure 15a shows a low magnification image of the as-synthesised nanoparticles. They possess a rounded spherical morphology and are 25 to 60 nm in size indicating a large polydispersity. Figure 15b shows a higher magnification image. The nanoparticles are randomly agglomerated which indicates OLA is not providing sufficient stabilisation for nanoparticles of this size. Figure 16 shows a EDS spectrum which shows 62 % Pb and 38% S. The peak ~ 1.9 keV is due to silicon contamination of the TEM grid.

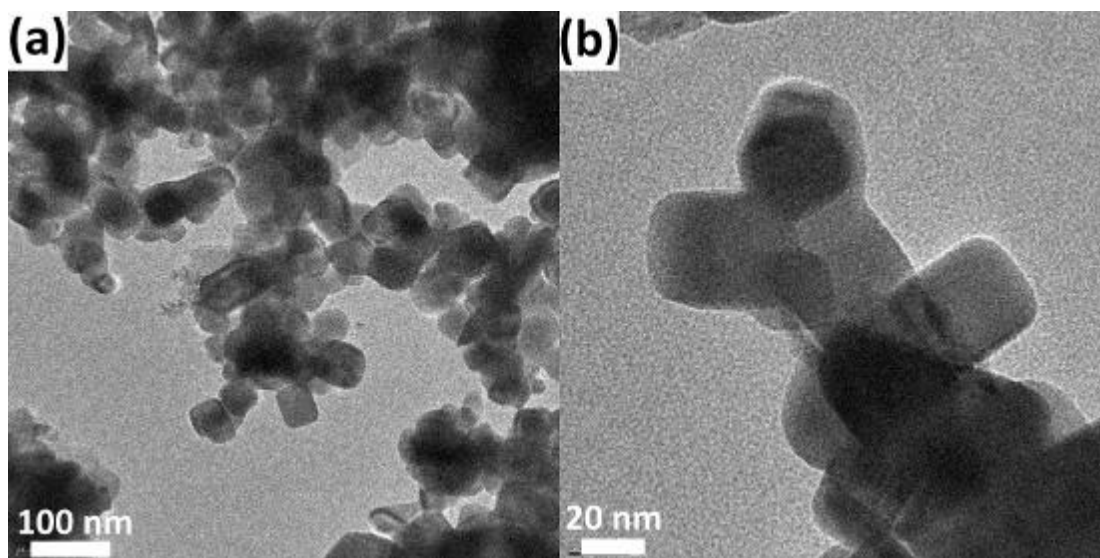


Figure 15. (a) Low magnification HREM image of PbS nanoparticles formed with a 1:1 ratio of Pb:S in oleylamine and (b) high magnification image.



Figure 16. EDS spectrum of the as synthesized PbS nanoparticles.

4.2.2.2 Experiment 12 : Reaction of PbCl₂ in OLA in a 1:1 ratio of Pb:S

The above experiment gave a polydisperse nanoparticle size and shape. Houtepen et al., recently observed that lead precursors completely free of acetate were required to

Chapter 4: *Solution Phase Syntheses of Lead Chalcogenide Nanoparticles*

obtain monodisperse spherical nanoparticles. In their method $\text{Pb}(\text{Ac})_2$ was converted to Pb-oleate through a preliminary reaction. In the present study it was decided to use PbCl_2 as the lead precursor and remove the acetate from the reaction scheme altogether. A 1:1 ratio of Pb:S was maintained in order to compare the effect of precursor substitution.

Experimental

In a three necked round bottomed flask 0.28 g of PbCl_2 was added to 4 mL OLA. The flask was then purged and filled with N_2 to create an oxygen free atmosphere. The reaction solution was heated to 160 °C where it was left to stir for 20 minutes to ensure the lead salt was fully dissolved. In a separate vial 32 mg of elemental S was added to 1 mL OLA. This was heated on a hot plate to dissolve the S.

The S/OLA mixture was then injected rapidly into the $\text{Pb}(\text{Ac})_2$ /OLA solution. This was left to react for 30 min at 160 °C. After reaction completion the solution was left to cool for purification which was carried out as above.

Results

After injection of the S/HDA mix the reaction solution went black immediately indicating the formation of PbS. An electron micrograph of the as-synthesised nanoparticles is shown in Fig 17.

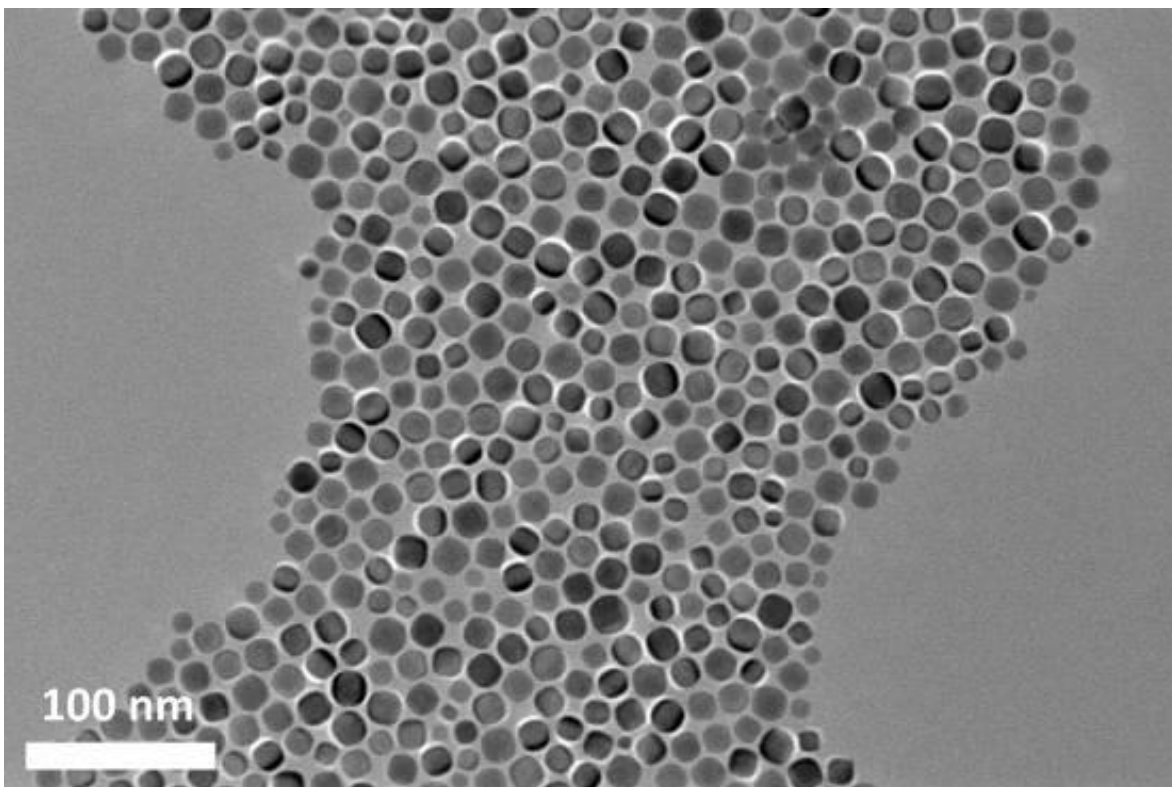


Figure 17. Low magnification HREM image of PbS nanoparticles formed with a 1:1 ratio of Pb:S using PbCl_2 as precursor.

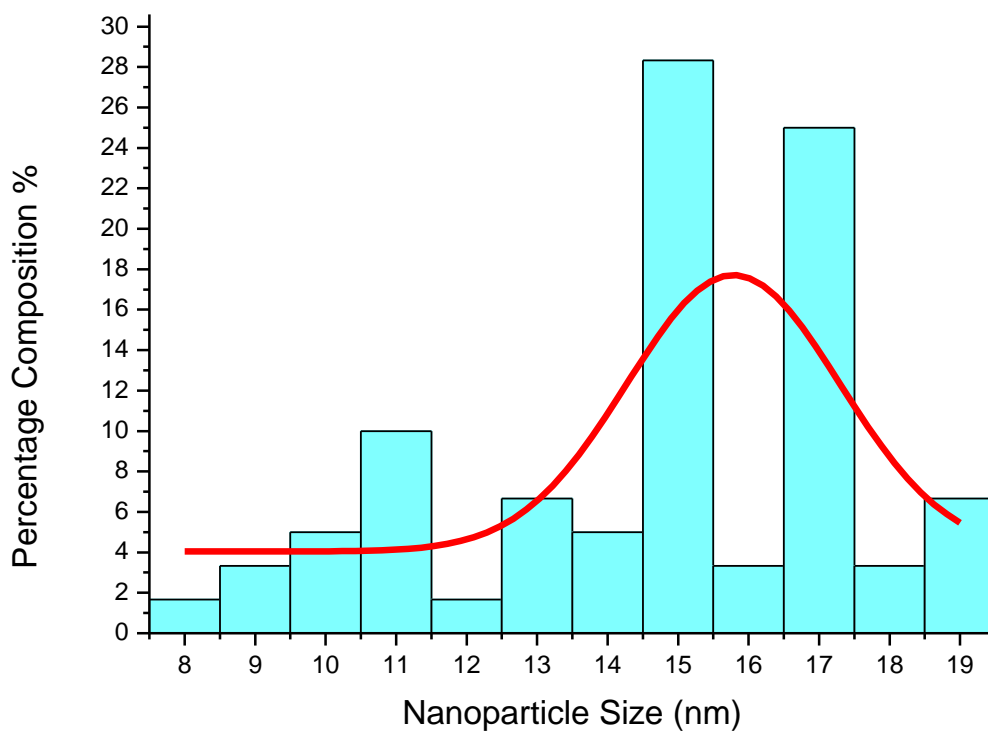


Figure 18. Size distribution analysis of the nanoparticles imaged in Fig. 17.

The nanoparticles have a rounded cubic morphology and are 14 ± 6 nm in size with a polydispersity from standard deviation of $\sigma = 22$ %. The size distribution is shown in Fig 18.

4.2.2.3 Experiment 13 : Reaction of PbCl₂ in OLA in a 1:2 ratio of Pb:S

The above experiment shows that by eliminating acetate from the reaction solution, a product with a uniform shape distribution can be realised. The size distribution is still relatively large at $\sigma = 22$ % therefore in the following two experiments the Pb:S ratio was systematically changed for the reasons outlined in Exp 10.

Experimental

In a three necked round bottomed flask 0.38 g of PbCl₂ was added to 4 mL OLA. The flask was then purged and filled with N₂ to create an oxygen free atmosphere. The reaction solution was heated to 120 °C where it was left to stir for 20 minutes to ensure the lead salt was fully dissolved. In a separate vial 32 mg of elemental S was added to 1 mL OLA. This was heated on a hot plate to dissolve the S.

The S/OLA mixture was then injected rapidly into the Pb(Ac)₂/OLA solution. This was left to react for 30 min at 120 °C. After reaction completion the solution was left to cool to room temperature for purification which was carried out as above.

Results

After injection of the S/HDA mix the reaction solution went black immediately indicating the formation of PbS. An electron micrograph of the as-synthesised nanoparticles is shown in Fig 19. Figure 19a shows rounded PbS nanocubes 12 ± 5 nm in size. There are small regions where the nanocubes are assembled in a 2D cubic arrangement however the polydispersity is too large to allow long range ordering. Fig 19b shows a close up HREM image of one of the PbS nanocubes. The nanoparticle is 10 nm in size and has a rounded cube-like morphology. From analysis of the atomic packing and the two fold symmetry of the power spectrum this nanoparticle can be characterised as being viewed down a $\langle 100 \rangle$ zone axis. Size distribution analysis is shown in Fig 20. The nanoparticle ensemble has a polydispersity from standard deviation of $\sigma = 21$ %. Figure 21 shows EDS analysis of the region of nanoparticles viewed in Fig 19a showing 58 % Pb and 42% S.

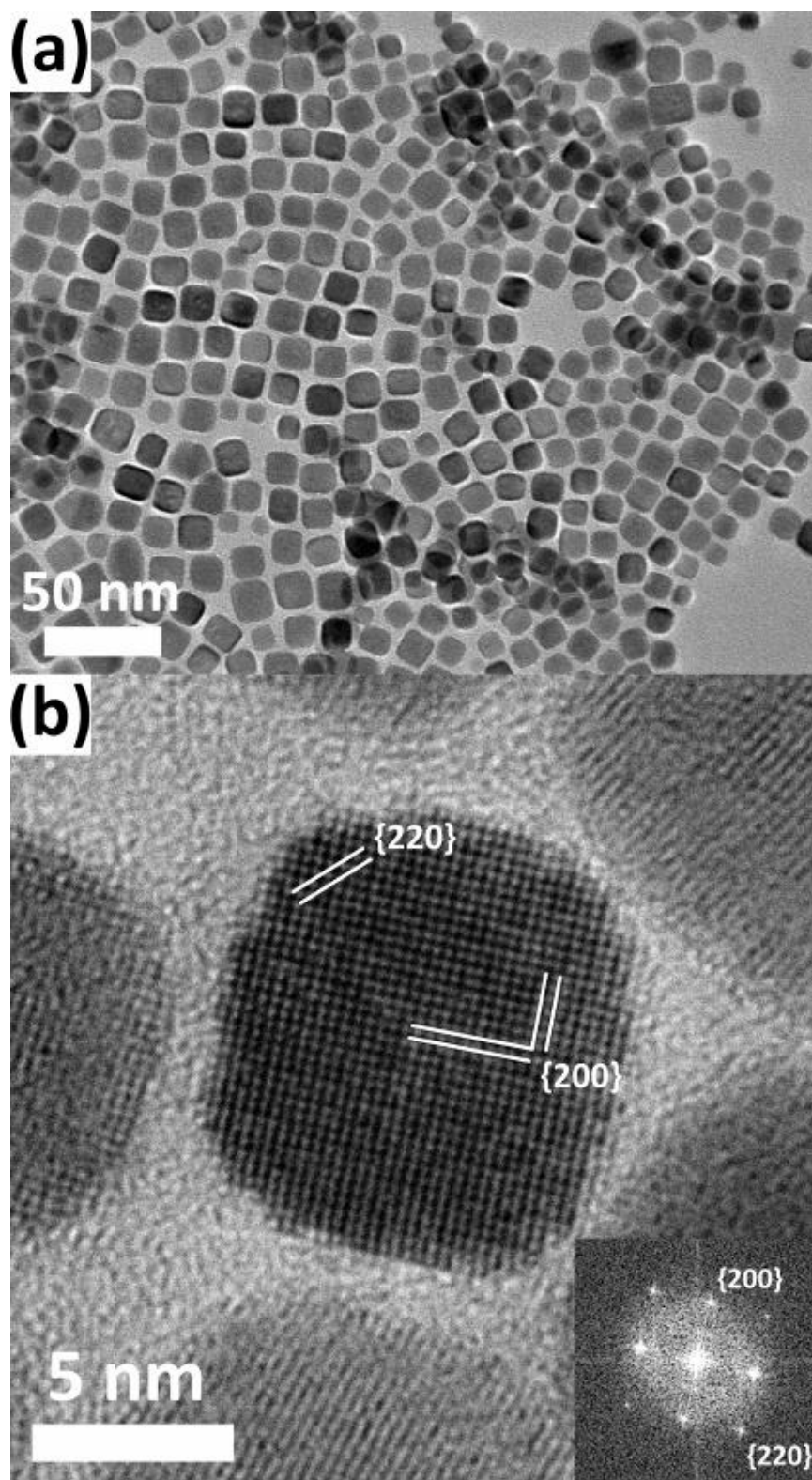


Figure 19. (a) Low magnification HREM image of PbS nanoparticles formed with a 1:2 ratio of Pb:S using PbCl_2 as precursor. (b) High magnification HREM image of a single PbS nanocube with corresponding power spectrum (inset).

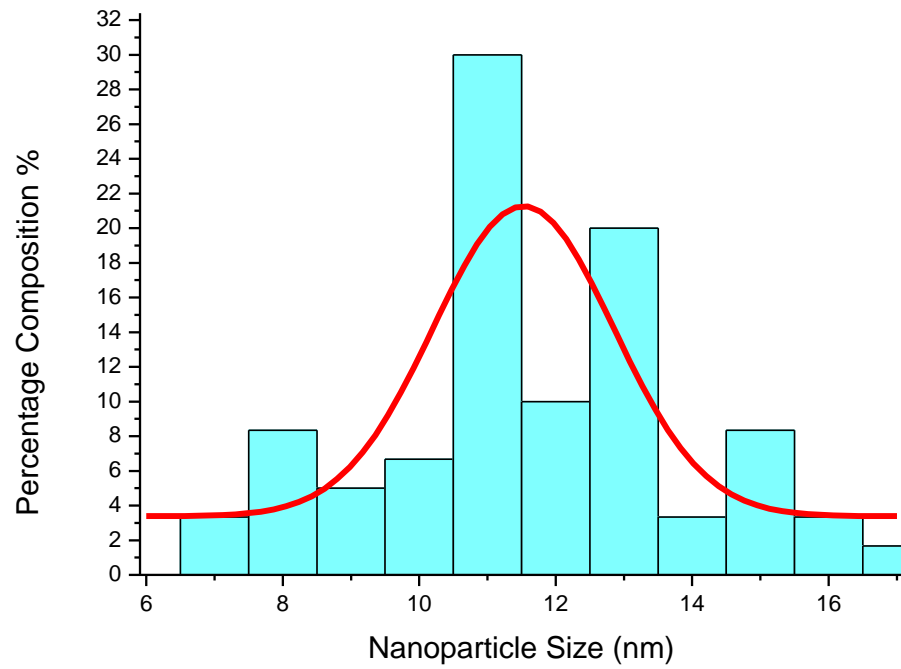


Figure 20. Size distribution profile of PbS nanoparticles formed with a 1:2 ratio of Pb:S using PbCl₂ as precursor.

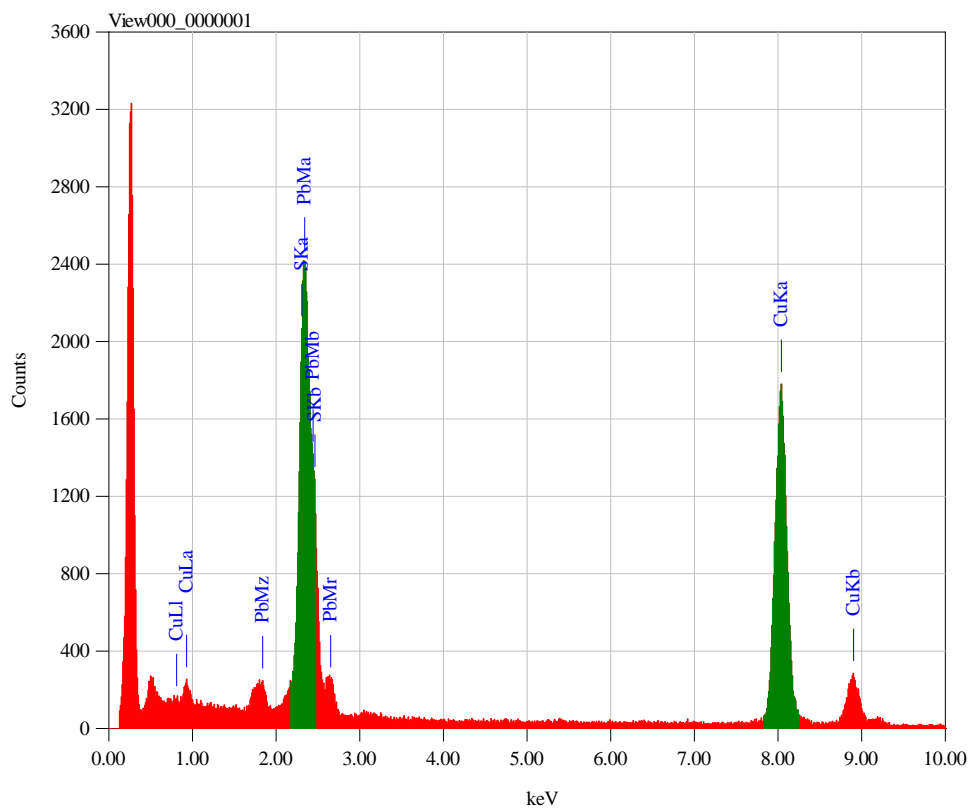


Figure 21. EDS spectrum of PbS nanoparticles formed with a 1:2 ratio of Pb:S using PbCl₂ as precursor.

4.2.2.4 Experiment 14 : Reaction of PbCl₂ in OLA in a 2:1 ratio of Pb:S

As seen above an excess of S produced rounded cube like nanoparticles with a relatively large polydispersity. In this experiment an excess of Pb was introduced in the hope that a Pb rich surface would experience increased stabilisation leading to monodisperse, isotropic nanoparticles.

Experimental

In a three necked round bottomed flask 0.56 g of PbCl₂ was added to 4 mL OLA. The flask was then purged and filled with N₂ to create an oxygen free atmosphere. The reaction solution was heated to 160 °C where it was left to stir for 20 minutes to ensure the lead salt was fully dissolved. In a separate vial 32 mg of elemental S was added to 1 mL OLA. This was heated on a hot plate to dissolve the S.

The S/OLA mixture was then injected rapidly into the Pb(Ac)₂/OLA solution. This was left to react for 30 min at 160 °C. After reaction completion the solution was left to cool for purification which was carried out as above.

Results

After injection of the S/HDA mix the reaction solution went black immediately indicating the formation of PbS. An electron micrograph of the as-synthesised nanoparticles is shown in Fig 22. Size distribution analysis is shown in Fig 23.

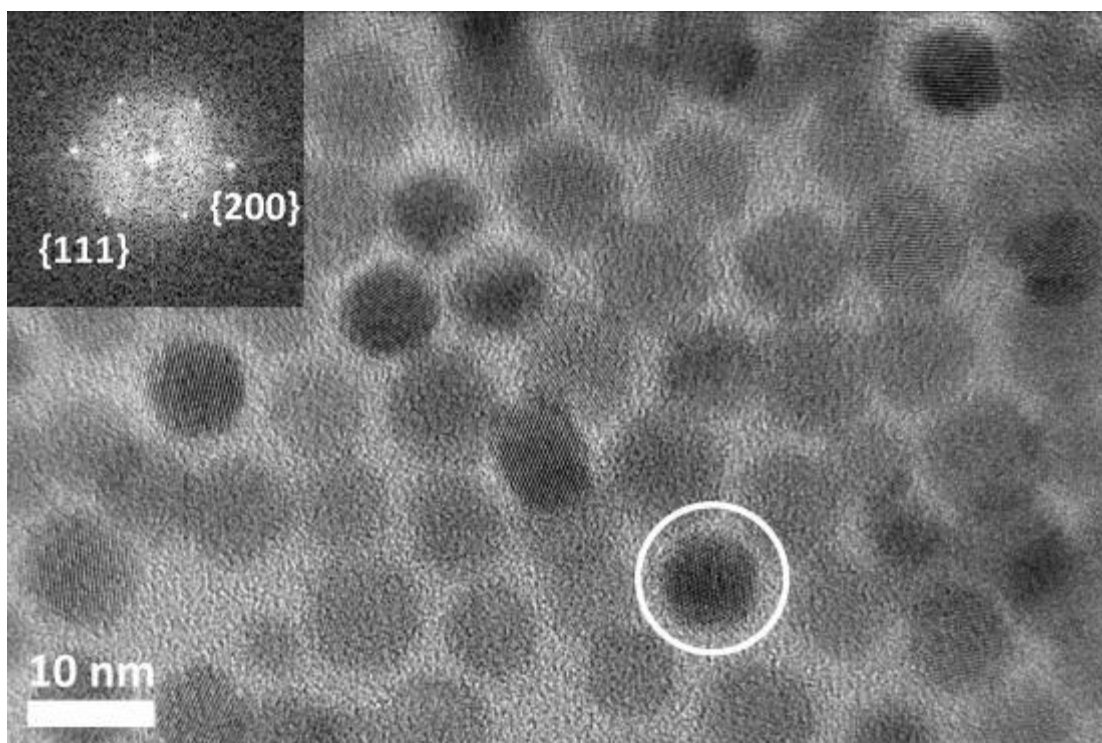


Figure 22. High magnification HREM image of PbS nanoparticles formed with a 2:1 ratio of Pb:S using PbCl_2 as precursor. The nanoparticle marked by a white circle has its corresponding power spectrum shown in the inset.

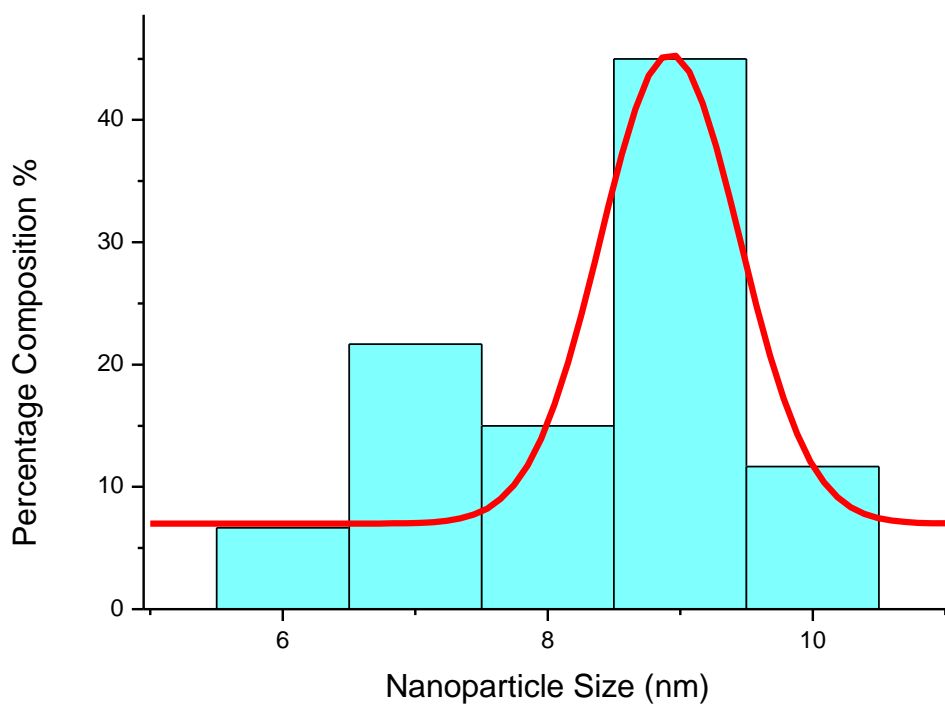


Figure 23. Size distribution profile of PbS nanoparticles formed with a 2:1 ratio of Pb:S using PbCl_2 as precursor.

Chapter 4: Solution Phase Syntheses of Lead Chalcogenide Nanoparticles

The nanoparticles formed here are spherical and have an average size of 8 ± 2 nm and a polydispersity from standard deviation of $\sigma = 14$ %. They possess a much more uniform size and shape distribution than previously achieved for PbS. The nanoparticle highlighted by the white circle shows atomic resolution and its power spectrum is shown in the inset. This nanoparticle can be characterised as being viewed down a $\langle 110 \rangle$ zone axis.

Exp #	Pb:S Ratio	Surfactant	Rxn Time (min)	Rxn Temp (oC)	Product
11	Pb(Ac) ₂ :S 1:1	OLA	60	200	rounded cubes 25 - 60 nm
12	PbCl ₂ :S 1:1	OLA	30	160	rounded cubes 14 ± 6 nm
13	PbCl ₂ :S 1:2	OLA	5	165	rounded cubes 12 ± 5 nm
14	PbCl ₂ :S 2:1	OLA	5	165	spheres 8 ± 2 nm

Table 4. Results of PbS synthesis using OLA as solvent and surfactant.

4.2.2.5 Discussion on Reactions in Oleylamine (OLA)

The introduction of OLA into the reaction solution as surfactant and solvent enabled sufficient control over the size and shape distribution of the resulting PbS nanoparticles. When a 1:1 ratio of Pb(Ac)₂:S was used a sample with a polydisperse size and shape distribution was obtained. This is due to the presence of the acetate counter ion which is thought to lead to a destabilisation of the growing nanoparticle and inhomogeneous growth {Houtepen 2006}. When the Pb(Ac)₂ precursor was replaced with PbCl₂ a sample with a uniform shape distribution was produced. With no coordinating acetate present in the reaction solution the growing nanoparticle experiences homogeneous stabilisation from the OLA leading to a uniform shape distribution. The nanoparticles produced in a 1:1 ratio of PbCl₂:S have a rounded

Chapter 4: *Solution Phase Syntheses of Lead Chalcogenide Nanoparticles*

cubic shape which indicates that the inherent crystalline energy is beginning to influence the thermodynamically favourable morphology {Pietryga 2004}.

When an excess of S is introduced (1:2 reaction) the nanocubes become more faceted. Here a larger proportion of the growing nanoparticle will be terminated by S species. Sulfur has a weaker binding interaction with amine than Pb and therefore the terminating facets will experience decreased stabilisation {Cademartiri 2006}. A faceted cube morphology is indicative of decreased stabilisation, and hence increased growth, on the {111} type facets.

When an excess of Pb was introduced (2:1) monodisperse, spherical nanoparticles were formed. This is due to the saturation of terminating facets by Pb. The strong Pb-N interaction leads to increased surface stabilisation and a more uniform product. The size of the nanoparticles was also reduced which is in agreement with the observations of Joo et al {Joo 2003}.

4.3 Capping Exchange Experiments on PbS Nanoparticles

As was observed above, long chain organic surfactants such as OLA are essential for gaining size and shape control in the growth of PbS nanoparticles. They also provide solubility in most organic solvents and a steric barrier to precipitation and agglomeration. However, when the final goal is to extract a photocurrent from the PbS nanoparticles, these long chain organics become a hindrance. Under IR irradiation lead chalcogenide nanoparticles produce an exciton (electron-hole pair). To produce a photocurrent this electron-hole pair must be spatially separated before recombination can occur. When a long chain organic species is used to cap the nanoparticle the electron tunnelling distance is too long to allow sufficient charge separation. A small interparticle spacing reduces the energy barrier to electron tunnelling and improves conductivity {Moody 2008}. Therefore decreasing the capping ligand chain length is imperative to extracting sufficient photocurrent from PbS QDs. This can however, lead to destabilisation of the nanoparticle with respect to precipitation and agglomeration. Therefore the size of the nanoparticles undergoing capping exchange must be relatively small to ensure adequate dispersion. Due to the uniform distribution of shape and small size of the nanoparticles grown from a 2:1 ratio of Pb:S, these reaction conditions were chosen for capping exchange experiments. This will also create nanoparticles that are surface terminated by Pb atoms which will provide sites for stabilisation and capping exchange.

Thioglycolic acid (TGA or mercaptopropionic acid) was chosen as the short chain organic stabiliser. It has a dual functionality with a carboxylate group at one end and a thiol at the other. Carboxylic acids have a strong affinity for TiO₂ whereas the thiol possesses a strong binding interaction with heavy metal cations {Lopez-Luke 2008}. Therefore it was hoped the thiol would displace the amine functionality of OLA at the nanoparticle surface leaving the carboxylate group available for attachment to a titania surface. Thiol treatment of lead chalcogenide nanoparticles has been shown to have beneficial effects on PV device performance through shortening the interparticle distance and improved surface passivation {Barkhouse 2008}.

Experimental

In a three necked round bottomed flask 0.56 g of PbCl_2 was added to 4 mL OLA. The flask was then purged and filled with N_2 to create an oxygen free atmosphere. The reaction solution was heated to 160 °C where it was left to stir for 20 minutes to ensure the lead salt was fully dissolved. In a separate vial 32 mg of elemental S was added to 1 mL OLA. This was heated on a hot plate to dissolve the S. The S/OLA solution is then rapidly injected into the Pb/OLA solution. The reaction solution is left to return to 165 °C where it is left to react for 30 min.

While still under nitrogen the reaction solution is cooled to 70 °C and a 10 % solution of TGA in toluene is injected. This is reacted at 70 °C for 3 h before being cooled to room temperature and left stirring for a further 12 h. PbS/TGA nanoparticles are recovered by the addition of a 50:50 toluene and ethanol solution and centrifuging at 4000 rpm. The nanoparticles were then washed twice with a 50:50 toluene and ethanol solution and dispersed in H_2O . A second aliquot was taken after the first centrifugation. To this was added toluene to suspend the nanoparticles still capped with OLA. This was washed twice and subsequently suspended in hexane.

Results

The TGA capped nanoparticles formed a clear brown solution in H_2O and were stable for weeks. Figure 24a shows a HREM image of the OLA capped nanoparticles as removed after the first centrifuging step with size distribution analysis shown in Fig 24b. The nanoparticles have a spherical morphology and are 8.2 ± 3.1 nm in size with a polydispersity from standard deviation of $\sigma = 32$ %.

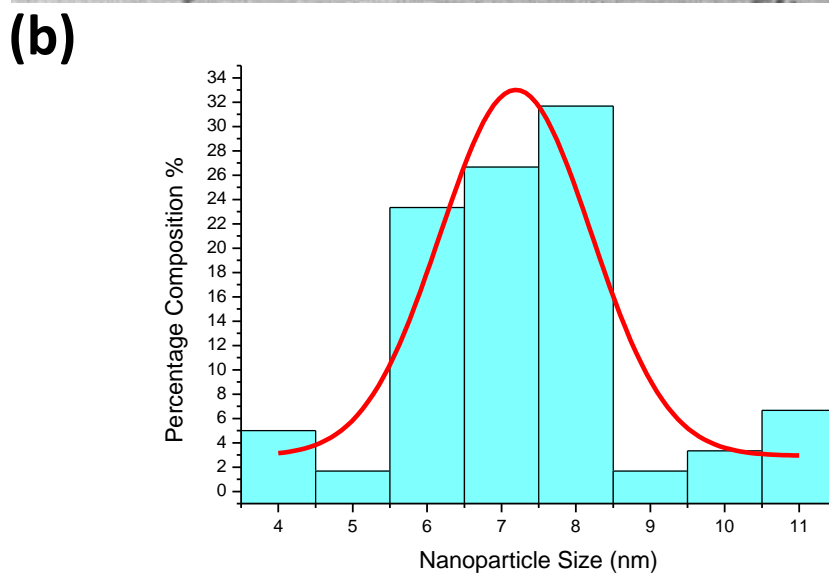
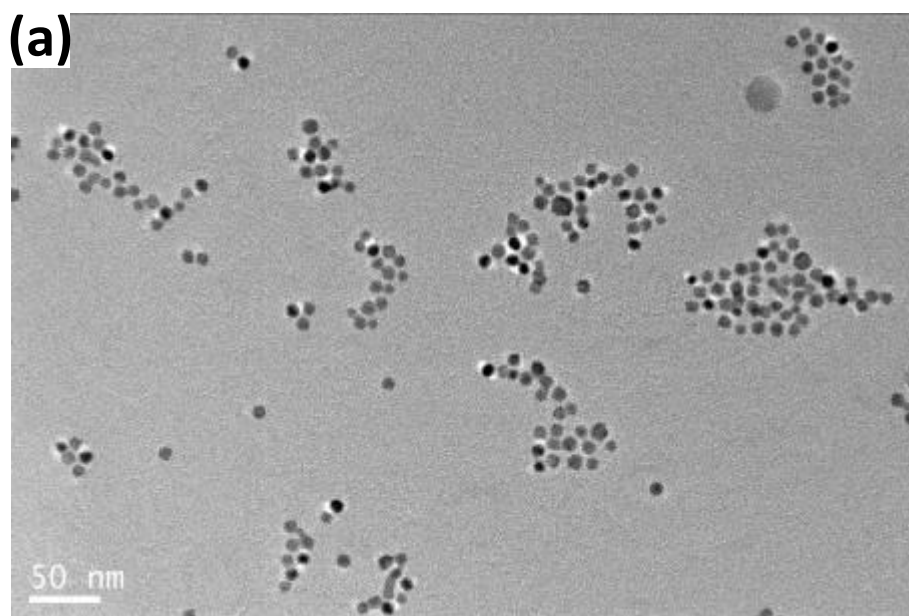


Figure 24. (a) Low magnification HREM image of OLA capped PbSe nanoparticles and (b) corresponding size distribution profile.

Figure 25a shows a HREM image of the TGA capped nanoparticles suspended in H₂O with size distribution analysis shown in Fig 25b. The nanoparticles have a spherical morphology and are 8.2 ± 1.3 nm in size with a polydispersity from standard deviation of $\sigma = 9.9$ %.

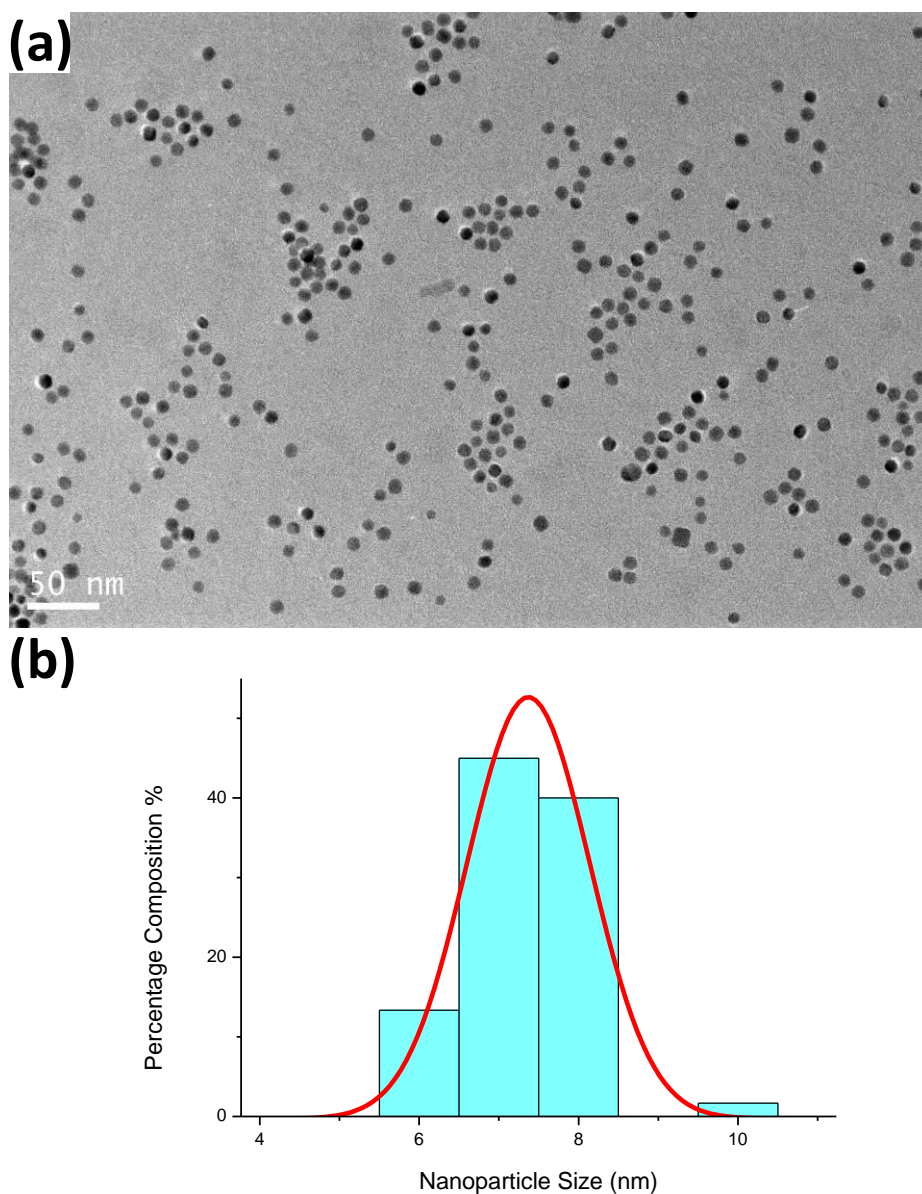


Figure 25. (a) Low magnification HREM image of TGA capped PbS nanoparticles and (b) corresponding size distribution profile .

Figure 26 shows two sample vials displaying PbS dispersed in hexane and H₂O respectively. The sample vial on the left contains OLA capped PbS nanoparticles. All the nanoparticles are suspended in the hexane layer with no mixing into the aqueous layer below. The sample vial on the right shows PbS nanoparticles capped with TGA and similarly, shows no mixing of nanoparticles into the upper organic layer.



Figure 26. OLA capped PbS nanoparticles suspended in hexane layer (left) and TGA capped PbS nanoparticles suspended in aqueous layer (right).

4.3.1 Discussion on Capping Exchange Experiments on PbS Nanoparticles

The above result shows that a successful capping exchange process has occurred for the as synthesised PbS nanoparticles. The nanoparticles shown in Fig 24a are capped with oleylamine and are readily dispersed in toluene. On the other hand, the nanoparticles shown in Fig 25a are capped with TGA and are readily dispersed in H₂O.

Therefore, a capping exchange process can be observed where the TGA ligands have readily displaced the oleylamine ligands on the surface of the nanoparticle. This is due to the stronger Pb-S interaction when compared to the Pb-N interaction {Ahrlund 1958}. Both Pb and thiol are soft bases with large electronegativities. This enables thiol to readily displace the hard base amine functionality on the surface Pb atoms.

The nanoparticles capped with TGA have a much smaller size distribution when compared to those nanoparticles capped with oleylamine. This indicates an *in-situ* size selection process occurring during the capping exchange process.

Chapter 4: *Solution Phase Syntheses of Lead Chalcogenide Nanoparticles*

The size distribution is narrowed due to the removal of smaller and larger nanoparticles when transferred from the organic to the aqueous phase. For the larger nanoparticles capping exchange has occurred however the smaller size of TGA when compared to oleylamine means they no longer provide sufficient stabilisation for the nanoparticles to be suspended in solution.

For the smaller nanoparticles it is most likely that the capping exchange process did not occur due to a stronger Pb-N interaction. Ligand to nanoparticle binding is usually driven by coordination to the surface atom {Wei 2009}. Smaller nanoparticles have a higher curvature which means the surface Pb possess a lower coordination to surrounding S species.

This reduces the electron density on the Pb and leads to a stronger contribution from the lone pair on the coordinating N species. Therefore, the higher curvature gives to a stronger Pb-N interaction and a more strongly bound oleylamine species resulting in an unsuccessful capping exchange process.

4.4 Summary

The above experiments present different synthetic methods for the synthesis of PbSe and PbS nanoparticles.

The synthesis of PbSe nanoparticles was carried out at different reaction temperatures using TOP as the organic surfactant. When carried out at 150 °C the size and shape of the nanoparticles could be determined by controlling the reaction time. As the reaction time was increased the size of the nanoparticles also increased. This was accompanied by a transition from a spherical to cubic shape at ~ 14 nm nanoparticle size. The transition in morphology is due to the domination of the inherent crystalline energy at larger nanoparticle sizes. The smaller spherical nanoparticle showed 2D hexagonal ordering which is characteristic of a monodisperse product. Likewise, a longer reaction time resulted in larger nanoparticles when the reaction was carried out at 200 °C. There was also shape control realised however the transition to cubic nanoparticles occurred at smaller sizes. So, using TOP as a surfactant the size and shape control of PbSe nanoparticles was realised by controlling the temperature and time of the reaction.

The synthesis of PbS nanoparticles was carried out using different precursor ratios using HDA and OLA as different organic surfactants. When PbS nanoparticles were synthesised using HDA no control over size and shape was realised. This synthesis resulted in large cubic nanoparticles and randomly agglomerated PbS platelet like structures. However, when Pb(Ac)₂ was replaced with PbCl₂ as precursor and OLA was employed as surfactant the size and shape of the resulting nanoparticles could be controlled. Here an increase in the Pb:S ratio resulted in smaller, more monodisperse nanoparticles.

A successful capping exchange process was performed on PbS nanoparticles which enabled their dispersion in water. This process replaced the long chain organic compound oleylamine with the smaller organic capping ligand TGA. The addition of a shorter chain capping ligand to the surface of the nanoparticle will enable extraction of a photocurrent when used in solar cell applications.

References

- Ahrland, S., Chatt, J., Davies, N. R., *Quarterly Reviews* **1958**, *12*, 265.
- Barkhouse, D. A. R., Pattantyus-Abraham, A. G., Levina, L., Sargent, E. H., *Acs Nano* **2008**, *2*, 2356.
- Bierman, M. J., Lau, Y. K. A., Jin, S., *Nano Letters* **2007**, *7*, 2907.
- Cao, H. Q., Wang, G. Z., Zhang, S. C., Zhang, X. R., *Nanotechnology* **2006**, *17*, 3280.
- Cademartiri, L., Bertolotti, J., Sapienza, R., Wiersma, D. S., von Freymann, G., Ozin, G. A., *Journal of Physical Chemistry B* **2006**, *110*, 671.
- Cho, K. S., Talapin, D. V., Gaschler, W., Murray, C. B., *Journal of the American Chemical Society* **2005**, *127*, 7140.
- Houtepen, A. J., Koole, R., Vanmaekelbergh, D. L., Meeldijk, J., Hickey, S. G., *Journal of the American Chemical Society* **2006**, *128*, 6792.
- Jian, X., Cui, D., Ting, Z., Paradee, G., Ziqi, L., Qing, W., Shengyong, X., Wang, A. Y., *Nanotechnology* **2006**, *17*, 5428.
- Jiang, Y., Wu, Y., Xie, B., Yuan, S. W., Liu, X. M., Qian, Y. T., *Journal of Crystal Growth* **2001**, *231*, 248.
- Joo, J., Na, H. B., Yu, T., Yu, J. H., Kim, Y. W., Wu, F. X., Zhang, J. Z., Hyeon, T., *Journal of the American Chemical Society* **2003**, *125*, 11100.
- Lee, S. M., Jun, Y. W., Cho, S. N., Cheon, J., *Journal of the American Chemical Society* **2002**, *124*, 11244.
- Mei, B. C., Oh, E., Susumu, K., Farrell, D., Mountziaris, T. J., Mattoussi, H., *Langmuir* **2009**, *25*, 10604.
- Murray, C. B., Sun, S. H., Gaschler, W., Doyle, H., Betley, T. A., Kagan, C. R., *Ibm Journal of Research and Development* **2001**, *45*, 47.
- Pietryga, J. M., Schaller, R. D., Werder, D., Stewart, M. H., Klimov, V. I., Hollingsworth, J. A., *Journal of the American Chemical Society* **2004**, *126*, 11752.
- Qi, L., Ni, Y. H., Gui, Y., Hong, J. M., Zheng, X., *Materials Chemistry and Physics* **2005**, *89*, 379.
- Shevchenko, E. V., Talapin, D. V., Murray, C. B., O'Brien, S., *Journal of the American Chemical Society* **2006**, *128*, 3620.
- Sima, M., Enculescu, I., Sima, M., *Optoelectronics and Advanced Materials-Rapid Communications* **2008**, *2*, 67.
- Sugimoto, T., *Journal of Colloid and Interface Science* **1983**, *91*, 51.

Chapter 4: Solution Phase Syntheses of Lead Chalcogenide Nanoparticles

Talapin, D. V., Rogach, A. L., Haase, M., Weller, H., *Journal of Physical Chemistry B* **2001**, *105*, 12278.

Warner, J. H., Djouahra, S., Tilley, R. D., *Nanotechnology* **2006**, *17*, 3035.

Yin, Y., Alivisatos, A. P., *Nature* **2005**, *437*, 664.

Chapter 5. Solution Phase Syntheses of Palladium Nanostructures

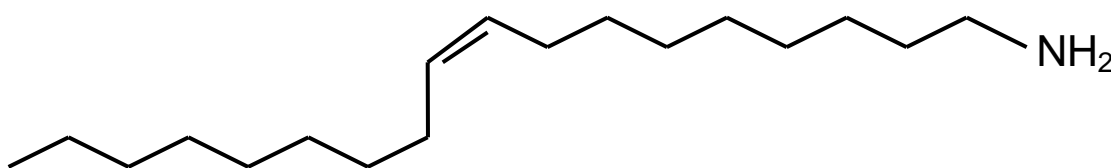
This chapter is concerned with the solution phase synthesis of palladium nanostructures. Novel synthetic techniques were developed to control the size and shape of the resulting nanostructures. The synthetic approach described here involves the reaction of an organometallic precursor in the presence of an organic surfactant in a pressure reaction vessel (Fischer-Porter bottle). Fischer-Porter bottles have previously been shown to be successful in the formation of platinum nanostructures {Ren 2007 (a), Ren 2007 (b)}.

The Fischer-Porter bottle consists of a pressure resistant glass reservoir that is attached to a bivalve system which allows the regulation of atmospheric pressure and composition. A small volume of reaction solution is placed in a secondary vial which is lowered into the bottle. This is typically accompanied by an excess of solvent in the base of the bottle. This reduces unwanted evaporation from the reaction solution by saturating the atmosphere. In the present synthesis hydrogen gas is introduced with a total pressure of between 1 and 3 bar. The whole apparatus is then placed in a laboratory oven to regulate reaction temperature.

The main goal of these experiments is the synthesis of Pd nanoparticles with morphological control. This is with the aim of increasing catalytic performance and gaining an understanding of the fundamentals of complex nanoparticle growth. Size distribution analysis is performed in the following experiments by measuring the sizes of at least 2000 nanoparticles.

5.1 Reactions with Pd(PPh₃)₄

The use of organometallic precursors in nanoparticle synthesis has previously allowed mild reaction conditions (low temperature, low pressure) while still delivering effective control over nanoparticle growth {Chaudret 2005}. Furthermore, the coordinating ligand of the organometallic precursor has previously been shown to be a factor in the shape control of palladium nanoparticles in solution phase synthesis {Ramirez 2004}. The coordinating ligands provide a means to control the reactivity of the precursor as well as providing an additional stabiliser for the growing nanoparticle in solution. For the first series of experiments tetrakis(triphenylphosphine)palladium(0) was chosen as the palladium precursor as it is readily available and only has one type of coordinating ligand. Oleylamine was chosen as the organic stabiliser as it has previously been shown to allow shape control in platinum nanoparticles {Ren 2007 (a)}.



Scheme 1. Molecular structure of oleylamine.

5.1.1 : Reaction of Pd(PPh₃)₄ in low concentration in anisole

In this experiment tetrakis(triphenylphosphine)palladium(0) (Pd(PPh₃)₄) was reacted at 100 °C under a hydrogen atmosphere in the presence of a stabilising agent. Anisole (B.P. 154 °C) was chosen as a suitable reaction solvent. It should be noted here that anisole has a terminating methoxy group which could possibly coordinate with the growing palladium nanoparticle. Coordinating solvents have previously been demonstrated to participate in the stabilisation of platinum nanoparticles {Bardaji 1997}.

Experimental

11.6 mg (0.01 mmol) of Pd(PPh₃)₄ was dissolved in 2 mL of anisole in a 10 mL reaction vial. To this was added 33 μL (0.1 mmol) of oleylamine. This reaction

mixture was sonicated until a clear yellow solution resulted. The vial was suspended in a Fischer-Porter bottle with 10 mL of excess anisole in the bottom of the bottle. The bottle was purged 5 times with hydrogen gas and then filled with 3 bar H₂. The Fischer-Porter bottle was then placed in a reaction oven at 100 °C for 20 h.

For purification of the sample, methanol was added to flocculate the as synthesised nanoparticles. The solution was centrifuged at 14 000 rpm for collection of the solid nanoparticles. These were subsequently washed by suspending the pellet in toluene and ultrasonicing for 5 minutes. Additional methanol was added again to flocculate the nanoparticles followed by centrifuging. The purification process was repeated and the resulting purified sample was suspended in toluene for TEM investigation.

Results

Following the reaction a dark brown/black solution resulted which indicated the formation of palladium nanoparticles. After purification a dark brown solution was obtained which was then prepared for TEM characterisation. The solution was stable on the timescale of observation.

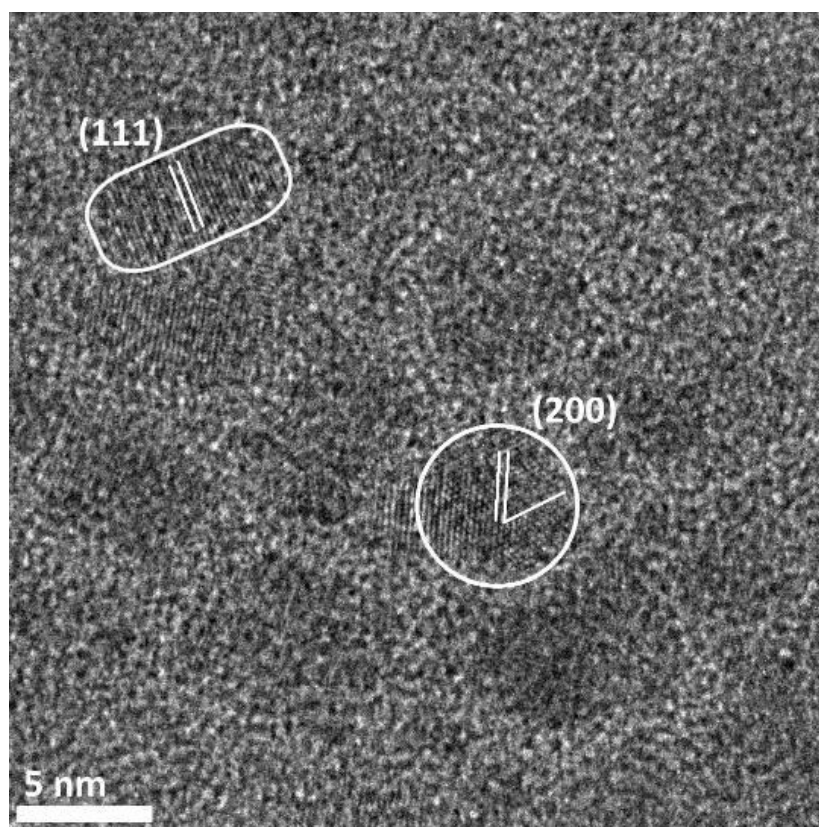


Figure 2. HREM image of palladium nanoparticles synthesised by the reaction of Pd(PPh₃)₄ in low concentration in anisole.

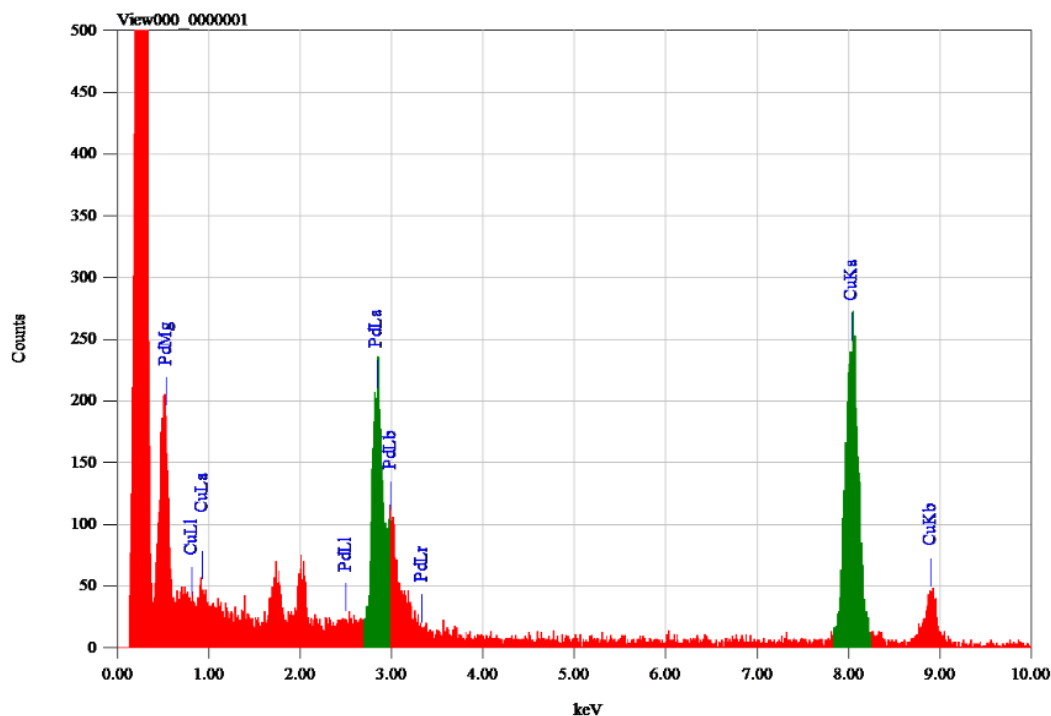


Figure 3. EDS spectrum of the as synthesised Pd nanoparticles.

The nanoparticle marked in the top right hand of Fig 2 has an elongated rod shape. It is 7 nm long with an aspect ratio of 2. The lattice planes are clearly visible and are indexed as (111) lattice planes. This indicates the nanoparticle is being viewed down a $\langle 110 \rangle$ zone axis. The nanoparticle marked in the middle of the image is spherical and 5.5 nm in size. Analysis of the atomic packing indicates the lattice planes visible are from the (200) reflection. The angle between the lattice planes is close to 60° which means the nanoparticle is being viewed down a $\langle 111 \rangle$ zone axis. Both the $\langle 111 \rangle$ and the $\langle 110 \rangle$ crystal faces are common terminating surfaces for palladium nanoparticles {Xiong 2007 (a)}. The remainder of the sample consists of similar sized nanoparticles and smaller nanoparticle nuclei around 1 nm in size. The nuclei are just visible on the above micrograph due to contrast issues associated with the presence of excess organic surfactant. Figure 3 is an EDS spectrum of region corresponding to the EM image. This EDS spectrum shows that the sample is 70% Pd with the remainder due to Si and P impurities from the TEM grid. There is no evidence of P in the EDS spectrum which indicates that the triphenylphosphine complex has been effectively purified.

5.1.2 : Reaction of Pd(PPh₃)₄ in high concentration in anisole

In this experiment the overall concentration of the organometallic precursor and the organic surfactant was increased by five times. An increase in concentration of precursor had previously been shown to induce morphological change in platinum nanoparticles {Ren 2007 (a), Ren 2007 (b)}. In this study, a high concentration reaction solution resulted in kinetically controlled growth conditions and the formation of highly monodisperse octapod nanocubes. This was in comparison to a low concentration reaction solution which produced primarily thermodynamically favoured faceted nanocubes. It was hoped that in the present palladium system the increase in concentration would produce nanostructures which were not thermodynamically favoured, i.e. had complex morphologies.

Experimental

116.1 mg (0.1 mmol) of Pd(PPh₃)₄ was dissolved in 4 mL of anisole in a 10 mL reaction vial. To this was added 0.329 mL (1 mmol) of oleylamine. This reaction mixture was sonicated until a clear yellow solution resulted. However, some particulate remained due to solubility issues. The vial was suspended in a Fischer-Porter bottle with 10 mL of excess anisole in the bottom of the bottle. The bottle was purged 5 times with hydrogen gas and then filled with 3 bar H₂. The Fischer-Porter bottle was then placed in a reaction oven at 100 °C for 20 h. Purification was carried out as above.

Results

This reaction resulted in a dark brown/black solution which was stable on the timescale of observation.

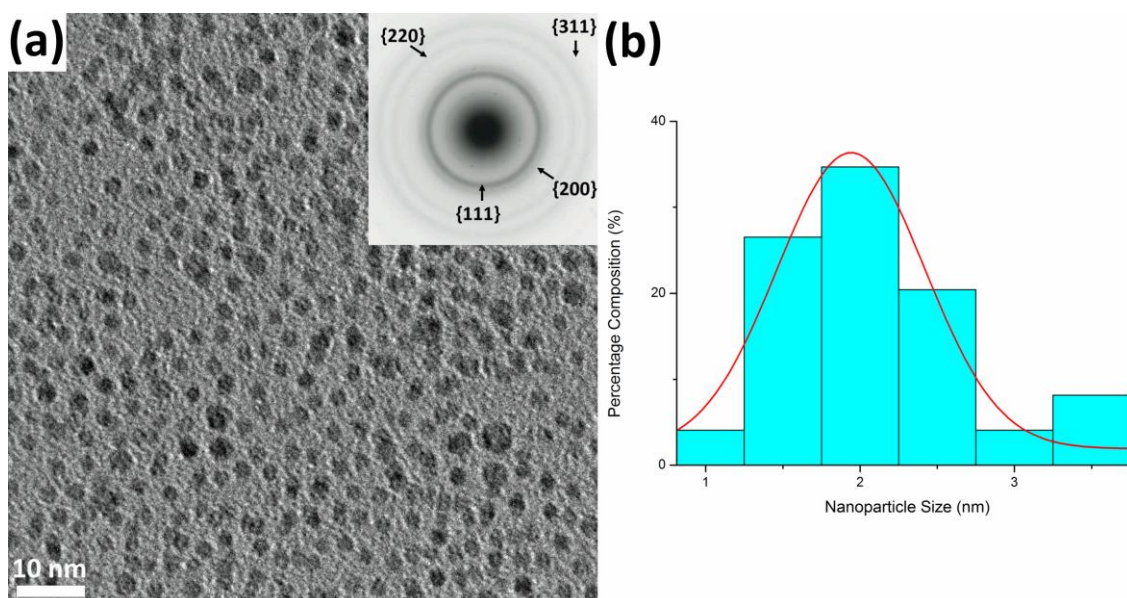


Figure 4. HREM image of palladium nanoparticles synthesised by the reaction of $\text{Pd}(\text{PPh}_3)_4$ in high concentration in anisole (a) and the corresponding size distribution profile (b).

Figure 4a shows an electron micrograph of the as synthesised palladium nanoparticles. They are 2.2 ± 1.3 nm in size and roughly spherical in shape. The selected area electron diffraction (SAED) pattern is shown in the inset and is indexed to *fcc* palladium metal. The size distribution of the sample is shown in Fig 4b. The nanoparticles have a polydispersity from standard deviation of 29 %.

5.1.3 : Reaction of $\text{Pd}(\text{PPh}_3)_4$ in toluene

In this experiment anisole was replaced with toluene as reaction solvent. Experiments 5.1.1 & 5.1.2 showed small spherical nanoparticles. It was thought the coordination ability of anisole to the growing nanoparticle was restricting growth as it provides a greater degree of stabilisation to the growing nanoparticle. By substituting non-coordinating toluene it was hoped that growth would occur at a faster rate resulting in growth conditions which were not thermodynamically favoured.

Experimental

116.1 mg (0.1 mmol) of $\text{Pd}(\text{PPh}_3)_4$ was dissolved in 2 mL of toluene in a 10 mL reaction vial. To this was added 0.329 mL (1 mmol) of oleylamine. This reaction mixture was sonicated resulting in a green/yellow turbid solution, presumably due to the decreased solubility of the palladium precursor in toluene when compared to

anisole. The vial was suspended in a Fischer-Porter bottle with 10 mL of excess anisole in the bottom of the bottle. The bottle was purged 5 times with hydrogen gas and then filled with 3 bar H₂. The Fischer-Porter bottle was then placed in a reaction oven at 70 °C for 40 h and 110 °C for 24 h. Purification was carried out as above.

Results

This reaction resulted in a dark brown/black solution which was stable on the timescale of observation.

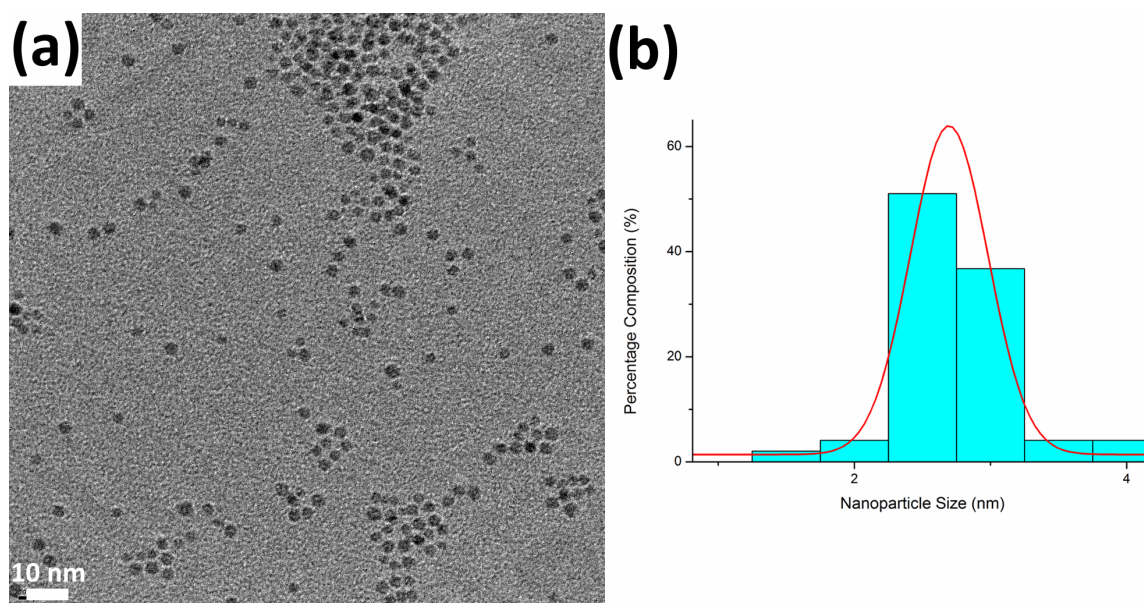


Figure 5. HREM image of palladium nanoparticles synthesised by the reaction of Pd(PPh₃)₄ in toluene (a) and corresponding size distribution profile (b).

Figure 5a shows an electron micrograph of the as synthesised palladium nanoparticles. The nanoparticles are 2.8 ± 1.1 nm and are roughly spherical in shape. The size distribution is shown in Fig 5b and the polydispersity from standard deviation is calculated to be 15 %.

5.1.4 : Reaction of Pd(PPh₃)₄ with low surfactant ratio - temperature profile

In this experiment the surfactant to precursor ratio was reduced to 3:1. The earlier change in the coordination ability of the solvent was unsuccessful in promoting shape control. Therefore it was hoped that a reduction in overall stabilising ability of the surfactant system would increase the growth rate and promote the formation of

complex nanoparticle shapes. A temperature profile was employed in an attempt to vary the rate of growth.

Experimental

116.1 mg (0.1 mmol) of Pd(PPh₃)₄ was dissolved in 3 mL of toluene in a 10 mL reaction vial. To this was added 0.099 mL (0.3 mmol) of oleylamine. The light green reaction mixture turned dark green upon sonication. The vial was suspended in a Fischer-Porter bottle with 10 mL of excess anisole in the bottom of the bottle. The bottle was purged 5 times with hydrogen gas and then filled with 3 bar H₂. The Fischer-Porter bottle was then placed in a reaction oven and subjected to a temperature profile of; 80 °C for 17 h, 110 °C for 24 h, 80 °C for 24 h and 107 °C for 12 h . Purification was carried out as above.

Results

This reaction resulted in a black solution with visible particulate. A typical EM image is shown in Fig 6.

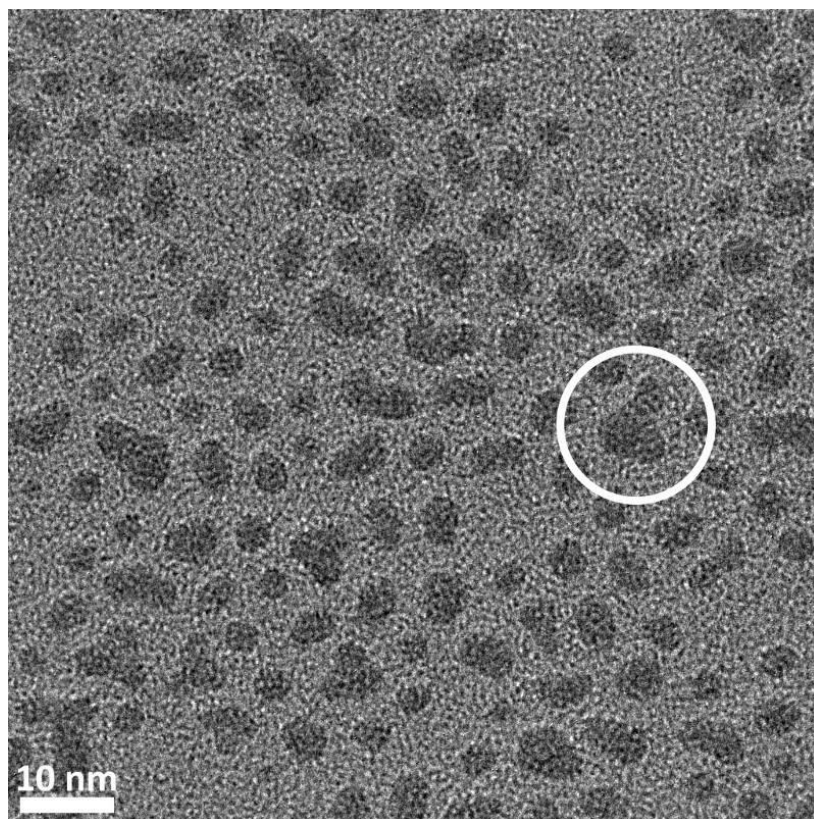


Figure 6. HREM image of palladium nanoparticles synthesised by the reaction of Pd(PPh₃)₄ with a low surfactant ratio.

The as synthesised nanoparticles range in size from 3 to 10 nm. There are various nanoparticle shapes present including spheres, elongated spheres and rounded triangles (see circled nanoparticle). An exact calculation of the polydispersity is not possible due to the shape variation present.

5.1.5 : Reaction of Pd(PPh₃)₄ – separation of nucleation and growth

The experiments performed above gave nanoparticles with large size distributions. In order to reduce this polydispersity greater control over the nucleation and growth processes is needed. In this experiment a temporal separation of nucleation and growth was explored as per the La Mer model {Park 2007}.

Experimental

55.7 mg (0.05 mmol) of Pd(PPh₃)₄ was dissolved in 1.5 mL of toluene in a 10 mL reaction vial. To this was added 0.165 mL (0.5 mmol) of oleylamine. The light green reaction mixture turned dark green upon sonication. The vial was suspended in a Fischer-Porter bottle with 10 mL of excess anisole in the bottom of the bottle. The bottle was purged 5 times with hydrogen gas and then filled with 3 bar H₂. The Fischer-Porter bottle was placed at room temperature and the solution left to react for 65 h. The bottle was then moved to an oven where it was left to react at 110 °C for 24 h. Purification was carried out as above.

Results

This reaction resulted in a black solution with an EM image of the sample shown in Fig 7. The sample consists of spherical nanoparticle nuclei and larger worm like nanoparticles. The spherical nanoparticles range in size from 1.5 nm to 5 nm and show a relatively large polydispersity. The worm-like nanoparticles vary greatly in length from 6 to 32 nm however they are relatively uniform in width (3 to 3.5 nm). The worm-like nanoparticle indicated by the white arrow was the longest observed with an aspect ratio of ~10.

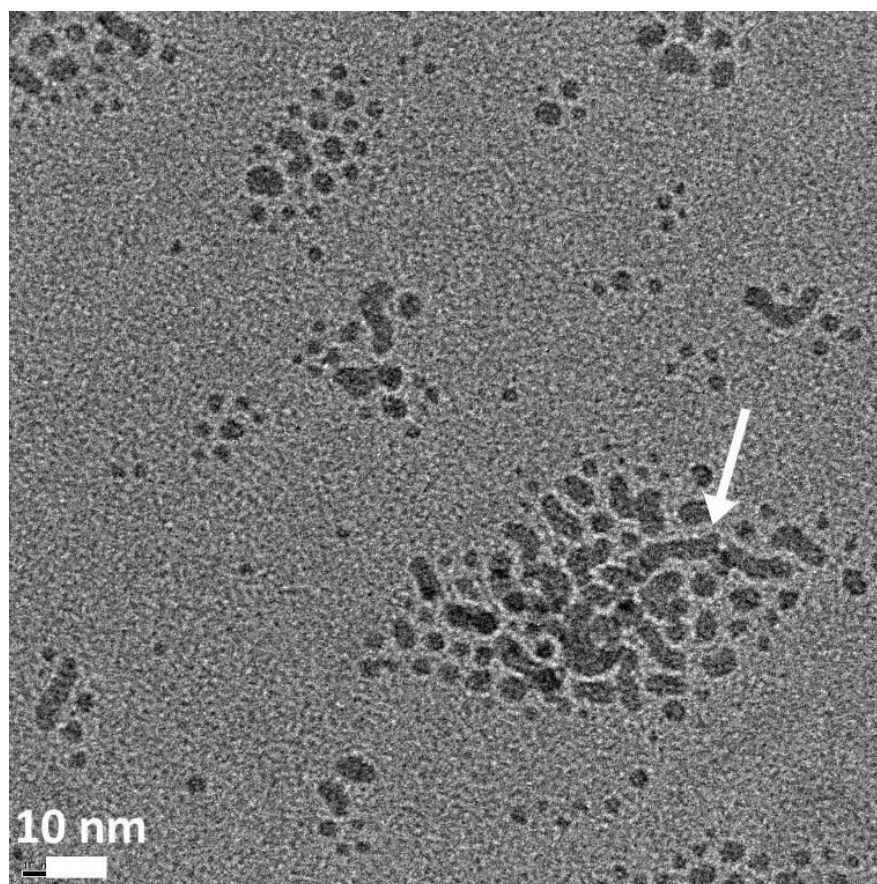


Figure 7. HREM image of palladium nanoparticles synthesised by the reaction of $\text{Pd}(\text{PPh}_3)_4$ in a process that temporally separated nucleation and growth.

5.1.6 Discussion of Reactions with $\text{Pd}(\text{PPh}_3)_4$

These results show that reactions of $\text{Pd}(\text{PPh}_3)_4$ predominantly lead to spherical nanoparticles 1-5 nm in size. This can be understood by the strong Pd-P interaction where the presence of strongly coordinating phosphine ligands typically leads to small spherical nanoparticles for palladium {Ramirez 2004, Son 2004}. The resulting black colour of the reaction solutions is expected as palladium nanoparticles <10 nm in size do not show a surface plasmon resonance between 300 and 1500 nm {Xiong 2005 (b)}.

Experiment 5.1.1 resulted in nanoparticles with a wide size distribution and a variation in shape (spheres and rods with a small aspect ratio). When the overall concentration of precursor and stabilising agent was increased (Experiment 5.1.2) the nanoparticles became purely spherical in shape and the size distribution was slightly reduced. This is due to the coordinating ability of anisole. It is known that the

Pd-O interaction is lower in binding strength when compared to the Pd-N interaction {Ahrland 1958}.

Since organic stabilisation is a dynamic effect this difference will lead to an inhomogeneous stabilisation of the growing nanoparticle even in the presence of the strong binding phosphine ligand {Murray 1993, Yin 2005}. Therefore, the selected facets interacting with anisole will experience a destabilisation when compared to those bound by oleylamine. This will result in the promotion of growth in the associated direction. In the low concentration regime (Exp 5.1.1) the amount of oleylamine available for stabilisation is small. Therefore certain faces of the growing nanoparticle will be stabilised by anisole. These particular faces will experience weaker stabilisation and enhanced growth leading to rod like nanoparticles. In contrast, the high concentration regime (Exp 5.1.2) contains sufficient oleylamine concentration to stabilise the entire surface of the growing nanoparticle. Therefore, the growing nanoparticle is fully stabilised leading to spherical nanoparticles.

When anisole is replaced by the non-coordinating solvent toluene (Exp 5.1.3) the nanoparticles formed remain spherical however the size distribution reduces from 29 % to 15 %. This is due to a faster nucleation event which gives a reduction in polydispersity {Park 2007}. In the presence of coordinating anisole the precursor will experience solvation which will serve to stabilise it against decomposition. However, in the absence of a coordinating solvent the precursor is more readily decomposed leading to a more rapid supersaturation and a faster, more homogeneous nucleation event.

For Exp 5.1.4 the overall surfactant ratio was reduced. This resulted in nanoparticles with a rounded shape 3-5 nm in size. These nanoparticles can be characterised as spherical nanoparticles which have coalesced. Coalescence occurs as there is an insufficient concentration of organic stabiliser present to provide a stable system. This coalescence effect was also seen in Exp 5.1.5 where a highly polydisperse sample including long worm-like coalesced nanostructures was formed. The formation of worm-like structures with a high aspect ratio indicates orientation alignment of the nanoparticles before coalescence however this could not be confirmed by HREM.

Chapter 5: *Solution Phase Syntheses of Palladium Nanostructures*

So, when Pd(PPh₃)₄ was used as palladium precursor, predominantly spherical nanoparticles were formed. There was some slight shape variation due to the interplay of interacting species present in the reaction solution however the difference in binding strengths was not large enough to form complex nanostructures. Due to the strong Pd-P interaction, growth is restricted isotropically leading to spherical nanoparticles. For shape control over the system a ligand with weaker binding characteristics must be introduced {Ramirez 2004}. This will enable the organic surfactant to play a greater role in shape control by selectively binding to different crystal facets.

5.2 Reactions with $[\text{PdCl}_2(\text{NCMe})_2]$

As the reactions with a strongly bound phosphine palladium complex consistently gave small spherical nanostructures a new organometallic palladium complex was investigated. Bis(acetonitrile)dichloropalladium(II) ($[\text{PdCl}_2(\text{NCMe})_2]$) was chosen as it contains an acetonitrile ligand which binds through a nitrogen moiety. Nitrogen has a weaker binding interaction with palladium than phosphorous in accordance with the theory of hard and soft acids and bases. Therefore it was expected that the stabilising effect of the organometallic ligands would be reduced and the organic surfactant would play a greater role in reaction and morphology control.

5.2.1: Reaction of $[\text{PdCl}_2(\text{NCMe})_2]$ in low concentration

In this experiment $[\text{PdCl}_2(\text{NCMe})_2]$ was reacted under a hydrogen atmosphere in the presence of oleylamine. Toluene was chosen as organic solvent as it is non-coordinating and the precursor is readily soluble. This reaction was performed at low overall precursor and surfactant concentration in accordance with previous Fischer-Porter bottle synthesis {Ren 2007 (a)}.

Experimental

25.9 mg (0.1 mmol) of $[\text{PdCl}_2(\text{NCMe})_2]$ was dissolved in 5 mL of toluene in a 10 mL reaction vial. To this was added 0.329 mL (1 mmol) of oleylamine. This reaction mixture was sonicated until a clear colourless solution resulted. The vial was suspended in a Fischer-Porter bottle with 10 mL of excess anisole in the bottom of the bottle. The bottle was purged 5 times with hydrogen gas and then filled with 3 bar H_2 . The Fischer-Porter bottle was then placed in a reaction oven at 80 °C for 24 h.

For purification of the sample, methanol was added to flocculate the as synthesised nanoparticles. The solution was centrifuged at 14 000 rpm for collection of the solid nanoparticles. These were subsequently washed by suspending the pellet in toluene and ultrasonicated for 5 minutes. Additional methanol was added again to flocculate the nanoparticles followed by centrifuging. The purification process was repeated once with dichloromethane and a second time with toluene. The resulting purified sample was suspended in toluene for TEM investigation.

Results

Following the reaction a black solution resulted which indicated the formation of palladium nanoparticles. The solution was stable on the timescale of observation.

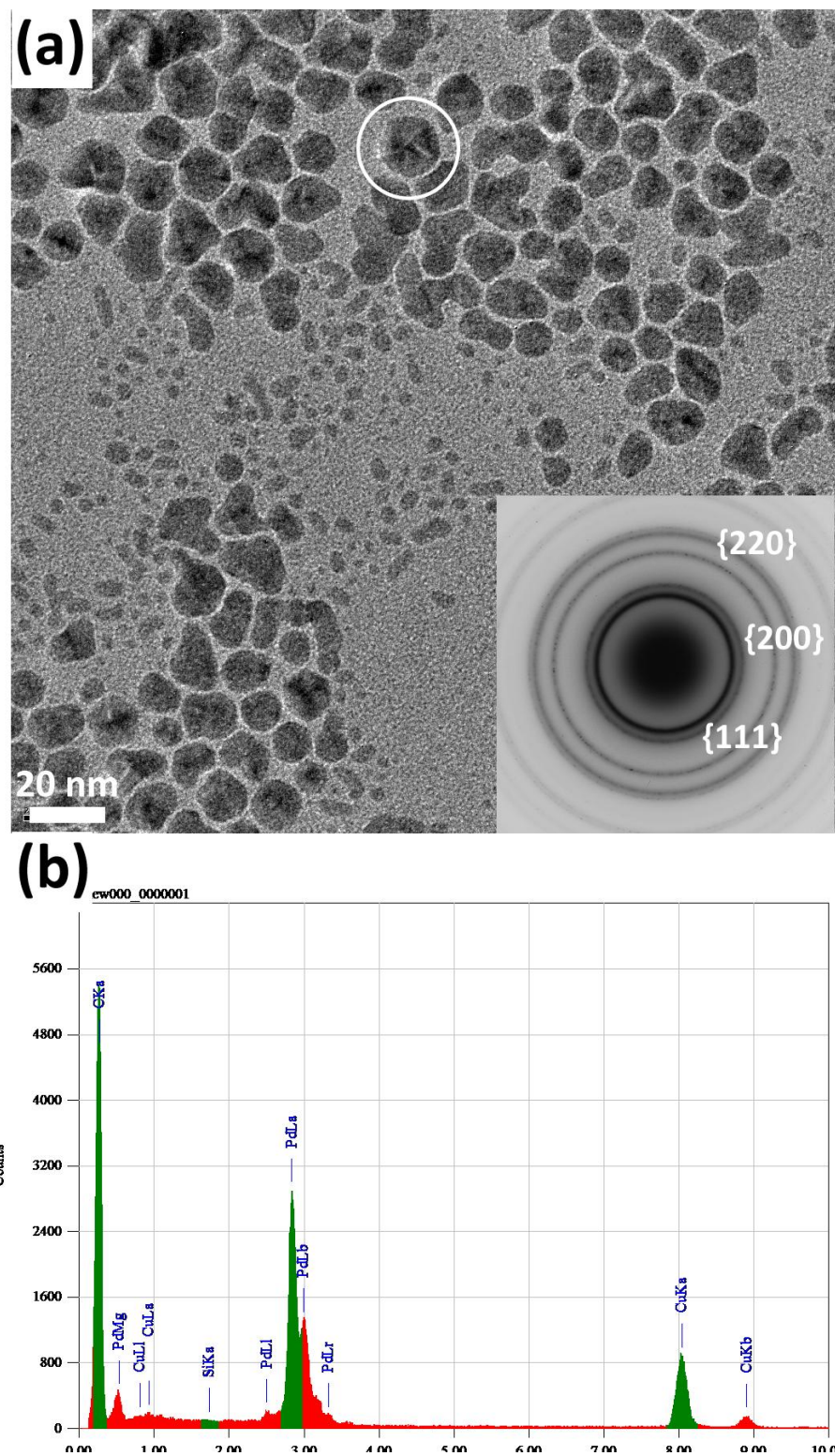


Figure 8. HREM image of palladium nanoparticles synthesised by the reaction of $[\text{PdCl}_2(\text{NCMe})_2]$ in low concentration (a) and corresponding EDS spectrum (b).

Figure 8a shows an EM image of the as synthesised nanoparticles. A SAED pattern is shown in the inset which is indexed as the *fcc* palladium crystal structure. The nanoparticle distribution in Fig 8a is bimodal; consisting of nanoparticles 8 to 16 nm in size and nanoparticle nuclei 1 to 5 nm in size. Unlike the small spherical nanoparticles synthesised with Pd(PPh₃)₄ as precursor the larger nanoparticles formed here are predominantly faceted polyhedra. The circled nanoparticle is 15 nm in size and displays 5-fold symmetry. This can be characterised as a multiply twinned decahedral nanoparticle which is a commonly synthesised morphology for palladium {Choo 2006, Xiong 2007 (a), Lim 2007}. An EDS spectrum is shown in Fig 8b which shows the sample is 100% Pd.

5.2.2: Reaction of [PdCl₂(NCMe)₂] in high concentration

In this experiment the overall precursor and surfactant concentration was increased in order to induce structural change. A high precursor concentration has previously been shown to be essential for the formation of complex nanoparticle morphologies through kinetic shape control {Yin 2005}.

Experimental

25.9 mg (0.1 mmol) of [PdCl₂(NCMe)₂] was dissolved in 1 mL of toluene in a 10 mL reaction vial. To this was added 0.329 mL (1 mmol) of oleylamine. This reaction mixture was sonicated until a clear colourless solution resulted. The vial was suspended in a Fischer-Porter bottle with 10 mL of excess anisole in the bottom of the bottle. The bottle was purged 5 times with hydrogen gas and then filled with 3 bar H₂. The Fischer-Porter bottle was then placed in a reaction oven at 80 °C for 20 h. Purification was carried out as above.

Results

Following the reaction a black solution resulted with a metallic layer covering the meniscus. Electron microscopy images of the as synthesised nanoparticles are shown in Fig 9a-d. Figure 9a shows faceted polyhedra nanoparticles 10 -25 nm in size. The nanoparticle indicated by the white circle projects a six-fold symmetry shape. This is

consistent with a multiply twinned *fcc* icosahedral structure {Kirkland 1991}. Present also are three fold symmetry triangle nanostructures 25 to 35 nm in size. The remainder of the nanoparticles have undefined morphologies.

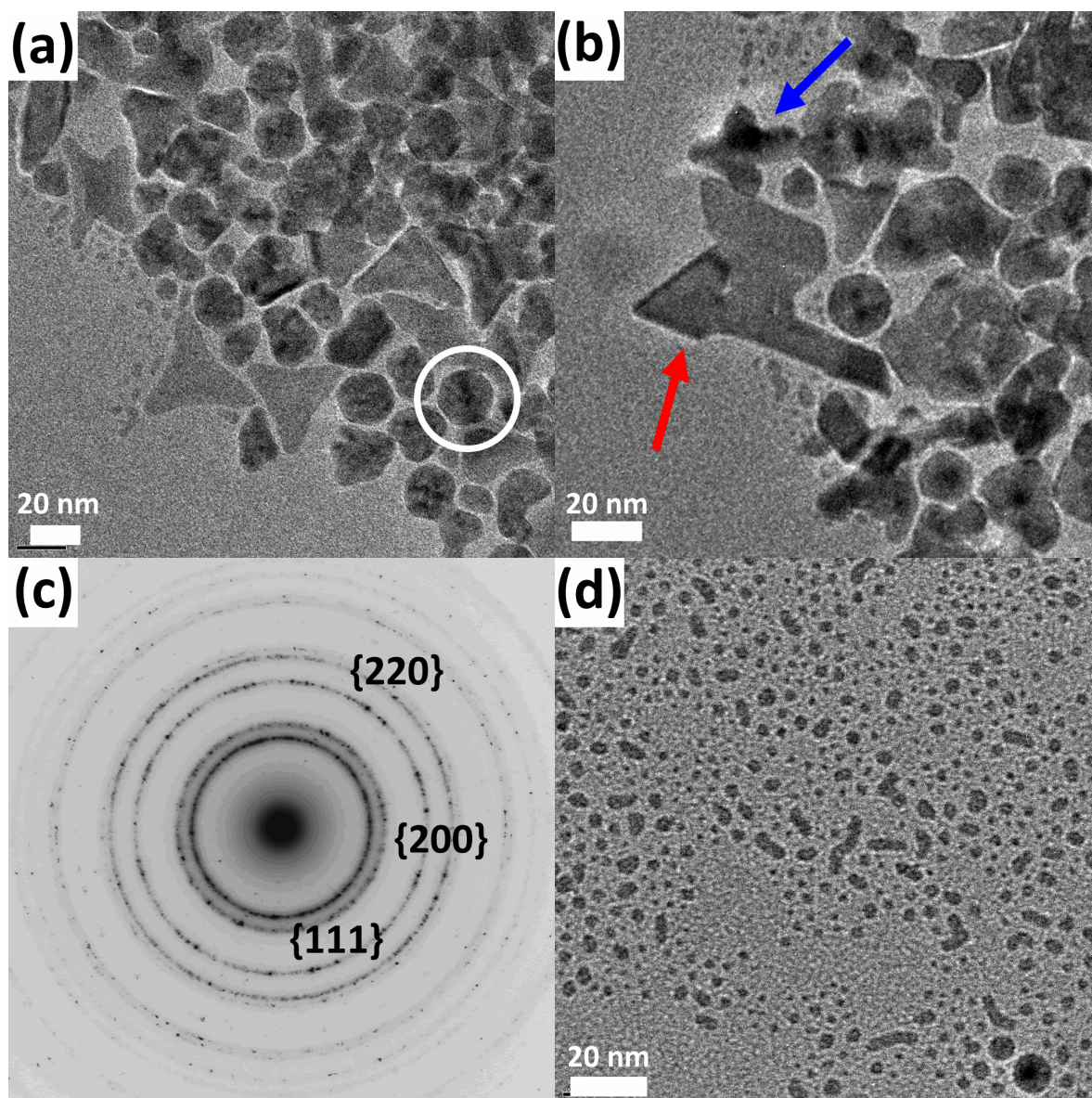


Figure 9. HREM image of palladium nanoparticles synthesised by the reaction of $[\text{PdCl}_2(\text{NCMe})_2]$ in high concentration (a). The nanoparticle highlighted by the white circle has a multiply twinned icosahedral morphology. (b) High magnification image of the palladium nanoparticles with pod-like and anisotropic morphologies highlighted. (c) SAED pattern of the as synthesised nanoparticles indexed to *fcc* crystal structure of palladium. (d) Nanoparticle nuclei 1 – 5 nm in size.

Figure 9b shows a close up image of the as synthesised nanoparticles. The nanoparticle indicated by the blue arrow is 30 nm in length. It clearly shows four ‘pod-like’ branches extending at right angles away from a central core. The dark contrast in the centre of the nanoparticle also indicates a fifth branch is extending

along the axis of the electron beam. The nanostructure indicated by the red arrow is 75 nm long and 45 wide and possesses a complex, indefinable shape. Figure 9c shows a SAED pattern for the as synthesised nanoparticles and is indexed to the *fcc* crystal structure of palladium. Figure 9d shows nanoparticle nuclei 1 – 5 nm in size which indicates a bimodal size distribution for this reaction. Again there is some obvious coalescence of the nuclei with ‘worm-like’ nanoparticles up to 15 nm in length.

5.2.3: Reaction of [PdCl₂(NCMe)₂] at 100 °C

The previous experiment produced nanoparticles with morphologies ranging from small spherical nuclei to polyhedra and triangles. Therefore the high concentration conditions chosen above are promising for the formation of complex morphologies however there is still the problem of a bimodal size and shape distribution. Therefore, in the next two experiments the reaction temperature was varied in an attempt to create a uniform sample. In this experiment reaction temperature was increased in an attempt to cause faster nucleation that is separated from the growth process.

Experimental

25.9 mg (0.1 mmol) of [PdCl₂(NCMe)₂] was dissolved in 1 mL of toluene in a 10 mL reaction vial. To this was added 0.329 mL (1 mmol) of oleylamine. This reaction mixture was sonicated until a clear colourless solution resulted. The vial was suspended in a Fischer-Porter bottle with 10 mL of excess anisole in the bottom of the bottle. The bottle was purged 5 times with hydrogen gas and then filled with 3 bar H₂. The Fischer-Porter bottle was then placed in a reaction oven at 100 °C for 42 h. Purification was carried out as above.

Results

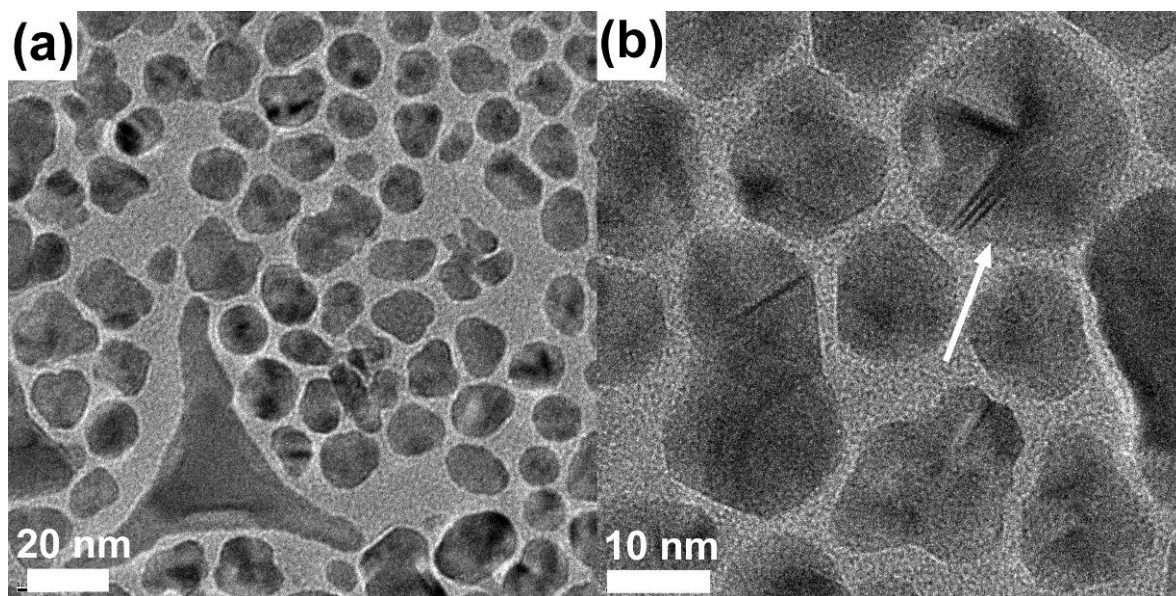


Figure 10. HREM image of palladium nanoparticles synthesised by the reaction of $[\text{PdCl}_2(\text{NCMe})_2]$ at $100\text{ }^\circ\text{C}$ (a) and high magnification HREM image (b).

Figure 10a shows an HREM image of the as-synthesised nanoparticles. There is a large size distribution with nanoparticles ranging in size from 8 to 20 nm. The nanoparticles are predominantly polyhedra with some indefinable shapes present. Interestingly there is a large 60 nm nanoparticle with three fold symmetry present in the bottom left of the micrograph. This type of structure can form through elongated growth from a twinned triangle nanoparticle {Maksimuk 2007}. Figure 10b shows a high magnification image of the as synthesised nanoparticles. The nanoparticles are highly faceted and display multiple twinning. The nanoparticle indicated by the white arrow is 22 nm in size and displays five fold symmetry characteristic of a multiply twinned decahedra structure. It should be noted that although there is no evidence of a bimodal distribution in this sample the polydispersity is very large.

5.2.4: Reaction of [PdCl₂(NCMe)₂] at room temperature

In this experiment the investigation into the effect of reaction temperature was continued by decreasing to room temperature.

Experimental

25.9 mg (0.1 mmol) of [PdCl₂(NCMe)₂] was dissolved in 1 mL of toluene in a 10 mL reaction vial. To this was added 0.329 mL (1 mmol) of oleylamine. This reaction mixture was sonicated until a clear colourless solution resulted. The vial was suspended in a Fischer-Porter bottle with 10 mL of excess anisole in the bottom of the bottle. The bottle was purged 5 times with hydrogen gas and then filled with 3 bar H₂. The Fischer-Porter bottle was then placed in a reaction oven at room temperature for 20 h. Purification was carried out as above.

Results

Figure 11a shows a low resolution EM image of the as synthesised palladium nanoparticles. The nanoparticles are predominantly formed as polyhedra that are 6 ± 1.5 nm in size. The inset shows a SAED which is indexed as *fcc* palladium. Figure 11b shows a close up HREM image of one of the polyhedra. The visible lattice planes are (111) and (200) in nature which means these facets are being viewed down a $\langle 110 \rangle$ zone axis. When compared to previous literature HREM experiments the nanoparticle can be characterised as a multiply twinned *fcc* icosahedra viewed along a $\langle 112 \rangle$ zone axis {Penisson 1989}. Figure 11c shows an EDS spectrum of the imaged nanoparticles and indicates the sample is 100% Pd. Figure 11d shows the size distribution analysis of the EM image in Fig 11a. The sample has a Gaussian size distribution with a polydispersity from standard deviation of $\sigma = 13$ %.

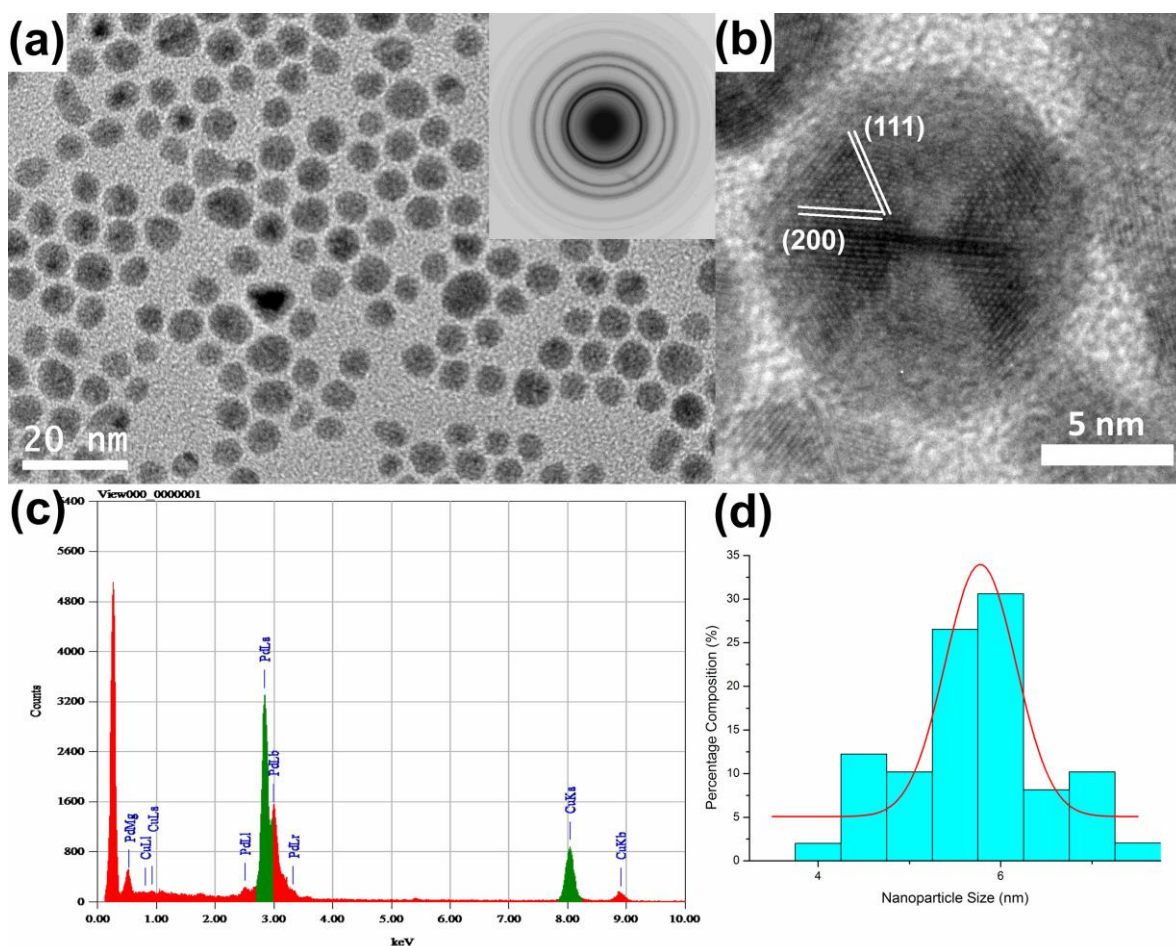


Figure 11. (a) HREM image of palladium nanoparticles synthesised by the reaction of $[\text{PdCl}_2(\text{NCMe})_2]$ at room temperature. (b) High magnification image of one the palladium nanoparticles which is characterised as having a multiply twinned icoshedra morphology. (c) EDS spectrum of the as synthesised nanoparticles. (d) Corresponding size distribution profile.

5.2.5 Discussion of Reactions with $[\text{PdCl}_2(\text{NCMe})_2]$

When $\text{Pd}(\text{PPh}_3)_4$ was used as precursor small spherical nuclei 1 – 5 nm in size were the major product due to the strong Pd-P binding interaction. At these sizes a spherical morphology is energetically preferred due to the minimisation of surface energy. However, it is known that once the nuclei grow past a certain size internal crystalline energy considerations begin to dominate and well-defined crystallographic facets form on the nanoparticle surface {Xiong 2007 (a)}. This is indeed what is observed in the above experiments with $[\text{PdCl}_2(\text{NCMe})_2]$ as precursor. The growth of the nanoparticles is not as strongly restricted due to the weaker binding strength of the nitrogen functionalities present (organic surfactant and acetonitrile ligand) resulting in larger, more faceted structures. The highlighted nanoparticle in Figure 8a (Exp 5.2.1) and the nanoparticle in Fig 11b (Exp 5.2.4) are bound by {111} facets and characterised as multiply twinned *fcc* decahedral and

icosahedral nanoparticles respectively {Choo 2006, Xiong 2007 (a), Lim 2007}. The formation of twin defects in nanoparticles is primarily driven by a minimisation in surface energy. The surface energies corresponding to commonly exposed crystallographic facets increases in the order $\{111\} < \{100\} < \{110\}$ {Wang 2000, Zhang 2004}. In nanoparticles the extra energy caused by twinning is compensated for by maximising the surface coverage with low energy $\{111\}$ crystal facets, thus achieving a lower overall energy {Ajayan 1988}. Therefore multiply twinned *fcc* icosahedra and decahedra are widely accepted as thermodynamically favoured morphologies for palladium nanoparticles {Elechiguerra 2006, Berhault 2007}.

For Exp 5.2.1 there is a bimodal distribution of nanoparticle size and shape which indicates insufficient separation between nucleation and growth. This problem persisted when the concentration was increased (Exp 5.2.2) however new more elaborate nanoparticle morphologies were observed, including triangle shapes. Triangle nanoparticles have previously been observed for palladium where the shape was explained by the presence of a single $\{111\}$ twin along the basal plane of the nanoparticle {Xiong 2005 (b)}. This experiment also produced evidence of new structures with indefinable morphologies. The nanostructure indicated by a blue arrow in Fig 9b was, at the time, the first observation of a pod-like morphology for palladium. Therefore, the conditions chosen for Exp 5.2.2 are promising for the formation of complex morphologies however the bimodal distribution present indicates that there is insufficient control over the reaction processes.

When the reaction temperature was increased to 100 °C (Exp 5.2.3) the distribution of the nanoparticles was no longer bimodal. The increase in temperature induced a single nucleation stage which lead to a Gaussian distribution of nanoparticle size and shape. However the polydispersity was still large which indicates insufficient control over the reaction. This is due to the high temperature of the reaction and the dynamic nature of the surfactant–nanoparticle interaction. If the reaction temperature is too high the surfactant molecules are more likely to leave the nanoparticle surface leading to uncontrolled growth {Yin 2005}.

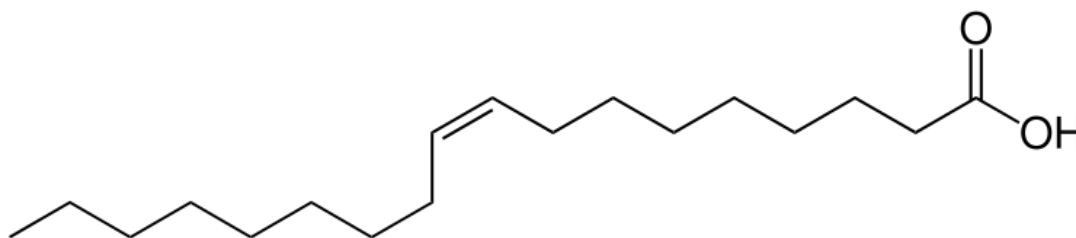
As the reaction temperature was decreased to room temp (Exp 5.2.4) we observed the formation of a relatively monodisperse product ($\sigma = 13\%$). This is because at room temperature the surfactant resides primarily on the nanoparticle surface

Chapter 5: *Solution Phase Syntheses of Palladium Nanostructures*

leading to sufficient stabilisation and control over nanoparticle growth. Therefore, room temperature can be considered as the appropriate temperature range for sufficient control over the growth of palladium nanoparticles for this technique.

5.3 Reactions with $[\text{PdCl}_2(\text{NCMe})_2]$ at Room Temperature : Changing the Surfactant System and Structural Evolution

The previous experiments showed that $[\text{PdCl}_2(\text{NCMe})_2]$ was a promising precursor for the formation of complex palladium nanoparticle morphologies. Sufficient control over the reaction processes was only observed at mild growth conditions. However, to introduce complex nanoparticle shapes the growth rate must be increased {Yin 2005}. To achieve this at room temperature variation of the organic surfactant system is required as the onset of shape control can be induced through selective adhesion {Yin 2005}. Therefore in the following experiments the nature of the surfactant system was varied in an attempt to introduce shape complexity while still maintaining reaction control. Oleic acid was introduced as it is structurally similar to oleylamine and the addition of a carboxylic acid functionality has previously been shown to induce shape change in nickel colloids {Bradley 2000}.



Scheme 1. Molecular structure of oleic acid.

5.3.1: Reaction of $[\text{PdCl}_2(\text{NCMe})_2]$ with a 1:1 mixture of oleylamine and oleic acid as surfactant at room temperature

In this experiment the effect of the surfactant system was investigated by introducing oleic acid in a 1:1 ratio with oleylamine. The Pd-O interaction is weaker than the Pd-N interaction (Ahrland 1958). Therefore it was hoped that the addition of oleic acid would lead to destabilisation of certain crystal facets and the introduction of shape complexity.

Experimental

25.9 mg (0.1 mmol) of $[\text{PdCl}_2(\text{NCMe})_2]$ was dissolved in 1 mL of toluene in a 10 mL reaction vial. To this was added 0.165 mL (0.5 mmol) of oleylamine and 0.158 mL (0.5

Chapter 5: *Solution Phase Syntheses of Palladium Nanostructures*

mmol) of oleic acid. This reaction mixture was sonicated until a clear yellow solution resulted. The vial was suspended in a Fischer-Porter bottle with 10 mL of excess anisole in the bottom of the bottle. The bottle was purged 5 times with hydrogen gas and then filled with 3 bar H₂. The Fischer-Porter bottle was then left at room temperature for 20 h.

For purification of the sample, methanol was added to flocculate the as synthesised nanoparticles. The solution was centrifuged at 14 000 rpm for collection of the solid nanoparticles. These were subsequently washed by suspending the pellet in toluene and ultrasonicing for 5 minutes. Additional methanol was added again to flocculate the nanoparticles followed by centrifuging. The purification process was repeated once with dichloromethane and a second time with toluene. The resulting purified sample was suspended in toluene for TEM investigation.

Results

Figure 12a shows an EM image of the as synthesised nanostructures. The nanostructures show long needle like projections extending away from a central core. Figure 12b shows a close up EM image of a palladium nanostructure 100 nm in size. It shows extensive needle like projections giving rise to a 'highly branched' palladium nanostructure with a high surface area. Another example is shown in Figure 12c, this nanostructure is 70 nm in size and shows branching occurring radially away from the centre in a pseudo-six fold symmetry. The branches are relatively uniform in size and shape with each having an aspect ratio of ~ 7 . An EDS spectrum of the as synthesised nanoparticles is shown in Fig 12d and indicates the product contains palladium only.

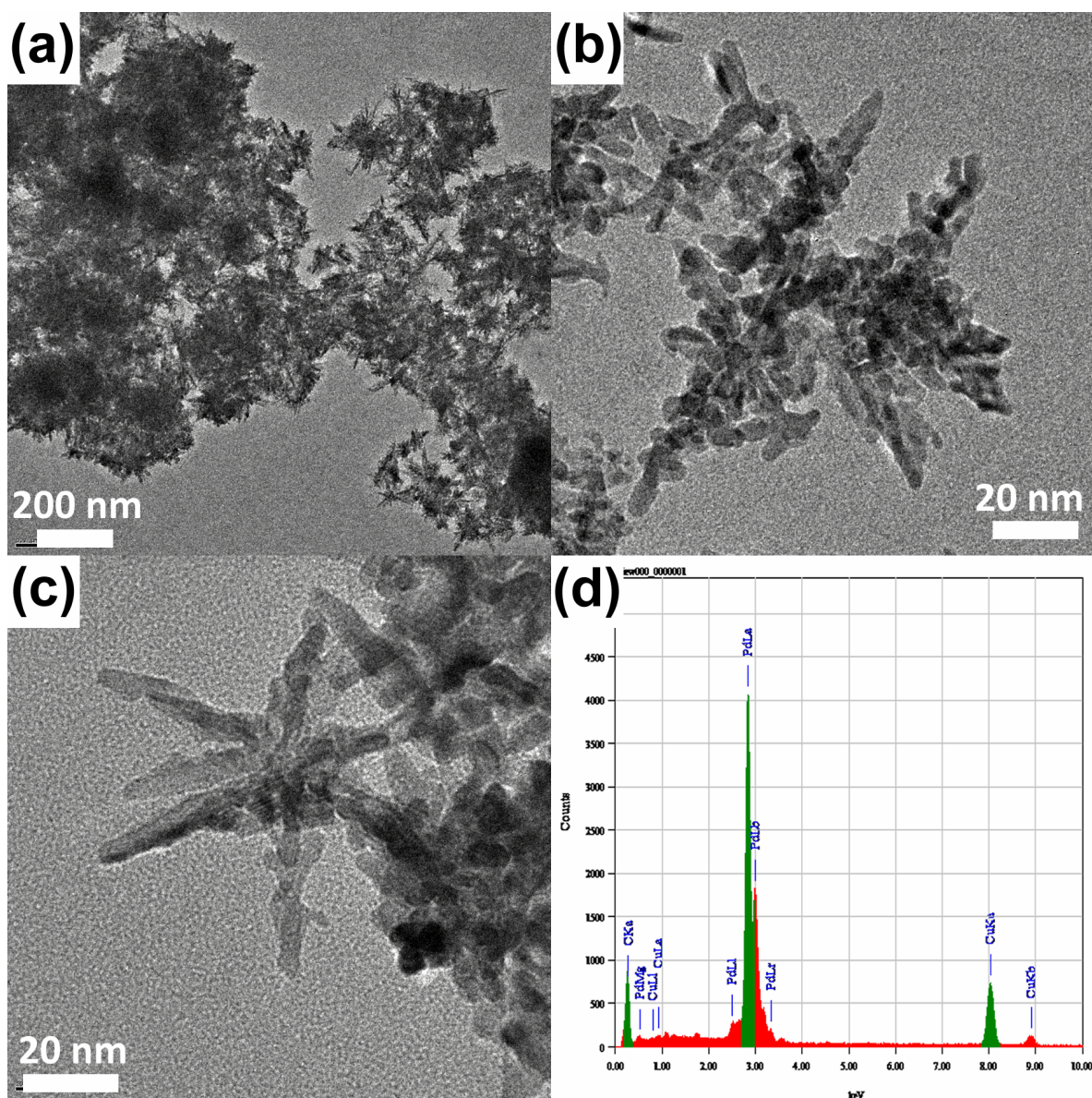


Figure 12. (a) HREM image of palladium nanostructures formed by the of $[\text{PdCl}_2(\text{NCMe})_2]$ with a 1:1 mixture of oleylamine and oleic acid as surfactant at room temperature. (b) High magnification image of a 100 nm highly branched palladium nanostructure. (c) High magnification image of a highly branched palladium nanostructure 70 nm in size and (d) EDS spectrum of the as-synthesised nanostructures.

5.3.2 : Reaction of $[\text{PdCl}_2(\text{NCMe})_2]$ with a 1:1 mixture of oleylamine and oleic acid as surfactant at RT for 10 minutes

The experiment above showed that by varying the nature of the surfactant system the size and morphology of the as synthesised nanostructures could be manipulated. A ratio of 1:1 oleylamine and oleic acid produced complex, highly branched nanostructures with a high surface area. This is in contrast to when only oleylamine

is used as the surfactant which lead to the formation of polyhedral nanostructures. The highly branched nanostructures are unexpected morphologies for palladium as when it crystallises it does so in the highly symmetrical *fcc* crystal structure. Therefore, to introduce shape complexity there must be a breaking of the crystal symmetry and the introduction of kinetic shape control {Yin 2005}. To investigate the underlying growth processes of these unexpected morphologies an insight into the structural evolution of the nanoparticles is required. To investigate the growth evolution of the highly branched nanostructures the reaction time was varied to isolate structural intermediates.

The current experiment was carried out to isolate palladium nanoparticles after 10 min reaction time.

Experimental

25.9 mg (0.1 mmol) of $[\text{PdCl}_2(\text{NCMe})_2]$ was dissolved in 1 mL of toluene in a 10 mL reaction vial. To this was added 0.165 mL (0.5 mmol) of oleylamine and 0.158 mL (0.5 mmol) of oleic acid. This reaction mixture was sonicated until a clear yellow solution resulted. The vial was suspended in a Fischer-Porter bottle with 10 mL of excess anisole in the bottom of the bottle. The bottle was purged 5 times with hydrogen gas and then filled with 3 bar H_2 . The Fischer-Porter bottle was then place in a reaction oven at room temperature for 10 min. Purification was carried out as above. The supernatant retrieved after the first purification step was a clear yellow indicating the presence of unreacted precursor.

Results

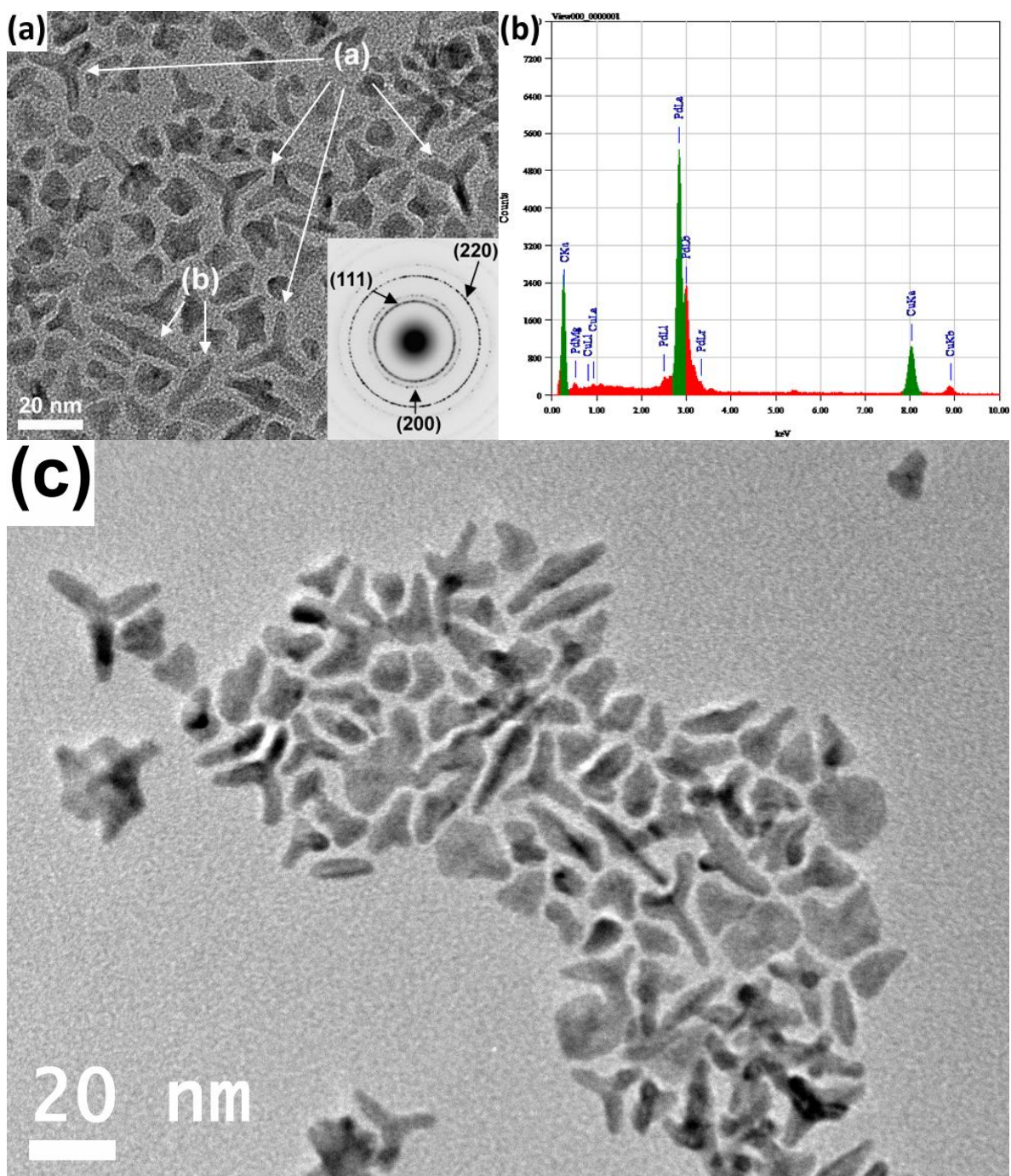


Figure 13. (a) High magnification HREM image of as synthesised pod-like palladium nanostructures. The nanoparticles marked by (a) are tripod in shape and the nanoparticles marked by (b) have a bipod shape. (b) EDS spectrum of the palladium pod-like nanostructures. (c) High magnification HREM image showing the tripod nanoparticles with the maximum yield obtained of 40% {Watt 2009}.

Figure 13a displays a typical EM image of the obtained nanoparticles. Various shaped nanoparticles are present in the solution including tripods and bipods, as well as other irregularly shaped anisotropic nanoparticles. The nanoparticles labelled (a)

are Pd tripods and the nanoparticles labelled (b) show a linear rod or bipod morphology. The remainder of the sample is made up of nanoparticles with various degrees of branching and other anisotropic morphologies. The inset in Fig 1 shows the selected area electron diffraction pattern of the sample in the image which was indexed to the *fcc* structure of Pd. Elemental analysis from EDS (Fig 13b) indicates that the sample is 100% Pd. Figure 13c shows an HREM image with a high yield of tripod nanoparticles. From analysis of TEM images of over 2000 nanoparticles, the relative yields of the morphologies formed were; bipods (in 17 % yield), tripods (28 %) and multipods (7%).

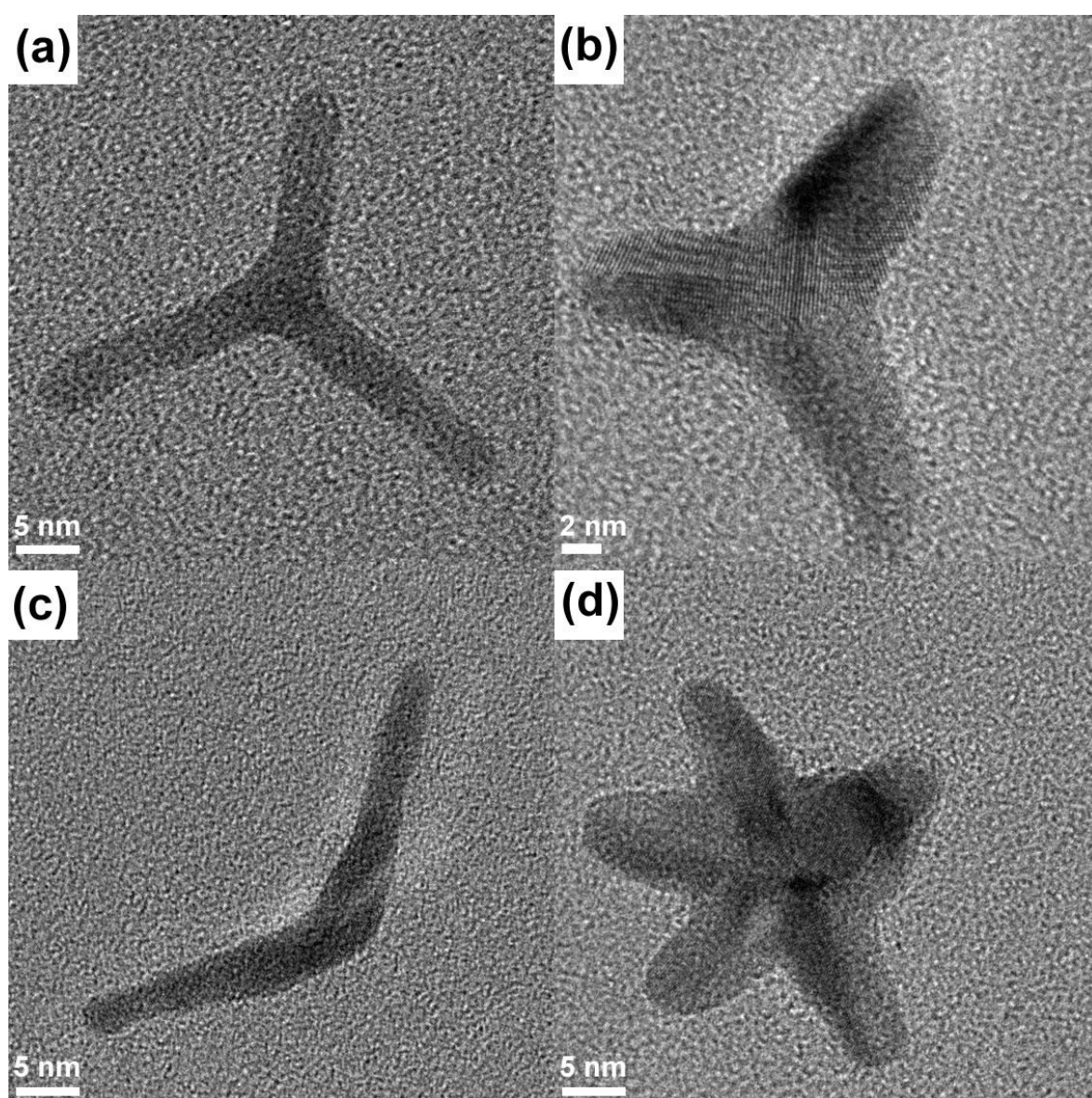


Figure 14. High magnification HREM images of pod-like palladium nanoparticles; (a) a tripod morphology, (b) a different type of tripod shaped nanoparticle, (c) a bipod nanoparticle and (d) a multipod nanoparticle.

Figure 14a-b shows some of the interesting nanoparticle morphologies formed in the present experiment. Fig 14a shows a tripod nanoparticle 30 nm in size. Its arms are relatively uniform in length ranging from 16 to 20 nm with aspect ratios of 5. The arms are exactly 60° apart indicating perfect three fold symmetry. The nanoparticle in Figure 14b is only 16 nm in size but also shows a tripod symmetry. Its arms are again uniform in length at 10 nm with aspect ratios of ~ 2 . Figure 14c shows a nanostructured palladium bipod with two arms extending at an angle of 125° from each other. They are both 22 nm in length with aspect ratios of ~ 5 . Note there is a small increase in angle between the bipod arms when compare those of the tripod morphology. Figure 14d shows a 30 nm multi-pod nanoparticle with 5 arms, 13 ± 2 nm in size, extending away from a central core. The arms all extend along the plane of the nanoparticle in a pseudo-five fold symmetry.

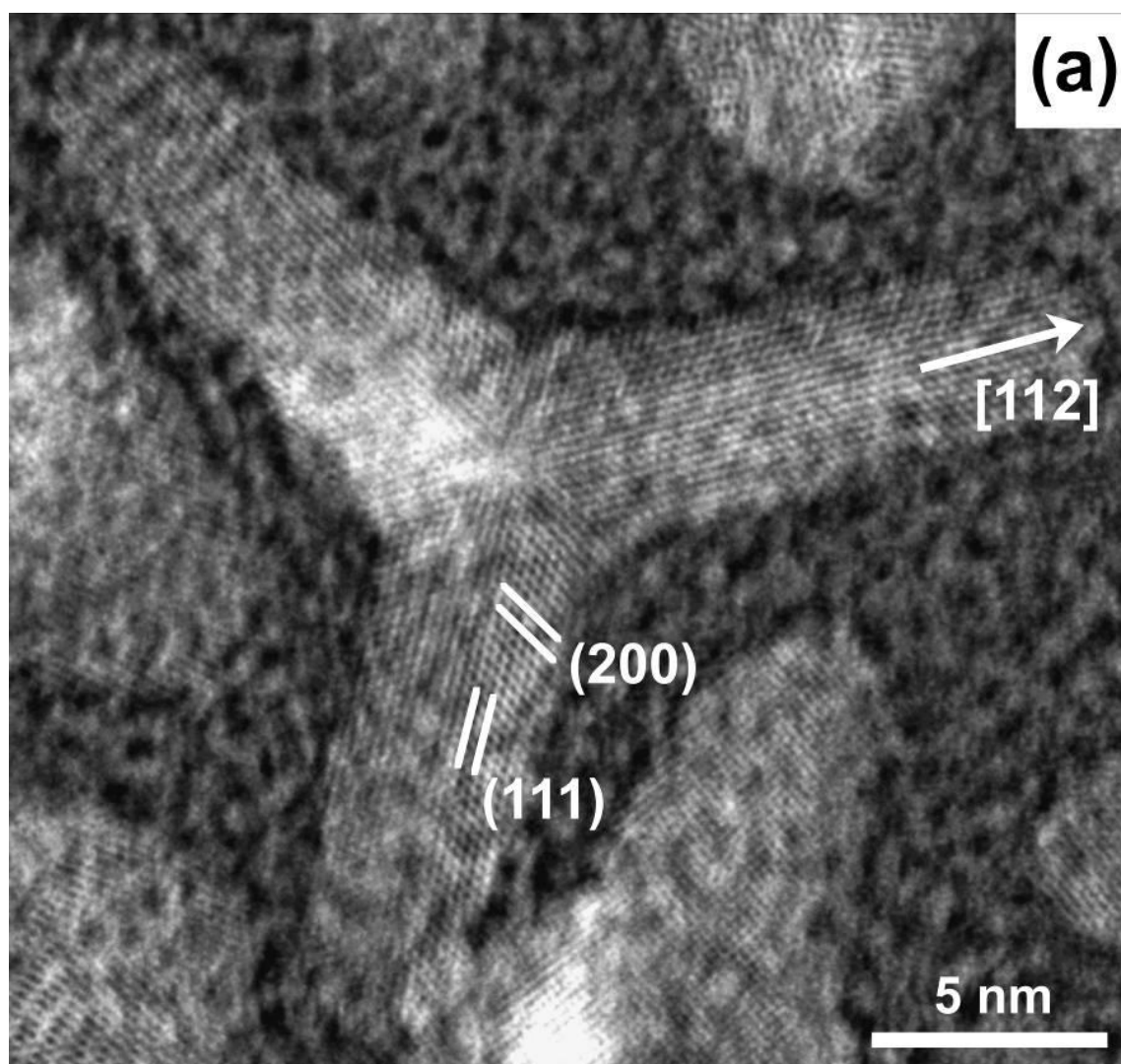


Figure 15. High magnification HREM image of an as synthesised tripod shaped palladium nanoparticle.

Figure 15 shows a HREM image of an as synthesized tripod. The nanoparticle consists of a central core with three arms extending away from the centre. The angle between each arm is 120° indicating perfect three fold symmetry. The arms are relatively uniform in length ranging from 12 - 13 nm with aspect ratios close to 3. The lattice planes visible on the tripod arms are (200) and (111) in nature indicating the tripod arms are viewed down a [110] zone axis. Each arm shows a twin plane running along its length in the direction of growth. The twin plane runs parallel to the {111} planes along the long axis of the tripod arm indicating that it is a (111) twin boundary. The tip of the arm exhibits a rounded contour. Analysis of the atomic packing in the image indicates that arm growth is occurring in the [112] direction. Note that the projection of lattice planes of the tripod in Fig 15 is different to the tripod in Fig 14b. This will be explained in detail in Chapter 6.1.

5.3.3 : Reaction of $[\text{PdCl}_2(\text{NCMe})_2]$ with a 1:1 mixture of oleylamine and oleic acid as surfactant at RT for 30 minutes

In this experiment the investigation into the nanoparticle structural evolution was continued by extending the reaction time to 30 min. The previous experiment isolated pod-like intermediates however a structural link between these and the highly branched nanostructures is also required.

Experimental

25.9 mg (0.1 mmol) of $[\text{PdCl}_2(\text{NCMe})_2]$ was dissolved in 1 mL of toluene in a 10 mL reaction vial. To this was added 0.165 mL (0.5 mmol) of oleylamine and 0.158 mL (0.5 mmol) of oleic acid. This reaction mixture was sonicated until a clear yellow solution resulted. The vial was suspended in a Fischer-Porter bottle with 10 mL of excess anisole in the bottom of the bottle. The bottle was purged 5 times with hydrogen gas and then filled with 3 bar H_2 . The Fischer-Porter bottle was then left at room temperature for 30 min. Purification was carried out as above. The supernatant retrieved after the first purification step was a clear yellow indicating the presence of unreacted precursor.

Results

Figure 16a-b shows HREM images of palladium nanoparticles synthesised after 30 minutes. The nanoparticles in Fig 16a are 18 to 30 nm in size and have indefinable

Chapter 5: *Solution Phase Syntheses of Palladium Nanostructures*

morphologies. The nanoparticles marked by white arrows have pseudo-three fold symmetry and therefore look to have grown from the tripod nanostructures isolated in Exp 5.3.2. However, a secondary type of growth has occurred along random crystallographic directions leading to a broad, leaf-like structure.

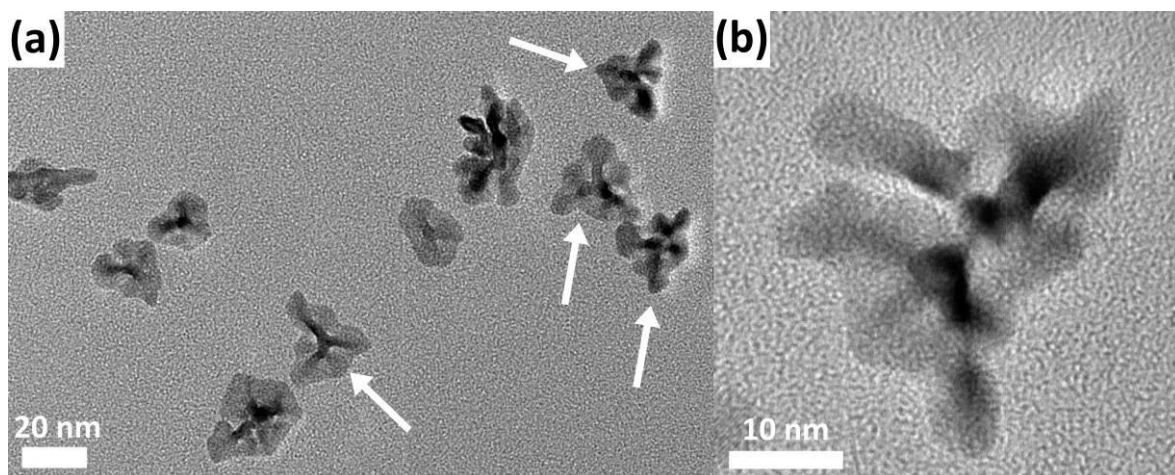


Figure 16. (a) High magnification HREM image of as synthesised palladium nanostructures formed from a reaction of $[\text{PdCl}_2(\text{NCMe})_2]$ with a 1:1 mixture of oleylamine and oleic acid as surfactant at RT for 30 minutes. (b) High magnification image of a palladium nanostructure clearly showing a secondary type of 'leaf-like' growth.

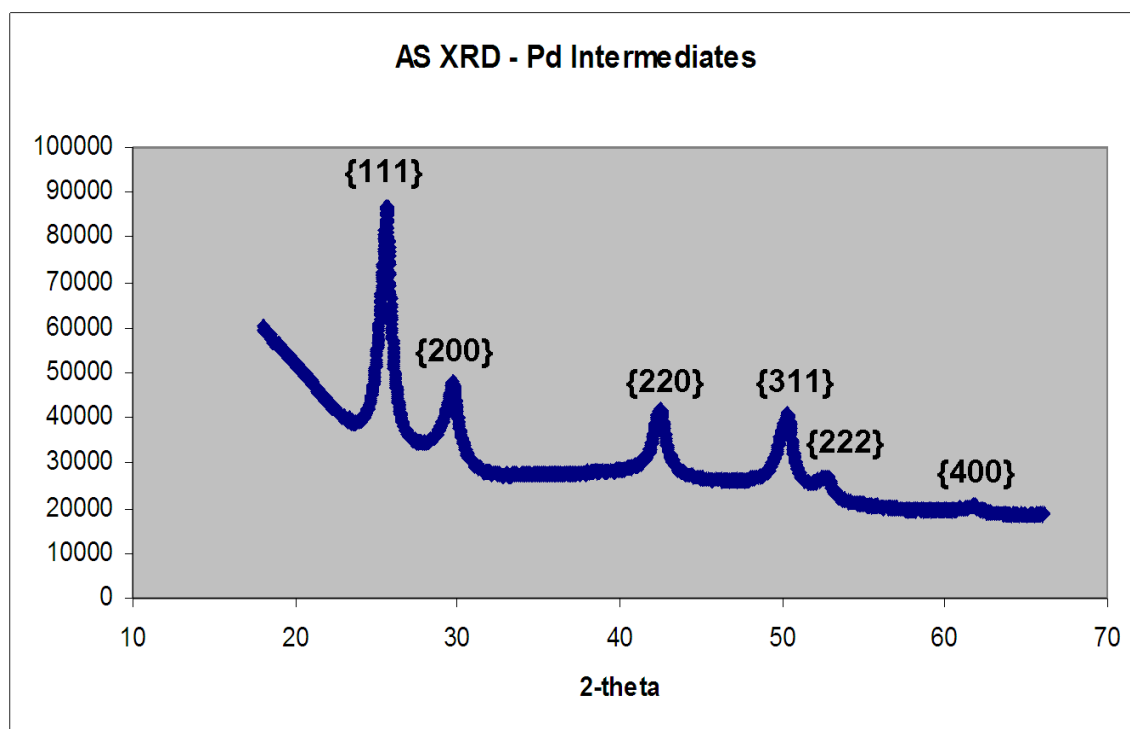


Figure 17. Synchrotron XRD pattern of the as synthesised palladium nanostructures formed from a reaction of $[\text{PdCl}_2(\text{NCMe})_2]$ with a 1:1 mixture of oleylamine and oleic acid as surfactant at RT for 30 minutes.

Figure 17 shows an XRD pattern taken from the Australian Synchrotron (AS) facility. The pattern is clearly indexed to *fcc* palladium with no impurities present.

5.3.4 : Reaction of $[\text{PdCl}_2(\text{NCMe})_2]$ with a 1:1 mixture of oleylamine and oleic acid as surfactant at RT for 20 minutes

Experiments 5.3.2 and 5.3.3 produced pod-like and leaf-like nanoparticles after 10 min and 30 min reaction time respectively. These nanoparticles are intermediates to the highly branched nanostructures. Equally important however in investigating the structural evolution is the isolation of nanoparticle nuclei, that is, the structural precursor to the pod-like nanoparticles. Because of the nature of the Fischer-Porter bottle it is difficult to quench the nanoparticle formation at reaction times less than 10 minutes. Therefore to slow the reaction and gain more control over the isolation of intermediates the pressure of the hydrogen atmosphere was reduced to 1 bar.

In this experiment structural precursors to the pod-like nanoparticles were isolated by reducing the pressure of the hydrogen atmosphere to 1 bar and extending the reaction time to 20 min.

Experimental

25.9 mg (0.1 mmol) of $[\text{PdCl}_2(\text{NCMe})_2]$ was dissolved in 1 mL of toluene in a 10 mL reaction vial. To this was added 0.165 mL (0.5 mmol) of oleylamine and 0.158 mL (0.5 mmol) of oleic acid. This reaction mixture was sonicated until a clear yellow solution resulted. The vial was suspended in a Fischer-Porter bottle with 10 mL of excess anisole in the bottom of the bottle. The bottle was purged 5 times with hydrogen gas and then filled with 1 bar H_2 . The Fischer-Porter bottle was then left at room temperature for 20 min. Purification was carried out as above.

Results

Figure 18a shows an EM image of the as synthesised nanoparticles. The sample consists of nanostructured polyhedra 6 to 10 nm in size. Also present are triangle shaped nanoparticles ~ 8 nm in size and nanostructured tripods 8 to 15 nm in size. The nanoparticle indicated by the white arrow is a tripod 12 nm in size. Figure 18b shows a high magnification HREM image of a nanoparticle 14 nm in size. Analysis of the atomic packing indicates this nanoparticle is a multiply twinned *fcc* icosahedra viewed down a $\langle 112 \rangle$ zone axis {Penisson 1989}. This is similar to the nanoparticle

seen in Fig 5.2.4b except the nanoparticle shown here displays the start of single branched growth in the $[112]$ direction.

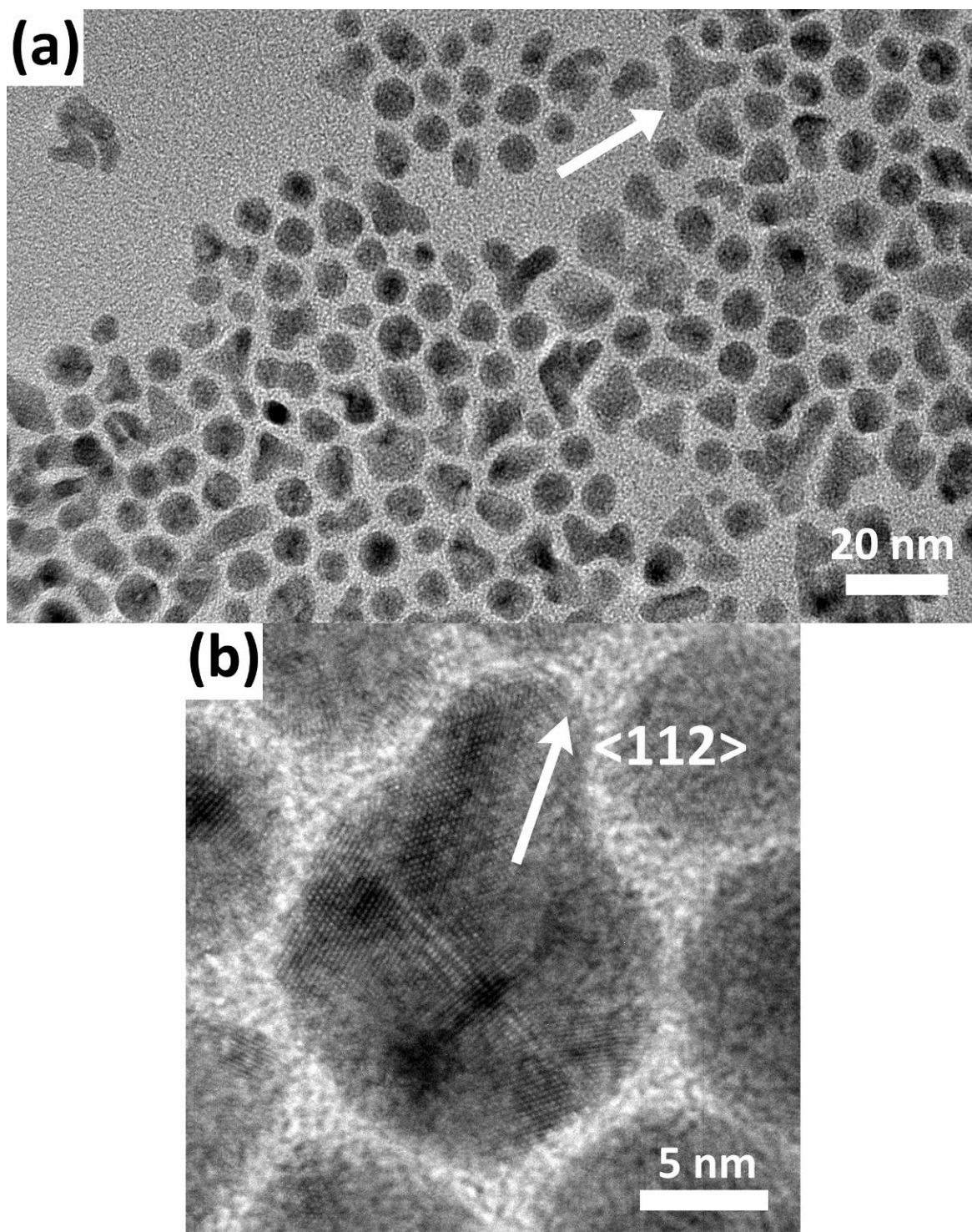


Figure 18. (a) HREM image of palladium nanoparticles formed from a Reaction of $[\text{PdCl}_2(\text{NCMe})_2]$ with a 1:1 mixture of oleylamine and oleic acid as surfactant at RT for 20 minutes. (b) High magnification HREM image of a multiply twinned icosahedra nanoparticle with the start of branched growth present.

5.3.5: Reaction of $[\text{PdCl}_2(\text{NCMe})_2]$ with a 1:1 mixture of oleylamine and oleic acid as surfactant at RT under 1 bar H_2 for 80 min

In this experiment the reaction time was extended to 80 min for the isolation of further structural intermediates.

Experimental

25.9 mg (0.1 mmol) of $[\text{PdCl}_2(\text{NCMe})_2]$ was dissolved in 1 mL of toluene in a 10 mL reaction vial. To this was added 0.165 mL (0.5 mmol) of oleylamine and 0.158 mL (0.5 mmol) of oleic acid. This reaction mixture was sonicated until a clear yellow solution resulted. The vial was suspended in a Fischer-Porter bottle with 10 mL of excess anisole in the bottom of the bottle. The bottle was purged 5 times with hydrogen gas and then filled with 1 bar H_2 . The Fischer-Porter bottle was then left at room temperature for 80 min. Purification was carried out as above. The supernatant retrieved after the first purification step was a clear yellow indicating the presence of unreacted precursor.

Results

Figure 19a-c shows EM images of palladium nanoparticles synthesised after 80 minutes. The low magnification EM image in Fig 19a shows examples of a relatively large variety of nanoparticle shapes and sizes. The sample contains nanostructured tripods 15 to 20 nm in size and bipods 20 to 35 nm in size similar to those seen in Exp 5.3.2 as well as other nanoparticles with indefinable morphologies. Present also are tripod and bipod nanoparticles which have experienced the secondary type of growth leading to leaf-like structures. Figure 19b shows an 80 nm bipod nanoparticle with secondary non-direction specific growth occurring on the sides of the nanoparticle. Figure 19c shows a 38 nm tripod nanoparticle with a similar leaf-like structure to that seen in Fig 5.3.3 b. Fig 19d shows an EDS spectrum which indicates the sample is 96% Pd with the remaining 4% coming from Si impurities on the TEM grid.

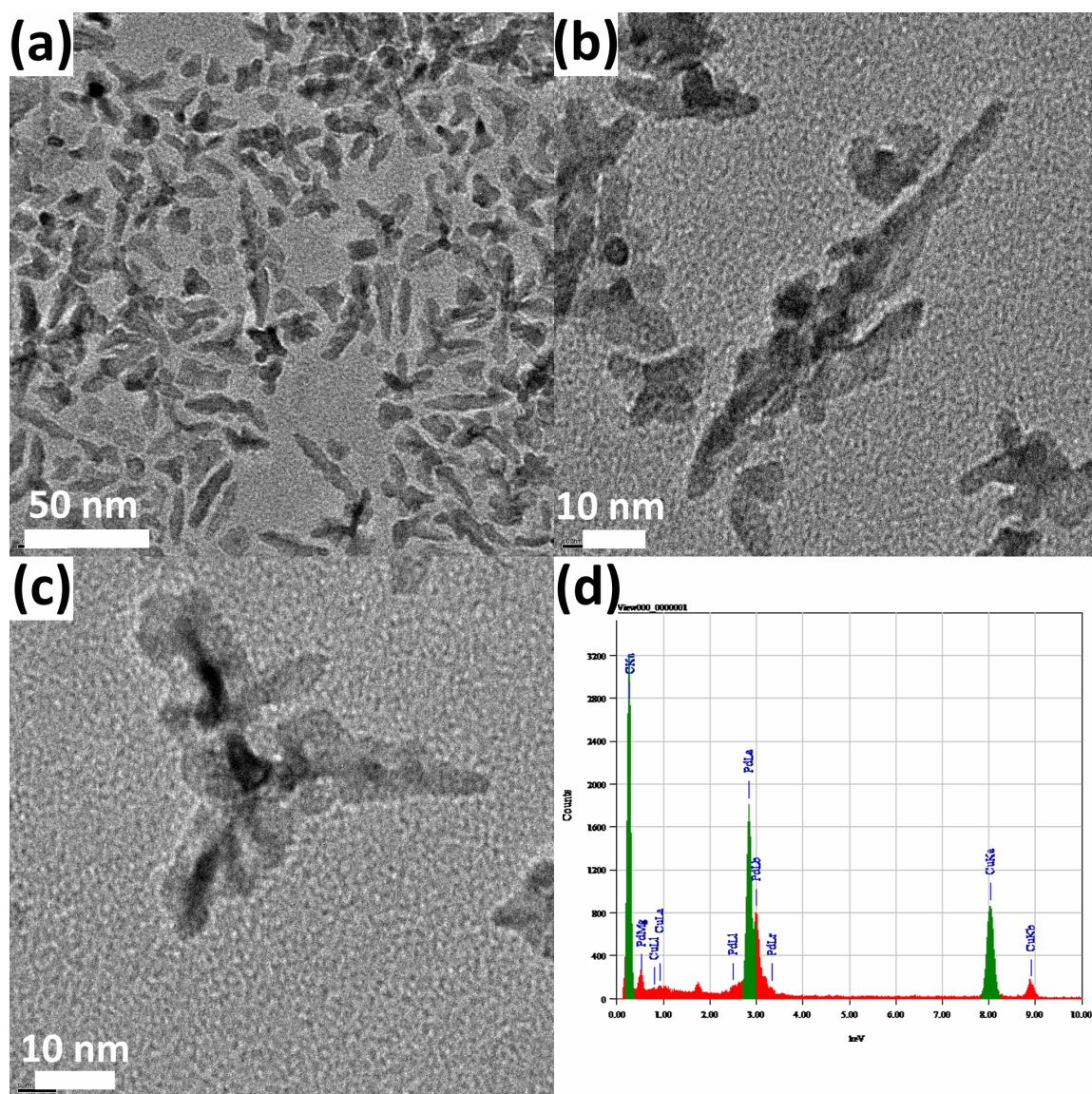


Figure 19. (a) HREM image of palladium nanoparticles formed from a reaction of $[\text{PdCl}_2(\text{NCMe})_2]$ with a 1:1 mixture of oleylamine and oleic acid as surfactant at RT under 1 bar H_2 for 80 min. (b) High magnification HREM image of a bipod nanoparticle with secondary growth evident. (c) High magnification HREM image of a tripod nanoparticle with the same type of secondary growth occurring and (d) EDS spectrum of the as-synthesised palladium nanoparticles.

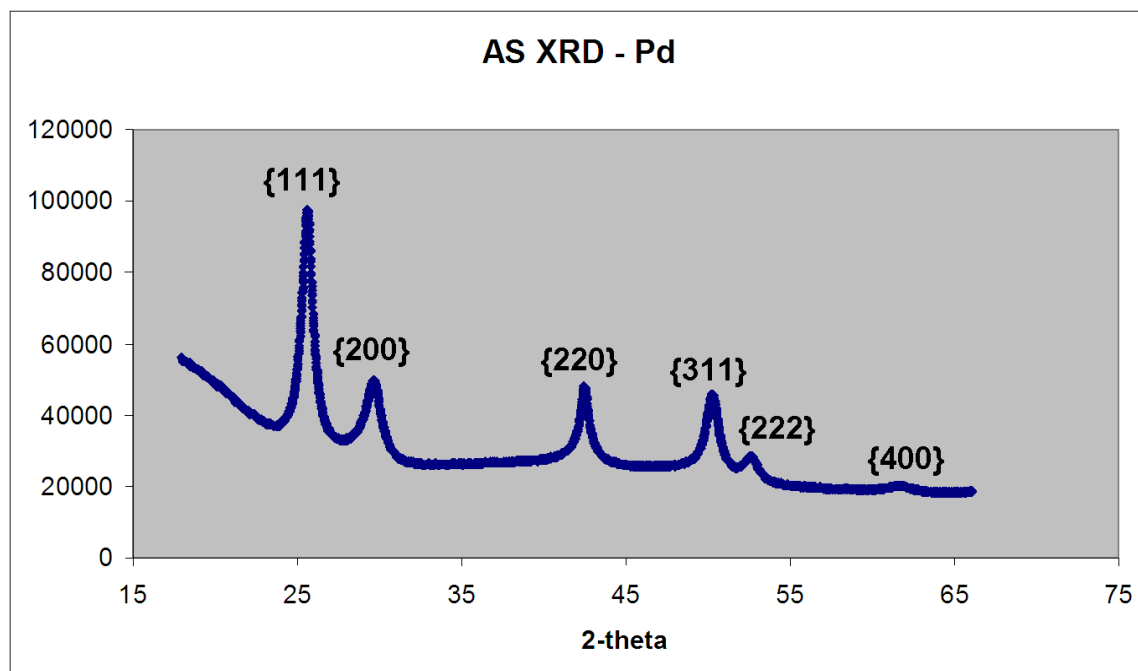


Figure 20. Synchrotron XRD pattern of the as synthesised palladium nanostructures formed from a reaction of $[\text{PdCl}_2(\text{NCMe})_2]$ with a 1:1 mixture of oleylamine and oleic acid as surfactant at RT under 1 bar H_2 for 80 min.

Figure 20 shows an XRD pattern taken from the Australian Synchrotron (AS) facility. The pattern is clearly indexed to *fcc* palladium with no impurities present.

5.3.6 : Reaction of $[\text{PdCl}_2(\text{NCMe})_2]$ with a 1:1 mixture of oleylamine and oleic acid as surfactant at RT under 1 bar H_2 for 160 min

In this experiment the investigation into the nanoparticle structural evolution was continued by extending the reaction time to 160 min.

Experimental

25.9 mg (0.1 mmol) of $[\text{PdCl}_2(\text{NCMe})_2]$ was dissolved in 1 mL of toluene in a 10 mL reaction vial. To this was added 0.165 mL (0.5 mmol) of oleylamine and 0.158 mL (0.5 mmol) of oleic acid. This reaction mixture was sonicated until a clear yellow solution resulted. The vial was suspended in a Fischer-Porter bottle with 10 mL of excess anisole in the bottom of the bottle. The bottle was purged 5 times with hydrogen gas and then filled with 1 bar H_2 . The Fischer-Porter bottle was then left at room temperature for 80 min. Purification was carried out as above. It should be noted here that the supernatant after the first purification step was clear and colourless which indicates the complete consumption of precursor.

Results

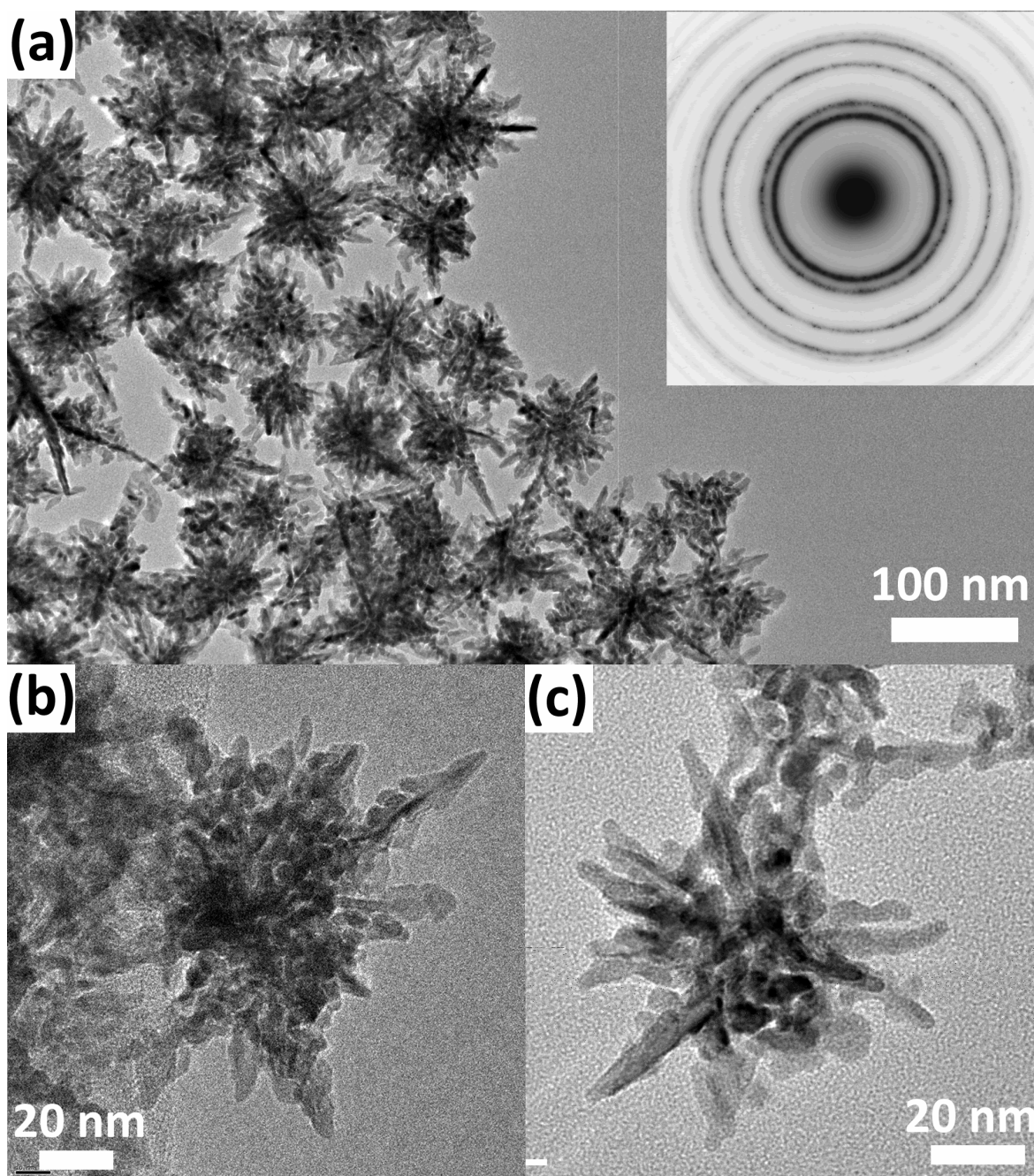


Figure 21. (a) HREM image of palladium nanoparticles formed from a reaction of $[\text{PdCl}_2(\text{NCMe})_2]$ with a 1:1 mixture of oleylamine and oleic acid as surfactant at RT under 1 bar H_2 for 160 min with corresponding SAED pattern (inset). (b) Highly branched palladium nanostructure 120 nm in size and (c) highly branched palladium nanostructure 80 nm in size.

Figure 21a shows a low magnification EM image of the highly branched palladium nanostructures synthesised in a surfactant system containing a 1:1 ratio of oleic acid and oleylamine. The palladium nanostructures are 85 ± 15 nm in size and each nanoparticle displays extensive branching with the branches growing radially away

Chapter 5: Solution Phase Syntheses of Palladium Nanostructures

from a central core. The selected area diffraction (SAED) pattern of the nanoparticles observed is shown in the inset and can be readily indexed to the *fcc* structure of palladium. Figure 21b-c show higher magnification images of single nanostructures. Figure 21b shows a close up image of a 120 nm palladium nanostructure. The nanoparticle branches have a broad leaf like structure and exhibit a rounded tip. The contrast difference across the nanoparticle indicates that the branches can grow along all radial directions. Likewise the 80 nm nanostructure in Fig 21c possesses branches extending in all radial directions from a central core.

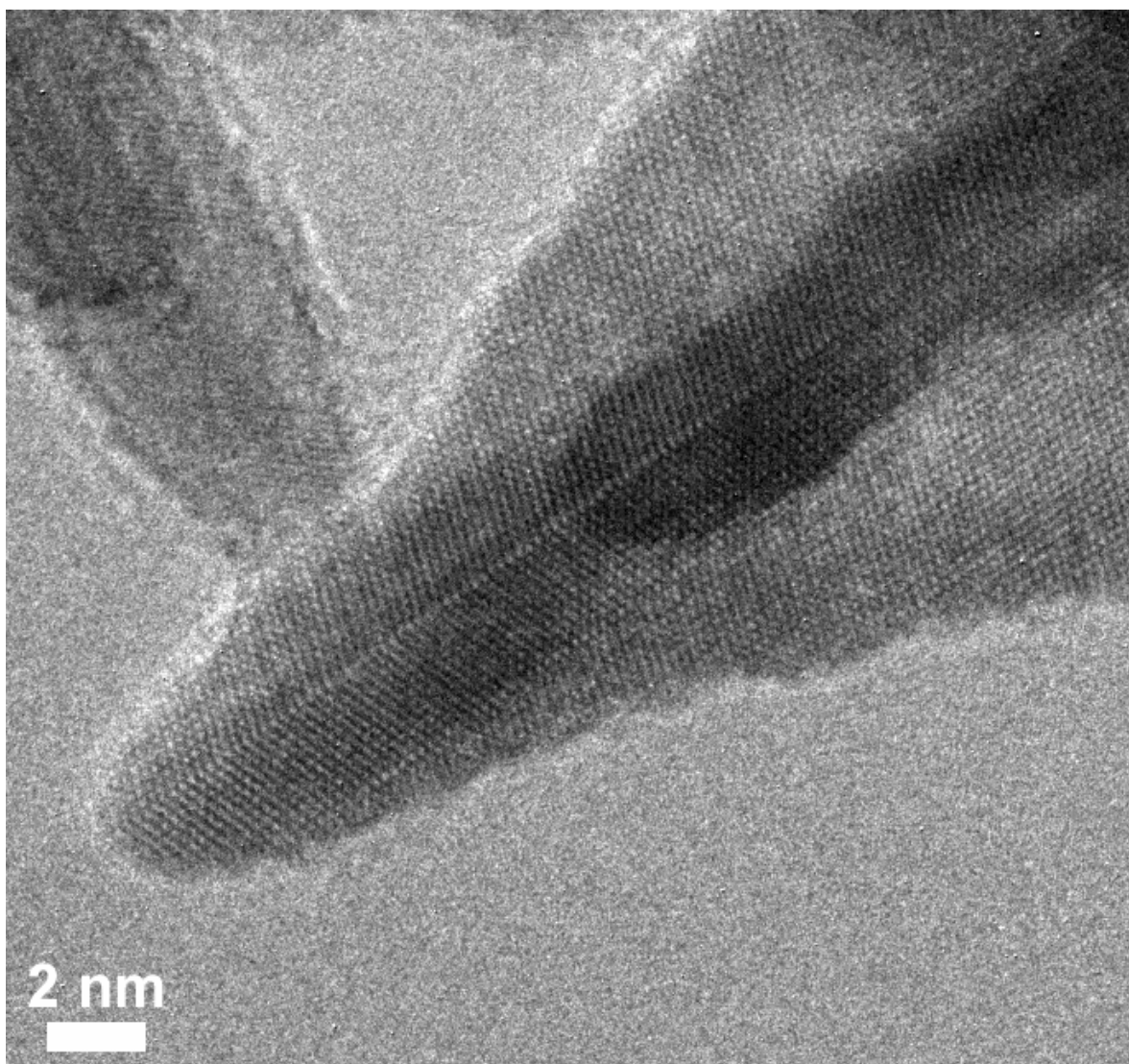


Figure 22. High resolution HREM image of one of the nanostructure branches clearly showing atomic packing.

Figure 22 shows an HREM image of one of the porous palladium branches. Atomic packing is clearly visible enabling characterization and shows that the branch is being viewed down the [110] direction. The branch has a twin boundary running down its length in the direction of growth. On the lower side of the twin there is a kink site

which changes the direction of the (200) lattice fringes by 20°. Along with the change in contrast, this indicates that from the edges of the branch towards the twin boundary there is an increase in thickness perpendicular to the basal plane. These palladium nanostructures also possess high index surfaces as will be shown in the next Chapter. Figure 23 shows an XRD pattern taken from the Australian Synchrotron (AS) facility. The pattern is clearly indexed to *fcc* palladium with no impurities present.

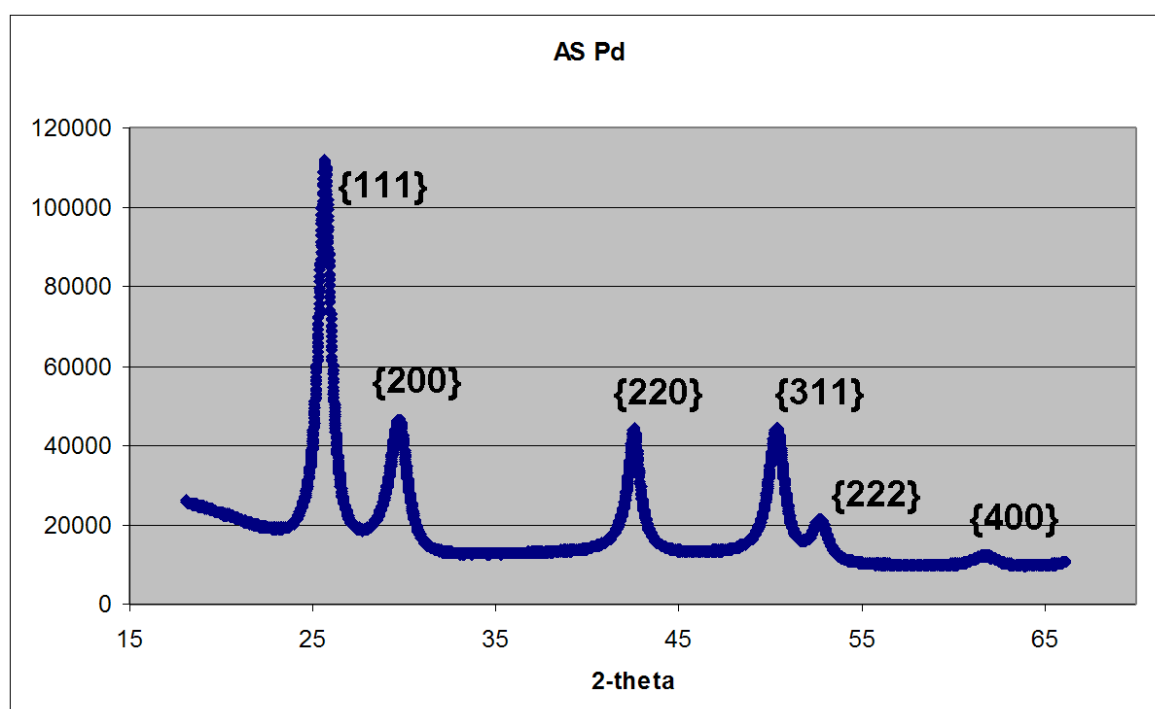


Figure 23. Synchrotron XRD pattern of the as synthesised palladium nanostructures formed from a reaction of $[\text{PdCl}_2(\text{NCMe})_2]$ with a 1:1 mixture of oleylamine and oleic acid as surfactant at RT under 1 bar H_2 for 160 min.

5.3.7 Discussion with $[\text{PdCl}_2(\text{NCMe})_2]$ at Room Temperature : Effect of Surfactant System and Structural Evolution

Experiment 5.3.1 showed that structural change could be induced by controlling the nature of the surfactant system. When a 1:1 ratio of oleylamine and oleic acid was used complex, highly branched nanostructures with a high surface area were formed. This is in contrast to when only oleylamine is used as the surfactant which lead to the formation of symmetrical polyhedral nanostructures. This presents an interesting result as the formation of these types of highly branched nanostructures has not

Chapter 5: Solution Phase Syntheses of Palladium Nanostructures

previously been observed for palladium. In solution phase synthesis, palladium nanostructures typically form as thermodynamically favoured polyhedra structures or 1-D nanorods {Xiong 2007 (b), Choo 2006}. The surfaces of these types of nanostructures are limited to low index facets due to their lower surface-solution interface energy {Xiong 2007 (a), Tian 2008}.

So, by altering the nature of the surfactant system a simple solution phase synthesis for the formation of highly branched, high surface area palladium nanostructures has been developed. These complex morphologies are not thermodynamically favoured which indicates nanoparticle growth is no longer thermodynamically controlled.

By quenching the reaction at 10 minutes (Exp 5.3.2), pod-like nanoparticles were isolated. This was also the first evidence of pod-like morphologies for nanostructured palladium.

The controlled growth of branched or pod-like shapes is well established in polymorphic materials such as CdS and CdSe {Joo 2003, Peng 2002, Asokan 2007}. For CdS and CdSe, pod-like shapes are made through the controlled nucleation of a zinc-blende core followed by the growth of wurtzite phase branches which occurs along the inherently anisotropic c-axis of the hexagonal unit cell. However, this type of polymorphism is not seen in most face centred cubic (*fcc*) metals such as palladium. Thus, while solution methods for producing faceted polyhedra structures are well established for *fcc* materials, the formation of pod-like and highly branched structures is less common and had not previously been achieved for palladium.

When the reaction time was extended to 30 min a secondary type of growth is observed from the pod-like nanoparticles (Exp 5.3.3). This growth occurs in no specific crystallographic direction leading to a broad leaf-like structure {Lou 2006}.

The shape distribution for the highly branched (Exp 5.3.1) and pod-like nanoparticles (Exp 5.3.2) was relatively large, with a wide range of morphologies present. Also, the maximum yield obtained was around 40 %. Therefore, it is apparent that in the current system Fischer-Porter bottle synthesis does not provide precise experimental control. This is most likely due to thermal gradients associated with heat transfer

from the reaction oven to the reaction solution through the bottle. This will cause inhomogeneous nucleation resulting in a range of nanoparticle shapes and sizes.

However, by reducing the pressure of the hydrogen atmosphere to 1 bar the reaction was slowed and greater reaction control was realised. Firstly, this enabled the isolation of structural precursors to the pod-like nanoparticles. These intermediates were largely symmetrical but showed evidence of a structural transition to complex morphologies. The nanoparticle in Figure 18b clearly shows the start of branched growth from a multiply twinned *fcc* icosahedra nanoparticle.

With a low hydrogen pressure leaf like intermediates were isolated at 80 min reaction time (Exp 5.3.5). These conditions were maintained and the reaction time extended to 160 min (Exp 5.3.6). The nanostructures formed after 160 min had a highly branched morphology similar to the nanostructures observed in Exp 5.3.1. However due to a higher degree of reaction control the size distribution was much smaller when formed under a low pressure hydrogen atmosphere.

In each reaction carried out to isolate structural intermediates the supernatant following the first centrifugation step had a yellow appearance with the intensity of the colour decreasing with increasing reaction time. This indicates unreacted precursor and confirms that the experiments were quenched at intermediary stages.

So, the above experiments show that the structural evolution of the highly branched nanostructures occurs through polyhedra nuclei and pod-like intermediates. A secondary type of growth then occurs from the pod-like nanostructures to give the highly branched morphologies. A complete structural characterisation of the pod-like and highly branched nanostructures will be given in the next Chapter along with the proposal of a full growth mechanism.

5.4 Reactions with $[\text{PdCl}_2(\text{NCMe})_2]$: Effect of Surfactant System

The previous experiments showed that the introduction of a carboxylic acid functionality into the surfactant system resulted in complex shaped palladium nanostructures. Therefore, in the following experiments the effect of the nature of the surfactant system on morphology was investigated. To do this the ratio of oleylamine to oleic acid was systematically adjusted. The reactions were all performed under mild conditions which were previously shown to give the sufficient reaction control. Along with Experiments 5.2.4 and 5.3.6 the experiments performed below will give show the effect of oleylamine:oleic acid ratio on the formation of palladium nanostructures. The surfactant ratios used will be 1:0, 3:1, 1:1, 1:3 and 0:1 (oleylamine:oleic acid).

5.4.1: Reaction of $[\text{PdCl}_2(\text{NCMe})_2]$ with a 3:1 mixture of oleylamine and oleic acid as surfactant at RT under 1 bar H_2 for 160 min

In this experiment a ratio of oleylamine to oleic acid of 3:1 was introduced into the reaction solution.

Experimental

25.9 mg (0.1 mmol) of $[\text{PdCl}_2(\text{NCMe})_2]$ was dissolved in 1 mL of toluene in a 10 mL reaction vial. To this was added 0.237 mL (0.75 mmol) of oleylamine and 0.083 mL (0.25 mmol) of oleic acid. This reaction mixture was sonicated until a clear light yellow solution resulted. The vial was suspended in a Fischer-Porter bottle with 10 mL of excess anisole in the bottom of the bottle. The bottle was purged 5 times with hydrogen gas and then filled with 1 bar H_2 . The Fischer-Porter bottle was then left at room temperature for 160 min.

For purification of the sample, methanol was added to flocculate the as synthesised nanoparticles. The solution was centrifuged at 14 000 rpm for collection of the solid nanoparticles. These were subsequently washed by suspending the pellet in toluene and ultrasonication for 5 minutes. Additional methanol was added again to flocculate the nanoparticles followed by centrifuging. The purification process was repeated

once with dichloromethane and a second time with toluene. The resulting purified sample was suspended in toluene for TEM investigation.

Results

Figure 24a shows an EM image of the as synthesised nanoparticles. This sample consisted of nanostructured polyhedra 5 to 10 nm in size and triangle nanoparticles 10 to 12 nm large. The remainder of the nanoparticles have indefinable morphologies due to the emergence of asymmetric growth. Figure 24b shows an SAED which is indexed to the *fcc* palladium crystal structure and Figure 24c shows an EDS which indicates the sample is 100% Pd.

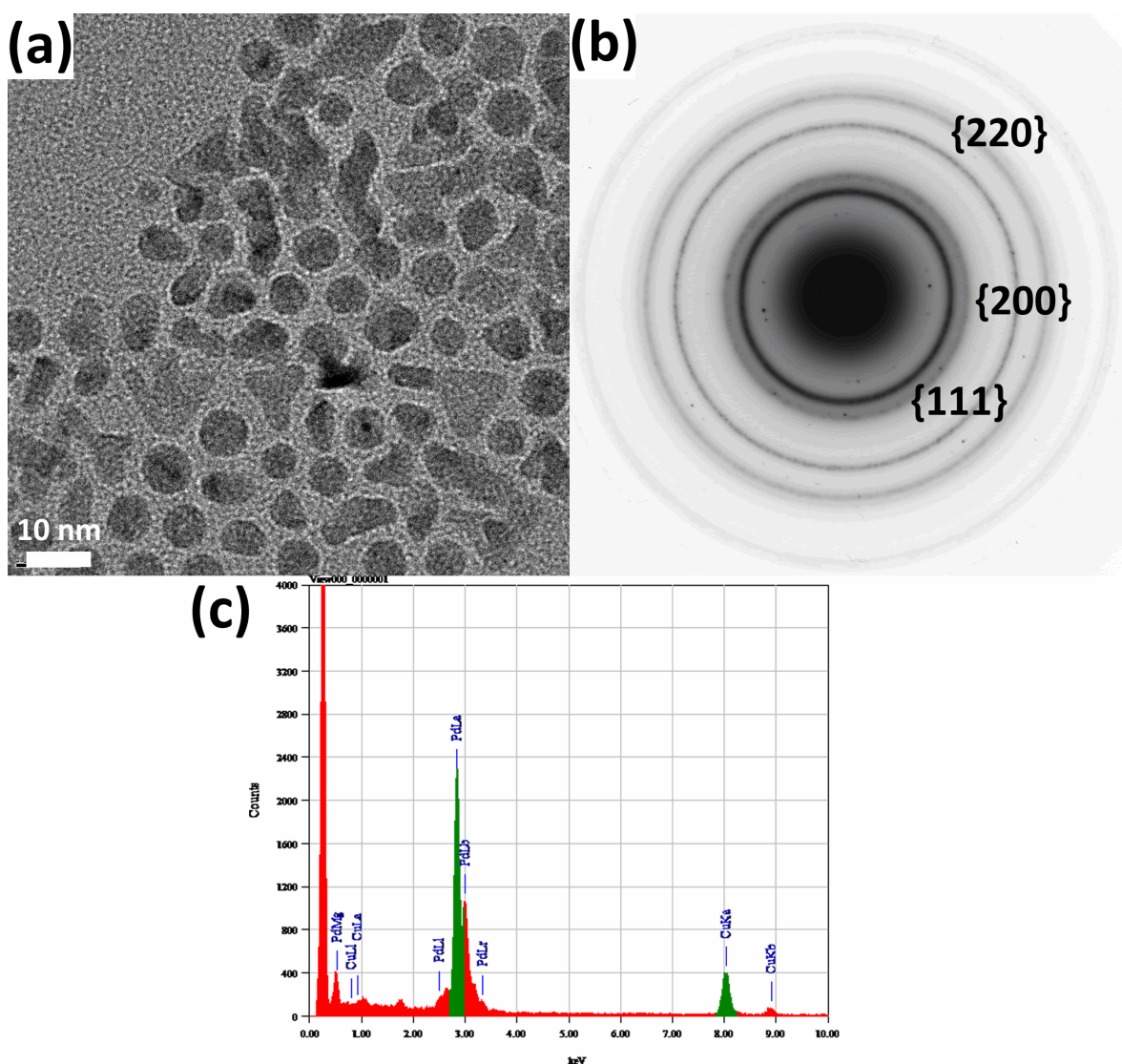


Figure 24. (a) HREM image of palladium nanoparticles formed from Reaction of $[\text{PdCl}_2(\text{NCMe})_2]$ with a 3:1 mixture of oleylamine and oleic acid as surfactant at RT under 1 bar H_2 for 160 min. (b) Corresponding SAED and EDS spectrum (c).

5.4.2: Reaction of [PdCl₂(NCMe)₂] with a 1:3 mixture of oleylamine and oleic acid as surfactant at RT under 1 bar H₂ for 160 min

In this experiment a ratio of oleylamine to oleic acid of 1:3 was introduced into the reaction solution.

Experimental

25.9 mg (0.1 mmol) of [PdCl₂(NCMe)₂] was dissolved in 1 mL of toluene in a 10 mL reaction vial. To this was added 0.079 mL (0.25 mmol) of oleylamine and 0.248 mL (0.75 mmol) of oleic acid. This reaction mixture was sonicated until a clear dark yellow solution resulted. The vial was suspended in a Fischer-Porter bottle with 10 mL of excess anisole in the bottom of the bottle. The bottle was purged 5 times with hydrogen gas and then filled with 1 bar H₂. The Fischer-Porter bottle was then left at room temperature for 160 min. Purification was carried out as above.

Results

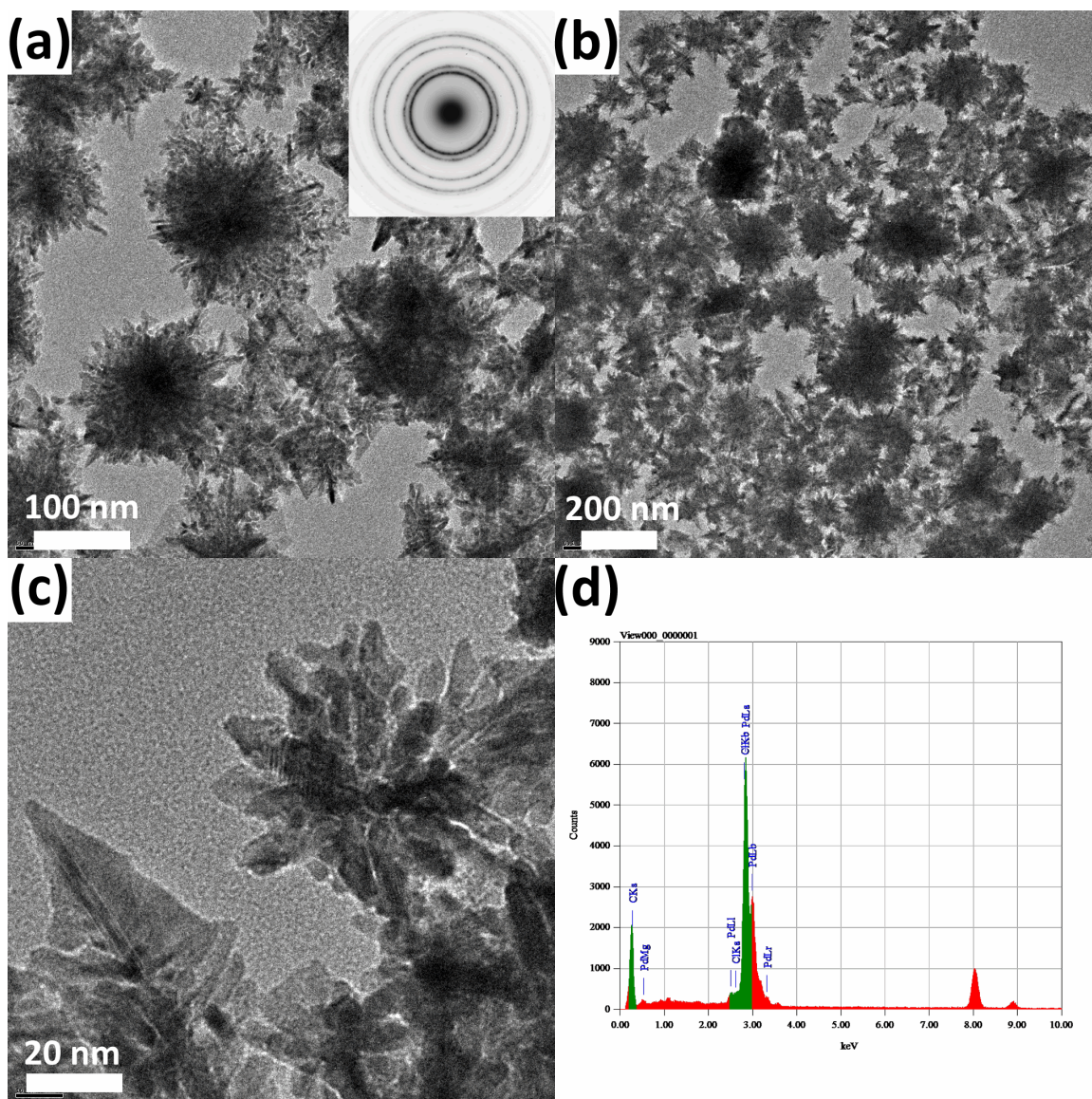


Figure 25. (a) HREM image of palladium nanoparticles formed from reaction of $[\text{PdCl}_2(\text{NCMe})_2]$ with a 1:3 mixture of oleylamine and oleic acid as surfactant at RT under 1 bar H_2 for 160 min with corresponding SAED pattern (inset). (b) Low magnification HREM image. (c) High magnification HREM image of the as synthesised palladium nanostructures and (d) EDS spectrum.

Figure 25a shows an EM image of the as synthesised nanostructures. They are relatively large in size ranging from 160 to 200 nm with extensive branching occurring radially away from a central core. The branches seen on these structures do not extend as far away from the central core as those structures seen in Exp 5.3.6. The inset shows a SAED which is indexed to the *fcc* palladium crystal structure. Figure 25b shows a low magnification image of a typical region of the EM grid. The nanostructures all show a highly branched morphology and have a relatively large polydispersity ranging in size from 80 to 300 nm. Figure 25c shows a high

magnification EM image of the palladium nanostructures. The branched nanostructure in the centre of the image is 70 nm in length and displays extensive branching. However, the branches observed here are shorter and more rounded than those seen in Exp 5.3.6. In the lower left of the image another type of palladium nanostructure is observed. This is 45 nm long and 35 nm at the base and converges to a rounded point to give a 'leaf' like morphology. Fig 25d shows an EDS spectrum which indicates the sample is 100% Pd.

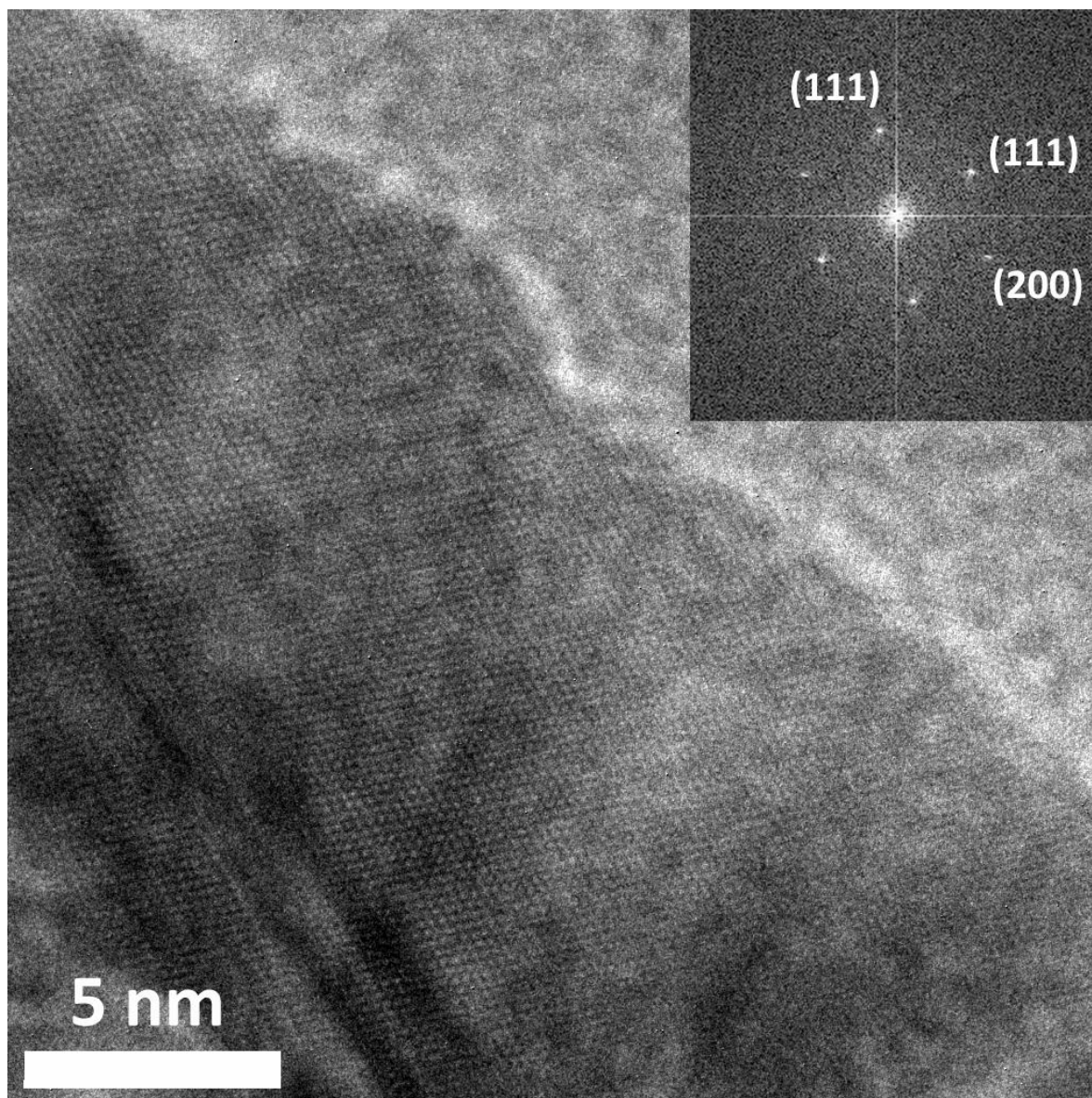


Figure 25. (a) High magnification HREM image of one of the palladium nanostructures branches with associated power spectrum (inset).

Figure 25 shows a high magnification HREM image of the 'leaf' like structure observed in Fig 24c. The fast Fourier transform (FFT) of the image is shown in the inset with spots corresponding to $\{111\}$ and $\{200\}$ reflections. Analysis of the atomic

packing and the power spectrum indicates this structure is being viewed down a $\langle 110 \rangle$ zone axis. The rough edge of the nanostructure indicates the presence of high index facets on the surface edges of the nanostructure. (Chapter 6 contains an in depth HREM analysis of the surface of one of the highly branched palladium nanostructures).

5.4.3: Reaction of $[\text{PdCl}_2(\text{NCMe})_2]$ with oleic acid only as surfactant at RT under 1 bar H_2 for 160 min

In this experiment oleic acid only was used as the organic surfactant for the reaction.

Experimental

25.9 mg (0.1 mmol) of $[\text{PdCl}_2(\text{NCMe})_2]$ was dissolved in 1 mL of toluene in a 10 mL reaction vial. To this was added 0.330 mL (1 mmol) of oleic acid. This reaction mixture was sonicated until a clear dark orange solution resulted. The vial was suspended in a Fischer-Porter bottle with 10 mL of excess anisole in the bottom of the bottle. The bottle was purged 5 times with hydrogen gas and then filled with 1 bar H_2 . The Fischer-Porter bottle was then left at room temperature for 160 min. Purification was carried out as above.

Results

Figure 26a-b show EM images of the as synthesised palladium structures. These are on the micrometre length scale yet still show some evidence of branching. A higher magnification EM image of one of the microstructures is shown in Fig 26b. Lattice planes are visible indicating the product is crystalline and the power spectrum in the inset shows the structure is being viewed down a $\{111\}$ zone axis. A SAED pattern is shown in Fig 26c. The presence of large spots and the absence of complete rings indicates the structure is polycrystalline with relatively large crystal domains. An EDS spectrum (Fig 26d) shows that the product is 100% Pd.

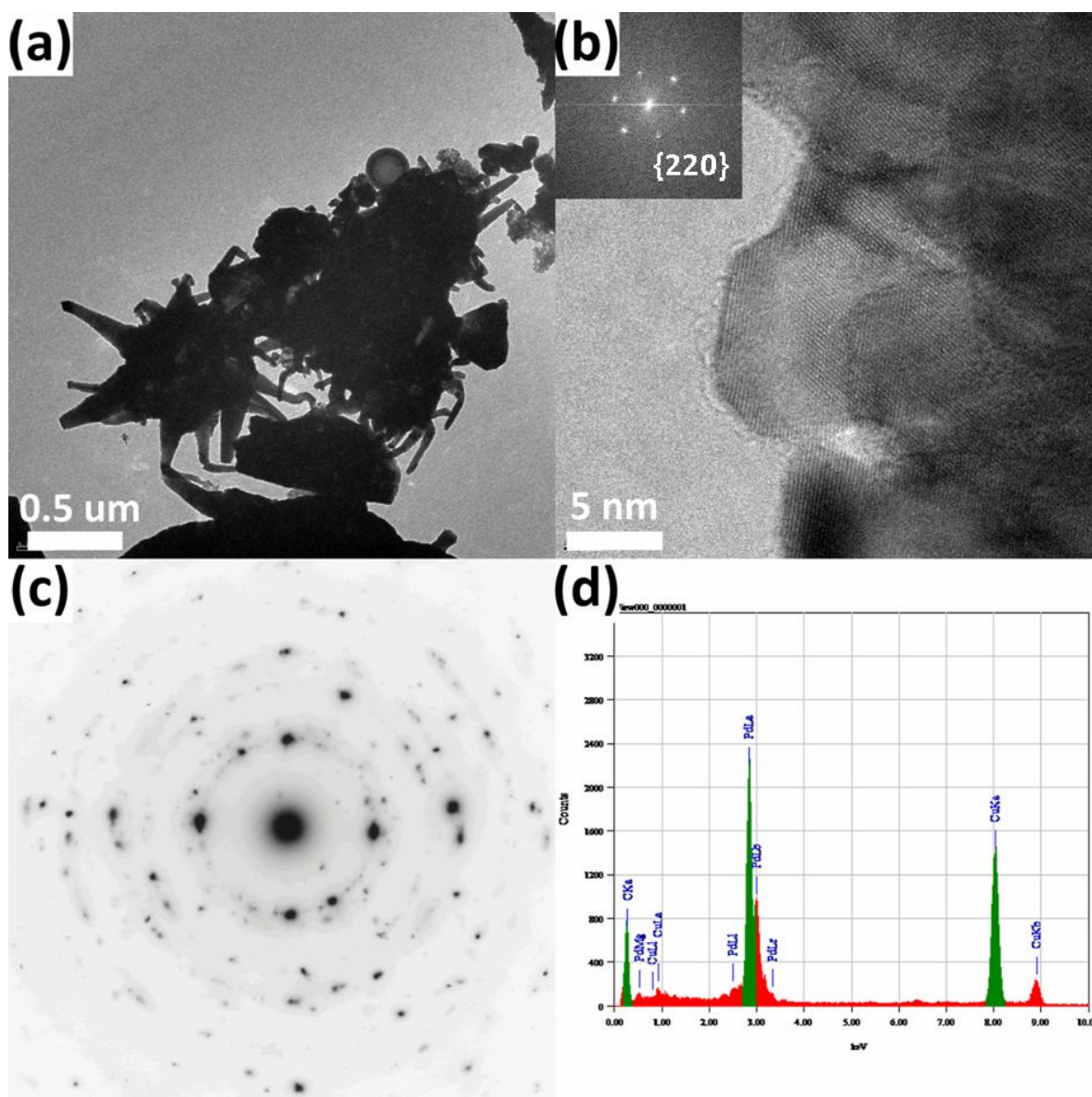


Figure 26. (a) HREM image of palladium nanoparticles formed from reaction of $[\text{PdCl}_2(\text{NCMe})_2]$ with oleic acid only as surfactant at RT under 1 bar H_2 for 160 min. (b) High magnification HREM image and corresponding power spectrum (inset). (c) SAED pattern and (d) EDS spectrum.

5.4.4 Discussion of Reactions with $[\text{PdCl}_2(\text{NCMe})_2]$: Effect of Surfactant System

Along with Exp 5.3.6 and Exp 5.2.4 the above experiments show the influence of the nature of the surfactant system on the morphology of the resulting nanoparticle. When oleylamine only is used small polyhedra nanoparticles result (Fig 11a). A ratio of 3:1 oleylamine to oleic acid gives predominantly polyhedra nanoparticles however there are some nanoparticles with the beginning of complex growth (Fig 24a). A 1:1 ratio of the surfactants gives highly branched palladium nanostructures (Fig 21a).

When the oleic acid concentration is increased to a ratio of 1:3 large nanostructures are formed (Fig 25a-b). They still possess extensive branching however the branches are shorter and more rounded with a smaller aspect ratio. Also, the polydispersity of the product has increased indicating a loss in reaction control. When purely oleic acid is used as the surfactant micrometre sized structures are formed (Fig 26a). So, as the oleic acid concentration is increased we observe the emergence of shape complexity in the resulting nanoparticles.

Purely oleylamine gives symmetrical polyhedral nanoparticles which are thermodynamically favoured morphologies for palladium {Elechiguerra 2006, Berhault 2007}. This indicates that when oleylamine is used as a surfactant growth is occurring under thermodynamically controlled conditions.

When oleic acid was introduced into the surfactant system shape complexity was observed. This indicates that the growth is not as effectively restricted as with purely oleylamine. This is to be expected due to the weak Pd-O binding interaction which will reduce the overall stabilisation of the growing nanoparticle {Ahrland 1958}. The complex, highly branched shapes observed with increased oleic acid concentration are examples of nanostructures grown under kinetic control {Yin 2005}. When purely oleic acid is used, large micrometre crystallites are formed. Presumably oleic acid does not have sufficient stabilising ability to restrict growth to the nanoscale for this system.



Figure 27. Precursor solution containing different ratios of oleylamine to oleic acid and $[\text{PdCl}_2(\text{NCMe})_2]$ in powder form (inset).

Figure 27 shows a photo of five precursor solutions containing $[\text{PdCl}_2(\text{NCMe})_2]$ and varying ratios of oleylamine and oleic acid. When purely oleylamine (far left) is used as the surfactant the precursor solution is clear and colourless. As the oleic acid concentration is increased the precursor solution gains a yellow colour. When purely oleic acid is used (far right) the precursor solution is a bright orange colour. This is the same colour as $[\text{PdCl}_2(\text{NCMe})_2]$ in powder form (inset). Also, the solubility of the precursor decreases with increasing oleic acid concentration. This indicates that there is a ligand exchange process occurring between the precursor and the oleylamine which facilitates dissolution and removes the distinct colour. Presumably the strong Pd-N binding interaction replaces the Cl ligands leading to a partly decomposed precursor. When purely oleic acid is used weak Pd-O binding interaction is not able to displace the Cl ligands.

Previous studies have argued that a strong ligand-metal binding strength will decrease the reactivity of the monomers leading to a high chemical potential in the growth stage {Yu 2003}. These conditions then lead to elongated or complex shapes.

Chapter 5: *Solution Phase Syntheses of Palladium Nanostructures*

In contrast, in the current system, symmetrical polyhedra nanoparticles are formed when a ligand (surfactant) with strong binding characteristics is introduced.

By introducing a weaker binding surfactant the growth conditions shift from thermodynamically controlled to kinetically controlled. This introduces shape complexity therefore an investigation into growth kinetics is required to understand the effect of the surfactant system on nanoparticle shape. A full investigation on the growth kinetics of the various palladium nanostructures was performed at the Stanford Synchrotron Radiation Lightsource at Stanford University, California. These results will be discussed in the following Chapter along with the development of a complete growth mechanism.

5.5 Summary

Palladium nanoparticles with a wide variety of sizes and morphologies have been synthesised through the reaction of organometallic precursors under a hydrogen atmosphere. The experiments were carried out in a pressure reaction vessel (Fischer-Porter bottle) which enabled facile control over the hydrogen pressure and reaction temperature. Organic surfactant molecules were used as stabilisers directing nanoparticle growth.

When the palladium precursor $\text{Pd}(\text{PPh}_3)_4$ was used predominantly small, spherical nanoparticles resulted due to the strong Pd-P binding interaction.

When this precursor was replaced with $[\text{PdCl}_2(\text{NCMe})_2]$ the first evidence of a complex morphology was observed. Here, the organic stabiliser species had a greater influence on the growth of the nanoparticles enabling new morphologies. When $[\text{PdCl}_2(\text{NCMe})_2]$ was reacted at mild reaction conditions a monodisperse sample of multiply twinned polyhedra nanoparticles was formed.

By introducing a second surfactant with weaker binding characteristics into the reaction mixture, highly branched, high surface area palladium nanostructures were formed. These were shown to evolve from multiply twinned *fcc* icosahedra nanoparticles via a pod-like (tripod) intermediate structure. A secondary type of growth then occurred from the tripod nanoparticles to give the highly branched structures.

Experiments involving different ratios of the two surfactant species showed that the nature of the surfactant system directly determines the resulting morphology of the nanostructure.

References

- Ahrland, S., Chatt, J., Davies, N. R., *Quarterly Reviews* **1958**, *12*, 265.
- Ajayan, P. M., Marks, L. D., *Physical Review Letters* **1988**, *60*, 585.
- Asokan, S., Krueger, K. M., Colvin, V. L., Wong, M. S., *Small* **2007**, *3*, 1164.
- Bardaji, M., Vidoni, O., Rodriguez, A., Amiens, C., Chaudret, B., Casanove, M. J., Lecante, P., *New Journal of Chemistry* **1997**, *21*, 1243.
- Berhault, G., Bausach, M., Bisson, L., Becerra, L., Thomazeau, C., Uzio, D., *Journal of Physical Chemistry C* **2007**, *111*, 5915.
- Bradley, J. S., Tesche, B., Busser, W., Masse, M., Reetz, R. T., *Journal of the American Chemical Society* **2000**, *122*, 4631.
- Chaudret, B., *Comptes Rendus Physique* **2005**, *6*, 117.
- Cho, K. S., Talapin, D. V., Gaschler, W., Murray, C. B., *Journal of the American Chemical Society* **2005**, *127*, 7140.
- Choo, H., He, B. L., Liew, K. Y., Liu, H. F., Li, J. L., *Journal of Molecular Catalysis a-Chemical* **2006**, *244*, 217.
- Elechiguerra, J. L., Reyes-Gasga, J., Yacaman, M. J., *Journal of Materials Chemistry* **2006**, *16*, 3906.
- Joo, J., Na, H. B., Yu, T., Yu, J. H., Kim, Y. W., Wu, F. X., Zhang, J. Z., Hyeon, T., *Journal of the American Chemical Society* **2003**, *125*, 11100.
- Kirkland, A. I., Jefferson, D. A., Tang, D., Edwards, P. P., *Proceedings of the Royal Society of London Series a-Mathematical Physical and Engineering Sciences* **1991**, *434*, 279.
- Lim, B., Xiong, Y. J., Xia, Y. N., *Angewandte Chemie-International Edition* **2007**, *46*, 9279.
- Lou, X. W., Yuan, C. L., Archer, L. A., *Chemistry of Materials* **2006**, *18*, 3921.
- Maksimuk, S., Teng, X., Yang, H., *Journal of Physical Chemistry C* **2007**, *111*, 14312.
- Murray, C. B., Norris, D. J., Bawendi, M. G., *Journal of the American Chemical Society* **1993**, *115*, 8706.
- Park, J., Joo, J., Kwon, S. G., Jang, Y., Hyeon, T., *Angewandte Chemie-International Edition* **2007**, *46*, 4630.
- Peng, Z. A., Peng, X. G., *Journal of the American Chemical Society* **2002**, *124*, 3343.
- Penisson, J. M., Renou, A., *Zeitschrift Fur Physik D-Atoms Molecules and Clusters* **1989**, *12*, 113.

Chapter 5: Solution Phase Syntheses of Palladium Nanostructures

Ramirez, E., Jansat, S., Philippot, K., Lecante, P., Gomez, M., Masdeu-Bulto, A. M., Chaudret, B., *Journal of Organometallic Chemistry* **2004**, 689, 4601.

(a) Ren, J., Tilley, R. D., *Small* **2007**, 3, 1508.

(b) Ren, J. T., Tilley, R. D., *Journal of the American Chemical Society* **2007**, 129, 3287.

Son, S. U., Jang, Y., Yoon, K. Y., Kang, E., Hyeon, T., *Nano Letters* **2004**, 4, 1147.

Tian, N., Zhou, Z. Y., Sun, S. G., *Journal of Physical Chemistry C* **2008**, 112, 19801.

Wang, Z. L., *Journal of Physical Chemistry B* **2000**, 104, 1153.

(a) Xiong, Y. J., McLellan, J. M., Chen, J. Y., Yin, Y. D., Li, Z. Y., Xia, Y. N., *Journal of the American Chemical Society* **2005**, 127, 17118.

(b) Xiong, Y. J., Chen, J. Y., Wiley, B., Xia, Y. A., Yin, Y. D., Li, Z. Y., *Nano Letters* **2005**, 5, 1237.

(a) Xiong, Y. J., Xia, Y. N., *Advanced Materials* **2007**, 19, 3385.

(b) Xiong, Y. J., Cai, H. G., Yin, Y. D., Xia, Y. N., *Chemical Physics Letters* **2007**, 440, 273.

Yin, Y., Alivisatos, A. P., *Nature* **2005**, 437, 664.

Yu, W. W., Wang, Y. A., Peng, X. G., *Chemistry of Materials* **2003**, 15, 4300.

Zhang, J. M., Ma, F., Xu, K. W., *Applied Surface Science* **2004**, 229, 34.

Chapter 6. Full Characterisation and Growth Mechanism of Palladium Nanostructures

In this chapter full characterisation of a selection of the palladium nanostructures synthesised in Chapter 3 is presented. This includes a full structural characterisation of the novel palladium tripod nanoparticles through tilting electron microscopy experiments. Structural investigations of a hexagonal platelet, a bipod nanostructure and a multipod nanostructure are also presented.

The kinetics of growth for highly branched palladium nanostructures are then presented through *in-situ* synchrotron XRD experiments. This section will show the effect of temperature and the surfactant system on the kinetics of the reaction and hence the morphology of the resulting nanoparticle.

A full growth mechanism for the formation of the highly branched palladium nanostructures will then be offered based on the above characterisations. Finally, the catalytic and hydrogen absorption properties of the highly branched palladium nanostructures will be presented.

6.1 Super High Resolution Electron Microscopy (SHREM) of Palladium Tripod Nanoparticles

The tripod nanostructures synthesised in Exp 5.3.2 were the first evidence of a pod-like morphology for nanostructured palladium. Due to its highly symmetrical *fcc* crystal structure the emergence of nanoparticles with three fold symmetry is unexpected for palladium. Therefore a full investigation into the nanoparticle structure was required. An understanding of the internal structure is critical to determine the mechanism of nanoparticle growth which will be valuable for future work with all nanostructured *fcc* materials. Therefore these structures were selected for Super High Resolution Electron Microscopy (SHREM) experiments. The following set of SHREM experiments were performed on a JEOL 2200MCO field-emission TEM with double aberration correctors located at Oxford University Department of Materials. SHREM gives a two dimensional image of a three dimensional object. Therefore the information gathered by this technique can be regarded as a 2D projection of the nanoparticle. For this reason certain images may not relate directly to the nature of the nanoparticle surface therefore reference is made to previous SHREM experiments and simulations.

6.1.1 Experiment 1 : SHREM Analysis of a Palladium Tripod viewed down a $\langle 111 \rangle$ Zone Axis

Results

Figure 1a shows an SHREM image of an as synthesised palladium tripod. The nanoparticle consists of a central core with three arms extending away. The atomic packing is visible on all three arms enabling characterization and the lattice planes can be seen to meet at a point in the centre of the tripod. The angle between each arm ranges from 115-126° which agrees with the three fold symmetry associated with a tripod. Each arm shows a twin plane running along its length in the direction of arm growth. The twin plane runs parallel to the $\{220\}$ planes along the long axis of the tripod arm. The tip of the arm exhibits a rounded contour.

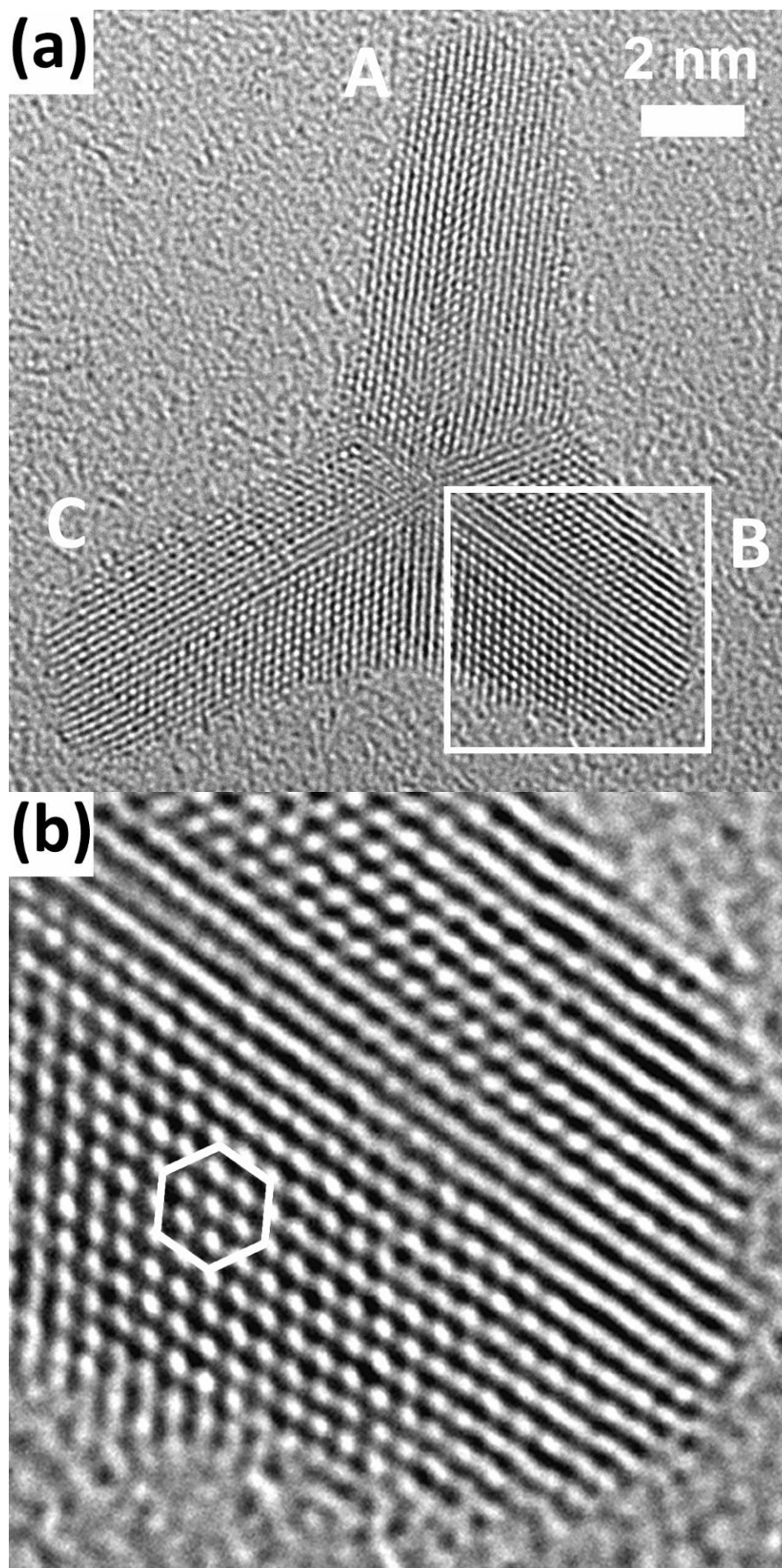


Figure 1. (a) Aberration corrected SHREM image of an as synthesised palladium tripod nanoparticle. (b) High magnification image of the palladium tripod arm as highlighted in Fig 1a. The image clearly shows the atoms in a hexagonal packing arrangement.

The arms labelled A and C are relatively uniform with lengths of 9.0 nm and 8.5 nm and aspect ratios of 2.3 and 2.1 respectively. Arm B is slightly shorter with a length of 6.2 nm and an aspect ratio of 1.3. Figure 1b shows the atomic packing on one of the tripod arms. The hexagonal symmetry is characteristic of $\langle 111 \rangle$ oriented close packed layers of the *fcc* structure.

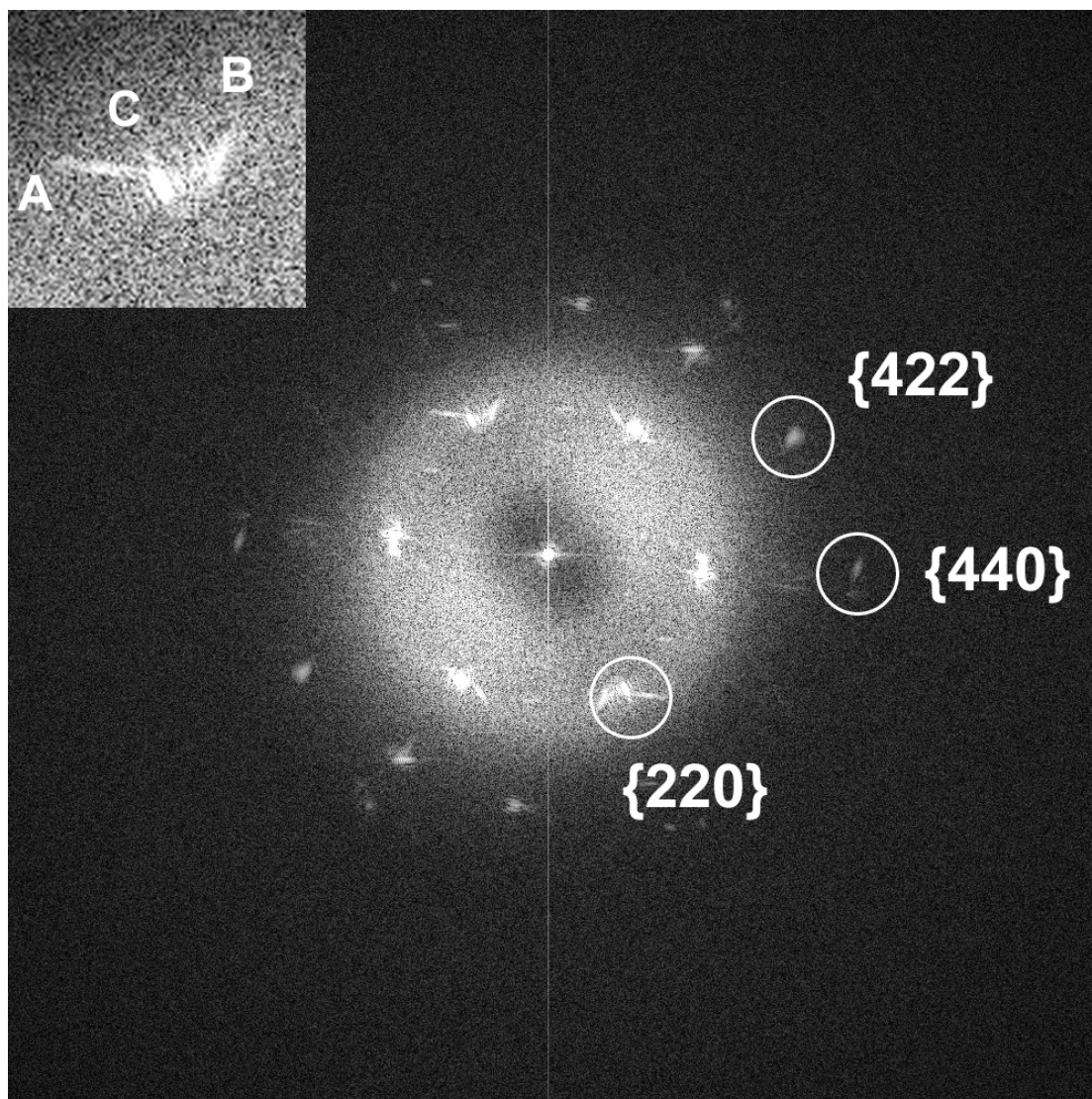


Figure 2. Power spectrum of the nanoparticle shown in Fig 1a. Indexed as the *fcc* palladium metal crystal structure viewed down a $\langle 111 \rangle$ zone axis. The inset shows the streaking in the spots due to crystal defects.

The three fold symmetry of lattice planes observed in the nanoparticle core above has previously been seen for multiply twinned *fcc* icosahedral nanoparticles being viewed down a $\langle 111 \rangle$ zone axis {Fleuli 1988, Penisson 1990, Ling 2009}. Multiply twinned *fcc* icosahedra are widely accepted as a thermodynamically stable morphology for

Chapter 6: Full Characterisation and Growth Mechanism of Palladium Nanostructures

nanostructured palladium {Ling 2009}. The fast Fourier transform FFT of the image of the entire nanoparticle is shown in Fig 2. The spots are arranged in three fold symmetry and can be indexed to the *fcc* palladium metal crystal structure viewed down a $\langle 111 \rangle$ zone axis. Therefore, the centre of the tripod nanoparticle can be characterised as a multiply twinned *fcc* icosahedral nanoparticle with branch growth occurring in three symmetry equivalent directions. From the FFT and analysis of the atomic packing the arm growth can be observed to occur in the $\langle 112 \rangle$ direction.

Further study of the power spectrum yields some interesting features. The $\{220\}$ spots show a streaking pattern that is often observed in electron diffraction patterns of structures possessing crystal defects or an anisotropic morphology {Zurbuchen 2001, Maksimuk 2007}. Streaks are commonly caused by an irregular arrangement of lattice planes; either because the *d* spacing varies or because the planes are randomly displaced, i.e. by a stacking fault, where the streaking occurs perpendicular to the defect. {Champness 2001}. A magnified image of a (220) spot is shown in the inset of Fig 2. Three distinct streaks are present in a three-fold rotational symmetry which correspond to the tripod arms. The streaks occur perpendicular to the twin planes on the tripod arms which indicates they arise due to the crystal defects.

6.1.2 Experiment 2 : SHREM Analysis of Palladium Tripods viewed down a $\langle 112 \rangle$ Zone Axis

When preliminary EM experiments were carried out on the tripod nanoparticles two different projections of the structure were observed (Chapter 5 Fig 15 and Fig 14b). The first has been described above and characterised as being viewing down a $\langle 111 \rangle$ zone axis. Here, a complete investigation of the second projection is given.

Results

Figure 3a shows an as synthesised palladium tripod viewed down a different orientation to the nanoparticle presented in Fig 1a and Fig 15. It has arm lengths between 5.8 and 6.7 nm with aspect ratios of between 1.3 and 1.7. Each arm possesses a twin boundary that runs along its entire length in the direction of growth. The twin boundary on arm A is bound by two facets viewed down a $\langle 110 \rangle$ orientation as determined by analysis of the atomic packing. Arms B and C are both

Chapter 6: *Full Characterisation and Growth Mechanism of Palladium Nanostructures*

bound by one (110) facet and one (111) facet. The (220) lattice planes corresponding to the (111) facet are just visible on the SHREM image.

The FFT of the image of the entire nanoparticle is shown in Fig 3b. The power spectrum is a superposition of spots originating from the different types of facets on the tripod arms.

The spots arise from the $\langle 111 \rangle$ and $\langle 110 \rangle$ zone axes of the tripod arms with additional spots from with the centre of the nanoparticle. From the power spectrum and analysis of the atomic packing the nanoparticle centre can be seen to possess two-fold symmetry and a set of (111) planes and (220) planes . This indicates a $\langle 112 \rangle$ orientation with respect to the beam. This $\langle 112 \rangle$ projection of the central core has previously been seen in HREM analysis of *fcc* icosahedra {Penisson 1989}. This projection is also confirmed through multi-slice HREM simulations where the same two-fold symmetry is observed {Kirkland 1991}. Therefore this palladium tripod nanoparticle also consists of a multiply twinned *fcc* icosahedra nanoparticle with arm growth occurring in three symmetry equivalent directions.

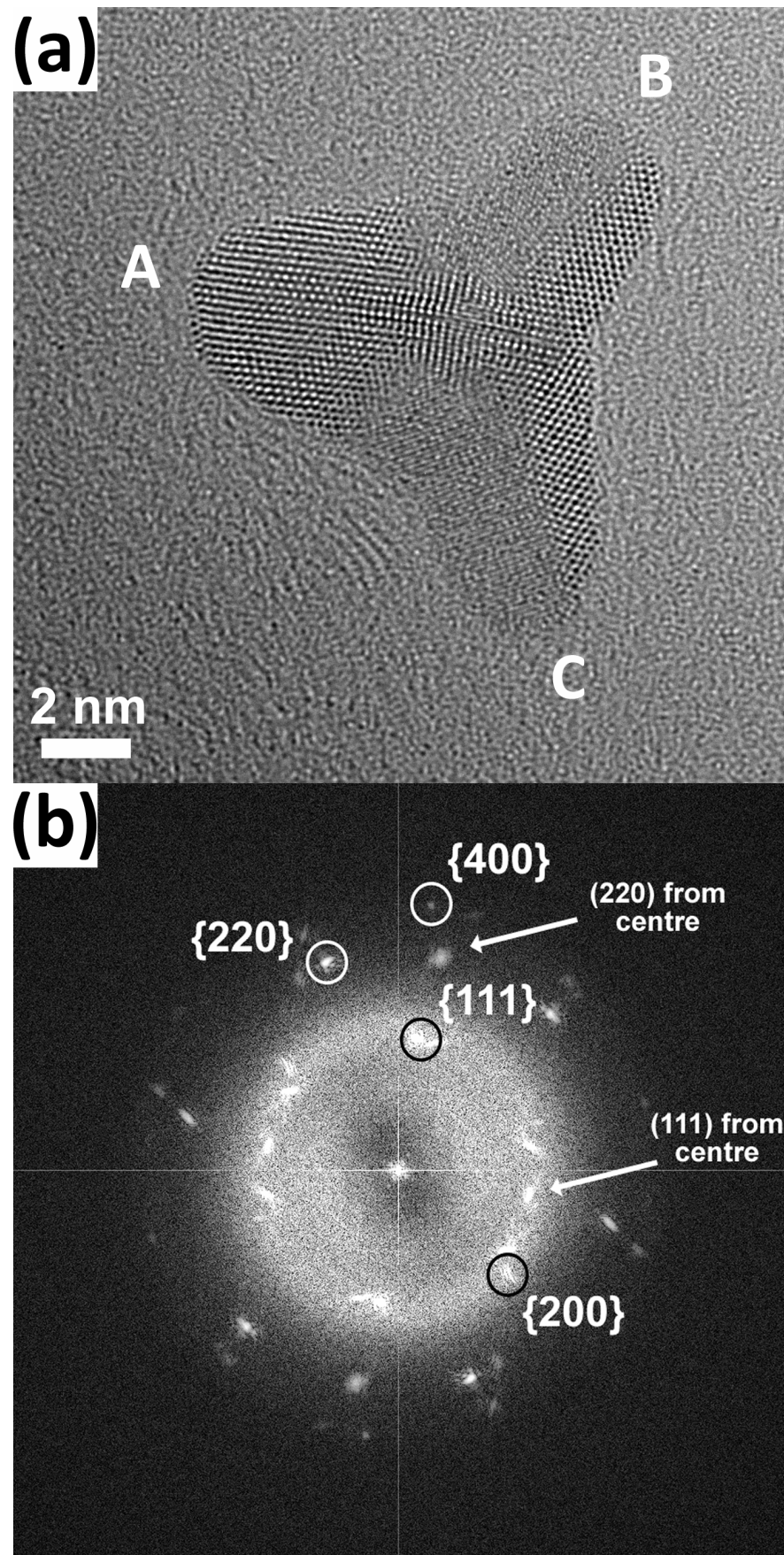


Figure 3. (a) Aberration corrected SHREM image of a Pd tripod nanoparticle viewed down a $\langle 112 \rangle$ zone axis with its corresponding power spectrum shown in (b).

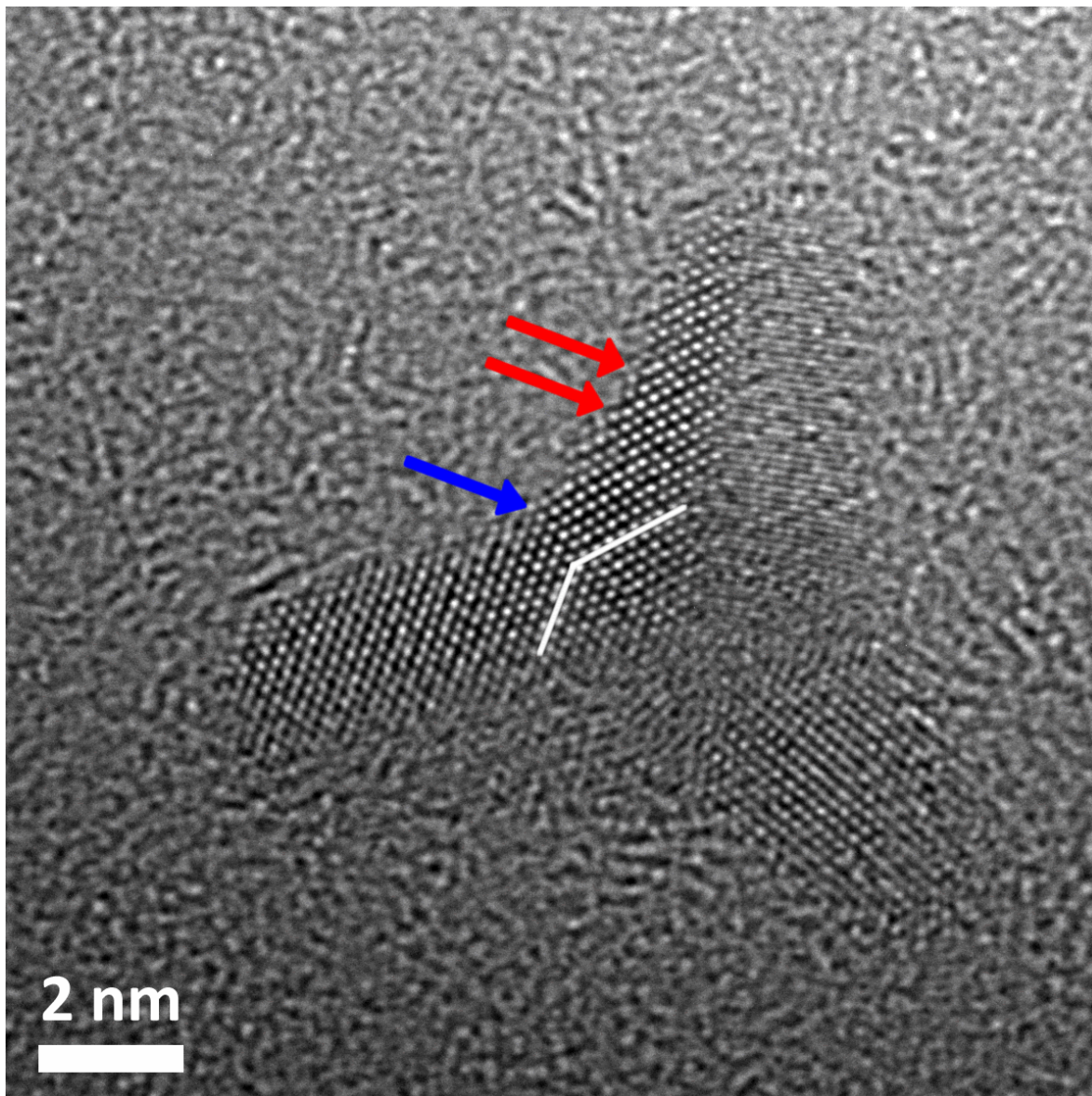


Figure 4. Aberration corrected SHREM image of an as synthesised Pd tripod nanoparticle viewed down a $\langle 112 \rangle$ zone axis. The blue arrow points to a twin plane in the nanoparticle and the red arrows point to step edges on the surface of the tripod arm.

Figure 4 shows a HREM image of another palladium tripod viewed down a $\langle 112 \rangle$ orientation with respect to the central core with the two (110) facets clearly showing atomic packing. A twin boundary is labelled with the blue arrow. The angle between (220) planes across the twin is 138° which is in good agreement with the theoretically expected angle of 141° . Step edges (labelled with red arrows) are visible on the side of the nanoparticle indicating the tripod is terminated by high index facets.

6.1.3 Experiment 3 : SHREM Tilting Experiment

The previous experiments show that the central core of the tripod nanoparticles analysed can be characterised as a multiply twinned *fcc* icosahedra viewed down either a $\langle 111 \rangle$ zone axis (Exp 6.1.1) or a $\langle 112 \rangle$ zone axis (Exp 6.1.2). To confirm that the structure of the tripod is identical in each instance a tilting experiment was carried out on an isolated tripod.

Results

Figure 5a shows the nanoparticle with the specimen stage set to standard viewing conditions. Analysis of the atomic packing and the power spectrum (Fig 5b) indicates the tripod is viewed along a $\langle 111 \rangle$ direction as previously observed in Exp 1. Figure 5c shows the nanoparticle with the specimen stage tilted by 14° in the goniometer x direction and it is clear from the atomic packing that the nanoparticle has changed its orientation in the electron beam. The power spectrum of the entire nanoparticle is shown in Figure 5d and contains a superposition of spots from an *fcc* structure viewed down $\langle 111 \rangle$ and $\langle 110 \rangle$ zone axes. This corresponds to the exposed facets on the tripod arms with additional spots originating from a $\langle 112 \rangle$ orientation of the icosahedral centre of the nanoparticle. Due to heating in the electron beam a reconstruction of the nanoparticle is also seen over the timescale of observation as atoms migrate to lower energy positions that are thermodynamically more stable.

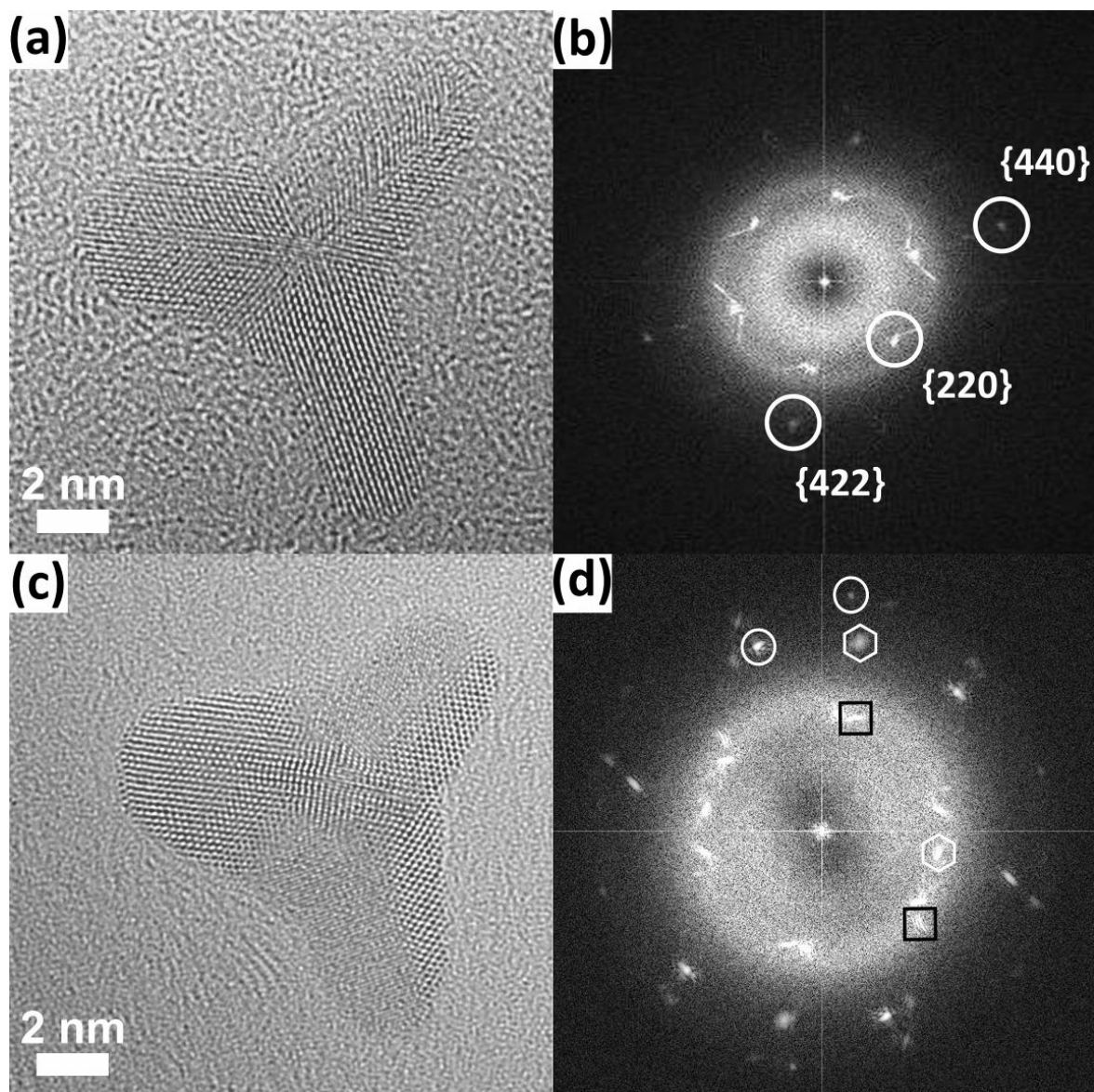


Fig 5. Aberration corrected SHREM images from a tilting experiment performed on an isolated tripod. (a) shows the nanoparticle viewed along a $\langle 111 \rangle$ zone axis with its corresponding power spectrum shown in (b). Panel (c) shows the nanoparticle tilted through 14° with the corresponding power spectrum shown in (d). The spots marked with white circles and black squares correspond to the $\{111\}$ and the $\{110\}$ facets of the tripod arms respectively and the spots marked with white hexagons correspond to the $\{112\}$ orientation of the nanoparticle core.

This experiment shows that a multiply twinned *fcc* icosahedra nanoparticle can give the same projections in the electron micrograph as seen in Exp 6.1.1 and Exp 6.1.2 depending on its orientation with respect to the electron beam. Therefore, the two tripod nanoparticles observed in Exp 6.1.1 and Exp 6.1.2 can be considered as possessing identical internal structure.

6.1.4 Discussion on Super High Resolution Electron Microscopy (SHREM) of Palladium Tripod Nanoparticles

SHREM experiments show that the as synthesised tripod nanoparticles consist of a multiply twinned *fcc* icosahedral core with arm growth occurring in three symmetry equivalent directions. Each arm contains a single twin plane. The icosahedral core is commonly viewed down either a $\langle 111 \rangle$ or $\langle 112 \rangle$ direction with the projection of the lattice planes differing according to its orientation in the beam. Tilting experiments confirm that both orientations are from the same internal structure. A reconstruction of the atoms on the nanoparticle under prolonged beam exposure indicates that this pod-like morphology is kinetically favoured.

Complex nanostructures are not uncommon for *fcc* materials, for example, nanorods have been synthesized for noble metals Au, Ag and Pd {Gai 2002, Chen 2004, Xiong 2007 (b)}. However, these were grown from the elongation of decahedral nuclei and did not show a branched or pod-like structure. Here the first pod-like growth for palladium was observed. Icosahedral nuclei have recently been used to explain the formation of pod like structures in platinum, but direct evidence for the morphology of the nuclei was not provided {Maksimuk 2007}. Therefore the first direct evidence of pod-like growth from icosahedral nuclei for any *fcc* metal is provided here.

6.2 Super High Resolution Electron Microscopy (SHREM) of Other Interesting Morphologies

Along with the tripod nanostructures, palladium nanoparticles of other interesting morphologies were formed. Three types were selected for SHREM experiments; a hexagonal platelet nanoparticle, a four-armed multipod nanoparticle and a bipod nanoparticle.

6.2.1 Experiment 4 : SHREM Analysis of Palladium Hexagonal Platelet

In this experiment a palladium nanoparticle with a six-fold symmetry hexagonal platelet morphology was isolated and examined. Hexagonal platelets have previously been synthesised for palladium however an investigation into their structure is of interest due to the nature of twinning {Xiong 2005 (a)}.

Results

Figure 6a shows a SHREM image of the as synthesised hexagonal platelet nanoparticle. It shows six-fold symmetry with rounded growth at each of the six vertices. The power spectrum from FFT analysis is shown in Fig 6b and contains six {220} spots in three fold symmetry. Therefore the nanoparticle can be indexed as possessing the *fcc* palladium crystal structure viewed down a $\langle 111 \rangle$ zone axis.

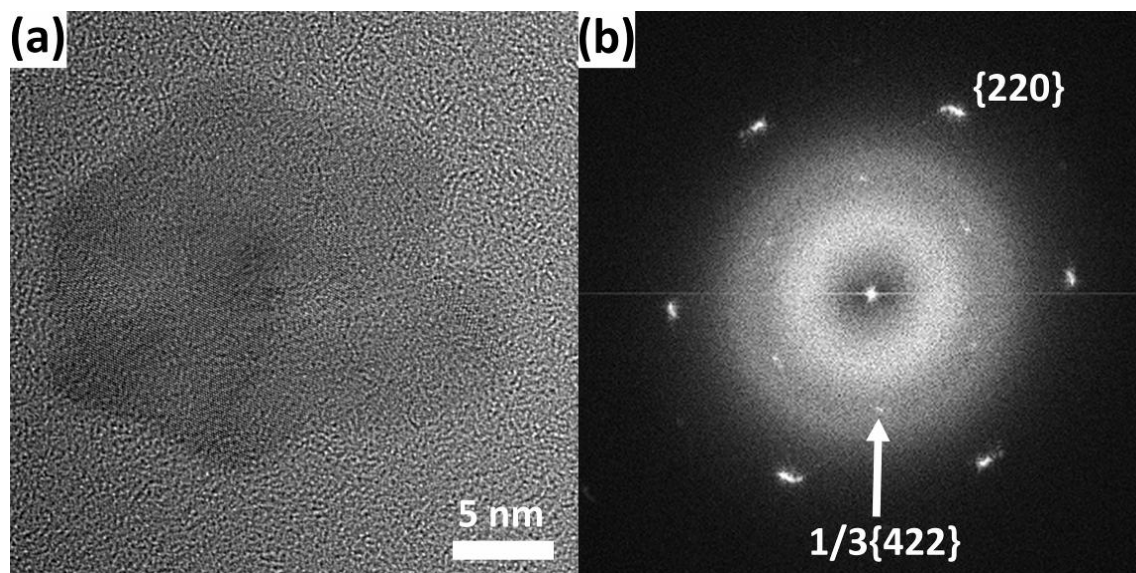


Figure 6. TEM image of an as synthesised Pd hexagonal platelet type nanoparticle (a) and its corresponding power spectrum (b). The power spectrum shows forbidden $1/3\{422\}$ reflections which are indicative of a single (111) twin boundary running parallel to the base of the nanoparticle.

The spots in the power spectrum labelled $1/3\{422\}$ are commonly seen for hexagonal platelet nanoparticles with the *fcc* crystal structure {Salzemann 2005, Xiong 2005 (a)}. These are usually forbidden reflections for *fcc* but arise due to a single (111) twin plane that runs parallel to the base of the nanoparticle {Germain 2003}. Therefore the hexagonal platelet observed here is bound by two (111) facets and contains a single (111) twin defect along its basal plane.

6.2.2 Experiment 5 : SHREM Analysis of Palladium Multipod

In this experiment the structure of an isolated palladium multipod nanoparticle with four arms was investigated using SHREM. Just as the palladium tripod nanoparticle was the first evidence of a pod-like morphology for nanostructure palladium, this nanoparticle is the first evidence of a multipod morphology. Therefore an investigation into its internal structure is required.

Results

Figure 7a shows an SHREM image of the as synthesised palladium multipod. It possess four arms which range in size from 10 to 12 nm with aspect ratios between 1.6 and 3. Analysis of the atomic packing of the multipod arms shows (111) and (200) lattice planes indicating a (110) terminated facet on each of the arms.

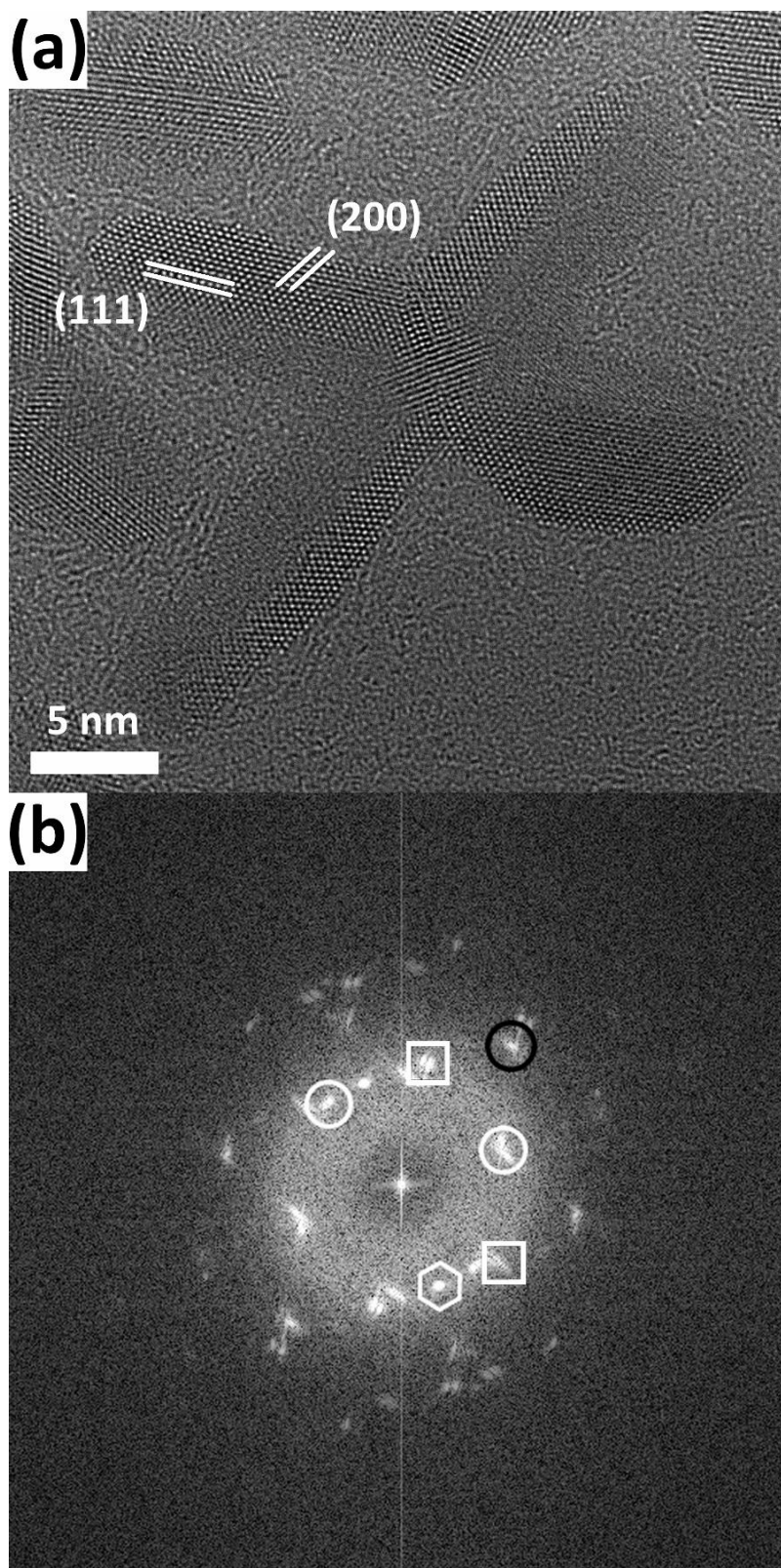


Figure 7. Aberration corrected SHREM image of an as synthesised Pd multipod nanoparticle viewed down a $\langle 112 \rangle$ zone axis (a) and its corresponding power spectrum (b). The spot marked with a white hexagon corresponds to the (111) lattice planes in the central core of the nanoparticle. The spots marked with white circles and squares correspond to the (111) and (200) lattice planes of the (110) terminated facets respectively. The spots marked with black circles correspond to (220) lattice planes originating from a (111) terminated facet on the other side of the twin plane.

Each arm possesses a (111) twin plane extending in the direction of growth. The arms are in a cross formation with the obtuse angle between them 114° . This is close to the angle between the arms of a tripod nanoparticle which indicates some structural similarities. An FFT is shown in Fig 7b which enables full characterisation of the nanoparticle. The spots marked with a white hexagon corresponds to (111) lattice planes in the central core of the nanoparticle. This is characteristic of a $\langle 112 \rangle$ oriented multiply twinned *fcc* icosahedra {Penisson 1989}. The spots marked with white circles and squares correspond to the (111) and (200) lattice planes of the (110) terminated facets respectively. The spots marked with black circles correspond to (220) lattice planes originating from a (111) terminated facet on the other side of the twin plane. Therefore, the nanoparticle can be characterised as possessing a multiply twinned *fcc* icosahedra core in a $\langle 112 \rangle$ orientation with arm growth extending in four symmetry related directions. Each arm contains a (111) twin plane and is terminated by one (110) facet and one (111) facet. This is isostructural with the palladium tripod nanoparticle examined in Exp 2 but with the addition of another arm. From looking at the orientation of the arms with respect to the lattice planes on the nanoparticle core the multipod can be seen to arise due to a 'split' in the upper arm of the tripod.

6.2.3 Experiment 6 : SHREM Analysis of Palladium Bipod

In this experiment a palladium bipod nanoparticle was isolated and examined. Two-dimensional nanostructures are relatively common for palladium however these are usually formed through the elongation of decahedral or cubic nanoparticles into nanorods or nanobars respectively {Xiong 2007 (a), Xiong 2007 (b)}. Therefore, the bipod morphology observed in the current experiments is a new type of two-dimensional structure for nanostructured palladium. Note, this experiment was performed at VUW on a JEOL 2010 operated at an acceleration voltage of 200 keV.

Results

Figure 8a shows an HREM image of an as-synthesised palladium bipod nanoparticle 30 nm long with an aspect ratio of 4. Analysis of the atomic packing shows that the resolved facet is (110) terminated. The power spectrum is shown in the inset and confirms this orientation. The bipod possesses a (100) twin plane running its entire length, this is in contrast to the tripod arms which possess a (111) twin plan (see Exp 2). Each end of the bipod extends in a $\langle 110 \rangle$ direction.

The overall shape of the nanoparticle is unusual as it has a central 'hump' with an undulating surface along the length of the nanoparticle. This indicates that the structure of the bipod is different to that previously observed for 2D palladium nanostructures. Unfortunately however, the bipod nanoparticles were not examined using SHREM and the resolution limit of the electron microscope at VUW was not sufficient to fully investigate the internal structure. Therefore the structure of the palladium bipod nanoparticle is still unknown and requires additional experimentation.

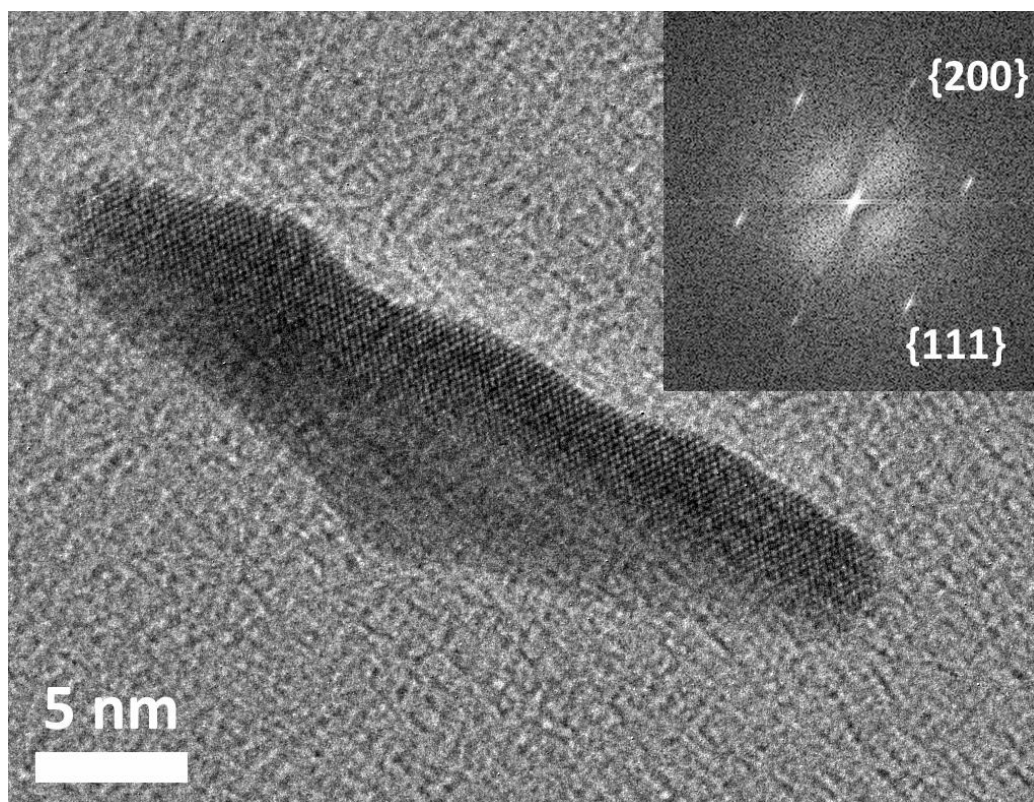


Figure 8. High magnification TEM image of an as-synthesised palladium bipod nanoparticle and its corresponding power spectrum (inset).

6.3 *In-Situ* Synchrotron X-ray Diffraction Studies on the Growth of Palladium Nanostructures

By careful manipulation of reaction conditions various sizes and morphologies of palladium nanostructures have been produced (see Chapter 3). These include thermodynamically favoured polyhedra nanoparticles as well as pod-like and highly branched nanostructures which are examples of morphologies not grown under thermodynamic control (i.e., kinetically controlled). It was shown that the nature of the surfactant system was directly involved in determining the morphology of the resulting nanostructures. This indicates that the surfactant system is also directly involved in controlling the kinetics of the reaction. Therefore an insight into the specific growth kinetics, and how these are effected by the surfactant system, is required.

To probe the kinetics of growth for palladium nanostructures, *in-situ* synchrotron X-ray diffraction (XRD) experiments were carried out at Stanford Synchrotron Radiation Lightsource (SSRL). Since it is difficult to gain information on growth kinetics with post synthetic characterisation techniques, *in-situ* XRD was needed as a method that can measure structural dynamics in real time.

In this section the effect of temperature and the nature of the surfactant system on the kinetics of the growth of palladium nanostructures is investigated using this technique.

Experimental – Synchrotron XRD Setup

Experiments were performed at the Stanford Synchrotron Radiation Lightsource (SSRL) on BL7-2 in a specially made reaction cell shown in Fig 9. The cell was developed by Soshan Cheong and Alan Rennie of VUW. The cell was 30 mm high and 20 mm wide and was placed in a ceramic heating block on the beamline. It contained a circular reaction chamber 5 mm in diameter and 1 mm thick which was aligned with the beam. The cell windows were made from X-ray transparent Kapton (polyimide) film. Fifty microlitres of reaction solution was injected into the reaction chamber which was then filled with 2 bar H₂. The experiments were conducted using

Chapter 6: Full Characterisation and Growth Mechanism of Palladium Nanostructures

radiation of $\lambda = 1.0 \text{ \AA}$ (12.4 keV). Diffractograms were collected over the Pd(111) peak between 2θ values of 18° and 22° , using step scans of $0.02^\circ/\text{step}$. Growth of the fcc Pd(111) diffraction peak was observed and monitored every 300 s, for 70 min.

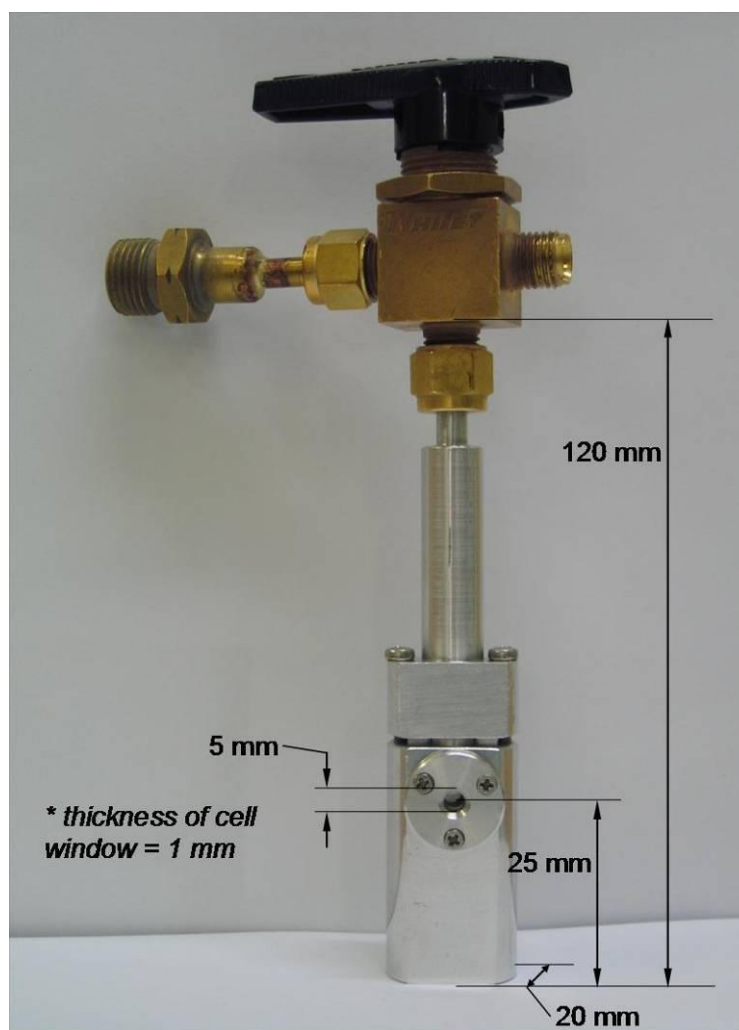


Figure 9. *In-situ* reaction cell for Synchrotron XRD experiments.

6.3.1 Experiment 7 : *In-situ* Synchrotron X-ray Diffraction on the Growth of Highly Branched Palladium Nanostructures – Effect of Temperature

In this set of experiments the effect of temperature on the kinetics of growth of the highly branched nanostructures was investigated. The experiments were performed with a surfactant system of 1:1 oleylamine and oleic acid as this surfactant ratio gave the most uniform product of complex nanostructures (see Exp 5.3.2).

Experimental

25.9 mg (0.1 mmol) of $[\text{PdCl}_2(\text{NCMe})_2]$ was dissolved in 1 mL of toluene. To this was added 0.165 mL (0.5 mmol) of oleylamine and 0.158 mL (0.5 mmol) of oleic acid. This reaction mixture was sonicated until a clear yellow solution resulted. Fifty microlitres of the reaction solution was injected into the reaction cell which was then purged and filled with 2 bar H_2 . The reaction cell was then placed on the ceramic heating block which was preheated to 25 °C.

This experiment was then repeated at 35 °C, 50 °C and 70 °C.

Results

Figure 10 shows the (111) reflection of palladium tracked over the course of a typical reaction displaying the formation of a crystalline product. The measured diffraction signal is from crystalline nanostructures in solution as there was no deposition of product on the cell window at the completion of the reaction. Fig 10 shows the evolution of the crystalline product grown at 25 °C and Figures 11-13 show the growth at 35 °C, 50 °C and 70 °C respectively. At 25 °C there is a relatively low yield in crystalline product. The yield increases as the temperature is increased except for the reaction performed at 70 °C where there is another decrease.

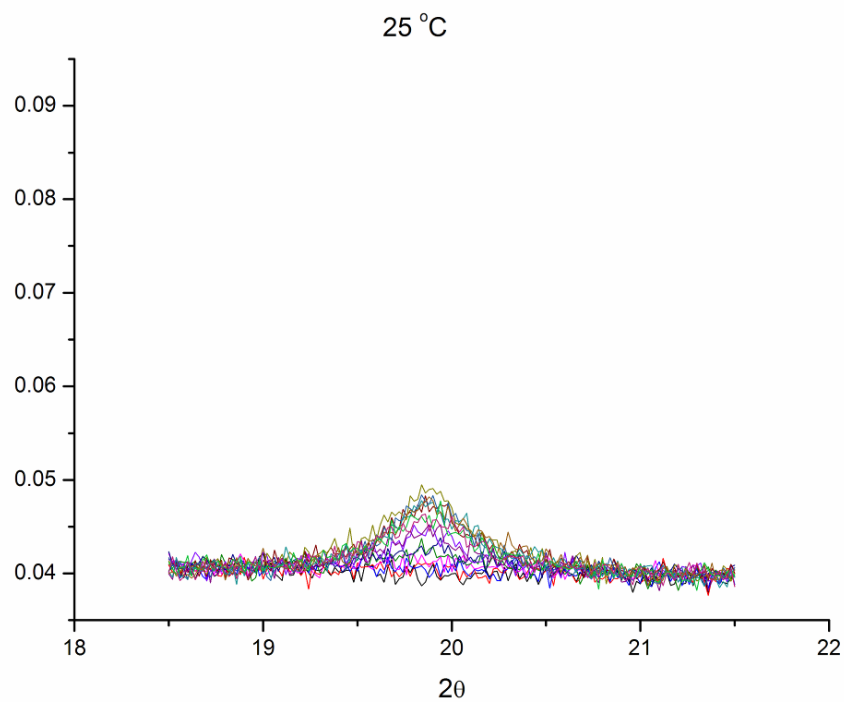


Figure 10. Plot showing the increase in the (111) reflection of palladium metal when nanoparticles were grown at 25 °C.

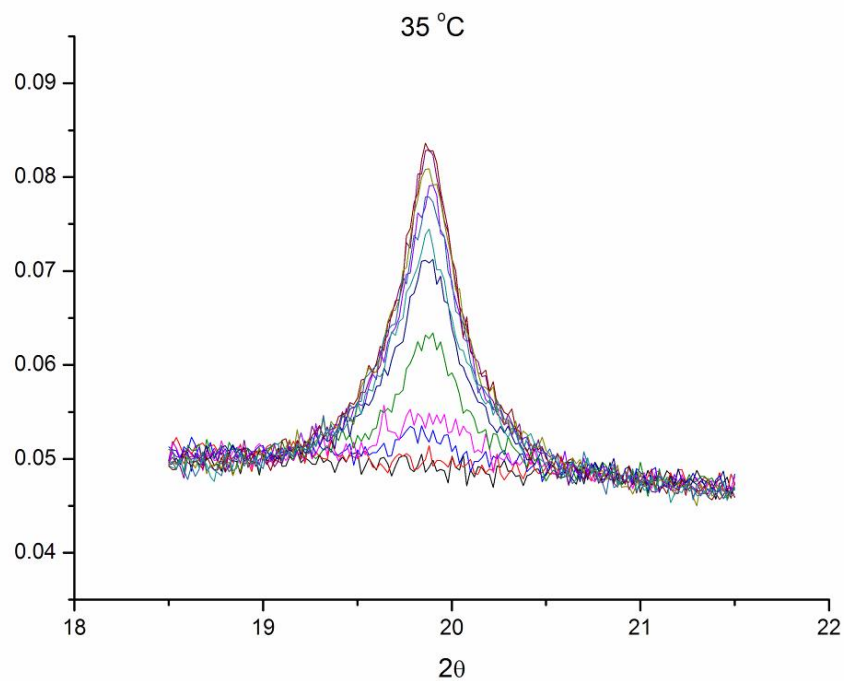


Figure 11. Plot showing the increase in the (111) reflection of palladium metal when nanoparticles were grown at 35 °C.

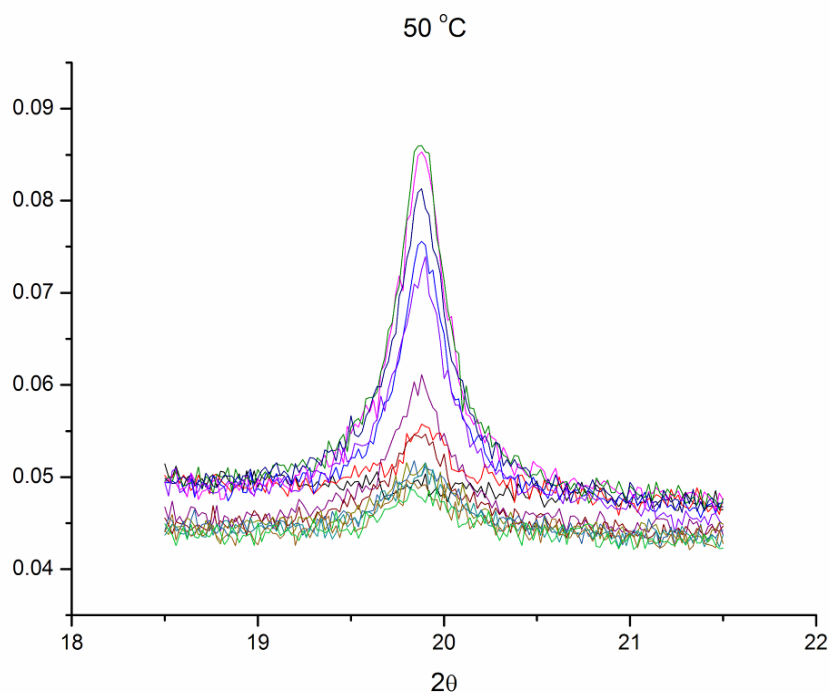


Figure 12. Plot showing the increase in the (111) reflection of palladium metal when nanoparticles were grown at 50 °C.

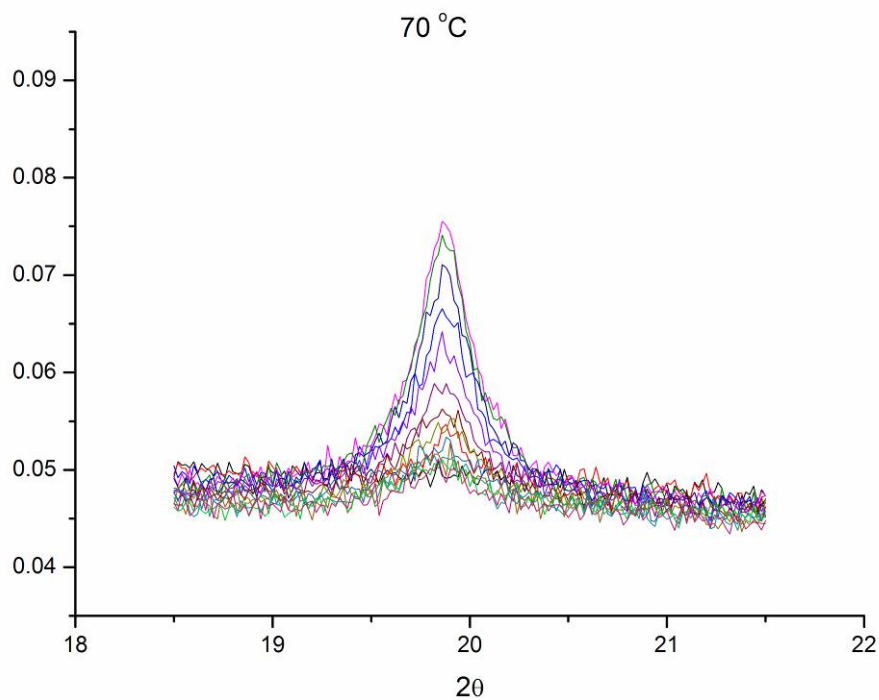


Figure 13. Plot showing the increase in the (111) reflection of palladium metal when nanoparticles were grown at 70 °C.

To gain information on the difference in reaction kinetics for the four different temperatures chosen the peak area was plotted against elapsed reaction time (Fig 181

Chapter 6: Full Characterisation and Growth Mechanism of Palladium Nanostructures

14). Each reaction showed an increase in peak area corresponding to the formation of crystalline palladium. The lattice parameter was calculated as 3.89 Å for each reaction which is consistent with bulk palladium. The lattice parameter is expected to decrease with decreasing nanoparticle diameter however the size of the nanostructures formed here are large enough to possess a lattice parameter close to the bulk {Qi 2002, Qi 2005}. Each plot reaches a maximum before the nanoparticles grow too large to remain in suspension and settle out of the beam path leading to a decrease in peak area. The time taken to reach a maximum area is plotted in Fig 15 for the four reaction temperatures. This plot clearly shows a decrease in the time taken to reach a maximum peak area.

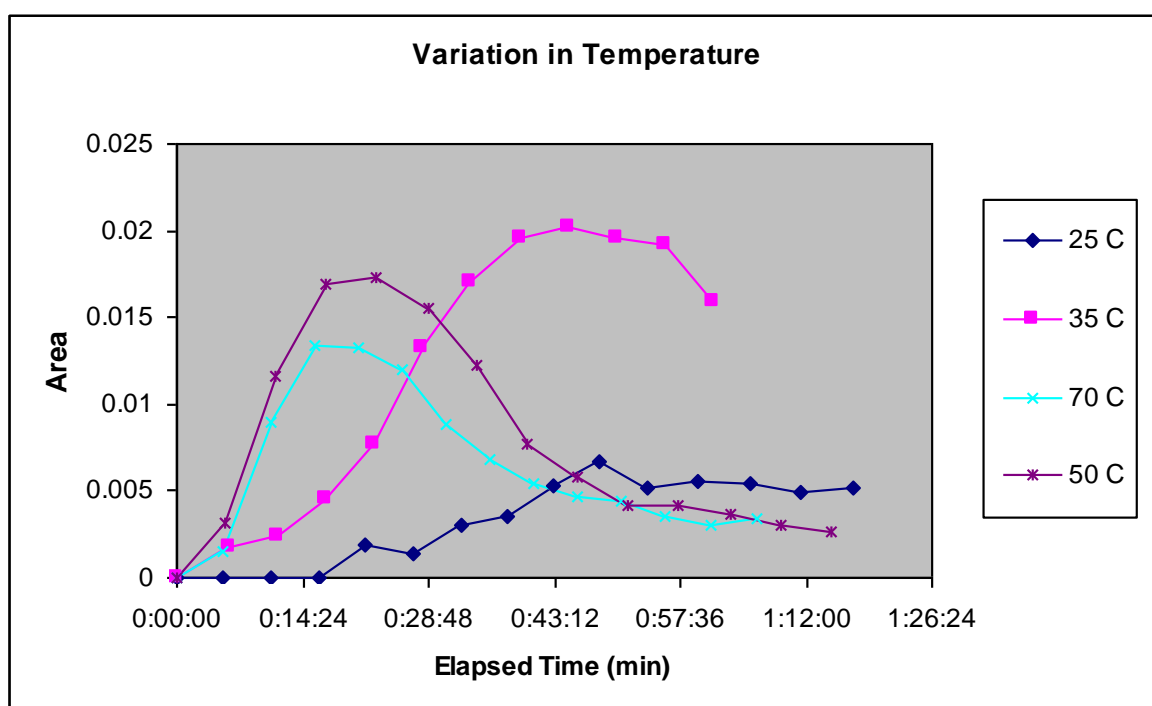


Figure 14. Peak area plotted against reaction time for palladium nanoparticles grown at different reaction temperatures.

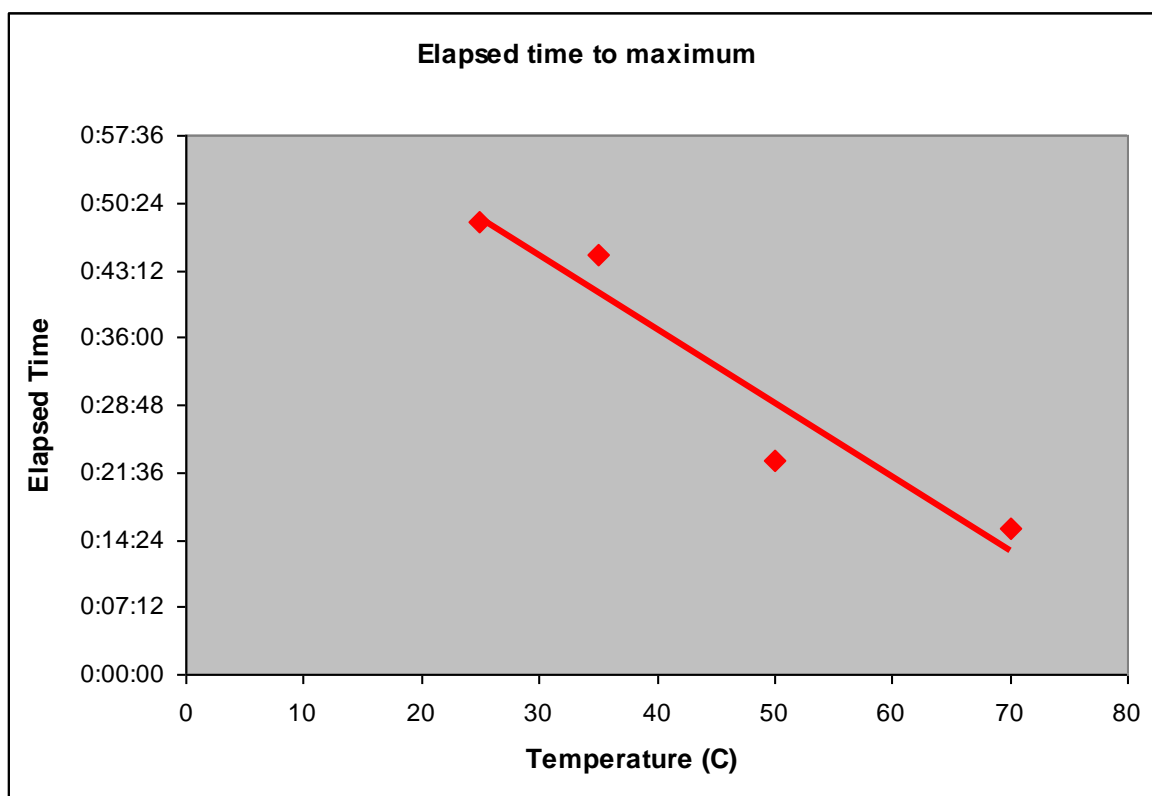


Figure 15. Plot showing the increase in the (111) reflection of palladium metal when nanoparticles were grown at 70 °C.

Figure 16 shows the grain size as calculated by the Scherrer equation using the full width at half maximum (FWHM). The nanostructures grown at 25 °C had an average grain size of around 7.5 nm. This remained relatively constant throughout the experiment, however due to peak broadening and uncertainty in the measurements, particularly at the initial reaction times when the diffraction peak is at its weakest and broadest, there may be some unobserved variation. For the 35 °C, the grain size grows from 8 nm at 10 min reaction time to 10 nm at 20 min reaction time. This then remains constant for the remainder of the reaction. As the temperature was increased to 50 °C different behaviour was observed. The grain size at the early stages of the reaction was ~ 14 nm. This steadily decreased to a 9 nm grain size at 50 min where it remained constant till the reaction completion. A similar behaviour was observed for the 70 °C reaction. The grain size was ~ 12 nm in the early stages of the reaction, lowering to 10 nm after ~ 30 min.

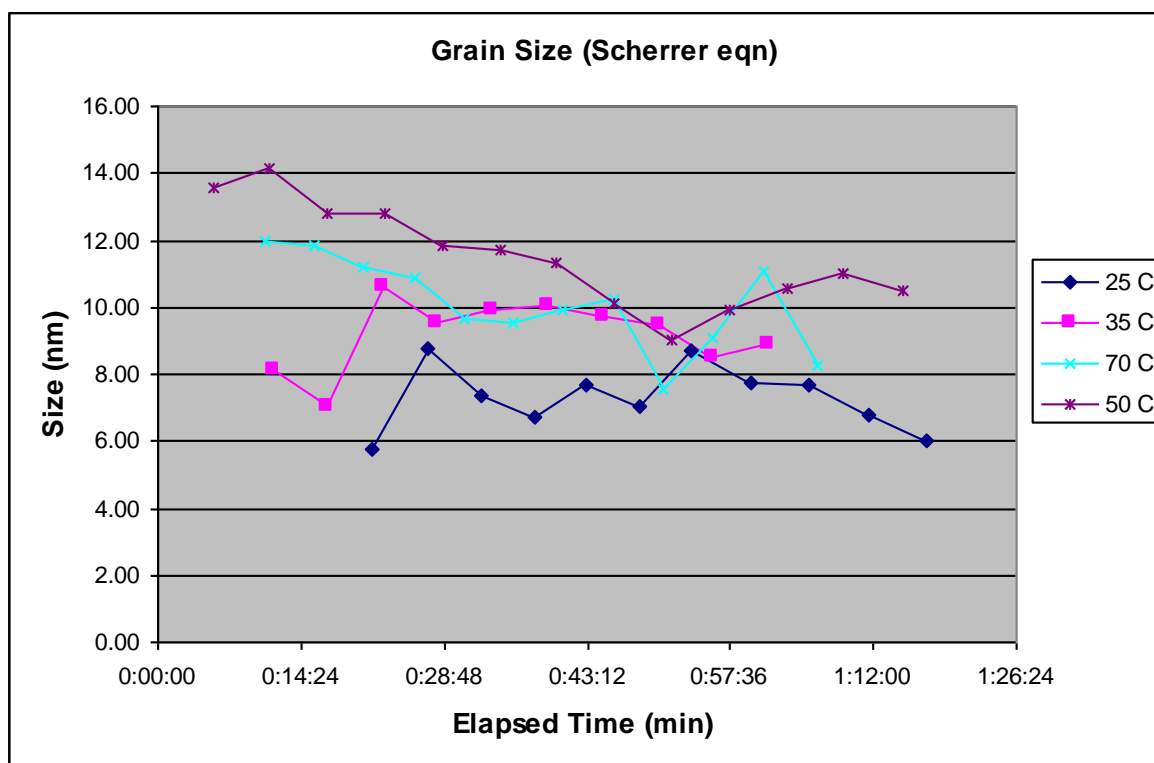


Figure 16. Real time tracking of the grain size of palladium nanoparticles when grown at differing temperatures as calculated by the Scherrer equation.

6.3.2 Experiment 8 : *In-situ* Synchrotron X-ray Diffraction on the Growth of Highly Branched Palladium Nanostructures – Effect of Surfactant Ratio

In the following set of experiments the reaction kinetics for the formation of various palladium nanoparticle morphologies was investigated. This was done by varying the nature of the surfactant system as in Sections 5.3 and 5.4. Oleylamine and oleic acid were introduced in different ratios; 1:0, 3:1, 1:1, 1:3 and 0:1. To ensure that the timescale of the reaction better suited synchrotron experiments the cell temperature was raised to 35 °C; 10 °C above that used to form the nanoparticles used in Fischer-Porter bottle synthesis. This led to a slight decrease in reaction times when compared to previous experiments performed in the Fischer-Porter bottle.

Experimental

25.9 mg (0.1 mmol) of $[\text{PdCl}_2(\text{NCMe})_2]$ was dissolved in 1 mL of toluene. To this was added 10 equivalents of total surfactant in varying ratios. This reaction mixture was sonicated until a clear solution resulted. Fifty microlitres of the reaction solution was injected into the reaction cell which was then purged and filled with 2 bar H_2 . The

Chapter 6: *Full Characterisation and Growth Mechanism of Palladium Nanostructures*

reaction cell was then placed on the ceramic heating block which was preheated to 35 °C.

Five experiments were carried out in these conditions corresponding to oleylamine and oleic acid in different ratios; 1:0, 3:1, 1:1, 1:3 and 0:1.

Results

Figures 17-21 show the (111) reflection of palladium tracked over the course of each reaction displaying the formation of a crystalline product. The measured diffraction signal is from crystalline nanostructures in solution as there was no deposition of product on the cell window at the completion of the reaction. The lattice parameter was calculated as 3.89 Å for each reaction which is consistent with bulk palladium. Again, the size of the nanostructures formed here are large enough to possess a lattice parameter close to the bulk {Qi 2002, Qi 2005}. Figure 17 shows the reaction progression when purely oleylamine is used as the surfactant. Figures 18-21 show the reaction progression for oleylamine to oleic acid ratios of 3:1, 1:1, 1:3 and purely oleic acid respectively. The overall reaction yield increases with an increase in oleic acid concentration to a maximum with a 1:1 ratio. The reaction yield then decreases for the 1:3 and 0:1 surfactant ratios. When purely oleic acid was used as the surfactant system a second peak emerged after ~ 14 min reaction time. This had a 2θ value of 19.21 which corresponds to a lattice parameter of 4.02 Å, a 3.34 % increase. This indicates the emergence of the β phase of palladium hydride.

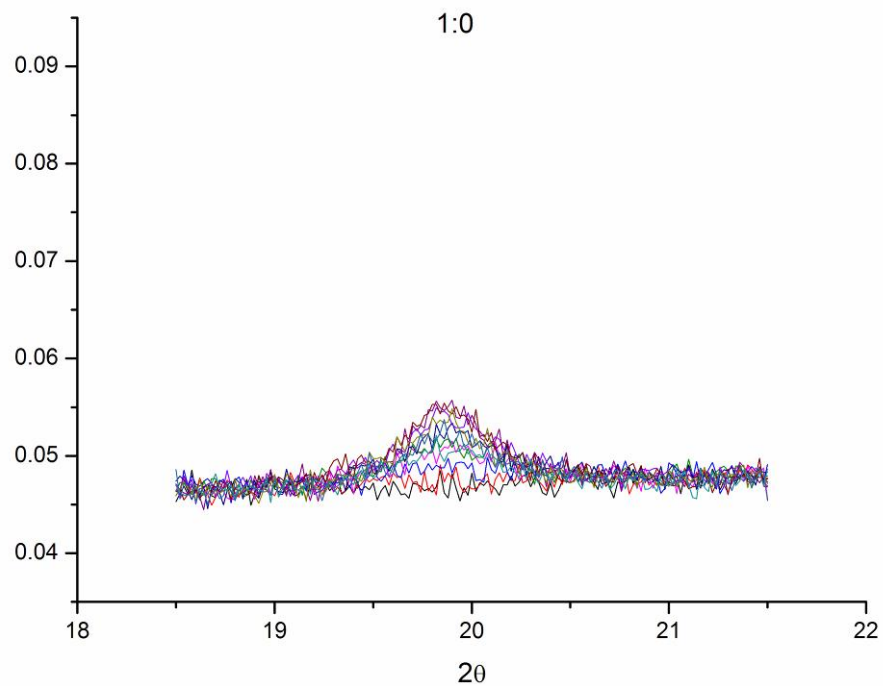


Figure 17. Plot showing the increase in the (111) reflection of palladium metal when nanoparticles with a surfactant ratio of 1:0 oleylamine to oleic acid at 35 °C.

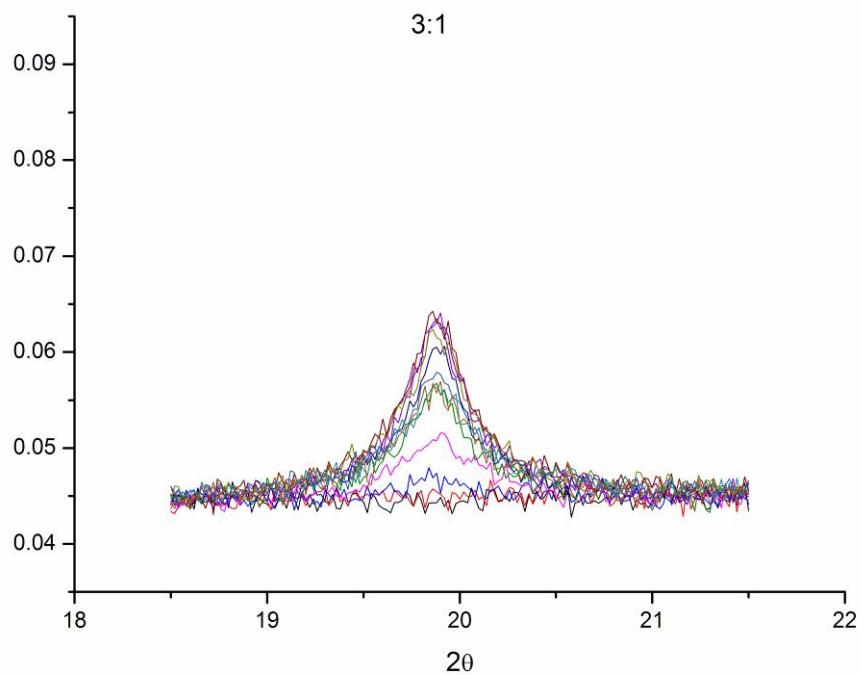


Figure 18. Plot showing the increase in the (111) reflection of palladium metal when nanoparticles with a surfactant ratio of 3:1 oleylamine to oleic acid at 35 °C.

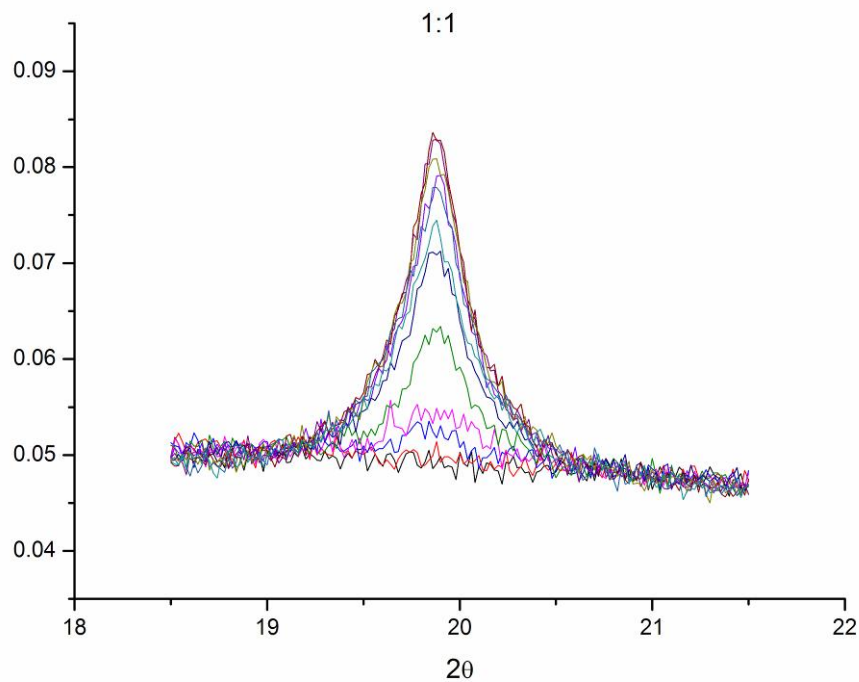


Figure 19. Plot showing the increase in the (111) reflection of palladium metal when nanoparticles with a surfactant ratio of 1:1 oleylamine to oleic acid at 35 °C.

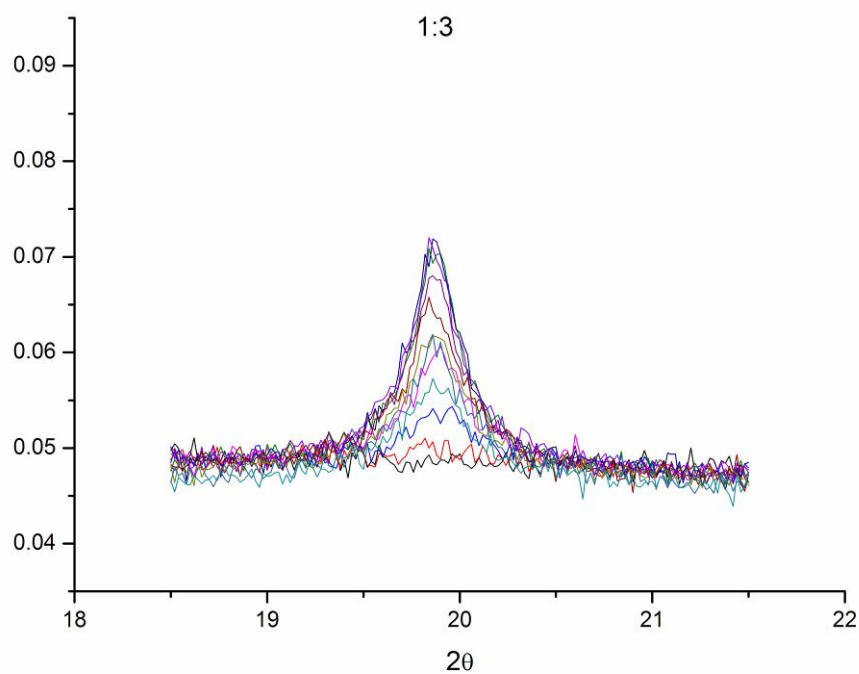


Figure 20. Plot showing the increase in the (111) reflection of palladium metal when nanoparticles with a surfactant ratio of 1:3 oleylamine to oleic acid at 35 °C.

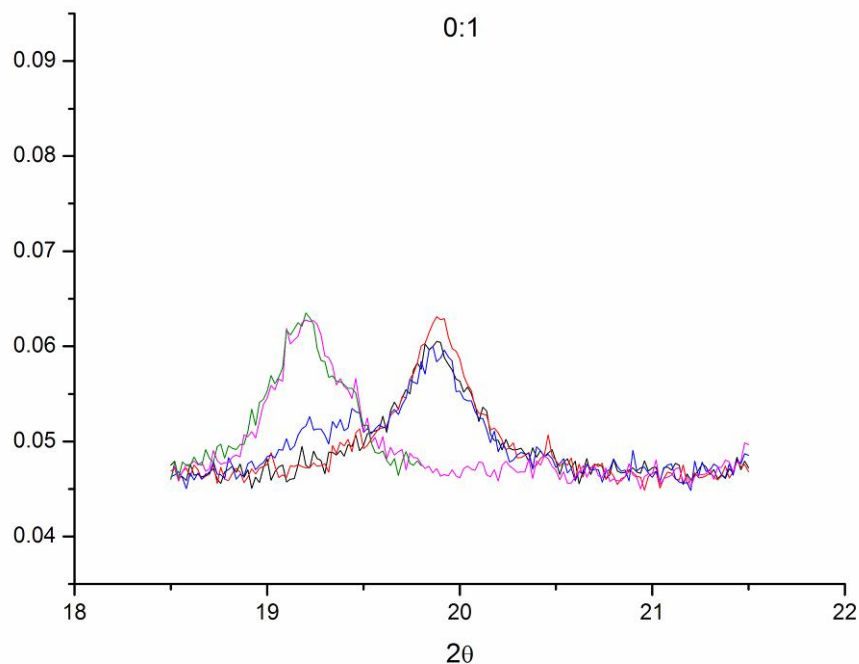


Figure 21. Plot showing the increase in the (111) reflection of palladium metal when nanoparticles with a surfactant ratio of 0:1 oleylamine to oleic acid at 35 °C.

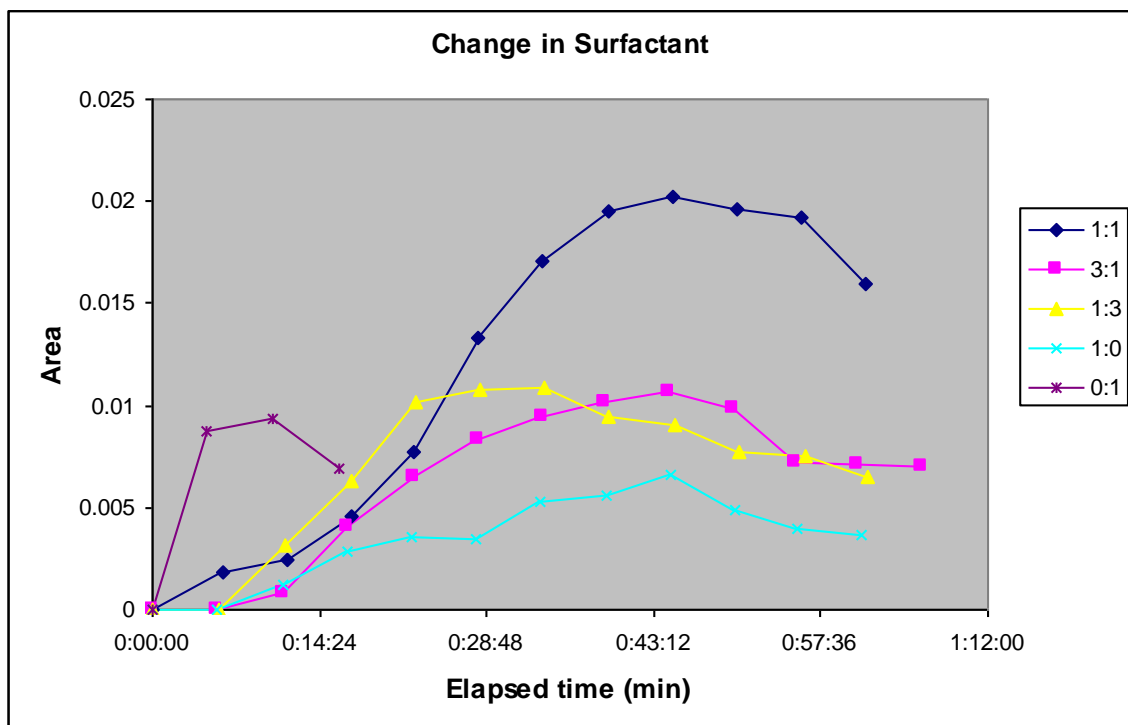


Figure 22. Peak area plotted against reaction time for palladium nanoparticles grown with different ratios of oleylamine and oleic acid.

Chapter 6: *Full Characterisation and Growth Mechanism of Palladium Nanostructures*

Figure 22 shows the elapsed reaction time as the relative concentration of oleic acid is increased which gives an insight into the kinetics of the reaction as a function of surfactant ratio. Again each plot reaches a maximum before the nanoparticles grow too large to remain in suspension and settle out of the beam path leading to a decrease in peak area. Both the samples with a majority oleylamine concentration and little or no oleic acid (1:0 and 3:1) show a long reaction time with the maximum for each occurring at around 44 min. The same reaction time is seen with the 1:1 ratio. As the oleic acid concentration ratio is increased there is a reduction in the reaction time. A ratio of 1:3 shows a maximum at 33 min and when the surfactant is purely oleic acid (0:1), the reaction time is reduced to ~10 min. These experiments clearly show that by increasing the oleic acid concentration the rate of the reaction is increased.

6.3.3 Discussion on SSRL

Experiment 7 showed that an increase in reaction temperature led to a decrease in the time taken to reach a maximum peak area. This corresponds to an increase in the reaction rate which is expected according to the Arrhenius equation.

For the reactions carried out at 25 °C and 35 °C the calculated grain size was relatively constant. This is consistent with a multiply twinned nanoparticle morphology. However, for the reactions performed at 50 °C and 70 °C there was a decrease in the average grain size over the course of the reaction. This can be attributed to rapid growth of relatively large crystallites which grow too large to be suspended and settle out of the beam path. This leaves only smaller crystallites contributing to the diffracted signal at the later stages of the reaction resulting in a smaller calculated grain size.

Experiment 8 showed that the nature of the surfactant system was directly involved in determining the kinetics of the reaction. As the oleic acid concentration was increased the elapsed time to maximum peak area declined indicating an increase in the reaction rate. A full discussion on the effect of the surfactant system will be given below in Section 6.4.

Chapter 6: *Full Characterisation and Growth Mechanism of Palladium Nanostructures*

When purely oleic acid was used as surfactant the emergence of a β -PdH signal was observed. This behaviour was noted and fully investigated at the Australian Synchrotron (see Section 4.6).

6.4 Growth Mechanism for the Formation of Highly Branched Palladium Nanostructures

In this thesis, two novel morphologies for nanostructured palladium metal have been formed; tripod nanoparticles (Exp 5.3.2) and the highly branched nanostructures (Exp 5.3.6). As these are unexpected morphologies for the highly symmetrical *fcc* crystal structure of palladium an investigation into their growth mechanism is of great concern. This will provide an understanding into the growth of complex nanostructures from all *fcc* materials including industrially important metals such as gold, silver, platinum and nickel.

In this section a growth mechanism and mechanism of action of the surfactant system is proposed for the formation of tripod nanoparticles and highly branched nanostructures. This is done in direct comparison to the commonly formed thermodynamically favoured polyhedra structures observed in Exp 5.2.4.

The thermodynamically favoured polyhedra nanoparticles were formed when purely oleylamine was used as surfactant (hereafter referred to as the 1:0 reaction). When oleic acid was introduced in a 1:1 ratio (hereafter referred to as the 1:1 reaction) the formation of tripod and highly branched nanostructures was observed.

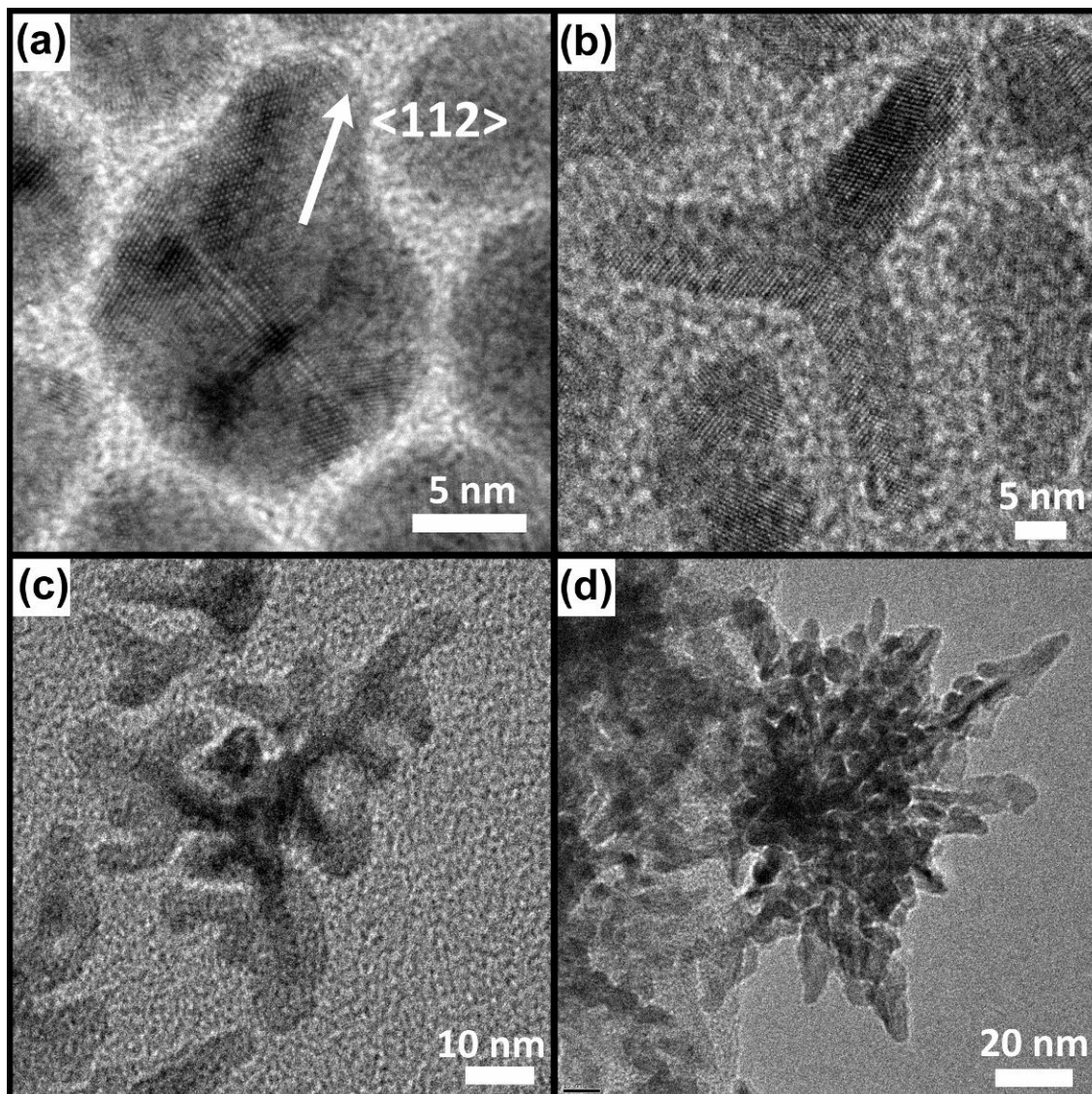


Figure 23. HREM images showing the evolution of the highly branched nanostructures. (a) A tripod shaped nanoparticle formed after 30 min, (b) an intermediate morphology after 80 min, (c) after 120 min and (d) a fully formed nanostructure after 160 min.

Figure 23 shows HREM analysis on the structural evolution of the highly branched nanostructures taken from experiments performed in Chapter 5. Figure 23a shows a nanoparticle 14 nm in size (see Exp 5.3.4). Analysis of the atomic packing indicates this nanoparticle is a multiply twinned *fcc* icosahedra viewed down a $\langle 112 \rangle$ zone axis {Penisson 1989}. This is similar to the polyhedra nanoparticles formed in the 1:0 reaction (Exp 5.2.4) except the nanoparticle shown here displays the start of single branched growth in a $\langle 112 \rangle$ direction.

Figure 23b shows a nanoparticle 45 nm in size which displays a tripod morphology (see Exp 5.3.2). A tripod morphology forms when arm growth occurs in three

Chapter 6: Full Characterisation and Growth Mechanism of Palladium Nanostructures

symmetry equivalent [112] directions from multiply twinned *fcc* icosahedra {Watt 2009}.

The nanoparticle in Fig. 23c is 65 nm in size and retains the tripod backbone with three fold symmetry (see Exp 5.3.5). This intermediate structure possesses a secondary type of growth which has occurred from the tripod arms. This growth occurs along random crystallographic directions and leads to a broad, leaf-like structure. Figure 23d displays a nanoparticle 120 nm in size and is the final reaction product formed after 160 min (see Exp 5.3.6). The secondary growth has continued at various angles away from the tripod backbone leading to a high surface area branched structure. Extensive branching has occurred along radial directions from the nanoparticle core to give a highly branched morphology.

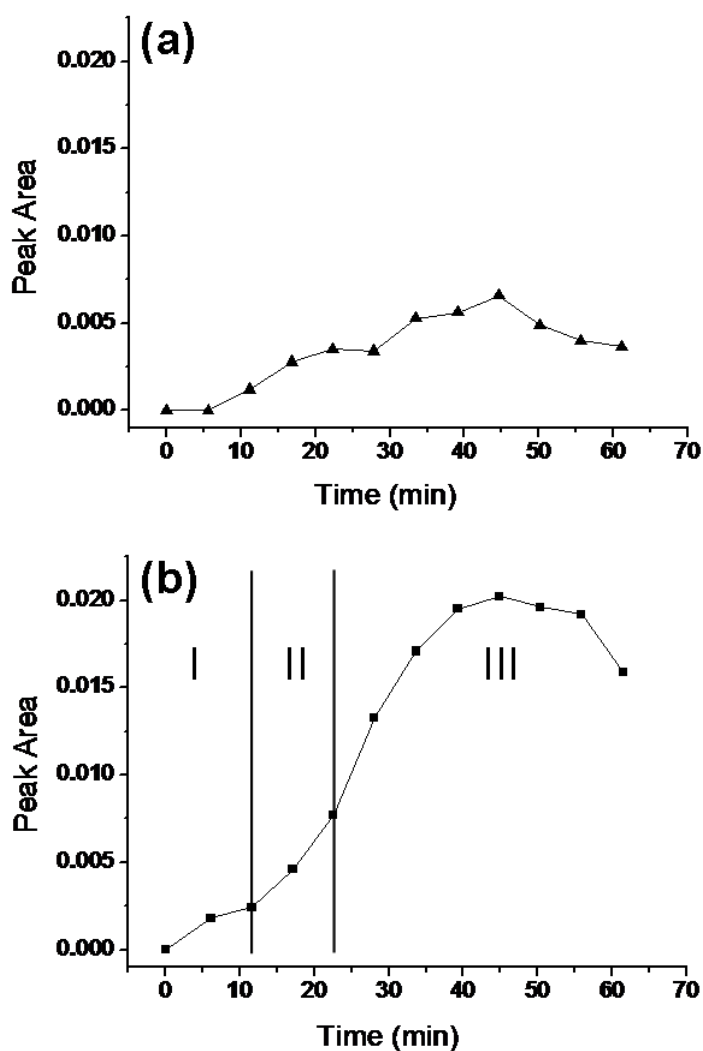


Figure 24. Time resolved synchrotron XRD results tracking the growth of the palladium nanostructures; (b) peak area vs reaction time plot for the 1:0 reaction and (c) for the 1:1 reaction.

Chapter 6: Full Characterisation and Growth Mechanism of Palladium Nanostructures

Figure 24 directly compares results from the *in-situ*-XRD experiments for the 1:0 and 1:1 reactions performed at 35 °C. For the 1:0 reaction there is a relatively slow and constant growth rate, as shown in Fig. 24a, which results in the polyhedra nanoparticle shapes observed in Exp 5.2.4. This slow, constant growth indicates that for the 1:0 reaction growth occurs under thermodynamic control to produce thermodynamically favoured polyhedra {Yin 2005}. In contrast, for the 1:1 reaction (Fig. 24b) there are three distinct growth stages leading to the formation of the highly branched nanostructures. Stages I-III each possesses different growth kinetics as described below and can be related to the structural evolution observed by HREM analysis (Fig 23).

Stage I

The growth rate for Stage I of the 1:1 reaction is relatively slow and comparable to the growth rate of the entire 1:0 reaction. For this stage, HREM analysis shows the formation of multiply twinned *fcc* icosahedral nuclei (Fig 23a). This is the same polyhedra structure formed in the 1:0 reaction (see Experiment 5.2.4) Therefore, during the slow growth of Stage I of the 1:1 reaction thermodynamically favoured multiply twinned *fcc* icosahedra nuclei form.

Stage II

During Stage II of the 1:1 reaction there is a two fold increase in the growth rate when compared to Stage I. This indicates growth is no longer thermodynamically controlled and kinetically controlled growth conditions are present {Yin 2005}.

In solution phase synthesis of nanoparticles, kinetically controlled growth conditions can lead to branched growth {Yin 2005}. This process was observed in Fig 23a with the start of branched growth from a multiply twinned icosahedra nuclei. In our case novel tripod shapes form due to branch growth occurring along three symmetry equivalent [112] directions from the icosahedra nuclei (Fig 23b) {Watt 2009}.

Therefore, as palladium crystallises in the highly symmetrical *fcc* crystal structure the formation of a branched shapes requires both a breaking of the crystal symmetry,

Chapter 6: Full Characterisation and Growth Mechanism of Palladium Nanostructures

introduced through defects in the icosahedral nanoparticle nuclei, and growth conditions which are kinetically controlled.

It should be noted that although the nanoparticles in Stage II are now growing under kinetic control, growth is still occurring along selected crystallographic directions.

Stage III

In Stage III there is another two-fold increase in the growth rate compared to Stage II. This increase follows the formation of the tripod branches and is due to the start of the secondary growth observed in Fig 23c. This secondary growth leads to the 'leaf-like' intermediate structures. The growth rate is now four times as fast as in Stage I which indicates this type of secondary growth is ultra-fast and kinetically controlled, occurring very far from thermodynamically controlled conditions.

Because of the rapid rate and distinctly kinetic nature of the ultra-fast growth, the adatom adsorption rate does not depend on the crystal facet where adsorption occurs. Hence growth occurs along no preferred crystallographic direction {Lou 2006}. This leads to randomly oriented branch growth occurring in any radial direction away from the nanoparticle core to give the highly branched morphology.

In contrast, the extensive branching observed in dendritic nanostructures formed in the solution phase is dependant on crystallographic direction and is typically a result of diffusion limited aggregation or oriented attachment mechanisms {Xiao 2001, Wen 2006, Zhou 2007}. The ultra-fast kinetic growth described here leads to branching irrespective of the crystal facet. Therefore, this growth provides a route towards the formation of complex nanoparticle shapes from nuclei with any morphology and surface energy.

Following the ultra-fast growth (after 45 minutes, end of stage III) the peak area begins to decline as the nanoparticles settle out of the beam path.

Therefore, from HREM and XRD experiments, the formation of the palladium polyhedra nanoparticles is shown to occur through slow, thermodynamically controlled growth. In contrast, formation of the highly branched nanostructures

Chapter 6: *Full Characterisation and Growth Mechanism of Palladium Nanostructures*

occurs through; (i) the formation of multiply twinned *fcc* icosahedra nuclei, (ii) kinetically controlled branch growth to form a tripod backbone and (iii) ultra-fast secondary kinetic growth occurring in any crystallographic direction from the tripod arms.

In the present system, the kinetics of growth, and hence the final nanoparticle morphology, are controlled by the surfactant system. The difference in surface stabilisation ability of the amine and acid functionalities determines the growth kinetics by controlling the rate of monomer supply to the nanoparticle surface {Sau 2004}.

When the rate of adatom diffusion across the nanoparticle surface to stable positions is faster than the rate of adatom adsorption, growth is thermodynamically controlled and thermodynamically favoured morphologies form. Conversely, when adatom adsorption occurs at a faster rate, growth becomes kinetically controlled leading to more complex nanoparticle shapes {Yin 2005}.

The carboxylic acid functionality of oleic acid possesses a weaker binding strength to palladium compared to the amine functionality of oleylamine {Ahrland 1958, Jun 2005}. Introducing weaker binding oleic acid (1:1 reaction) will reduce the overall degree of surface stabilisation of the growing nanoparticle by the surfactant system. This allows rapid adatom adsorption and kinetically controlled growth conditions resulting in highly branched structures.

This is in contrast to the 1:0 reaction where oleylamine binds strongly to the surface of the growing nanoparticle. Therefore, the icosahedral nuclei experience strong stabilisation effects hindering adatom adsorption. Growth conditions are then thermodynamically controlled and thermodynamically favoured polyhedral structures are maintained.

When purely oleic acid is used as surfactant micron sized crystallites form; presumably because there is not enough stabilising ability by oleic acid to restrict growth to the nano-scale for this system (see Exp 5.4.3).

6.5 Catalytic Studies of Highly Branched Palladium Nanostructures

Highly branched nanostructures are ideally suited to catalysis as a high surface area and the presence of high index facets are well known to lead to increases in catalytic activity {Tian 2008}. High index facets have a higher density of atomic steps, ledges, kinks and dangling bonds, all of which often exhibit much higher reaction activities {Tian 2007, Ma 2008}. Here, high magnification HREM was performed to probe the nature of the nanostructure surface and determine if high index facets were present. The catalytic properties of the highly branched palladium nanostructures were then investigated by James Cookson of Johnson Matthey, UK.

The palladium nanostructures were supported onto activated carbon and the resulting catalysts (Pd-NS/C) were examined and compared to commercially available palladium catalysts (Johnson Matthey 1% Pd/C 87L) for the hydrogenation of nitrobenzene. The catalytic hydrogenation of nitrobenzene to aniline is commonly used as a standard test for the activity of heterogeneous catalyst systems {Gelder 2002}. In addition to this, the reaction has great commercial importance in its own right, in the industrial production of aniline for the polyurethane industry {Weissermel 2007}.

Experimental

The HREM experiment was performed at VUW on a JEOL 2010 operated at an acceleration voltage of 200 keV.

Pd NS/C catalysts were prepared by dissolving Pd NS in toluene, via sonication. The resulting black suspension was stirred at room temperature for 18 hours with sufficient activated carbon (1.0g of activated carbon) to generate a 1% (by weight) Pd NS/C catalyst. After this time, the resulting suspension was filtered, revealing a clear filtrate. The subsequent black solid was thoroughly washed with toluene (100ml), methanol (100ml), water (100ml) and methanol (100ml) in order to remove any excess ligands present. The solid was then dried in a vacuum oven before use.

The Pd NS/C was compared in the hydrogenation of nitrobenzene with 1% Pd/C (Johnson Matthey, 87L). The test was undertaken using a Baskerville autoclave

Chapter 6: *Full Characterisation and Growth Mechanism of Palladium Nanostructures*

connected to a Buchi pressflow gas controller. The reaction occurred at 50°C, under 2 bar of dihydrogen, and stirred at approximately 1000 rpm. In each test, 5ml of a 0.1M methanol solution of nitrobenzene (containing 0.1M of mesitylene) was used with a 1:1000 molar ratio of metal to substrate. Subsequent GC analysis was undertaken using a CPSIL-5 column, with mesitylene as an internal standard.

Results

Figure 25a shows an HREM image of one of the nanoparticle branches viewed down a $\langle 110 \rangle$ direction. A close up of the branch is shown in Fig 25b. Analysis of the atomic packing in Fig 25b confirms the presence of high index facets. The arrows point to atomic vacancies on the branch edge which create a series of alternating (200) and (111) microfacets. These microfacets combine to form the high index (113) facet. This is shown schematically in Fig. 25c.

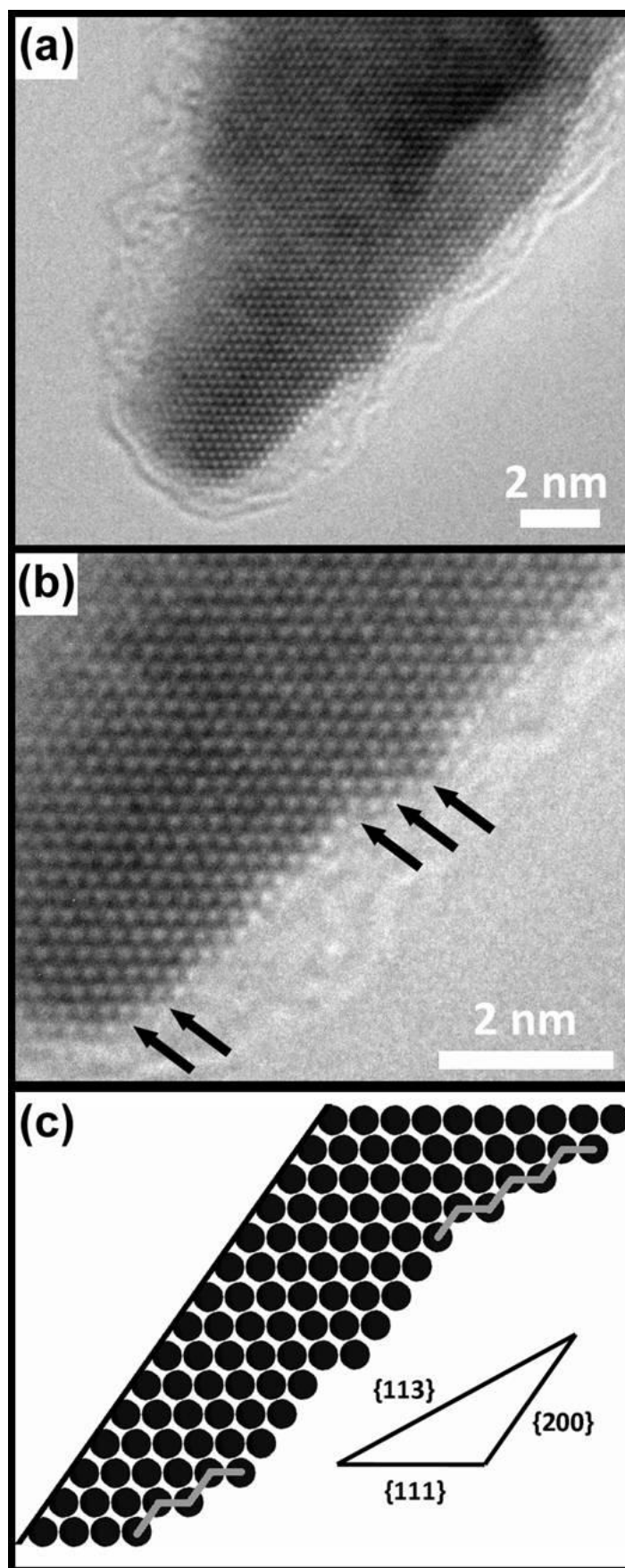


Figure 25. Analysis of the surface of one of the highly branched nanostructures. (a) HREM image of one of the nanoparticle branches, (b) close up HREM image of the nanoparticle branch showing clear atomic packing. The black arrows point to atomic vacancies on the nanoparticle surface. (c) Schematic showing how the atomic vacancies lead to high index {113} facets.

The Pd-NS/C material showed considerable activity for the hydrogenation of nitrobenzene. After 30 minutes, there was no further hydrogen uptake, indicating that the reaction had reached completion. Subsequent analysis by gas chromatography confirmed this, revealing that all of the starting material had been consumed and aniline was the sole product. The formation of intermediate products such as hydroxylamines, oximes or para-aminophenols was not observed; the presence of which can be observed in less active catalytic systems or those that have been deliberately poisoned {Gao 1998}.

The commercially available catalyst was also examined under the same reaction conditions. In this case, the reaction was complete within 20 minutes, again with complete conversion to the desired product. However, with the higher dispersion of this catalyst, this increase in activity is to be expected. What is significant is that the Pd NS/C catalysts display activities nearly the same as that of commercially available analogues, despite the presence of residual oleylamine stabilising ligands. The novel shapes of the palladium nanostructures offer the possibility of the unique facets to provide alternative selectivities for specific chemoselective reactions. The investigation into such transformations is ongoing.

6.6 *In-Situ* Synchrotron X-ray Diffraction Studies on the Formation of Palladium Hydride

Palladium is well known for its ability to absorb hydrogen in high concentrations and is a promising material in hydrogen storage and gas sensing applications {Suleiman 2006, Pundt 2004}. It shows exceptional promise for practical use as it absorbs hydrogen at ambient temperature and pressure {Yamauchi 2008}. Palladium exists in two distinct hydride phases labelled as α - and β - corresponding to low and high concentrations respectively. The α -phase is a solid solution with hydrogen atoms randomly occupying interstitial sites within the *fcc* metal lattice {Ingham 2008}. As more hydrogen dissolves the lattice constant increase linearly with pressure until the β -phase appears. In the β -phase hydrogen atoms occupy octahedral lattice sites. If all octahedral sites were occupied the crystal structure would be analogous to NaCl. However, the stoichiometric composition has never been attained so the structure can be considered a defective NaCl type arrangement {Jewell 2006}. The gap between these two phases is known as the miscibility gap. The existence of the miscibility gap is due to an energy barrier associated with the incorporation of hydrogen atoms onto lattice sites and the accompanying structural transition {Ingham 2006}. Previous studies have shown that a decrease in nanoparticle size leads to a narrowing of the miscibility gap {Pundt 1999, Sachs 2001, Suleiman 2003, Yamauchi 2006}. That is, in smaller nanoparticles the α - and β -phases of palladium hydride can co-exist.

In Experiment 7 the emergence of the β -phase of palladium hydride (β -PdH) was observed. To investigate the hydrogen absorption properties of the palladium nanostructures, *in-situ* XRD experiments were carried out at the Australian Synchrotron (AS) in Melbourne, Australia.

Experimental - Synchrotron XRD Setup

Experiments were performed at AS on the Powder Diffraction Beamline in the same reaction cell used at SSRL (see Fig 9). The cell windows were made from X-ray transparent Kapton (polyimide) film. The experiments were conducted using radiation of $\lambda = 1.0 \text{ \AA}$ (12.4 keV). Diffractograms were collected between 2θ values of 2° and 35° which included the {111} and {200} reflections of both α -PdH and the β -

Chapter 6: Full Characterisation and Growth Mechanism of Palladium Nanostructures

PdH phases. Information on hydrogen absorption on each species was taken from the corresponding {111} reflection only.

Experimental

The reaction solution used was identical to that used for the 0:1 experiment in Section 4.3.2.

25.9 mg (0.1 mmol) of $[\text{PdCl}_2(\text{NCMe})_2]$ was dissolved in 1 mL of toluene. To this was 0.330 mL (1 mmol) of oleic acid. This reaction mixture was sonicated until a clear dark orange solution resulted. Fifty microlitres of the reaction solution was injected into the reaction cell which was then purged and filled with 3 bar H_2 . The entire reaction cell was then placed in a reaction oven and left to react at the desired temperature and reaction time. The reaction cell was then quickly transferred to the beamline and measurements were initiated.

6.6.1 Reaction for 30 min at 90 °C

For this reaction the solution was placed in an oven and the nanostructures grown at 90 °C for 30 min. The reaction cell was then removed from the oven and quickly transferred to the beamline where the measurements were carried out at room temperature. The kapton windows appeared black after reaction in the oven indicating the formation of nanocrystalline palladium.

Results

Figure 26 shows an XRD spectrum of the reaction solution showing the {111} and {200} reflections for both α - and the β - phase.

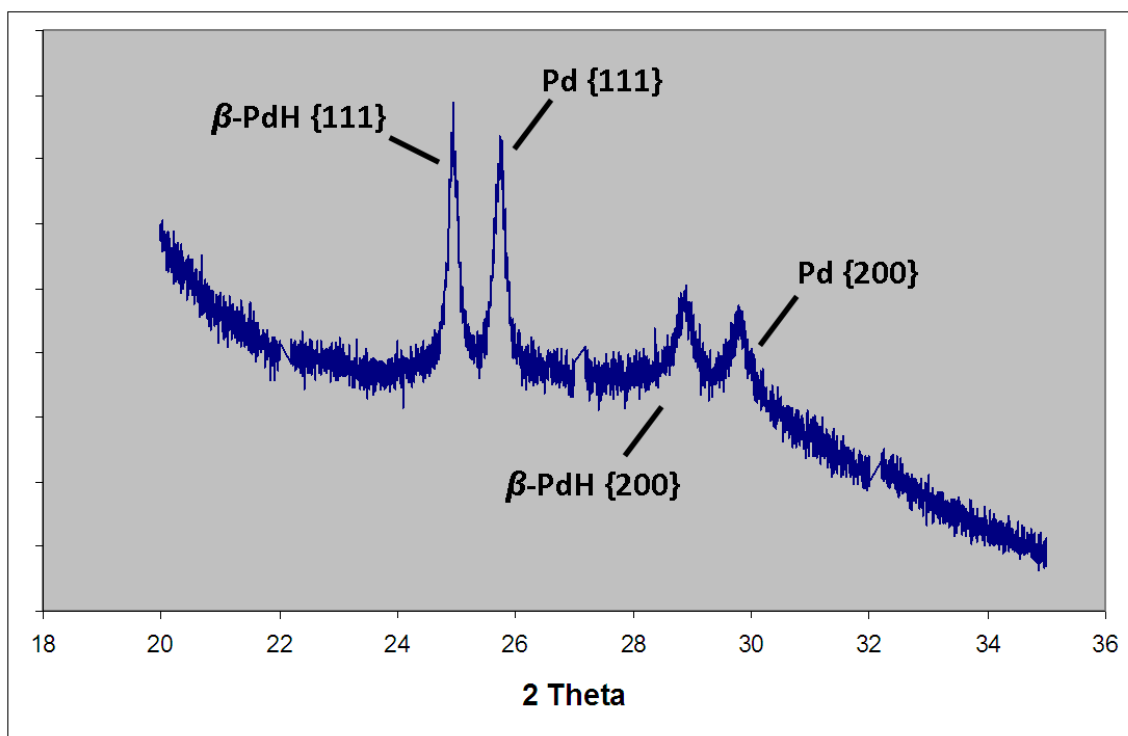


Figure 26. Synchrotron XRD spectrum showing the {111} and {200} reflections for both α - and the β -phase.

Figure 27 shows a plot of peak area against time for the {111} reflection of both α -PdH and β -PdH. At $t = 0$ min the peak area of α -PdH is roughly 2.5 times that of the β -PdH. The β -PdH signal then increases rapidly and after 3 min on the beamline becomes larger than the α -PdH signal. The β -PdH then increases slowly to a maximum at 15 min observation time. This is accompanied by a similar decrease in the area of the α -PdH signal. At 15 min the valve on the reaction cell is opened to the atmosphere (indicated by the black arrow). This sees an immediate and rapid decrease in the β -PdH signal accompanied by an equally sharp increase in the signal of α -PdH phase.

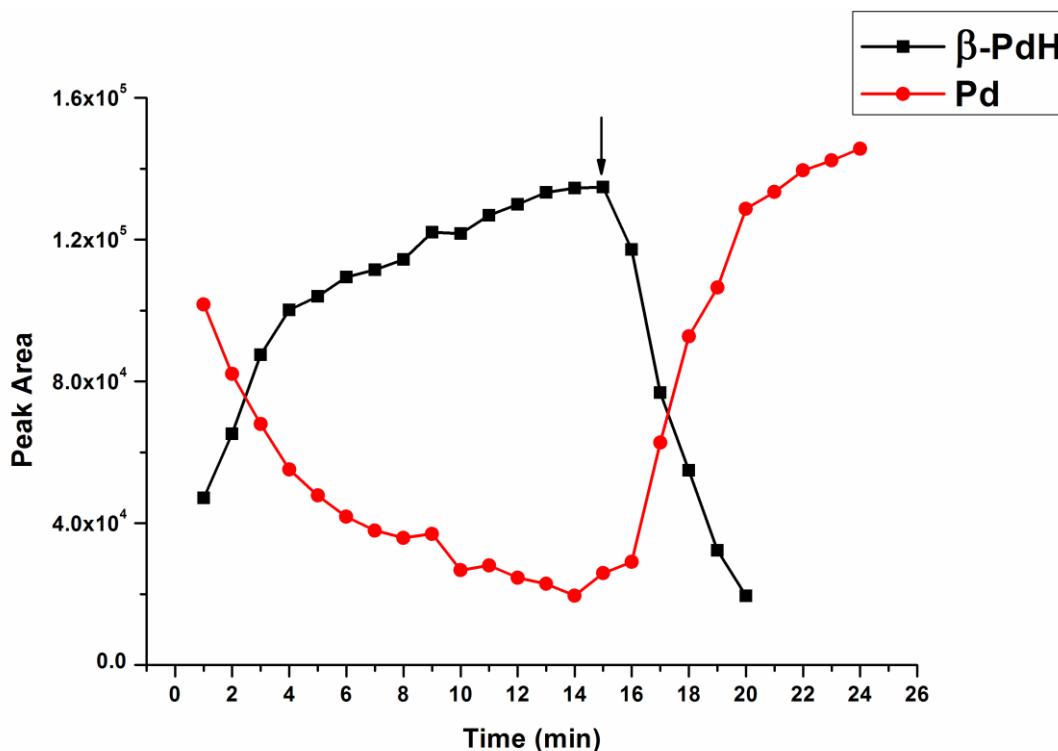


Figure 27. Plot of peak area against time for the {111} reflection of both α -PdH and β -PdH for nanostructures grown at 90 °C for 30 min.

6.6.2 Reaction for 30 min at 70 °C

For this reaction the solution was placed in an oven and the nanostructures grown at 70 °C for 30 min. The reaction cell was then removed from the oven and quickly transferred to the beamline where the measurements were carried out at room temperature. The kapton windows appeared black after reaction in the oven indicating the formation of nanocrystalline palladium.

Results

Figure 28 shows a plot of peak area against time for the {111} reflection of both the α -PdH and β -PdH phases. At $t = 0$ min there is no signal from α -PdH which indicates that the entire volume of palladium exists in the β -PdH phase. At $t = 20$ min the reaction cell was exposed to the atmosphere (black arrow). There is a sharp decrease in the peak area which can be attributed to manual error in opening the valve moving the sample in the beam path. In this instance there is a lag of ~ 60 min before the β -PdH signal begins to decline. At $t = 84$ min the α -PdH signal appears and begins to grow gradually until a maximum at $t = 151$ min. This is accompanied by a decrease in the β -

PdH which occurs over the same time period. At $t = 114$ min both signals have the same peak area.

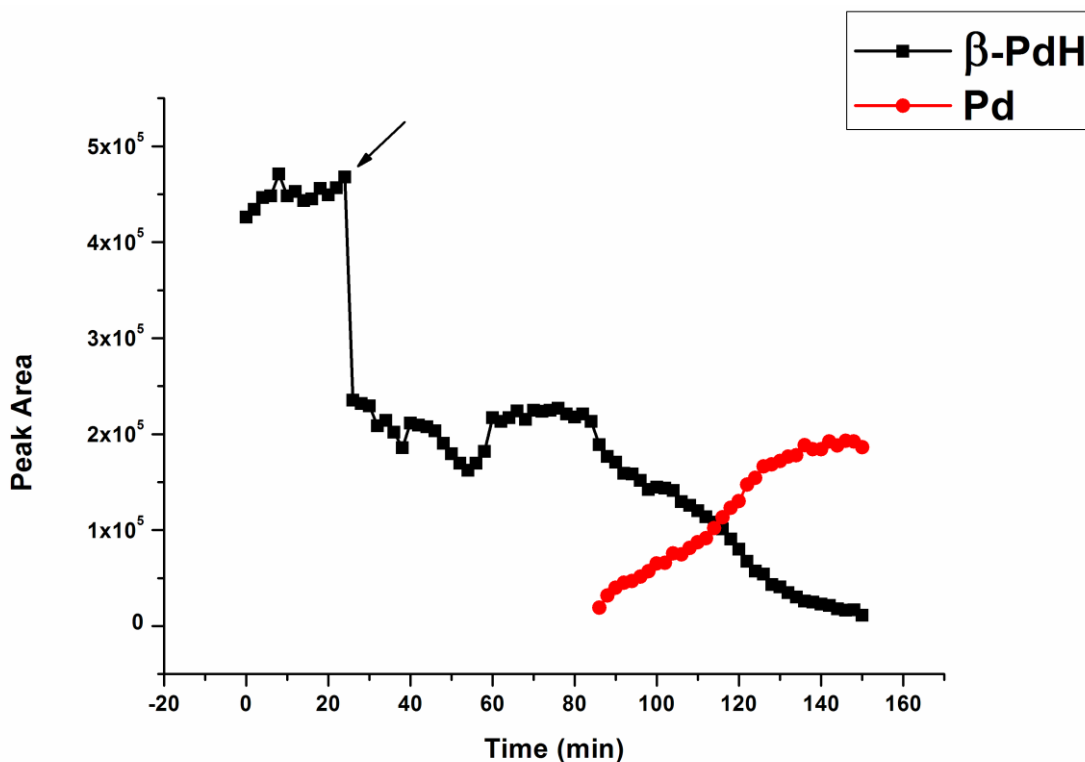


Figure 28. Plot of peak area against time for the {111} reflection of both α -PdH and β -PdH for nanostructures grown at 70 °C for 30 min.

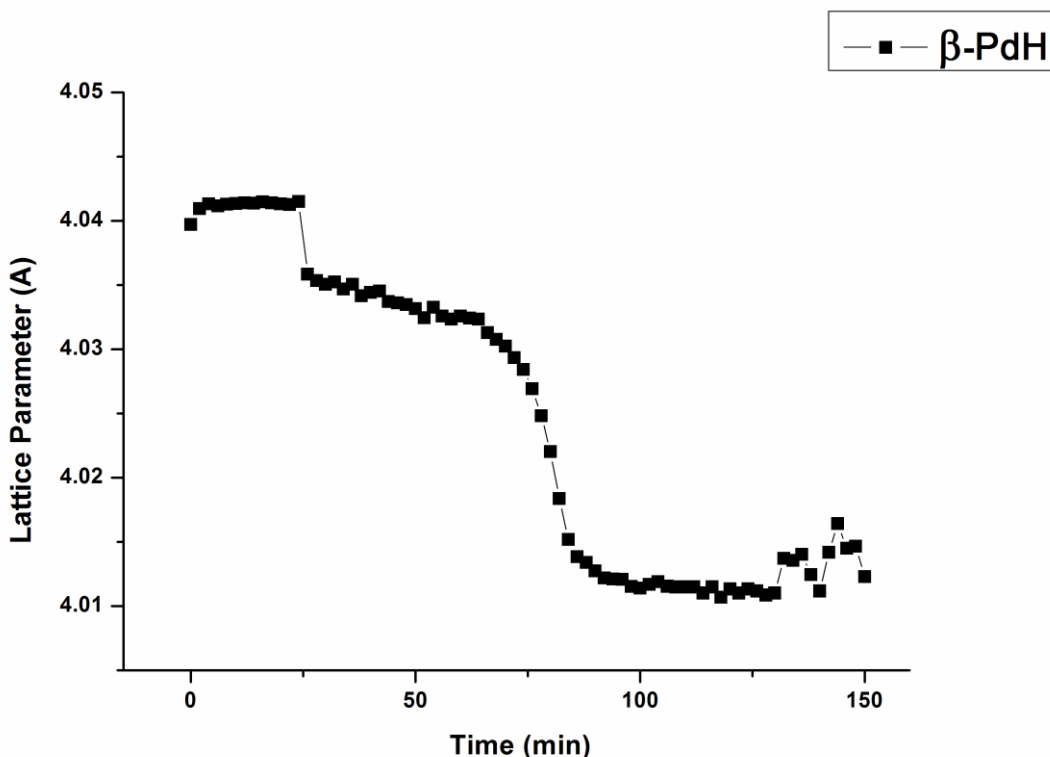


Figure 29. Plot of lattice parameter against time for palladium nanostructures when grown at 70 °C for 30 min.

Fig 29 shows a plot of the lattice parameter for the β -PdH phase against observation time. The lattice parameter is constant at $a = 4.041 \text{ \AA}$ in the initial stages of the reaction. This corresponds to a 3.9 % expansion of the lattice parameter when compared to palladium metal. When the reaction cell is exposed to the atmosphere at $t = 24 \text{ min}$ the lattice parameter drops sharply to $a = 4.035 \text{ \AA}$. The lattice parameter then decreases gradually over the next 60 min to $a = 4.022 \text{ \AA}$. At $t = 64 \text{ min}$ there is a rapid decrease in the lattice parameter to $a = 4.011 \text{ \AA}$ (β_{\min}). The lattice parameter then remains relatively constant at this value until the end of observation. The increase in lattice parameter at the end of observation is due to uncertainty in the measurement.

Comparing the plot of lattice parameter to the plot of peak area of both α -PdH and β -PdH shows that, after exposure to the atmosphere, the α -PdH phase is not observed until β_{\min} is reached.

6.6.3 Reaction for 2 h at 90 °C

For this reaction the solution was placed in an oven and the nanostructures grown at 90 °C for 2 h. The reaction cell was then removed from the oven and quickly transferred to the beamline where the measurements were carried out at room temperature. The kapton windows appeared black after reaction in the oven indicating the formation of nanocrystalline palladium.

Results

Figure 30 shows a plot of peak area against time for the {111} reflection of both α -PdH and β -PdH phases. In the initial stage of the reaction ($t = 0$ min to $t = 25$ min) there is a sharp decrease in the strength of the α -PdH signal accompanied by an increase in the β -PdH. The β -PdH signal remains constant after reaching a maximum. At $t = 45$ min the reaction cell was exposed to the atmosphere (black arrow). After exposure, the β -PdH signal remains constant for ~ 60 min before beginning to decrease at $t = 100$ min. The β -PdH signal decreases rapidly until around $t = 120$ min where the rate of decrease slows. The signal reaches a minimum at $t = 200$ min. This decrease in β -PdH signal is accompanied by an increase in the α -PdH signal. Again this increase begins rapidly before gradually slowing and reaching a maximum at $t = 200$ min.

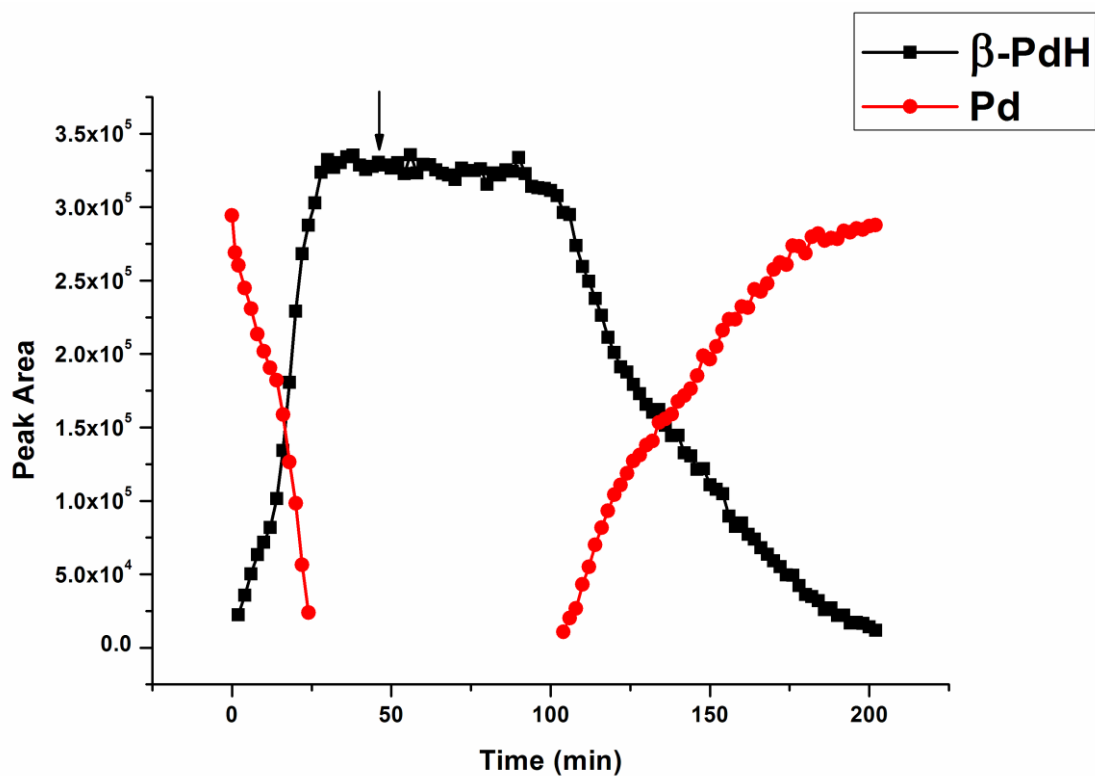


Figure 30. Plot of peak area against time for the {111} reflection of both α -PdH and β -PdH for nanostructures grown at 90 °C for 2 h.

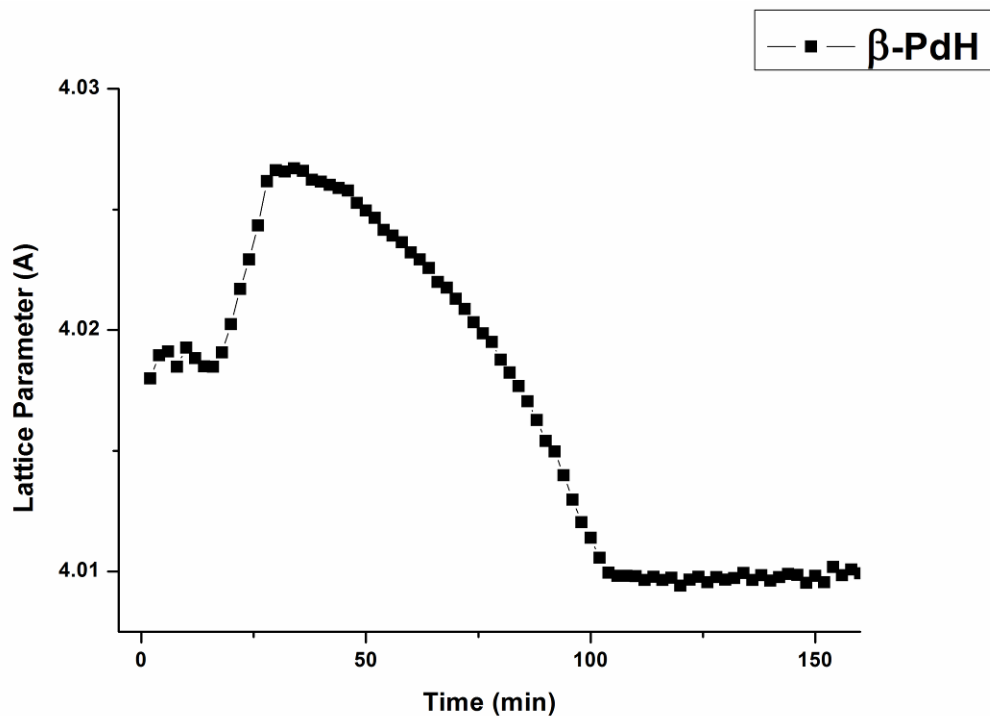


Figure 31. Plot of lattice parameter against time for palladium nanostructures when grown at 70 °C for 30 min.

Chapter 6: Full Characterisation and Growth Mechanism of Palladium Nanostructures

Fig 31 shows a plot of the lattice parameter for the β -PdH phase against observation time. From $t = 0$ min to $t = 10$ min the lattice parameter is constant ($a = 4.020 \text{ \AA}$). At $t = 10$ min there is a rapid increase in the lattice parameter to a maximum of $a = 4.027 \text{ \AA}$. This corresponds to a 3.5 % expansion of the lattice parameter when compared to palladium metal. When the reaction solution is exposed to the atmosphere there is a decrease in the lattice parameter. This rate of decrease is initially slow but become more rapid until a minimum lattice parameter (β_{\min}) is reached at $t = 100$ min ($a = 4.010 \text{ \AA}$). The lattice parameter then remains constant at this value until the end of observation.

Comparing the plot of lattice parameter to the plot of peak area of both α -PdH and β -PdH shows that, after exposure to the atmosphere, the α -PdH phase is not observed until β_{\min} is reached.

6.6.4 Discussion on Formation of Palladium Hydride

The above results show that the as synthesised palladium nanostructures are able to easily absorb hydrogen.

In the initial stage of Exp 6.6.1 α -PdH is the dominant phase. The β -PdH then grows at the expense of the α -PdH as the reaction solution cools. This is due to the increased solubility of hydrogen in both toluene and Pd at lower temperatures. When the reaction solution is exposed to the atmosphere there is an immediate and rapid desorption of hydrogen.

For Exp 6.6.2 there is slightly different behaviour. In the initial stages of the reaction there is no α -PdH signal present and β -PdH is the dominant phase. Presumably $70 \text{ }^\circ\text{C}$ is cool enough to allow sufficient absorption of hydrogen to form the β phase. After the reaction solution is exposed to the atmosphere there is a gradual decrease in the β -PdH signal accompanied by a decrease in the lattice parameter as shown in Fig 29. This is associated with desorption of hydrogen and the relaxation of the crystal lattice to β_{\min} .

Chapter 6: Full Characterisation and Growth Mechanism of Palladium Nanostructures

In this instance, the decrease in lattice parameter begins gradually but becomes rapid before reaching β_{\min} .

When β_{\min} is reached the miscibility gap is crossed and a transformation occurs and α -PdH is formed. The α -PdH signal then increases steadily at the cost of the β -PdH signal until all hydrogen has been desorbed from octahedral lattice sites.

For Exp 6.6.3 we again observe α -PdH to be the dominant phase in the initial stages of the reaction. This is due to the high reaction solution temperature of 90 °C which does not allow sufficient hydrogen concentration for the formation of the β - phase. As the reaction solution cools the α -PdH signal decreases along with a rapid increase in the β -PdH signal. When the reaction solution is exposed to the atmosphere there is an immediate decrease in the lattice parameter as shown in Fig 31. When the lattice parameter reaches β_{\min} a transformation to α -PdH occurs. Again this signal increases at the expense of the β -PdH signal with H desorption beginning slowly but becoming more rapid before reaching β_{\min} .

So, for both Experiments 6.6.2 and 6.6.3, as the lattice parameter decreases there is an increase in the rate of desorption of hydrogen.

The nanostructures grown at 70 °C experience a 3.9 % expansion of the lattice parameter when compared to α -PdH. Those nanostructures grown 90 °C see a 3.5 % increase. Both have a similar β_{\min} of $a = 4.01 \text{ \AA}$. This indicates that those nanostructures grown at 70 °C absorb a greater concentration of hydrogen than those grown at 90 °C.

This is due to the likely difference in surface area of the two types of nanostructures. Those structures formed at 90 °C will possess a higher surface area as faster reaction kinetics are known to lead to more complex nanostructures {Watt 2009}. It has previously been shown that a decrease in the surface area to volume ratio of a nanoparticle leads to an increase in lattice expansion {Suleiman 2003}. This is indeed what is observed here where the less complex nanostructures formed at 70 °C experience a larger lattice expansion.

Chapter 6: *Full Characterisation and Growth Mechanism of Palladium Nanostructures*

It should be noted that the as formed nanostructures experience desorption of hydrogen at RT. This is in stark contrast to most hydrides which must be heated to ~ 200 °C for hydrogen release {Berube 2007}.

6.7 Summary

We have synthesized palladium nanoparticles of varying shapes including tripod, bipod, multipod and highly branched type nanostructures using a pressure reaction vessel (Fischer-Porter bottle). The formation of branched or pod-like structures is the first evidence of these types of morphologies for palladium metal nanoparticles.

Using High Resolution Transmission Electron Microscopy (HREM) techniques we have shown that the palladium tripod nanoparticles grow from multiply twinned *fcc* icosahedral nuclei. The growth of highly branched palladium nanostructures has been tracked using synchrotron XRD and compared to HREM analysis to show that these structures also grow from multiply twinned *fcc* icosahedra nuclei via a tripod intermediate.

The growth mechanism involves surface selective capping by the organic surfactant which determines the resulting morphology. When a surfactant with strong binding characteristics is used a thermodynamic growth regime occurs and the nuclei grow into isotropic shapes. When a surfactant with weaker binding characteristics is introduced the growth regime becomes kinetic in nature. The combination of twinning in the nuclei and kinetic growth conditions causes anisotropic branch growth to occur and pod-like structures are formed. When this occurs in three equivalent directions a tripod morphology results. A type of secondary ultra-fast kinetic growth then occurs from the tripod intermediate along no specific crystallographic direction resulting in highly branched nanostructures.

The palladium nanostructures demonstrate good activity in the hydrogenation of nitrobenzene to aniline where the formation of the desired product occurs at a similar rate to commercially available catalysts.

The palladium nanostructures also show good absorption of hydrogen gas – an important application for palladium in the possible hydrogen economy. The formation of β -PdH was observed which was followed by desorption of hydrogen at room temperature upon exposure to the atmosphere. However, the more complex the nanostructure the less hydrogen absorbed. Therefore, the highly branched palladium

Chapter 6: *Full Characterisation and Growth Mechanism of Palladium Nanostructures*

nanostructures investigated here may not possess the optimal morphology for hydrogen absorption characteristics.

References

- Ahrland, S., Chatt, J., Davies, N. R., *Quarterly Reviews* **1958**, *12*, 265.
- Berube, V., Radtke, G., Dresselhaus, M., Chen, G., *International Journal of Energy Research* **2007**, *31*, 637.
- Champness, P. E., *Electron Diffraction in the Transmission Electron Microscope, Vol. 47*, BIOS Scientific Publishers Limited, **2001**.
- Chen, H. Y., Gao, Y., Zhang, H. R., Liu, L. B., Yu, H. C., Tian, H. F., Xie, S. S., Li, J. Q., *Journal of Physical Chemistry B* **2004**, *108*, 12038.
- Flueli, M., Spycher, R., Stadelmann, P. A., Buffat, P. A., Borel, J. P., *Europhysics Letters* **1988**, *6*, 349.
- Gai, P. L., Harmer, M. A., *Nano Letters* **2002**, *2*, 771.
- Gao, J., Wang, F. D., Liao, S. J., Yu, D. R., *Reaction Kinetics and Catalysis Letters* **1998**, *64*, 351.
- Gelder, E. A., Jackson, S. D., Lok, C. M., *Catalysis Letters* **2002**, *84*, 205.
- Germain, V., Li, J., Ingerl, D., Wang, Z. L., Pileni, M. P., *Journal of Physical Chemistry B* **2003**, *107*, 8717.
- Ingham, B., Toney, M. F., Hendy, S. C., Cox, T., Fong, D. D., Eastman, J. A., Fuoss, P. H., Stevens, K. J., Lassesson, A., Brown, S. A., Ryan, M. P., *Physical Review B* **2008**, *78*,
- Jewell, L. L., Davis, B. H., *Applied Catalysis a-General* **2006**, *310*, 1.
- Jun, Y. W., Lee, J. H., Choi, J. S., Cheon, J., *Journal of Physical Chemistry B* **2005**, *109*, 14795.
- Kirkland, A. I., Jefferson, D. A., Tang, D., Edwards, P. P., *Proceedings of the Royal Society of London Series a-Mathematical Physical and Engineering Sciences* **1991**, *434*, 279.
- Ling, T., Xie, L., Zhu, J., Yu, H., Ye, H., Yu, R., Cheng, Z., Liu, L., Liu, L., Yang, G., Cheng, Z., Wang Y., Ma, X. *Nano Letters* **2009**, *9*, 1572.
- Lou, X. W., Yuan, C. L., Archer, L. A., *Chemistry of Materials* **2006**, *18*, 3921.
- Ma, Y. Y., Kuang, Q., Jiang, Z. Y., Xie, Z. X., Huang, R. B., Zheng, L. S., *Angewandte Chemie-International Edition* **2008**, *47*, 8901.
- Maksimuk, S., Teng, X., Yang, H., *Journal of Physical Chemistry C* **2007**, *111*, 14312.
- Penisson, J. M., Renou, A., *Zeitschrift Fur Physik D-Atoms Molecules and Clusters* **1989**, *12*, 113.
- Penisson, J. M., Renou, A., *Journal of Crystal Growth* **1990**, *102*, 585.

Chapter 6: Full Characterisation and Growth Mechanism of Palladium Nanostructures

- Pundt, A., Sachs, C., Winter, M., Reetz, M. T., Fritsch, D., Kirchheim, R., *Journal of Alloys and Compounds* **1999**, 295, 480.
- Pundt, A., Suleiman, M., Bahtz, C., Reetz, M. T., Kirchheim, R., Jisrawi, N. M., *Materials Science and Engineering B-Solid State Materials for Advanced Technology* **2004**, 108, 19.
- Qi, W. H., Wang, M. P., Su, Y. C., *Journal of Materials Science Letters* **2002**, 21, 877.
- Qi, W. H., Wang, M. P., *Journal of Nanoparticle Research* **2005**, 7, 51.
- Sachs, C., Pundt, A., Kirchheim, R., Winter, M., Reetz, M. T., Fritsch, D., *Physical Review B* **2001**, 64,
- Salzemann, C., Urban, J., Lisiacki, I., Pileni, M. P., *Advanced Functional Materials* **2005**, 15, 1277.
- Sau, T. K., Murphy, C. J., *Journal of the American Chemical Society* **2004**, 126, 8648.
- Suleiman, M., Jisrawi, N. M., Dankert, O., Reetz, M. T., Bahtz, C., Kirchheim, R., Pundt, A., *Journal of Alloys and Compounds* **2003**, 356, 644.
- Tian, N., Zhou, Z. Y., Sun, S. G., Ding, Y., Wang, Z. L., *Science* **2007**, 316, 732.
- Tian, N., Zhou, Z. Y., Sun, S. G., *Journal of Physical Chemistry C* **2008**, 112, 19801.
- Watt, J., Young, N., Haigh, S., Kirkland, A., Tilley, R. D., *Advanced Materials* **2009**, 21, 2288.
- Weissermel, K., Arpe, H. J., *Industrial Organic Chemistry*, 3rd ed., VCH, Weinheim, **1997**.
- Wen, X. G., Xie, Y. T., Mak, W. C., Cheung, K. Y., Li, X. Y., Renneberg, R., Yang, S., *Langmuir* **2006**, 22, 4836.
- Xiao, J. P., Xie, Y., Tang, R., Chen, M., Tian, X. B., *Advanced Materials* **2001**, 13, 1887.
- Xiong, Y. J., McLellan, J. M., Chen, J. Y., Yin, Y. D., Li, Z. Y., Xia, Y. N., *Journal of the American Chemical Society* **2005**, 127, 17118.
- (a) Xiong, Y. J., Cai, H. G., Wiley, B. J., Wang, J. G., Kim, M. J., Xia, Y. N., *Journal of the American Chemical Society* **2007**, 129, 3665.
- (b) Xiong, Y. J., Cai, H. G., Yin, Y. D., Xia, Y. N., *Chemical Physics Letters* **2007**, 440, 273.
- Yamauchi, M., Ikeda, R., Kitagawa, H., Takata, M., *Journal of Physical Chemistry C* **2008**, 112, 3294.
- Yin, Y., Alivisatos, A. P., *Nature* **2005**, 437, 664.
- Zhou, P., Dai, Z. H., Fang, M., Huang, X. H., Bao, J. C., Gong, J. F., *Journal of Physical Chemistry C* **2007**, 111, 12609.
- Zurbuchen, M. A., Schlom, D. G., Streiffer, S. K., *Applied Physics Letters* **2001**, 79, 887.

Chapter 7. Conclusions & Future Work

In this thesis the synthesis, structural characterisation and self assembly of various nanocrystalline materials was investigated. Using solution phase chemical methods nanoparticles of gold, lead sulfide, lead selenide and palladium were produced. Various techniques including SHREM, HREM, XRD, EDS and SAED were then used to give a full characterisation of the as synthesised nanoparticles.

The major outcomes of this work will be presented below along with their relevance in comparison to current literature. The following sections will also give ideas for future research.

7.1 Nanoparticle Superlattices

By simple evaporation of a colloidal solution onto a TEM grid the formation of Au NPSLs was observed. To investigate their formation the concentration of the colloidal solution was varied and structural intermediates produced. It was shown that the superlattices grew from a hexagonally packed monolayer into an energetically unfavourable bilayer. The addition of a third layer of nanoparticles lead to thermodynamically preferred close cubic packing. The formation of an energetically unfavourable bilayer was found to be due to the presence of the organic capping ligand. This work provides a fundamental understanding of the formation of single species NPSLs and will be of value for future research.

Future Work

Future work should focus on the optimisation of conditions for growing NPSLs and the incorporation of various other NP types with the goal of producing binary nanoparticle superlattices (BNSLs).

The NPSLs formed here show a considerable amount of defects in their structure. Therefore the growth conditions need to be optimised to produce the largest, most defect free NPSLs possible. This will be accomplished by varying the temperature, pressure, solvent type and concentration of the colloidal solution. In order to produce

BNSLs a second type of monodisperse NP needs to be introduced to the colloidal solution. These also need to be highly monodisperse with a size distribution of $\sigma < 5\%$. The scope for this next stage of research is immense as it is only limited by the library of different nanoparticle types available. Recent studies have produced BNSLs with a wide array of analogous crystal structures including one example of quasicrystals possessing rotational symmetry but lacking translational symmetry {Shevchenko 2006, Talapin 2009}. These studies indicate that the structural investigation into different types of BNSLs is far from complete.

Full structural characterisation is required for all NPSLs formed. This includes defect analysis and investigation into their thermal stability. High thermal stability is an essential property if these types of materials are to be used in practical applications. Recent studies on Au NPSLs have shown them to be fluorescent and useful for SERS {Nishida 2009, Shibu 2009}. Therefore future research should also include the investigation of new properties and applications. This will be realised by conducting optical, electronic and magnetic measurements.

7.2 Solution Phase Syntheses of Lead Chalcogenide Nanoparticles

Through a hot injection method this study produced a wide array of PbS and PbSe nanoparticles. These included spherical, cubic and platelet morphologies. A new ligand exchange method was established which allows for facile fabrication of TGA capped PbSe nanoparticles. Thiol treatment of lead chalcogenide nanoparticles has been shown to have beneficial effects on PV device performance through shortening the interparticle distance and improved surface passivation {Barkhouse 2008}. Therefore, this new method is an exciting advance for the incorporation of lead chalcogenide nanoparticles into photovoltaic devices.

Future Work

The next stage in this work is a complete characterisation of the optical properties of the as synthesised PbS and PbSe nanoparticles. Absorption and photoluminescent profiles for each type of monodisperse lead chalcogenide nanoparticle is required.

Special focus needs to be placed on the sample used for capping ligand exchange as this will provide another means to observe the *in-situ* size selection procedure.

Lead chalcogenide nanoparticles have previously been shown to undergo multiple exciton generation (MEG); that is a quantum efficiency greater than 1. Recent work has demonstrated MEG in a photovoltaic device with an increase in internal gain of 2.7 times the quantum confined bandgap {Sukhovatkin 2009}. Therefore, a full calculation of quantum efficiency is also required for the monodisperse samples produced here to investigate their potential as MEG materials.

Recent studies have demonstrated power conversion efficiencies as high as 4.2 % from a PbS colloidal quantum dot photovoltaic device {Johnston 2008}. This shows that the field of harvesting IR radiation is seeing rapid progress. Therefore, the application of PbS-TGA nanoparticles into solar cells needs to be investigated by linking the PbS-TGA NPs to a conducting substrate. This can include but is not limited to indium tin oxide (ITO) and titania (TiO₂) surfaces or spheres. The next step will be their incorporation into a prototype cell to investigate the extraction of a photocurrent. After this proof of principle has been established a refinement of the nanoparticle size and shape can be performed to optimise the photocurrent from a working cell.

7.3 Synthesis, Characterisation and Growth of Palladium Nanoparticles

Through the use of a pressure reaction vessel (Fischer-Porter bottle) the growth of palladium nanoparticles was controlled to produce a large range of sizes and shapes. The developed method used organic surfactants as growth directing agents in a solution phase synthesis. It was shown that by varying the nature of the surfactant system the kinetics of nanoparticle growth could be controlled and hence the resulting size and shape of the palladium nanoparticles.

Thermodynamically preferred nanoparticle morphologies were formed when a strong binding surfactant was used due to a slow growth rate. When a weaker binding surfactant was introduced faster growth kinetics were observed resulting in the formation of pod-like and highly branched complex morphologies.

The observation of a tripod nanoparticle was the first evidence of a pod-like morphology for nanostructured palladium. Through SHREM experiments it was shown that the nanoparticle grew from a multiply twinned icosahedral core. This was the first direct evidence of complex growth from the highly symmetrical *fcc* crystal structure. This is an exciting result as the techniques established here both in synthesis and characterisation can be extended to all *fcc* materials.

The growth of the highly branched nanostructures was tracked in real time which showed that they grow from nanoparticle nuclei through tripod intermediates. A type of ultra-fast growth was observed to occur from the tripod intermediates which lead to high surface area nanostructures with high index facet terminated surfaces. This work therefore provides a novel route to high energy nanostructures from the solution phase.

The highly branched nanostructures showed excellent catalytic activity for the hydrogenation of nitrobenzene to aniline. The absorption and desorption of hydrogen into the nanostructures was also investigated which shows they are promising as hydrogen storage materials.

These results and the proposed growth mechanism contribute to the understanding of the formation of highly branched nanostructures from the highly symmetrical *fcc* crystal structure. The ultra-fast kinetic growth observed is not dependant on crystal facet energy and therefore provides a route to complex nanoparticle shapes from any nuclei morphology. The development of a room temperature solution phase synthesis for the formation of highly branched palladium nanoparticles is important for catalytic applications where high surface area and high index facets are known to greatly improve catalytic performance. The development of a synthetic method for the formation of pod-like and highly branched palladium nanoparticles is important for applications in catalysis, gas sensing and SERS devices.

Future Work

In the future work should be focussed on those highly branched palladium nanostructures. Their high surface area and high index surfaces make them very promising candidates for catalytic applications as these characteristics are both well known to increase catalytic performance. The synthetic method developed here is very appealing for industry as it is carried out at room temperature under a low pressure atmosphere. Also, the extraction of the nanoparticles is simple due to their relatively large size and mass. This reduces environmental impact of the synthesis as the solvents and surfactant can be distilled and re-used.

Further work should be done on this synthesis to make the as synthesised nanostructures more monodisperse. Gaining control over the degree of branching and the nature of the nanostructure surface will also allow for nanostructures with tailored catalytic properties.

Furthermore, this synthesis should be extended to other catalytically interesting noble metals such as Ag, Au and Pt. Finally an investigation into alloy nanostructures is required as alloys often show increased catalytic performance.

Further catalytic studies need to be carried out to investigate the selectivity of these structures towards different organic transformation reactions. An eventual application for these types of nanostructures is in catalytic converters in automobiles where they would be responsible for the removal of toxic gas species from the exhaust stream. Therefore, catalytic studies for the reduction of toxic gas species such as CO and NO_x are required. Furthermore, tuning of the morphology and surface nature of the metal nanoparticles offers the possibility of creating palladium nano-catalysts with tailored catalytic properties.

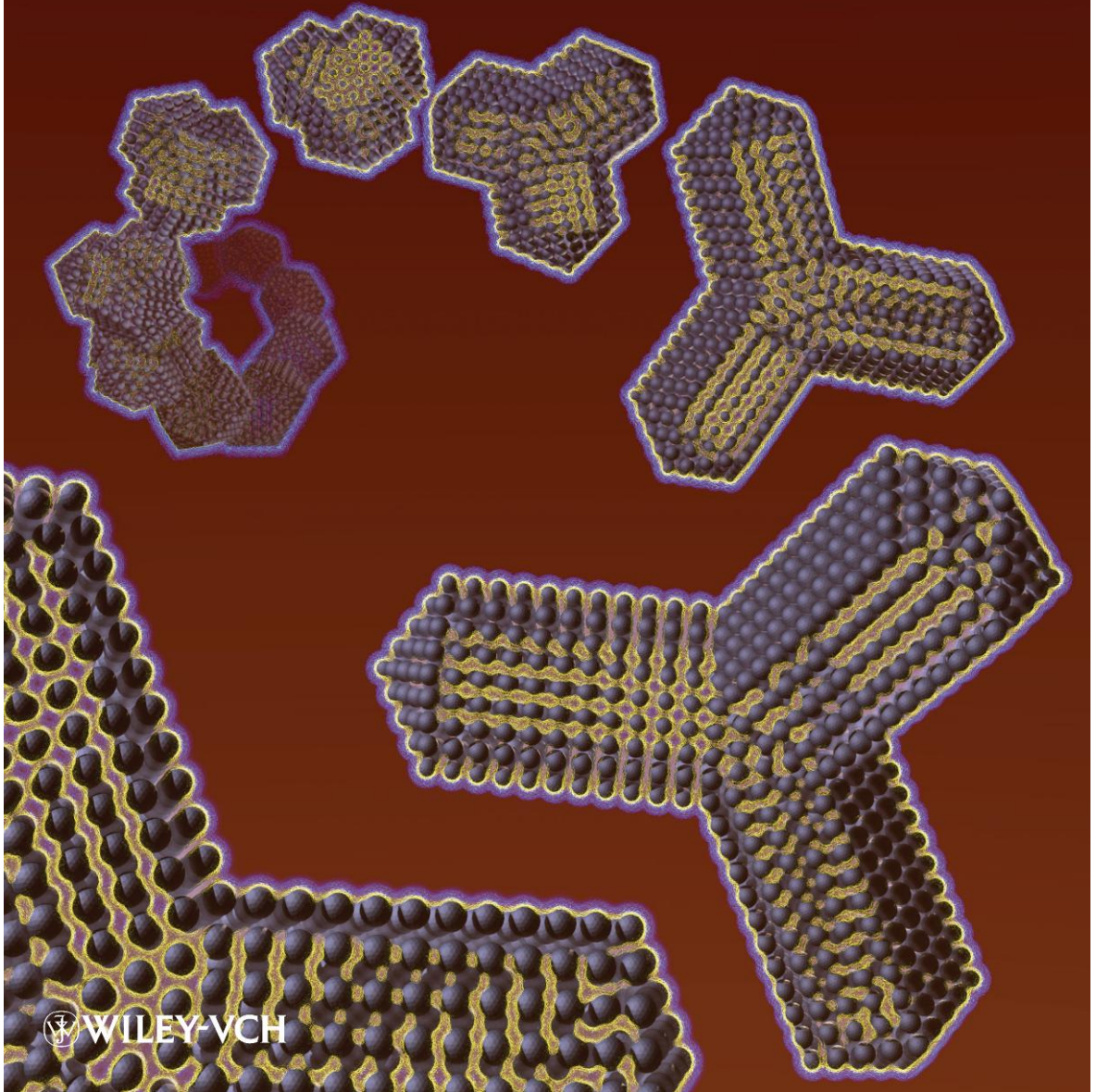
It has been shown above that the as synthesised palladium nanostructures absorb hydrogen however this was not performed quantitatively. Therefore, pressure-composition isotherms need to be carried out to investigate the %H loading for the nanostructures when exposed to hydrogen. This further work needs to include loading/unloading cycles and hysteresis analysis.

References

- Barkhouse, D. A. R., Pattantyus-Abraham, A. G., Levina, L., Sargent, E. H., *Acs Nano* **2008**, *2*, 2356.
- Johnston, K. W., Pattantyus-Abraham, A. G., Clifford, J. P., Myrskog, S. H., MacNeil, D. D., Levina, L., Sargent, E. H., *Applied Physics Letters* **2008**, *92*,
- Nishida, N., Shibu, E. S., Yao, H., Oonishi, T., Kimura, K., Pradeep, T., *Advanced Materials* **2008**, *20*, 4719.
- Shevchenko, E. V., Talapin, D. V., Kotov, N. A., O'Brien, S., Murray, C. B., *Nature* **2006**, *439*, 55.
- Shibu, E. S., Kimura, K., Pradeep, T., *Chemistry of Materials* **2009**, *21*, 3773.
- Sukhovatkin, V., Hinds, S., Brzozowski, L., Sargent, E. H., *Science* **2009**, *324*, 1542.
- Talapin, D. V., Shevchenko, E. V., Bodnarchuk, M. I., Ye, X. C., Chen, J., Murray, C. B., *Nature* **2009**, *461*, 964.

Appendix

ADVANCED MATERIALS



 WILEY-VCH

Synthesis and Structural Characterization of Branched Palladium Nanostructures

By John Watt, Neil Young, Sarah Haigh, Angus Kirkland, and Richard D. Tilley*

The synthesis of inorganic nanocrystals with controllable morphologies is a key goal in modern materials chemistry and has attracted substantial interest in recent years.^[1] The shape- and size-dependant properties of nanoparticles are well established and a fine degree of control over size and morphology can lead to the formation of materials with specific chemical and physical properties.^[2] For example, anisotropic morphologies such as branched nanocrystals that include bipods, tripods, tetrapods, and multipods show great promise in many applications, as they often exhibit unique electronic, magnetic, photonic, and catalytic properties.^[2]

Palladium is used extensively in industry as a heterogeneous catalyst with significant focus on the low temperature catalytic reduction of automobile emissions and in Suzuki, Heck, and Stille coupling reactions.^[3a,b] For catalytically active materials, anisotropic shape can greatly enhance performance by increasing surface area and selectively, exposing specific (high-index) crystal facets.^[3a,b] For example, Meng et al. produced anisotropic palladium nanothorns that showed increased catalytic performance for the oxidation of formic acid.^[3c] Palladium is also a promising material for hydrogen storage and gas-sensing applications, as it absorbs hydrogen in high concentrations.^[4] Nanostructured palladium also shows potential as a surface-enhanced Raman spectroscopy (SERS) substrate, where the spectral range and enhancement intensity have been shown to be morphology dependent.^[5] Thus, the development of synthetic methods for the formation of palladium nanoparticles with controlled morphologies, particularly pod-like structures, is important for a range of future applications.

Palladium nanoparticles have previously been synthesized using a number of different methods.^[6–8] Choo et al. produced isotropic morphologies through the controlled reduction of PdCl₂.^[6] Xiong et al. formed anisotropic palladium structures including nanobars, nanorods, triangular, and hexagonal particles using ethylene glycol as the reductant.^[7] Teng et al. showed the evolution of palladium nanoparticles into ultrathin nanowires.^[8]

The controlled growth of branched or pod-like shapes is well established in polymorphic materials such as CdS and CdSe.^[9] For these, pod-like shapes are obtained through the controlled nucleation of a zinc-blende core followed by the growth of wurtzite phase branches, which occurs along the inherently anisotropic c-axis of the hexagonal unit cell. However, this type of polymorphism is not seen in most face centered cubic (fcc) metals, such as palladium. Thus, while solution methods for producing faceted polyhedra structures are well established for fcc materials, the formation of pod-like structures is less common, and has not previously been achieved for palladium.

In this work, we present a simple protocol for solution phase synthesis of pod-like palladium nanostructures at room temperature followed by their characterization. The particles are formed in a pressure reaction vessel (Fischer–Porter bottle) that allows control over the reaction pressure. This method has previously been shown to be effective for the formation of metal nanoparticles.^[10] The use of organic surfactant molecules to control growth is commonly used in nanoparticle synthesis. Here, we show that by varying the nature of the organic surfactant we are able to shift the growth conditions from a thermodynamic to a kinetic regime, and thus induce anisotropy and control the final morphology of the particles. To our knowledge, this is the first evidence for the synthesis of nanostructured palladium pod-like structures.

It is well established that by using surfactants with different functional groups that have different binding strengths, such as acids or amines, the morphology of the resulting nanoparticles may be controlled.^[10] To compare the effects of surfactant in our system, two experiments were performed. The first used pure oleylamine as surfactant, which was chosen as it has previously been shown to be effective in forming platinum nanoparticles of various shapes.^[11] The second reaction system contained a 1:1 mixture of oleylamine and oleic acid. Oleic acid was chosen as the second surfactant as use of carboxylic-acid functionalities have been shown to induce structural change in nickel colloids.^[12] In this study, experiments were each reacted for 1 h at room temperature and were carried out under 3 bar of hydrogen gas (1 bar = 10⁵ Pa).

* Dr. R. D. Tilley, J. Watt
School of Chemical and Physical Sciences,
Diamond Institute of Advanced Materials and Nanotechnology
Victoria University of Wellington (New Zealand)
Email: richard.tilley@vuw.ac.nz
Dr. N. Young, Dr. S. Haigh, Prof. A. Kirkland
Department of Materials
University of Oxford (UK)
Parks Road, Oxford OX1 3PH (United Kingdom)

DOI: 10.1002/adma.200900272

Figure 1 shows transmission electron microscopy (TEM) images that illustrate control over nanoparticle morphology. Figure 1a shows a low-resolution TEM image of palladium nanoparticles when pure oleylamine was used as the surfactant. The particles are predominantly formed as polyhedra that are (6 ± 1.5) nm in size. Figure 1b shows a low-resolution TEM image of pod-like palladium nanostructures formed when using a surfactant mixture of 1:1 oleylamine and oleic acid. From analysis

S
a
v
E
C
U
E
DOI:



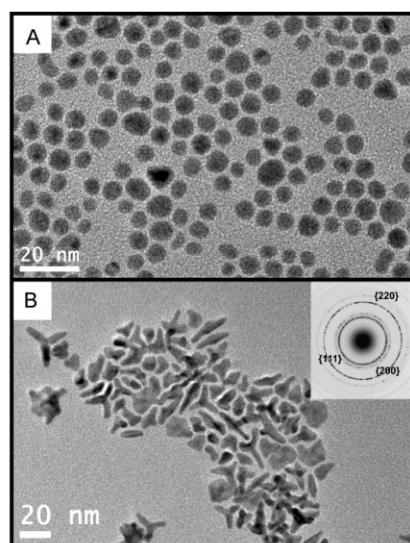


Figure 1. TEM images of palladium nanoparticles prepared after 1 h at room temperature. A) Isotropic particles prepared with oleylamine as surfactant and B) anisotropic particles formed when using a 1:1 mixture of oleylamine and oleic acid.

of TEM images of over 2000 particles, the relative yields of morphologies formed were found to be 17% bipods, 28% tripods, and 7% multipods. The remainder of the sample was made up of particles with random anisotropic morphologies.

The above experiment illustrates that the organic surfactant has a strong effect on the final nanoparticle shape, and that by changing the surfactant we can induce anisotropy in the palladium nanoparticles.

The reaction with pure oleylamine produced polyhedra as shown in Figure 1a. The formation of nanostructured polyhedra is common for fcc metals, including palladium. Berhault et al. produced icosahedra in a seed-mediated process, and Lim et al. have produced icosahedra and decahedra using poly(vinyl) pyrrolidone as a stabilizer.^[13] Polyhedra of fcc materials have an isotropic and symmetric shape that preferentially exposes low-energy {111} facets. For the size regime observed here, polyhedra are widely accepted as thermodynamically stable morphologies for palladium nanoclusters.^[13a,14] This suggests that with pure oleylamine as the surfactant, nanoparticle growth is occurring under thermodynamic conditions.

When oleic acid is introduced into the surfactant system, in a 1:1 ratio with oleylamine, branched or pod-like structures are formed, as shown in Figure 1b. The bipod particles display two-fold symmetry, which has previously been observed for palladium in the form of nanorods and rectangular nanoparticles.^[7b,15] The formation of tripods with three-fold symmetry is to our knowledge the first evidence of this type of morphology for palladium, and is hence the focus of the present work.

Further experiments were carried out in an attempt to increase the yield of tripods; however, this resulted in a maximum yield of 40%. It is apparent that in this system Fischer–Porter bottle

synthesis does not provide precise experimental control. This is most likely due to thermal gradients associated with heat transfer from the reaction oven to the reaction solution through the bottle. This will cause inhomogeneous nucleation, resulting in a range of particle shapes and sizes.

Branched structures have previously been observed for fcc metals other than palladium for reactions carried out under kinetic control. Chen et al. used kinetic control to explain the formation of branched platinum nanostructures in a polyol synthesis, and Lou et al. presented a surfactant-free synthesis of hyperbranched nanostructures where the branch growth was kinetically controlled, and occurred in nonspecific directions.^[16,17] Chen et al. produced pod-like gold nanocrystals with various degrees of branching, and Maksimuk et al. showed the formation of platinum bipods, tripods, and multipods along with the self-assembly of the as-synthesized tripods.^[18,19]

The formation of anisotropic morphologies from fcc materials requires breaking the crystal symmetry and control over the nature of the growth regime.^[20] An investigation of nucleation and growth mechanism is therefore essential for an understanding of how anisotropy arises from fcc palladium in the present system. To help elucidate these processes, experiments were carried out to isolate nanoparticle intermediates by varying the reaction time. The results are shown in Figure 2.

Reaction times were shortened to 10 min and 30 min and the corresponding nanocrystals formed at those times are shown in Figure 2a and b, respectively. Figure 2c shows a fully formed tripod after a 1 h reaction time.

The nanocrystal in Figure 2a is 3.5 nm in size, and shows multiple twinning, three-fold symmetry, and indications of the start of branched growth. Through image interpretation, the left-hand side and lower right-hand side of the particle show {110} terminated facets on each side of a twin plane. The rest of the particle contains unresolved lattice planes. Figure 2b shows a nanocrystal with the tripod arms beginning to grow. The nanocrystal has grown to 8 nm in size with branches growing to 5 nm. The aspect ratio of the arms is 1.5. The nanoparticle is still multiply twinned, with each arm possessing a single twin plane running along the direction of the arm. Figure 2c shows a fully formed tripod of 16 nm in size. The arms have grown to 12 nm with aspect ratios of 3. The presence of the same twin relationships indicates that this particle is formed from the intermediates shown.

As demonstrated above, the formation of anisotropic morphologies from fcc metals requires i) twinning in the nanoparticle nuclei and ii) kinetically controlled growth conditions.

Palladium adopts the highly symmetrical fcc crystal structure, and that does not contain any inherent anisotropy, which means that to break the crystal symmetry nanoparticle nuclei need to form with defects, such as twin planes. The final particle morphology is then directly dependent on nature of the twinning in the nuclei. For example, the formation of hexagonal platelets and nanotriangles has been explained by the presence of a single twin along the flat basal plane of the nuclei.^[7a,14] In this case, the formation of stacking faults gives rise to re-entrant edges or step edges that can be energetically favorable for adatom addition.^[21]

The selective binding or nonbinding of surfactant molecules to different facets of the growing nanocrystal can also explain the

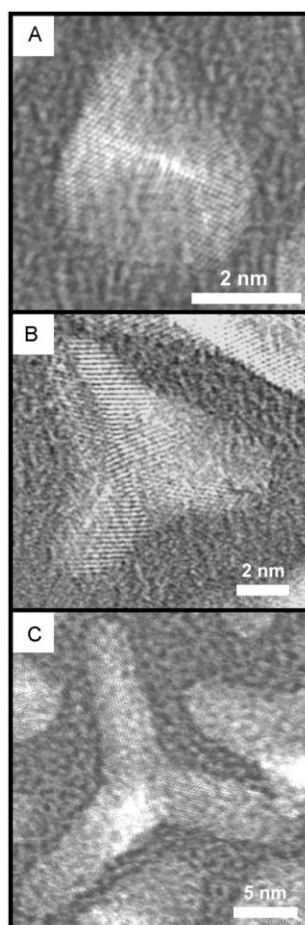


Figure 2. HRTEM images of isolated palladium tripod intermediates after differing reaction times: A) after 10 min, B) after 30 min, and C) after 1 h, a fully formed tripod.

emergence of anisotropy, wherein surface-selective capping reduces the energy of the bound facet and restricts the growth in this direction. Therefore, growth is promoted in the opposite directions leading to anisotropy. This is shown in the formation of nanorods with cetyltrimethylammonium bromide (CTAB) as surfactant, and with the surface-selective capping of bromide species on growing palladium nanostructures.^[1b,22]

In the present system, the carboxylic-acid functionality of oleic acid possesses a weaker binding strength to palladium when compared to the amine functionality of oleylamine.^[23] Particles growing with only oleylamine as a surfactant will therefore experience a strong stabilization of the growing faces, resulting in thermodynamically stable morphologies. When oleic acid is introduced into the surfactant system, there is a destabilization of

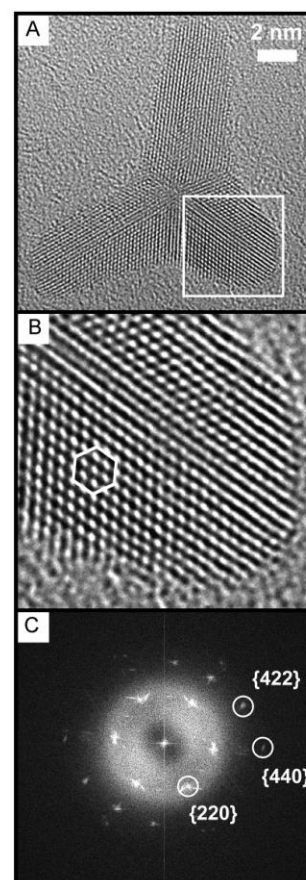


Figure 3. A) Aberration-corrected HRTEM image of a palladium tripod viewed down the $[111]$ zone axis. B) Enlargement of the hexagonal atomic packing characteristic of an arm in a $\langle 111 \rangle$ orientation. C) Power spectrum for the particle shown in A).

the growing particle surfaces, leading to kinetic growth conditions and anisotropy in the resulting nanoparticles. In our system, the oleic acid binds weakly to the faces along the direction of the tripod arms allowing fast growth in these directions.

The emergence of a particle with three-fold symmetry is unexpected for fcc systems, and therefore a comprehensive investigation into the particle twinning is required. An understanding of the internal structure is critical to determine the mechanism of particle growth. This will be valuable for future work with all nanostructured fcc materials.

Figure 3a shows an aberration-corrected HRTEM image of an as-synthesized palladium tripod. A close-up projection of the marked area in Figure 3a, shown in Figure 3b, clearly shows the hexagonal symmetry of the atomic packing. The power spectrum

is shown in Figure 3c, and can be indexed as fcc palladium projected along a $\langle 111 \rangle$ zone axis. Each arm of the particle in Figure 3a shows a $\{111\}$ twin plane running along its entire length, and from the power spectrum it is clear that the growth direction of the arm is in a $\langle 112 \rangle$ direction. The streaking of the spots observed in the power spectrum can be ascribed to the stacking faults in the tripod arms.^[24] The observed projection of the tripod center has been seen previously for fcc icosahedral particles on an axis of three-fold symmetry, indicating a $\langle 111 \rangle$ orientation.^[25]

To confirm the structure of the tripod, a tilting experiment was carried out on an isolated tripod. Figure 4a shows the particle with

the specimen stage set to standard viewing conditions. The tripod is viewed along a $\langle 111 \rangle$ direction, as previously observed. Figure 4b shows the particle with the specimen stage tilted by 14° in the goniometer x direction, and it is clear from the atomic packing that the particle has changed its orientation in the electron beam. The power spectrum of the entire particle is shown in Figure 4c, and contains a superposition of spots from an fcc structure viewed down $\langle 111 \rangle$ and $\langle 110 \rangle$ zone axes. This corresponds to the exposed facets on the tripod arms with additional spots originating from a $\langle 112 \rangle$ orientation of the icosahedral center of the particle.

Due to heating in the electron beam, a reconstruction of the particle is also seen over the timescale of observation, as atoms migrate to lower-energy positions that are thermodynamically more stable, supporting the proposed kinetic nature of the tripod morphology. The $\langle 112 \rangle$ projection of the central core has previously been observed in the HRTEM analysis of fcc icosahedra.^[26]

HRTEM analysis confirms that the central core of the particle is a multiply twinned fcc icosahedron. Face centered cubic icosahedra possess two-, three-, and five-fold axes of symmetry, and consist of 20 $\{111\}$ terminated tetrahedral building blocks in $\{111\}$ twin relationship. In order to fill 3D space, the tetrahedral subunits are strained, and it has been shown that the lowest-energy icosahedral motifs contain re-entrant facets.^[27] These provide higher-surface-energy facets on which the energy barrier to adatom addition is lowered, leading to growth being promoted in the specific direction.^[21a] In icosahedra nuclei of a certain size, the strain may be relieved by the formation of three equivalent re-entrant edges along the $\langle 112 \rangle$ direction. Subsequent kinetic growth along these directions can therefore lead to tripod formation. Further experimental and modeling work is required to confirm the growth mechanism.

Scheme 1 shows an outline of the reaction pathway to palladium nanostructures. The Pd (II) precursor is first reduced to form multiply twinned icosahedral nuclei 3.5–4 nm in size. Control over the growth regime then dictates the final nanoparticle morphology.

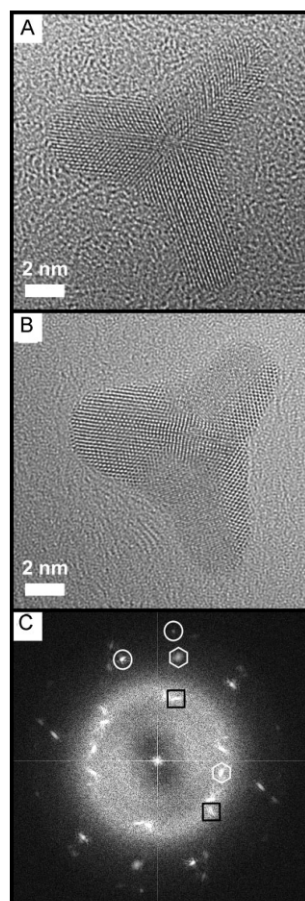
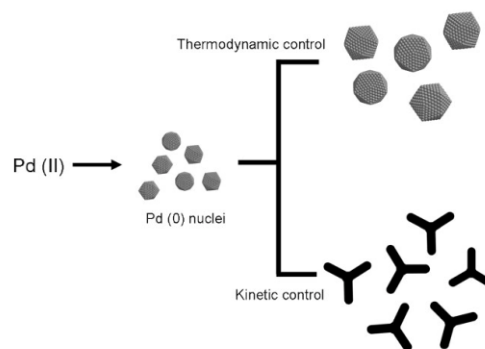


Figure 4. Aberration corrected HRTEM images from a tilting experiment performed on an isolated tripod. A) Particle viewed along a $\langle 111 \rangle$ zone axis. B) Particle tilted through 14° with the corresponding power spectrum shown in C). The spots marked with white circles and black squares correspond to the $\{111\}$ and the $\{110\}$ facets of the tripod arms, respectively, and the spots marked with white hexagons correspond to the $\langle 112 \rangle$ orientation of the particle core.



Scheme 1. Schematic showing proposed growth mechanism for palladium nanostructures. Nuclei are formed from the reduction of the palladium precursor. Under thermodynamic growth conditions, these form isotropic particles, whereas under kinetic growth control they form anisotropic pod-like shapes.

Under thermodynamic growth conditions, icosahedral nuclei will commonly retain their morphology, and this is indeed what is seen in the above experiments, when pure oleylamine is used as the surfactant.^[13a] Nanoparticles formed under thermodynamic growth conditions typically show an isotropic aspect dominated by low-energy facets. These types of particles were observed in Figure 1a. Such equilibrium structures are produced when the rate of adatom diffusion to thermodynamically stable positions is greater than adatom arrival.^[20] Oleylamine leads to a high degree of stabilization, which provides hindrance to incoming adatoms promoting the formation of thermodynamically stable morphologies.

However, under kinetic control, when a 1:1 mixture of oleylamine and oleic acid is used, anisotropic growth can occur. In this system, kinetically controlled growth is introduced through the addition of oleic acid to the surfactant system. A kinetic-growth regime requires the rate of adatom arrival to be greater than adatom diffusion.^[20] Here, this is achieved through the addition of oleic acid, where the weaker binding strength of the carboxylic-acid functionality destabilizes the surface of the growing particle and allows for increased rate of adatom addition.

Anisotropic nanostructures are not uncommon for fcc materials; for example, nanorods have been synthesized for noble metals Au, Ag, and Pd.^[7a,28] However, these were grown from the elongation of decahedral nuclei, and did not show a branched structure. In the present study, we are able to change the growth conditions to produce the first pod-like particles from icosahedral nuclei for palladium. Icosahedral nuclei have recently been used to explain the formation of pod-like structures in platinum, but direct evidence for the morphology of the nuclei was not provided.^[19b] Therefore, we also provide the first direct evidence of pod-like growth from icosahedral nuclei for any fcc metal.

We have synthesized palladium nanoparticles of varying shapes using a pressure reaction vessel (Fischer–Porter bottle). By varying the nature of the surfactant system, we were able to shift from a thermodynamic growth regime, favoring isotropic morphologies, into kinetic growth control, which results in branched morphologies. The formation of branched or pod-like structures is the first evidence of these morphologies in palladium metal nanoparticles.

High-resolution TEM images show that the palladium nanoparticles grow from multiply twinned fcc icosahedral nuclei. Surface-selective capping by the organic surfactant determines the resulting morphology. When a surfactant with strong binding characteristics is used, a thermodynamic growth regime occurs, and the nuclei grow into isotropic shapes. When a surfactant with weaker binding characteristics is introduced, the growth regime becomes kinetic in nature. The combination of twinning in the nuclei and kinetic growth conditions causes anisotropic branch growth to occur, and pod-like structures are formed. When this occurs in three equivalent directions, a tripod morphology results.

These results and the proposal of a growth mechanism will contribute to the understanding of anisotropic growth from highly symmetrical fcc crystal structures. The development of a synthetic method for the formation of pod-like palladium nanoparticles is important for applications in catalysis, gas sensing, and SERS devices.

Experimental

In a typical synthesis, 0.1 mmol of palladium precursor (bis(acetonitrile) palladium dichloride, 99%, Aldrich) was added to 1 mL of toluene. To this was added 10 equivalents of organic surfactant in total. The palladium precursor was then decomposed under hydrogen in a pressure reaction vessel (Fischer–Porter bottle). Samples were purified by addition of an equal amount of methanol to flocculate the nanoparticles, use of a centrifuge at 14 000 rpm for collection, and subsequent washing with dichloromethane and toluene. The samples for TEM studies were prepared by resuspending the precipitate in toluene. One drop of toluene suspension was placed on a copper TEM grid and allowed to evaporate under ambient conditions. The TEM images and corresponding diffraction patterns in Figures 1 and 2 were obtained using a JEOL 2010 operated at an acceleration voltage of 200 keV. Those shown in Figures 3 and 4 were obtained using a JEOL 2200MCO field-emission TEM with double aberration correctors at Oxford University Department of Materials.

Acknowledgements

R.D.T. and J.W. gratefully acknowledged financial support from the MacDiarmid Institute, VUW, RSNZ, and Education New Zealand. A.I.K., N.Y., and S.H. gratefully acknowledged financial support from EPSRC (Grant EP/F048009/1).

Received: January 24, 2009

Revised: February 23, 2009

Published online: April 14, 2009

- a) Y. W. Jun, J. S. Choi, J. Cheon, *Angew. Chem. Int. Ed.* **2006**, *45*, 3414. b) C. J. Murphy, T. K. San, A. M. Gole, C. J. Orendorff, J. X. Gao, L. Gou, S. E. Hunyadi, T. Li, *J. Phys. Chem. B* **2005**, *109*, 13857. c) C. Burda, X. B. Chen, R. Narayanan, M. A. El-Sayed, *Chem. Rev.* **2005**, *105*, 1025.
- Nanoscale Materials in Chemistry*, (Eds: K. J. Klabunde), John Wiley & Sons, **2001**.
- a) N. Tian, Z. Y. Zhou, S. G. Sun, Y. Ding, Z. L. Wang, *Science* **2007**, *316*, 732. b) R. Narayanan, M. A. El-Sayed, *Nano Lett.* **2004**, *4*, 1343. c) H. Meng, S. Sun, J.-P. Masse, J.-P. Dodelet, *Chem. Mater.* **2008**, *20*, 6998.
- a) M. Suleiman, N. M. Jisrawi, O. Dankert, M. T. Reetz, C. Bahtz, R. Kirchheim, A. Pundt, *J. Alloys Compd.* **2003**, *356*, 644. b) S. Kishore, J. A. Nelson, J. H. Adair, P. C. Eklund, *J. Alloys Compd.* **2005**, *389*, 234.
- a) L. A. Dick, A. D. McFarland, C. L. Haynes, R. P. Van Duyne, *J. Phys. Chem. B* **2002**, *106*, 853. b) R. Narayanan, M. A. El-Sayed, *J. Phys. Chem. B* **2004**, *108*, 5726. c) T. R. Jensen, L. Kelly, A. Lazarides, G. C. Schatz, *J. Cluster Sci.* **1999**, *10*, 295. d) J. P. Kottmann, O. J. F. Martin, D. R. Smith, S. Schultz, *Phys. Rev. B* **2001**, *64*, 235402. e) S. H. Im, Y. T. Lee, B. Wiley, Y. Xia, *Angew. Chem. Int. Ed.* **2005**, *44*, 2154.
- H. Choo, B. L. He, K. Y. Liew, H. F. Liu, J. L. Li, *J. Mol. Catal. A: Chem.* **2006**, *244*, 217.
- a) Y. J. Xiong, J. M. McLellan, J. Y. Chen, Y. D. Yin, Z. Y. Li, Y. N. Xia, *J. Am. Chem. Soc.* **2005**, *127*, 17118. b) Y. J. Xiong, H. G. Cai, B. J. Wiley, J. G. Wang, M. J. Kim, Y. N. Xia, *J. Am. Chem. Soc.* **2007**, *129*, 3665.
- X. W. Teng, W. Q. Han, W. Ku, M. Hucker, *Angew. Chem. Int. Ed.* **2008**, *47*, 2055.
- a) J. Joo, H. B. Na, T. Yu, J. H. Yu, Y. W. Kim, F. Wu, J. Z. Zhang, T. Hyeon, *J. Am. Chem. Soc.* **2003**, *125*, 11100. b) Y. W. Jun, S. M. Lee, N. J. Kang, J. Cheon, *J. Am. Chem. Soc.* **2001**, *123*, 5150. c) X. Peng, *Adv. Mater.* **2003**, *15*, 459. d) L. Manna, E. C. Scher, A. P. Alivisatos, *J. Am. Chem. Soc.* **2000**, *122*, 12700. e) S. Asokan, K. M. Krueger, V. L. Colvin, M. S. Wong, *Small* **2007**, *3*, 1164.

- [10] E. Ramirez, S. Jansat, K. Philippot, P. Lecante, M. Gomez, A. M. Masdeu-Bulto, B. Chaudret, *J. Organomet. Chem.* **2004**, *689*, 4601.
- [11] a) J. T. Ren, R. D. Tilley, *J. Am. Chem. Soc.* **2007**, *129*, 3287. b) J. Ren, R. D. Tilley, *Small* **2007**, *3*, 1508.
- [12] J. S. Bradley, B. Tesche, W. Busser, M. Masse, R. T. Reetz, *J. Am. Chem. Soc.* **2000**, *122*, 4631.
- [13] a) G. Berhault, M. Bausach, L. Bisson, L. Becerra, C. Thomazeau, D. Uzio, *J. Phys. Chem. C* **2007**, *111*, 5915. b) B. Lim, Y. J. Xiong, Y. N. Xia, *Angew. Chem. Int. Ed.* **2007**, *46*, 9279.
- [14] J. L. Elechiguerra, J. Reyes-Gasga, M. J. Yacaman, *J. Mater. Chem.* **2006**, *16*, 3906.
- [15] Y. Sun, L. H. Zhang, H. W. Zhou, Y. M. Zhu, E. Sutter, Y. Ji, M. H. Rafailovich, J. C. Sokolov, *Chem. Mater.* **2007**, *19*, 2065.
- [16] J. Y. Chen, T. Herricks, Y. N. Xia, *Angew. Chem. Int. Ed.* **2005**, *44*, 2589.
- [17] X. W. Lou, C. L. Yuan, L. A. Archer, *Chem. Mater.* **2006**, *18*, 3921.
- [18] S. H. Chen, Z. L. Wang, J. Ballato, S. H. Foulger, D. L. Carroll, *J. Am. Chem. Soc.* **2003**, *125*, 16186.
- [19] a) S. Maksimuk, X. W. Teng, H. Yang, *Phys. Chem. Chem. Phys.* **2006**, *8*, 4660. b) S. Maksimuk, X. W. Teng, H. Yang, *J. Phys. Chem. C* **2007**, *111*, 14312.
- [20] Y. Yin, A. P. Alivisatos, *Nature* **2005**, *437*, 664.
- [21] a) J. W. Lee, U. J. Chung, N. M. Hwang, D. Y. Kim, *Acta Crystallogr. Sect. A: Found. Crystallogr.* **2005**, *61*, 405. b) R. Jagannathan, R. V. Mehta, J. A. Timmons, D. L. Black, *Phys. Rev. B* **1993**, *48*, 13261.
- [22] Y. J. Xiong, Y. N. Xia, *Adv. Mat.* **2007**, *19*, 3385.
- [23] a) S. Ahrland, J. Chatt, N. R. Davies, *Q. Rev. Chem. Soc.* **1958**, *12*, 265. b) Y. W. Jun, J. H. Lee, J. S. Choi, J. Cheon, *J. Phys. Chem. B* **2005**, *109*, 14795.
- [24] M. A. Zurbuchen, D. G. Schlom, S. K. Streiffer, *Appl. Phys. Lett.* **2001**, *79*, 887.
- [25] a) M. Flueli, R. Spycher, P. A. Stadelmann, P. A. Buffat, J. P. Borel, *Europhys. Lett.* **1988**, *6*, 349. b) J. M. Penisson, A. Renou, *J. Cryst. Growth* **1990**, *102*, 585.
- [26] a) J. M. Penisson, A. Renou, *Z. Phys. D: At, Mol. Clusters* **1989**, *12*, 113. b) A. I. Kirkland, D. A. Jefferson, D. Tang, P. P. Edwards, *Proc. R. Soc. A* **1991**, *434*, 279.
- [27] a) L. D. Marks, *Phil. Mag. A* **1984**, *49*, 81. b) L. D. Marks, D. J. Smith, *J. Microsc.* **1981**, *54*, 425. c) J. Buhler, Y. Prior, *J. Cryst. Growth* **2000**, *209*, 779.
- [28] a) P. L. Gai, M. A. Harmer, *Nano Lett.* **2002**, *2*, 771. b) H. Y. Chen, Y. Gao, H. R. Zhang, L. B. Liu, H. C. Yu, H. F. Tian, S. S. Xie, J. Q. Li, *J. Phys. Chem. B* **2004**, *108*, 12038.

Ultrafast Growth of Highly Branched Palladium Nanostructures for Catalysis

John Watt,[†] Soshan Cheong,[†] Michael F. Toney,[‡] Bridget Ingham,[§] James Cookson,[‡] Peter T. Bishop,[‡] and Richard D. Tilley^{†,*}

[†]Victoria University of Wellington MacDiarmid Institute of Advanced Materials and Nanotechnology, Kelburn Pde, Wellington, New Zealand, [‡]Stanford Synchrotron Radiation Laboratory, 2575 Sand Hill Road, Menlo Park, California 94025, [§]Industrial Research Limited MacDiarmid Institute of Advanced Materials and Nanotechnology, 69 Gracefield Road, Lower Hutt, New Zealand, and [‡]Johnson Matthey Technology Centre, Blount's Court, Sonning Common, Reading, RG4 9NH, U.K.

ABSTRACT Palladium is widely used as a catalyst in pharmaceutical and chemical syntheses as well as in the reduction of harmful exhaust emissions. Therefore, the development of high performance palladium catalysts is an area of major concern. In this paper, we present the synthesis of highly branched palladium nanostructures in a simple solution phase reaction at room temperature. By varying the nature of the organic stabilizer system we demonstrate control over the reaction kinetics and hence the shape of the nanostructures. Investigations into the structural evolution of the nanostructures show that they form from multiply twinned face centered cubic (fcc) nanoparticle nuclei. Reaction kinetics then determine the resulting shape where ultrafast growth is shown to lead to the highly branched nanostructures. These results will contribute greatly to the understanding of complex nanoparticle growth from all fcc metals. The nanostructures then show excellent catalytic activity for the hydrogenation of nitrobenzene to aniline.

KEYWORDS: palladium · nanocrystals · nanoparticles · catalysis · X-ray diffraction · electron microscopy

The synthesis of inorganic nanocrystals with controllable morphologies is a key goal in modern materials science and has attracted substantial interest in recent years.^{1–4} The shape and size dependent properties of nanoparticles are well established and a fine degree of control over size and morphology can lead to the formation of materials with specific chemical and physical properties. Complex morphologies, in particular, show great promise in many applications as they often exhibit unique electronic, magnetic, photonic, and catalytic properties.⁵

Palladium is well-known for its ability to absorb hydrogen in high concentrations and is a promising material in hydrogen storage and gas sensing applications.^{6,7} Nanostructured palladium also shows potential as a surface enhanced Raman spectroscopy (SERS) substrate where the spectral range and intensity enhancement have been shown to be morphology dependent.^{8,9}

Palladium is also the most versatile and widely used catalyst in pharmaceutical and

fine chemical syntheses.¹⁰ Here, both homogeneous and heterogeneous palladium-based catalysts are required to deliver high selectivities in the desired functional group transformations or couplings. Additionally, palladium serves as an important catalyst for the reduction of harmful exhaust emissions. In this situation, poor accessibility and poisoning of the metal surface can reduce overall efficiency.¹¹ Therefore, development of high surface area, high performance palladium catalysts is a major concern. To be an economically viable catalyst, the amount of metal consumed in production must be minimized without a reduction in catalytic performance. Highly branched nanostructures are promising candidates as they possess a large surface area available for reaction, while selectively exposing specific (high index) crystal facets.

In the present study we demonstrate the formation of extensively branched palladium nanostructures in a room temperature solution phase synthesis. The synthesis is performed in a pressure reaction vessel (Fischer–Porter bottle) which gives control over atmospheric pressure and composition. This method has previously been shown to be effective for the formation of spherical metal nanoparticles.¹² The use of organic surfactant molecules to control growth is commonly used in nanoparticle synthesis. Here we show that by varying the nature of the organic surfactant system we are able to control the growth kinetics and form highly branched nanostructures.

RESULTS

In solution phase nanoparticle synthesis, variation of the organic stabilizer is routinely used to control nanoparticle morphology.¹² Here we demonstrate through two experiments that by changing the sur-

*Address correspondence to Richard.Tilley@vuw.ac.nz.

Received for review September 23, 2009 and accepted December 11, 2009.

Published online December 22, 2009. 10.1021/nn901277k

© 2010 American Chemical Society

factant system we can induce structural changes in palladium nanostructures. The first experiment we describe used solely oleylamine as the surfactant.

Oleylamine was selected as it has previously been effective for the shape control of platinum nanostructures in the Fischer–Porter bottle.^{13,14} The second experiment employed the organic surfactants oleic acid and oleylamine in a 1:1 ratio. The addition of a carboxylic acid functionality has previously been shown to induce shape change in nickel colloids.¹⁵ Both reactions were carried out at room temperature under 3 bar (1 bar = 10^5 Pa) hydrogen for 160 min.

Figure 1a shows a transmission electron microscopy (TEM) image of the reaction product when oleylamine only is used as the surfactant. As can be seen in the image, the nanoparticles consist of nanostructured polyhedra 6 ± 1.5 nm in size. Figure 1b shows a high resolution transmission electron microscopy (HRTEM) image of one of the polyhedra. The particle is characterized as a multiply twinned face centered cubic (fcc) icosahedra viewed along a $\langle 112 \rangle$ zone axis.^{16,17}

Figure 1c shows a low magnification TEM image of the highly branched palladium nanostructures synthesized in a surfactant system containing a 1:1 ratio of oleic acid and oleylamine. The palladium nanostructures are 85 ± 15 nm in size and each particle displays extensive branching with the branches growing radially away from a central core. The selected area diffraction (SAED) pattern of the nanoparticles observed is shown in the inset and can be readily indexed to the fcc structure of palladium. Figure 1d shows a higher magnification image of a single nanostructure. The particle branches have a broad leaflike structure and exhibit a rounded tip, similar to dendritic growth.^{18–20} Flower-like nanostructures have previously been produced for Pd and Pt; however, these were grown hierarchically from smaller nanoparticle building blocks and hence were covered by low index facets.^{21,22}

The above set of experiments illustrates that changing the surfactant system directly affects the nanoparticle shape. The reaction with oleylamine produced polyhedra as shown in Figure 1a,b. Polyhedra are commonly formed for palladium and are widely accepted as a thermodynamically favored morphology.^{23,24}

When oleic acid is introduced, in a 1:1 ratio with oleylamine, highly branched nanostructures are formed which possess a high surface area to volume ratio. This presents an interesting result as the formation of these types of highly branched nanostructures terminated by high index facets has not previously been observed for palladium. In solution phase synthesis, palladium nanostructures typically form as thermodynamically favored polyhedra structures or 1-D nanorods.^{25–27} The surfaces of these nanostructures are limited to low index facets due to their lower surface–solution interface energy.^{28,29}

www.acsnano.org

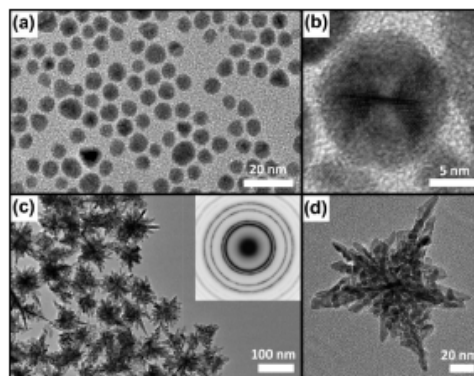


Figure 1. Transmission electron microscopy (TEM) images of palladium nanostructures prepared after 160 min at room temperature: (a) polyhedra nanoparticles formed using purely oleylamine as surfactant, (b) high resolution image of one of the polyhedra nanoparticles characterized as a multiply twinned fcc icosahedra, (c) highly branched nanostructures formed using a 1:1 mixture of oleylamine and oleic acid, and (d) high resolution image of one of the nanostructures.

Thus, by altering the nature of the surfactant system we present a simple solution phase synthesis for the formation of highly branched, high surface area palladium nanostructures.

Time Dependent Reactions. To investigate the mechanism of growth for the highly branched nanostructures intermediates were isolated by varying the reaction time of a 1:1 mixture of oleic acid and oleylamine.

Reaction times were shortened to 20, 30, 80, and 120 min, and images of the individual nanoparticles formed are shown in Figure 2 panels a, b, c, and d, respectively.

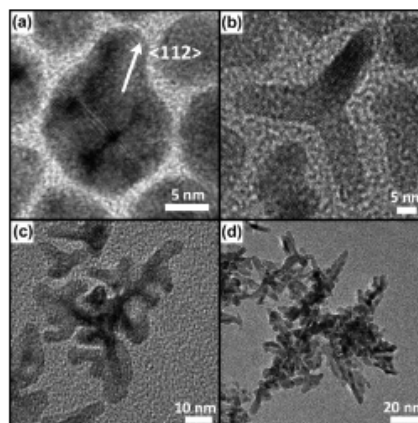


Figure 2. HRTEM images showing the evolution of the highly branched nanostructures: (a) icosahedra with small leg beginning to grow in the $[112]$ direction; (b) tripod-shaped nanoparticle formed after 30 min; (c) intermediate morphology after 80 min; and (d) fully formed nanostructure after 120 min.

VOL. 4 • NO. 1 • 396–402 • 2010 ACSNANO

397

A low magnification TEM image of the nanoparticles formed after 20 min is also shown in Supporting Information, Figure S1. The nanoparticles formed after 20 min were predominantly nanoparticles with polyhedra shapes similar to those shown in Figure 1a,b.

Figure 2a (20 min) shows a nanoparticle 14 nm in size. Analysis of the atomic packing indicates this nanoparticle is a multiply twinned fcc icosahedra viewed down a $\langle 112 \rangle$ zone axis. This is similar to the nanoparticle seen in Figure 1b except the nanoparticle shown here displays the start of single branched growth in the $[112]$ direction.

Figure 2b (30 min) shows a nanoparticle 45 nm in size which displays a tripod morphology. A tripod morphology forms when arm growth occurs in three symmetry equivalent $[112]$ directions from multiply twinned fcc icosahedra.³⁰

The particle in Figure 2c (80 min) is 65 nm in size and retains the tripod backbone with 3-fold symmetry. However, a secondary type of growth has now occurred from the tripod arms. This growth occurs along random crystallographic directions and leads to a broad, leaflike structure.

Figure 2d (120 min) displays a nanoparticle 100 nm in size. The secondary growth has continued at various angles away from the tripod backbone leading to a high surface area branched structure. The final reaction product formed after 160 min was shown in Figure 1d. Extensive branching has occurred along radial directions from the particle core to give a highly branched morphology.

In-Situ X-ray Diffraction. To understand the kinetics of nanoparticle growth for the as synthesized palladium nanostructures, *in situ* synchrotron X-ray diffraction (XRD) experiments were carried out. Since it is difficult to gain information on growth kinetics with post synthetic characterization techniques, *in situ* XRD was needed as a method that can measure structural dynamics in real time. Experiments were performed at the Stanford Synchrotron Radiation Lightsource (SSRL) on beamline 7-2 (see Supporting Information for experimental procedure). These were carried out in a specially made reaction cell shown in Supporting Information, Figure S2.

Figure 3a shows the (111) reflection of palladium tracked over the course of a typical reaction displaying the formation of a crystalline product in a 1:1 reaction with oleic acid and oleylamine. To ensure that the time scale of the reaction better suited synchrotron experiments, the cell temperature was raised to 35 °C; 10 °C above that used to form the nanoparticles used in EM observation. This leads to a slight decrease in reaction times when compared to HRTEM experiments. The full width at half-maximum of the diffraction peak provides a measure of the crystallite size in the nanostructures. This remained relatively constant throughout both experiments, which is consistent with the multiply

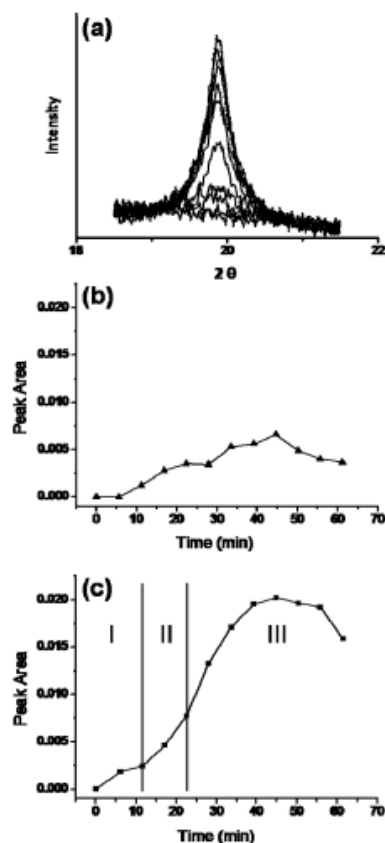


Figure 3. Time resolved synchrotron XRD results tracking the growth of the palladium nanostructures: (a) *In-situ* XRD results showing the evolution of crystalline palladium by tracking the Pd(111) reflection for the 1:1 reaction, (b) peak area vs reaction time plot for the 1:0 reaction and (c) for the 1:1 reaction.

twinned nature of the nanostructures. The lattice parameter calculated from the peak positions was independent of reaction time and close to the bulk value indicating little or no lattice strain. However, due to peak broadening and uncertainty in the measurements some undetected strain may be present, particularly at the initial reaction times when the diffraction peak is at its weakest and broadest. The measured diffraction signal is from crystalline nanostructures in solution as there was no deposition of product on the cell window at the completion of the reaction.

To investigate the difference in reaction kinetics between the formation of palladium polyhedra and highly branched nanostructures, experiments in oleylamine and a 1:1 mixture of oleic acid and oleylamine were carried out as shown in Figure 3b,c, respectively. These

both show the continuous growth of the Pd(111) peak area over time.

Figure 3b shows the growth of nanocrystalline palladium to form palladium polyhedra when only oleylamine is used (1:0 reaction). The plot shows a steady, nearly linear increase that reaches a maximum at 45 min. The slope of the growth line is constant which indicates a steady growth rate throughout the experiment. The peak area then decreases as the particles grow too large to remain in suspension and settle out of the beam path.

When a surfactant system containing oleic acid in a 1:1 ratio with oleylamine is employed (1:1 reaction) different growth characteristics emerge (Figure 3c). Here, the growth of the nanostructures progresses in three distinct stages. Stage I shows steady initial growth with a slope similar to the 1:0 case. In Stage II the slope and growth rate increases 2-fold and continues at this rate for 10 min. Stage III shows a further 2-fold increase in growth rate when compared to Stage II. The peak area then begins to decrease as growth ceases and settling occurs.

Growth Mechanism. The above HRTEM and XRD experiments show that the growth and kinetics of formation of highly branched palladium nanostructures are distinctly different to the formation of the palladium polyhedra.

For the 1:0 reaction there is a relatively slow and constant growth rate, as shown in Figure 3b, which results in the polyhedra nanoparticle shapes observed in Figure 1a. This slow, constant growth indicates that for the 1:0 reaction, growth occurs under thermodynamic control to produce thermodynamically favored polyhedra.³¹

In contrast, for the 1:1 reaction (Figure 3c) there are three distinct growth stages leading to the formation of the highly branched nanostructures. Each stage possesses different growth kinetics as described as follows (Stages I–III).

Stage I. The growth rate for Stage I of the 1:1 reaction is relatively slow and comparable to the growth rate of the entire 1:0 reaction. For this stage, HRTEM analysis shows the formation of multiply twinned fcc icosahedral nuclei (Supporting Information, Figure S1). This is the same polyhedra structure formed in the 1:0 reaction (see Figure 1a,b). Therefore, during the slow growth of Stage I of the 1:1 reaction, thermodynamically favored multiply twinned fcc icosahedral nuclei form.

Stage II. During Stage II of the 1:1 reaction there is a 2-fold increase in the growth rate when compared to Stage I. This indicates growth is no longer thermodynamically controlled and kinetically controlled growth conditions are present.³¹

In solution phase synthesis of nanoparticles, kinetically controlled growth conditions can lead to branched growth. This process was observed in Figure 2a with

the start of branched growth from a multiply twinned icosahedral nuclei. In our case novel tripod shapes form due to branch growth occurring along three symmetry equivalent [112] directions from the icosahedral nuclei (Figure 2b).³⁰

Therefore, as palladium crystallizes in the highly symmetrical fcc crystal structure the formation of a branched shape requires both a breaking of the crystal symmetry, introduced through defects in the icosahedral nanoparticle nuclei, and growth conditions which are kinetically controlled.

It should be noted that although the nanoparticles in Stage II are now growing under kinetic control, growth is still occurring along selected crystallographic directions.

Stage III. In Stage III there is another 2-fold increase in the growth rate compared to Stage II. This increase follows the formation of the tripod branches and is due to the start of the secondary growth observed in Figure 2c. This secondary growth leads to a "leaflike" structure off the tripod backbone. The growth rate is now four times as fast as in Stage I which indicates this type of secondary growth is fast and kinetically controlled, occurring very far from thermodynamically controlled conditions.

Because of the rapid rate and distinctly kinetic nature of the ultrafast growth, the adatom adsorption rate does not depend on the crystal facet where adsorption occurs. Hence growth occurs along no preferred crystallographic direction.³² This leads to randomly oriented branch growth occurring in any radial direction away from the particle core to give the highly branched morphology.

In contrast, the extensive branching observed in dendritic nanostructures formed in the solution phase is dependent on crystallographic direction and is typically a result of diffusion limited aggregation or oriented attachment mechanisms.^{18–20} The ultrafast kinetic growth described here leads to branching irrespective of the crystal facet. Therefore, this growth provides a route toward the formation of complex nanoparticle shapes from nuclei with any morphology and surface energy.

Following the ultrafast growth (after 45 min, end of stage III) the peak area begins to decline as the nanoparticles settle out of the beam path.

Therefore, from HRTEM and XRD experiments, the formation of the palladium polyhedra nanoparticles is shown to occur through slow, thermodynamically controlled growth. In contrast, formation of the highly branched nanostructures occurs through (i) the formation of multiply twinned fcc icosahedral nuclei, (ii) kinetically controlled branch growth to form a tripod backbone, and (iii) ultrafast secondary kinetic growth occurring in any crystallographic direction from the tripod arms.

Effect of Surfactant System on Reaction Kinetics. In the present system, the kinetics of growth, and hence the final particle morphology, are controlled by the surfactant system. The difference in surface stabilization ability of the amine and acid functionalities determines the growth kinetics by controlling the rate of monomer supply to the nanoparticle surface.³³

When the rate of adatom diffusion across the particle surface to stable positions is faster than the rate of adatom adsorption, growth is thermodynamically controlled and thermodynamically favored morphologies form. Conversely, when adatom adsorption occurs at a faster rate, growth becomes kinetically controlled leading to more complex nanoparticle shapes.³¹

The carboxylic acid functionality of oleic acid possesses a weaker binding strength to palladium compared to the amine functionality of oleylamine.^{34,35} Introducing weaker binding oleic acid (1:1 reaction) will reduce the overall degree of surface stabilization of the growing particle by the surfactant system. This allows rapid adatom adsorption and kinetically controlled growth conditions resulting in highly branched structures.

This is in contrast to the 1:0 reaction where oleylamine binds strongly to the surface of the growing particle. Therefore, the icosahedral nuclei experience strong stabilization effects hindering adatom adsorption. Growth conditions are then thermodynamically controlled and thermodynamically favored polyhedral structures are maintained.

An additional experiment was performed to verify the proposed surface capping mechanism. When purely oleic acid is used as surfactant micrometer sized crystallites form; presumably because there is not enough stabilizing ability by oleic acid to restrict growth to the nanoscale for this system (see Supporting Information, Figure S3).

Catalysis. Highly branched nanostructures are ideally suited to catalysis as high surface area and the presence of high index facets lead to increases in catalytic activity. High index facets have a higher density of atomic steps, ledges, kinks, and dangling bonds, all of which often exhibit much higher reaction activities.^{36,37}

Here, HRTEM experiments were used to probe the nature of the surface for the highly branched nanostructures. Figure 4a shows an HRTEM image of one of the nanoparticle branches viewed down a $\langle 110 \rangle$ direction. A close up of the branch is shown in Figure 4b. Analysis of the atomic packing in Figure 4b confirms the presence of high index facets. The arrows point to atomic vacancies on the branch edge which create a series of alternating (200) and (111) microfacets. These microfacets combine to form the high index (113) facet. This is shown schematically in Figure 4c.

To test the catalytic properties, the palladium nanostructures were supported onto activated carbon and the resulting catalysts (Pd-NS/C) were examined and

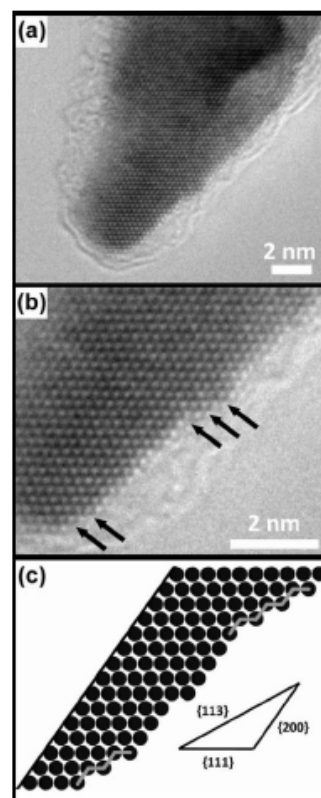


Figure 4. Analysis of the surface of one of the highly branched nanostructures: (a) HRTEM image of one of the particle branches; (b) close-up HRTEM image of the particle branch showing clear atomic packing. The black arrows point to atomic vacancies on the particle surface. (c) Schematic showing how the atomic vacancies lead to high index (113) facets.

compared to commercially available palladium catalysts (Johnson Matthey 1% Pd/C 87 L) for the hydrogenation of nitrobenzene (see Supporting Information for experimental procedure). The catalytic hydrogenation of nitrobenzene to aniline is commonly used as a standard test for the activity of heterogeneous catalyst systems.³⁸ In addition to this, the reaction has great commercial importance in its own right. In the industrial production of aniline for the polyurethane industry.³⁹ The carbon-supported palladium was used at a 1:1000 ratio with respect to the substrate, under 2 bar of H_2 at 50 °C in a Buchi pressflow gas-controlled Baskerville autoclave.

The Pd-NS/C material reproducibly showed considerable activity for the hydrogenation of nitrobenzene. After 30 min, there was no further hydrogen uptake, indicating that the reaction had reached completion.

Subsequent analysis by gas chromatography confirmed this, revealing that all of the starting material had been consumed and aniline was the sole product. The formation of intermediate products such as hydroxylamines, oximes, or para-aminophenols was not observed; the presence of which can be observed in less active catalytic systems or those that have been deliberately poisoned.⁴⁰

The commercially available catalyst was also examined under the same reaction conditions. In this case, the reaction was complete within 20 min, again with complete conversion to the desired product. However, with the higher dispersion of this catalyst, this increase in activity is to be expected. What is significant is that the Pd NS/C catalysts display activities nearly the same as that of commercially available analogues, despite the presence of residual oleylamine stabilizing ligands. The novel shapes of the palladium nanostructures offer the possibility of the unique facets to provide alternative selectivities for specific chemoselective reactions. The investigation into such transformations is ongoing.

CONCLUSION

In conclusion, we have synthesized highly branched palladium nanostructures terminated by high index facets in a room temperature solution phase synthesis. By varying the nature of the surfactant system we are able

to control the growth kinetics and hence the particle morphology. The highly branched nanostructures grow from multiply twinned fcc icosahedra nuclei via a tripod intermediate. A type of secondary ultrafast kinetic growth then occurs from the tripod intermediate along no specific crystallographic direction resulting in highly branched nanostructures.

The palladium nanostructures demonstrate good activity in the hydrogenation of nitrobenzene to aniline where the production of the desired product occurs at a similar rate to commercially available catalysts. The tuning of the morphology of the metal also offers the possibility of varying the selectivity of industrially important organic transformations.

These results and the proposed growth mechanism contribute to the understanding of the formation of highly branched nanostructures from the highly symmetrical fcc crystal structure. The ultrafast kinetic growth observed is not dependent on crystal facet energy and therefore provides a route to complex nanoparticle shapes from any nuclei morphology. The development of a room temperature solution phase synthesis for the formation of highly branched palladium nanoparticles is important for catalytic applications where high surface area and high index facets are known to greatly improve catalytic performance.

EXPERIMENTAL SECTION

Synthesis of Highly Branched Palladium Nanoparticles. In a typical synthesis, 0.1 mmol of palladium precursor (bis(acetonitrile) palladium dichloride, 99%, Aldrich) was added to 1 mL of toluene. To this was added 10 equiv of organic surfactant in total. The palladium precursor was then decomposed under hydrogen in a pressure reaction vessel (Fischer–Porter bottle). Samples were purified by the addition of an equal amount of methanol to flocculate the nanoparticles, use of a centrifuge at 14 000 rpm for collection, and subsequent washing with dichloromethane and toluene. The samples for TEM studies were prepared by resuspending the precipitate in toluene. One drop of toluene suspension was placed on a copper TEM grid and allowed to evaporate in ambient conditions. The TEM images and corresponding diffraction patterns were taken on a JEOL 2010 operated at an acceleration voltage of 200 keV.

Synchrotron X-ray Diffraction (XRD). Experiments were performed at the Stanford Synchrotron Radiation Lightsource (SSRL) on BL7-2 in a specially made reaction cell shown in Supporting Information, Figure S2.⁴¹ The cell was 30 mm high and 20 mm wide and was placed in a ceramic heating block on the beamline. It contained a circular reaction chamber 5 mm in diameter and 1 mm thick which was aligned with the beam. The cell windows were made from X-ray transparent Kapton (polyimide) film. A 50 μ L portion of reaction solution was injected into the reaction chamber which was then filled with 3 bar H₂. The experiments were conducted using radiation of $\lambda = 1.0 \text{ \AA}$ (12.4 keV). Diffraction patterns were collected over the Pd(111) peak between 2θ values of 18° and 22°, using step scans of 0.02°/step. Growth of the fcc Pd(111) diffraction peak was observed and monitored every 300 s, for 70 min.

Catalysis. Pd NS/C catalysts were prepared by dissolving Pd NS in toluene, using sonication. The resulting black suspension was stirred at room temperature for 18 h with sufficient activated carbon (1.0 g of activated carbon) to generate a 1% (by weight)

Pd NS/C catalyst. After this time, the resulting suspension was filtered, revealing a clear filtrate. The subsequent black solid was thoroughly washed with toluene (100 mL), methanol (100 mL), water (100 mL), and methanol (100 mL) in order to remove any excess ligands present. The solid was then dried in a vacuum oven before use. The Pd NS/C was compared in the hydrogenation of nitrobenzene with 1% Pd/C (Johnson Matthey, 87 L). The test was undertaken using a Baskerville autoclave connected to a Buchi pressflow gas controller. The reaction occurred at 50 °C, under 2 bar of dihydrogen, and stirred at approximately 1000 rpm. In each test, 5 mL of a 0.1 M methanol solution of nitrobenzene (containing 0.1 M of mesitylene) was used with a 1:1000 molar ratio of metal to substrate. Subsequent GC analysis was undertaken using a CPSIL-5 column, with mesitylene as an internal standard.

Acknowledgment. R.D.T. and J.W. gratefully acknowledged financial support from the MacDiarmid Institute and VUW. Portions of this research were carried out at the Stanford Synchrotron Radiation Laboratory, a national user facility operated by Stanford University on behalf of the U.S. Department of Energy, Office of Basic Energy Sciences.

Supporting Information Available: HRTEM image of palladium nanoparticles formed after 20 min; image of Synchrotron reaction cell; and HRTEM image of palladium nanostructures formed using only oleic acid as surfactant. This material is available free of charge via the Internet at <http://pubs.acs.org>.

REFERENCES AND NOTES

- Murphy, C. J.; San, T. K.; Gole, A. M.; Orendorff, C. J.; Gao, J. X.; Gou, L.; Hunyadi, S. E.; Li, T. Anisotropic Metal Nanoparticles: Synthesis, Assembly, and Optical Applications. *J. Phys. Chem. B* **2005**, *109*, 13857.

2. Jun, Y. W.; Choi, J. S.; Cheon, J. Shape Control of Semiconductor and Metal Oxide Nanocrystals Through Nonhydrolytic Colloidal Routes. *Angew. Chem., Int. Ed.* **2006**, *45*, 3414.
3. Burda, C.; Chen, X. B.; Narayanan, R.; El-Sayed, M. A. Chemistry and Properties of Nanocrystals of Different Shapes. *Chem. Rev.* **2005**, *105*, 1025.
4. Xia, Y.; Xiong, Y. J.; Lim, B.; Skrabalak, S. E. Shape-Controlled Synthesis of Metal Nanocrystals: Simple Chemistry Meets Complex Physics. *Angew. Chem., Int. Ed.* **2009**, *48*, 60.
5. Klabunde, K. J., *Nanoscale Materials in Chemistry*, John Wiley & Sons, 2001.
6. Suleiman, M.; Jlsrawi, N. M.; Dankert, O.; Reetz, M. T.; Bahtz, C.; Kirchheim, R.; Pundt, A. Phase Transition and Lattice Expansion During Hydrogen Loading of Nanometer Sized Palladium Clusters. *J. Alloy. Comp.* **2003**, *356*, 644.
7. Pundt, A.; Suleiman, M.; Bahtz, C.; Reetz, M. T.; Kirchheim, R.; Jlsrawi, N. M. Hydrogen and Pd-Clusters. *Mater. Sci. Eng., B* **2004**, *108*, 19.
8. Xiong, Y. J.; Wiley, B.; Chen, J. Y.; Li, Z. Y.; Yin, Y. D.; Xia, Y. N. Corrosion-Based Synthesis of Single-Crystal Pd Nanoboxes and Nanocages and Their Surface Plasmon Properties. *Angew. Chem., Int. Ed.* **2005**, *44*, 7913.
9. Younan, X.; McLellan, J. M.; Yujie, X.; Min, H. Surface-Enhanced Raman Scattering of 4-Mercaptopyridine on Thin Films of Nanoscale Pd Cubes, Boxes, and Cages. *Chem. Phys. Lett.* **2006**, *417*, 230.
10. Blaser, H. U.; Indolese, A.; Schnyder, A.; Steiner, H.; Studer, M. Supported Palladium Catalysts for Fine Chemicals Synthesis. *J. Mol. Catal.* **2001**, *173*, 3.
11. Bowker, M. Automotive Catalysis Studied by Surface Science. *Chem. Soc. Rev.* **2008**, *37*, 2204.
12. Ramirez, E.; Jansat, S.; Philippot, K.; Lecante, P.; Gomez, M.; Masdeu-Bulto, A. M.; Chaudret, B. Influence of Organic Ligands on the Stabilization of Palladium Nanoparticles. *J. Organomet. Chem.* **2004**, *689*, 4601.
13. Ren, J. T.; Tilley, R. D. Preparation, Self-Assembly, and Mechanistic Study of Highly Monodispersed Nanocubes. *J. Am. Chem. Soc.* **2007**, *129*, 3287.
14. Ren, J.; Tilley, R. D. Shape-Controlled Growth of Platinum Nanoparticles. *Small* **2007**, *3*, 1508.
15. Bradley, J. S.; Tesche, B.; Busser, W.; Masse, M.; Reetz, R. T. Surface Spectroscopic Study of the Stabilization Mechanism for Shape-Selectively Synthesized Nanostructured Transition Metal Colloids. *J. Am. Chem. Soc.* **2000**, *122*, 4631.
16. Penisson, J. M.; Renou, A. Structure of an Icosahedral Palladium Particle. *Z. Phys. D: At., Mol. Clusters* **1989**, *12*, 113.
17. Penisson, J. M.; Renou, A. Structure of an Icosahedral Palladium Particle. *J. Cryst. Growth* **1990**, *102*, 585.
18. Zhou, P.; Dai, Z. H.; Fang, M.; Huang, X. H.; Bao, J. C.; Gong, J. F. Novel Dendritic Palladium Nanostructure and Its Application in Biosensing. *J. Phys. Chem. C* **2007**, *111*, 12609.
19. Wen, X. G.; Xie, Y. T.; Mak, W. C.; Cheung, K. Y.; Li, X. Y.; Renneberg, R.; Yang, S. Dendritic Nanostructures of Silver: Facile Synthesis, Structural Characterizations, and Sensing Applications. *Langmuir* **2006**, *22*, 4836.
20. Xiao, J. P.; Xie, Y.; Tang, R.; Chen, M.; Tian, X. B. Novel Ultrasonically Assisted Templated Synthesis of Palladium and Silver Dendritic Nanostructures. *Adv. Mater.* **2001**, *13*, 1887.
21. Zhang, H. T.; Ding, J.; Chow, G. M. Morphological Control of Synthesis and Anomalous Magnetic Properties of 3-D Branched Pt Nanoparticles. *Langmuir* **2008**, *24*, 375.
22. Yin, Z.; Zheng, H. J.; Ma, D.; Bao, X. H. Porous Palladium Nanoflowers That Have Enhanced Methanol Electro-oxidation Activity. *J. Phys. Chem. C* **2009**, *113*, 1001.
23. Elchiguerra, J. L.; Reyes-Gasca, J.; Yacaman, M. J. The Role of Twinning in Shape Evolution of Anisotropic Noble Metal Nanostructures. *J. Mater. Chem.* **2006**, *16*, 3906.
24. Berhaut, G.; Bausach, M.; Bisson, L.; Becerra, L.; Thomazeau, C.; Uzio, D. Seed-Mediated Synthesis of Pd Nanocrystals: Factors Influencing a Kinetic- or Thermodynamic-Controlled Growth Regime. *J. Phys. Chem. C* **2007**, *111*, 5915.
25. Xiong, Y. J.; Cai, H. G.; Yin, Y. D.; Xia, Y. N. Synthesis and Characterization of Fivefold Twinned Nanorods and Right Bipyramids of Palladium. *Chem. Phys. Lett.* **2007**, *440*, 273.
26. Choo, H.; He, B. L.; Liew, K. Y.; Liu, H. F.; Li, J. L. Morphology and Control of Pd Nanoparticles. *J. Mol. Catal.* **2006**, *244*, 217.
27. Xiong, Y. J.; Cai, H. G.; Wiley, B. J.; Wang, J. G.; Kim, M. J.; Xia, Y. N. Synthesis and Mechanistic Study of Palladium Nanobars and Nanorods. *J. Am. Chem. Soc.* **2007**, *129*, 3665.
28. Xiong, Y. J.; Xia, Y. N. Shape-Controlled Synthesis of Metal Nanostructures: The Case of Palladium. *Adv. Mater.* **2007**, *19*, 3385.
29. Tian, N.; Zhou, Z. Y.; Sun, S. G. Platinum Metal Catalysts of High-Index Surfaces: From Single-Crystal Planes to Electrochemically Shape-Controlled Nanoparticles. *J. Phys. Chem. C* **2008**, *112*, 19801.
30. Watt, J. Young, N. Haigh, S.; Kirkland, A.; Tilley, R. D. Synthesis and Structural Characterization of Branched Palladium Nanostructures. *Adv. Mater.* **2009**, In press.
31. Yin, Y.; Alivisatos, A. P. Colloidal Nanocrystal Synthesis and the Organic-Inorganic Interface. *Nature* **2005**, *437*, 664.
32. Lou, X. W.; Yuan, C. L.; Archer, L. A. An Unusual Example of Hyperbranched Metal Nanocrystals and Their Shape Evolution. *Chem. Mater.* **2006**, *18*, 3921.
33. Sau, T. K.; Murphy, C. J. Room Temperature, High-Yield Synthesis of Multiple Shapes of Gold Nanoparticles in Aqueous Solution. *J. Am. Chem. Soc.* **2004**, *126*, 8648.
34. Jun, Y. W.; Lee, J. H.; Choi, J. S.; Cheon, J. Symmetry-Controlled Colloidal Nanocrystals: Nonhydrolytic Chemical Synthesis and Shape Determining Parameters. *J. Phys. Chem. B* **2005**, *109*, 14795.
35. Ahlrand, S.; Chatt, J.; Davies, N. R. The Relative Affinities of Ligand Atoms for Acceptor Molecules and Ions. *Quart. Rev.* **1958**, *12*, 265.
36. Ma, Y. Y.; Kuang, Q.; Jiang, Z. Y.; Xie, Z. X.; Huang, R. B.; Zheng, L. S. Synthesis of Trisoctahedral Gold Nanocrystals with Exposed High-Index Facets by a Facile Chemical Method. *Angew. Chem., Int. Ed.* **2008**, *47*, 8901.
37. Tian, N.; Zhou, Z. Y.; Sun, S. G.; Ding, Y.; Wang, Z. L. Synthesis of Tetrahexahedral Platinum Nanocrystals with High-Index Facets and High Electro-oxidation Activity. *Science* **2007**, *316*, 732.
38. Gelder, E. A.; Jackson, S. D.; Lok, C. M. A Study of Nitrobenzene Hydrogenation Over Palladium/Carbon Catalysts. *Catal. Lett.* **2002**, *84*, 205.
39. Weissmehl, K. Arpe, H. J., *Industrial Organic Chemistry*, 3rd ed.; VCH: Weinheim, Germany, 1997.
40. Gao, J.; Wang, F. D.; Liao, S. J.; Yu, D. R. Selective Hydrogenation of Nitrobenzene to *p*-Aminophenol by the Polymer-Supported Palladium-Based Mono- and Bimetallic Catalyst. *React. Kinet. Catal. Lett.* **1998**, *64*, 351.
41. Cheong, S.; Watt, J.; Ingham, B.; Toney, M. F.; Tilley, R. D. In Situ and ex Situ Studies of Platinum Nanocrystals: Growth and Evolution in Solution. *J. Am. Chem. Soc.* **2009**, *131*, 14590-14595.